☑ neuro imaging II
☑ neurophilosophy
☐ matlab

$$e^{i\varphi} = \cos\varphi + i\sin\varphi$$
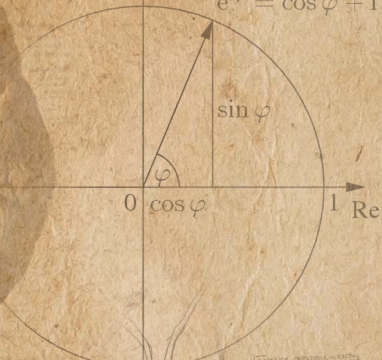
See your brain
as a sacred vase
with the right amount
of time & ingredients
incredible flowers
will prosper
even in the hardest conditions

COVID-19
Physically distant
Mentally connected

DONDERS INSTITUTE

Radboud University

Radboudumc

Proceedings of the Master's Programme Cognitive Neuroscience of the Radboud University

Table of Contents

From the Editors in Chief

Dear Reader,

As punctual as always, we are glad to present the second issue of the 16th volume of the CNS Journal.

Isn't it paradoxical that the year with the least movement and interaction between people was also the year that marked the biggest change in most people's life? This year of pandemic crisis has provided us more time and less craze from the everyday life routine, giving us the opportunity to question and rethink consolidated practices. The journal and its members felt in similar ways, looking at the entire journal structure with a new light, allowing creativity to take place where before there was normative acceptance. For instance, we recognised that the journal has not changed its layout since it was founded, hence debating over the merits of either transforming or maintaining the current design. Although at first there was some scepticism over the need for reform, we noticed increasing numbers of scientific journals are showing alternative and innovative designs, providing a friendlier exposure to scientific findings. We understood we wanted the same, creating a unique layout for our journal and, in doing so, offering a more contemporary experience to the readers as well. Therefore, differently from the last years, we would like to give a special thanks to our Layout team for the great work they have done and for their amazing creativity, making each issues and the 16.2 in particular an outstanding piece of art.

However, having begun our metamorphosis, the desire to change did not stop with the journal's appearance, leading to even more diverse ideas. For instance, we also increased internet presence by producing informative videos that cover both the general missions that this student-led journal has and the experience of its subgroups and members. Last but not least, we increased our social media presence, allowing us to reach and inform a much broader audience regarding the newest updates and events that take place. Thus, we would like to thank our only PR member, Brittany, and the EiC Annika for the impressive job done with the promotion videos and for making our journal more "social". In conclusion, the journal in this last period decided to change, to evolve, and to improve because we understood that **"To improve is to change, so to be perfect is to have changed often"** (Winston Churchill). Therefore, keep your heads up because future changes and news are coming!

Nijmegen, July 2021

Annika Mordelt, Gregorio Borghi, and Minke Schurink

Editors in Chief

From Dr. Nils Kohn

Wow, you look different in real life! This is the phrase that I've heard most often in 2021. This might be a sliver of the SciFi future that is awaiting us, but currently it's the reality for me, and I guess it's not unfamiliar to students and researchers in this academic year 20/21. Covid-19 has shaped our lives in the last year, and it has shaped the journey of all CNS master students that today publish their final thesis in this very fine outlet! They were probably expecting a rather different journey and different experiences. Nevertheless, looking at the end product of their respective traineeships, can we actually spot a difference? I can imagine that in a double blind, randomized experiment, where people had to pick out papers from before and after the pandemic, few would be able to do it. Maybe they would tend to label a paper on open source data as pandemic-paper, but that's about it.

Quite obviously, the journey was different, even if the resulting product cannot be differentiated. This fits with the topic of this issue of the CNS master journal: "The journey is the destination". I would assume that most students would not have chosen the journey they embarked upon, had they been given the choice. Does this mean you all have to despair over the fact that you did your thesis in Covid times? I would definitely argue against that. Yes, you might have missed out on some nice social aspects, like the legendary DCCN Christmas party or the equally fun Dagje Uit, and also some practical issues were maybe more difficult, as you couldn't walk into your daily supervisors office on your personal whims and ghosting you just doesn't works as well in the Trigon. For some, this period was devastating. But, there were also positive aspects. Most likely, you've been forced to be more independent than you otherwise would have been. We've all done a few things we otherwise wouldn't. Covid changed the path of our year. Sometimes, being forced to do things differently from the conventional ways can create a completely different and astonishing perspective. We will have to determine which things we surely do want to change back again after this pandemic, and which things were not too bad. We've all taken a few extraordinary lessons in the past year, time will tell which of those were the most important ones! In the spirit of this issue, it was special, and it's on every one of us to make the best of this!

You've learned new things more independently and perhaps did not receive as much guidance. This might have been a hindrance, but you came up with own ways of doing things, this provides an opportunity; an opportunity to break things! Or, at least change them. Many parts of academic life are highly antiquated and incentivise behavioural patterns that are detrimental to open and curious academic discourse. Be it old fashioned, publisher-benefiting publishing, broken peer reviewing or inefficient grant rat-races. There's a lot that deserves to be broken up. Indeed, they're in danger of staying in lethal rigidity in fear of change. A little pushing and shoving won't make them fall apart. I hope all of you play their part in breaking down and rebuilding science, to make it fairer, driven by curiosity and awe, gentleness and ingenuity, rather than greed or fear.

Finally, best of all, this was only the start of the journey! In your career as researcher, or any other calling, the most central aspect (besides having fun!) is learning and growing with every step. You've had a tough year with sub-optimal conditions, but this will prepare you even more for the things to come. I'm really curious about the lessons we take from this period, just as curious as I am about the contributions to science and society you all will be making after your graduation!

Nils Kohn

About the Cover

I find the sketches and drafts in notebooks of great artists significantly more interesting than their final masterpieces. It is like immersing yourself in their fluctuating thoughts. It gives us the opportunity to read their feelings while they were drawing, writing, preparing their masterpiece of art.

From here the idea to not design a final masterpiece, but to collect all the unique sketches made during the last months of this CNS master. I was inspired by the notebooks of Leonardo da Vinci and hopefully I have been able to transmit a bit of the same style and energy.
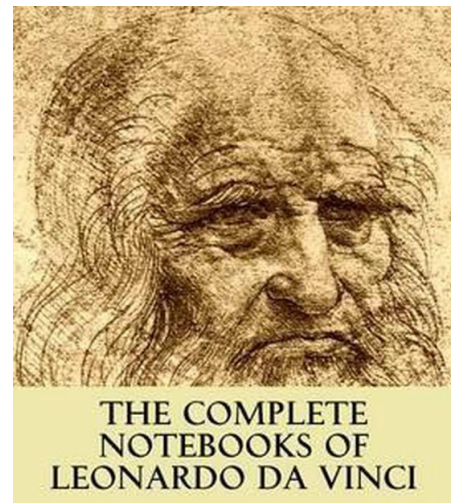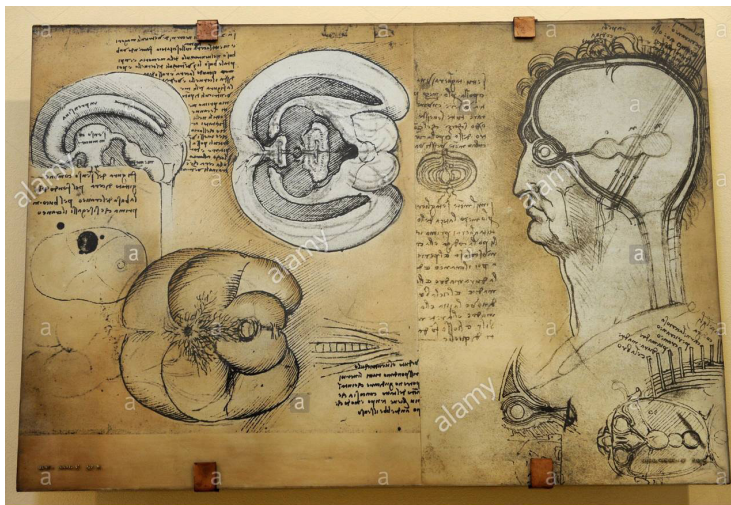
Furthermore, when you zoom in on the cover, many other little drawings, notes and to do lists will appear; study for Neuroimaging 2, failed for Matlab, Euler's formula, feelings regarding COVID-19 like we are physically all so far from each other but mentally still connected thanks to online activities.
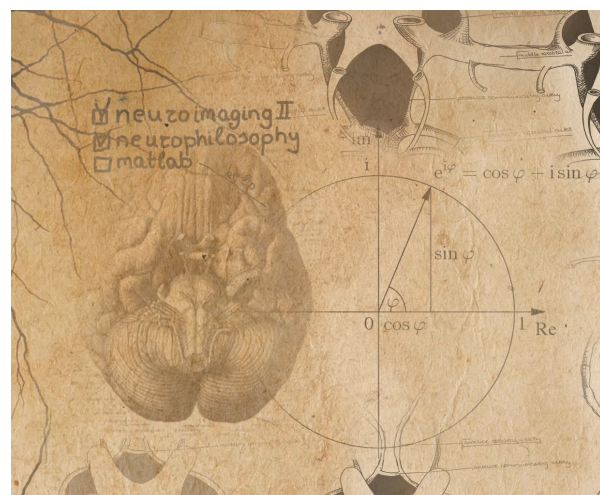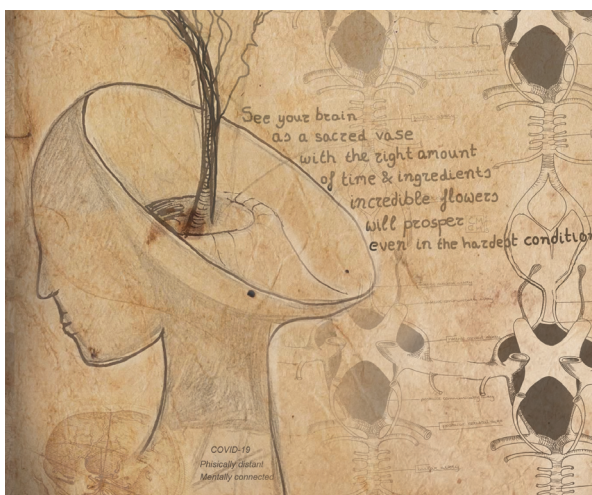
Carmen Heuvelmans

Meet the Journal Team: Subeditors

Do you also get overly excited to correct typos? Are you confident you **actually** know the difference between you're and your? Then you should probably join the subediting team! Our job is to ensure that all the theses published in the journal are well-written and coherent, but also that they adhere to the journal's guidelines. I am fully aware that this makes us sound like a glorified grammar police, but trust me when I say that being a subeditor is much more than that. I personally was drawn to this role as here you get the most familiar with the actual thesis; both with its words and writing style, but also the content. When subediting a paper, you get the chance to revise every paragraph and edit every figure, so you really get a feel for the student's work. I always enjoy looking through the text, ensuring that the author is making the point that they want to make in the most comprehensible way.

I remember that for my first ever issue, I subedited a thesis from a previous student that was about the role of white matter tracts on language production in individuals with Aphasia – exactly the kind of research I was interested in conducting myself. Reading her paper actually motivated me to do my first lab rotation with one of her supervisors which ended up being a great experience. Thus, as a subeditor, you really get to learn about the kind of research the previous CNS cohorts have done and can get inspired with ideas for your own internship. Besides that, I think that being a subeditor also prepares you extremely well for writing your own thesis and future journal articles. You learn how to structure your work in a convincing and articulate way, and you also get familiar with the publishing process in general.

After four issues of being a subeditor, I can say that I have learnt a few things. First of all, I used to think that a neuroscientist's biggest struggle is finding funding for their research or getting significant results, but now I know that doing correct APA citations seems to be equally challenging. Moreover, I learnt that having a completely student-led journal is not only possible, but also a lot of fun. Lastly, I realized that we do pretty incredible research in this Master's programme and I really enjoyed having the opportunity to share our students' amazing work with every new issue.

Antonia Jordan Monteiro de Barros

Time-Varying Temporal Functional Modes: A Novel Model to Probe Time-Varying Functional Reconfigurations in fMRI While Accounting for Shared Anatomical Infrastructure

Tamara de Kloe[1,2]

Supervisors: Alberto Llera Arenas[1,2], Nils Kohn[1,2], and Christian F Beckmann[1,2,3]

Corresponding author: Tamara Jedidja de Kloe
E-mail: t.dekloe@donders.ru.nl

[1]*Donders Institute for Brain, Cognition and Behaviour, Radboud University, Nijmegen, The Netherlands*
[2]*Department of Cognitive Neuroscience, Radboud University Medical Centre, Nijmegen, The Netherlands*
[3]*Wellcome Centre for Integrative Neuroimaging, FMRIB Building, Nuffield Department of Clinical Neurosciences, University of Oxford, Oxford, United Kingdom*

The core cognitive neuroscientific aim is to determine how the brain gives rise to mental function. The answers provided to this ontological question depend in part on predominant methodology. Initial functional magnetic resonance imaging (fMRI) studies were mainly segregationist, that is, focused on mapping psychological functions to individual brain sites. The modularity hypothesis underlying this approach, however, has been questioned since its conception. Conversely, it is argued that mental function relies on interactions within and between integrated functional brain networks. This is, for example, studied using functional connectivity methods, which examine co-variation of spatially distributed signals emitted from the brain. Time-averaged estimates of functional connectivity are commonly obtained. A recent line of research, however, aims to probe time-varying changes in connectivity, based on the premise that biologically meaningful changes in inter-regional relations are expected to occur. In this work, we present a novel time-varying functional connectivity method that explicitly accounts for spatial overlap, that is, for functional networks to share a common anatomical infrastructure. The model is an extension of the work by Smith et al. (2012), in which a spatial decomposition and a temporal independent component analysis are applied consecutively, resulting in functionally distinct and spatially overlapping networks called "Temporal Functional Modes" (TFMs). The extent to which TFMs recruit spatial parcels (described by the TFM mixing matrix) remains time-invariant in the original model. Here, we introduce a time-resolved version of TFMs to account for the time-varying nature of functional connectivity. We show analytically that the fixed mixing matrix in classical TFM analysis is the temporal average of a time-varying mixing matrix which can be obtained in closed form and which represents moment-by-moment estimations of brain network reconfigurations. We apply the novel method to a high-temporal resolution fMRI dataset and demonstrate that the retrieved network reconfigurations follow the expectation based on the task design.

KEYWORDS time-varying functional connectivity, dynamic functional connectivity, independent component analysis, temporal functional modes, spatial overlap

Much like glasses through which one views the world, the choice of method critically determines the questions that can be asked and the limits of what can be observed in studying brain function. In the last few decades, neuroimaging has become an essential tool for studying the temporal dynamics and spatial topology of the brain in vivo. The former is usually studied using electroencephalography (EEG), and for the latter, functional magnetic resonance imaging (fMRI) is most common due to their relatively high temporal and spatial resolution, respectively (Bandettini, 2009; Rosa et al., 2010). Initial fMRI studies probed the neural substrates of brain function within a segregationist paradigm, focusing on mapping psychological function to individual activation sites. The corresponding methodological approach consists of per-voxel comparisons of blood oxygen level-dependent (BOLD) signals to the expected time series, based on experimental designs constructed to single out a cognitive function. Statistical tests on these comparisons provide maps that show what parts of the brain are associated with that particular cognitive function (Poldrack et al., 2011; Smith et al., 2004). Inherent to this mass-univariate approach is that voxels are studied independently, hence precluding examination of integration or collaboration. Since the discovery that spatially distinct and temporally synchronized brain regions can be differentiated in fMRI (Biswal et al., 1995), the field has started to characterise these integrated functional networks. A complementary integrationist approach is adopted, focused on characterizing integrated, spatially distributed functional brain networks and their role in cognition (Eickhoff & Muller 2015).

Methods for Studying Integration in fMRI

Integrated functional brain networks can be probed using functional connectivity methods. Popular methods such as seed-based correlation analysis (SCA; Biswal et al., 1995) and spatial independent component analysis (ICA; Beckmann and Smith, 2004; Beckmann, 2012; McKeown and Sejnowski, 1998) have reliably differentiated these networks termed resting-state networks across participants (Beckmann et al., 2005; Damoiseaux et al., 2006), both in rest and during tasks (Smith et al., 2009). Alterations in functional connectivity of large-scale brain networks have proven to relate to cognition (e.g., Laird et al., 2011), behaviour (Rosazza and Minati, 2011), human development (Uddin, Supekar & Menon, 2010), and personality (Mulders et al., 2018). Moreover, they show promise as a biomarker, as they relate to a variety of pathologies such as depression (Mulders et al., 2015; Greicius et al., 2007), schizophrenia (Lynall et al., 2010), and Alzheimer's disease (Damoiseaux et al., 2012; Greicius et al., 2004; Lehmann et al., 2015; Lustig et al., 2003).

Functional connectivity is conceptually described as communication between brain areas to support cognitive function. Methodologically, it concerns statistical association between spatially distinct brain regions (Friston et al., 1993). The first described method, SCA, obtains correlations between a previously defined region of interest and all other parts of the brain. This allows for hypothesis-driven analyses, for example, probing whole-brain connectivity of an area that has previously been related to a particular cognitive function. This approach, however, restricts the analysis to one chosen region or system, although connectivity changes between other regions might occur (Bijsterbosch, 2017). The second method, spatial ICA, is a multivariate and model-free blind source separation technique that assumes that the fMRI signal consists of a linear combination or mixture of signals from different sources. The signals are decomposed ("unmixed") into a set of spatial components that are statistically maximally independent by extracting non-Gaussian sources (Beckmann and Smith, 2004; Beckmann et al., 2005; Beckmann, 2012). The extracted components are generally understood as brain networks that show similar BOLD activity (McKeown, 2003). The data can also be decomposed in temporally independent sources using temporal ICA. Of the two, spatial ICA is more common in fMRI. An important reason is that in fMRI, the spatial dimension is generally much larger than the temporal dimension (i.e., more voxels than volumes are obtained; Smith et al., 2012; Calhoun et al., 2001). In either case, the sources are described by means of a

spatial map and a corresponding time series. Both these spatial and temporal features can subsequently be related to behaviour or be compared between certain groups of individuals. Almost all available ICA-based functional connectivity studies are performed in resting-state. In part, because this does not provide a behavioural benchmark to which the time series can be related like in task-based fMRI, the gold standard is to statistically compare the spatial maps across individuals or groups, for example, to inform on significant differences in strength, shape or location of the networks (Bijsterbosch et al., 2018).

Time-varying functional connectivity

Rationale

Most functional connectivity methods assume that the dependence structure between brain regions is constant over the course of an fMRI scan or experimental condition. In SCA, for example, average correlations between BOLD signals of specific seed and target regions over an entire scan duration or condition are used as a proxy for the network behaviour. In spatial ICA, the spatial map weights, which reflect the connection strengths between regions, are constant over time (Hutchison et al., 2013). Many significant advances have been made in understanding large-scale brain networks while working under this assumption. A recent line of research, however, posits that it fails to capture the expected changes in interactions between, or shifts in dominance of, large-scale brain networks (Liégeois et al., 2017, 2019; Lurie et al., 2020; Preti et al., 2017). It is argued that characterisation of time-varying functional connectivity metrics is required, that is, time-varying changes in integration of spatially distributed functional brain networks should be examined. The term often used in the literature is "dynamic functional connectivity" (Preti et al., 2017). In a recent joint article by various leading experts in this developing field (Lurie et al., 2020), it was argued that standardisation of terminology is paramount. "Time-varying functional connectivity" (TVFC) was proposed, as differences between disciplines in use and definitions of the term "dynamic" can cause

ambiguity. Conceptually, TVFC is defined as functional connectivity that varies as a function of time, and hence concerns temporal reconfiguration of functional entities (Iraji et al., 2020). Methodologically, it means that the parameters used to describe the dependence structure between these functional entities vary across time. It was pointed out that TVFC is broader than the static-dynamic distinction, whereas this has previously (mistakenly) been taken to mean the same thing (Lurie et al., 2020). Moreover, it has been shown that certain TVFC processes fall within the space of stationary models (Liégeois et al., 2017). Thus, not every TVFC metric implies non-stationarity, which is defined by a non-constant mean and covariance (or other higher-order moments; Hutchison et al., 2013).

Time-varying functional connectivity methods

A range of TVFC methods has been suggested in recent years, which differ in several aspects. First, a distinction can be made between methods that explicitly model the underlying neural processes (i.e., dynamic biophysical models) and those that characterise the time-resolved dependence structure from the BOLD signals. A first important differentiation between methods of the latter category is the temporal window considered, ranging from individual frames or time points (i.e., instantaneous connectivity) to larger time windows (Preti et al., 2017). The functional connectivity metrics that are obtained per time point or window are either directly summarised using graph-theoretic measures, or "brain-states" are estimated using matrix factorisation techniques (e.g., k-means clustering or principal component analysis). These brain states are subsequently described using time-varying parameters such as transition probabilities and dwell times (Lurie et al., 2020; Preti et al., 2017).

Sliding-window approaches. Most methods that characterise the time-resolved dependence structure directly from the BOLD signals are variations of the sliding-window pairwise correlation approach (for a review see Preti et al., 2017). In its most rudimentary form, this consists of segmenting the entire

scan duration into smaller windows and computing a functional connectivity metric over successive (overlapping or non-overlapping) windows (Preti et al., 2017). Many extensions of this framework have been proposed, aiming to deal with the strong objection that window type and length have a substantial impact on the characterisation of the functional dynamics. On the one hand, small windows can introduce spurious correlations because of insufficient information to estimate TVFC robustly (Leonardi & Van De Ville, 2015). Given the inverse relationship between periodicity and frequency, another problem is that short windows, by definition, only allow probing high frequencies. Although there is some evidence that resting-state networks are broadband processes (Niazy et al., 2011; van Oort et al., 2012), they are generally assumed to be dominated by low-frequency oscillations (around .015Hz; Niazy et al., 2011), which will appear constant for short time windows. On the other hand, large windows smooth out the time-varying properties of interest (Hindriks et al., 2016; Iraji et al., 2020). A multivariate, ICA-based approach to sliding-window analysis has also been suggested (Kiviniemi et al., 2011). Performing spatial ICA on a sliding-window basis results in a set of independent components per window. Using this approach to analyse Default Mode Network (DMN) activity, Kiviniemi et al. (2011) concluded that DMN subnetworks dynamically change interactions throughout a full acquisition length and that activity of the whole DMN (as identified by stationary ICA) never occurs. Splitting of the DMN into multiple sub-networks, however, depends on the dimensionality of the ICA. A second objection to this multivariate ICA-based sliding window approach is that components need to be matched across windows, which is problematic since the order of components extracted using ICA is relatively arbitrary (Bijsterbosch, 2017).

Time-frequency approaches. The seminal approach in electrophysiology called time-frequency analysis has also been applied to TVFC. It explores connectivity at multiple frequencies and circumvents the described window constraints of sliding window approaches. The seminal time-frequency approach to TVFC in fMRI is Wavelet Transform Coherence (Chang & Glover, 2010), where the size of the "window", that is, the wavelet, is adjusted based on the time scale of the frequencies under inspection. Time-frequency analyses result in a description of the amount of joint power between two time series and their relative phase as a function of time and frequency. Using this approach, it has been found that within and between-network connectivity patterns differ across frequencies, suggesting the presence of overlapping interactions that are potentially averaged in classical approaches (Chang & Glover, 2010; Yaesoubi et al., 2015). A longstanding idea is that low frequency, slow-wave signals drive resting-state networks. Probing their spectral characteristics using a Hilbert-Huang transform, Niazy et al. (2011) found that although low-frequency signals indeed dominate resting-state networks, they are characterised by different frequencies at different levels of phase synchrony. That is, they were found to be broadband processes. Leading Eigenvector Decomposition Analysis (LEiDA, Cabral et al., 2017) focuses specifically on phase-coherence of the BOLD signals, where the phases are obtained using a Hilbert Transform (Deco and Kringelbach, 2016; Deco et al., 2017; Glerean et al., 2012). Identifying TVFC states is done according to the BOLD phase relative to the leading eigenvector (i.e., largest magnitude), which captures the dominant pattern of functional connectivity per time point. Focusing on the leading eigenvector per time point deals with the main objection raised against time-frequency approaches: that the output is very extensive, which limits interpretability (Hutchison et al., 2013).

Point-process and co-activation approaches. Point-process analysis assumes that all relevant information about TVFC can be extracted from short periods where BOLD signals exceed a certain threshold (Petridou et al., 2013; Tagliazucchi et al., 2016). The metric of interest here is the number of co-activations between voxels, defined by simultaneously crossing the threshold. The selection of this threshold, however, is arbitrary. Liu and Duyn (2013) suggested to only use frames where a seed time-course exceeded the threshold. Moreover, where

the metric in the original method was binary (exceeded vs. not exceeded), they suggested clustering the original fMRI volumes obtained at those frames generating so-called co-activation patterns. This brings us to a second important differentiation between data-driven TVFC methods (in addition to the time frame considered), namely, whether the temporal ordering of the data is considered. Some methods ignore temporal structure altogether, for example, clustering applied to obtain co-activation patterns, which treats time points interchangeably. Other TVFC approaches make use of the temporal structure at some stages of the analysis, for example, in estimating the phase-coherence of BOLD in LEiDA, but ignore it at other stages, for example, by subsequently applying k-means clustering (Cabral et al., 2017; Lurie et al., 2020).

Modelling approaches. Another line of TVFC methods aims not just to estimate time-varying functional connectivity fluctuations over time, but to explicitly model to temporal structure (Preti et al., 2017). Promising approaches of this sort fit multivariate dynamic models, that is, Hidden Markov Models (HMMs; Vidaurre et al., 2016, 2017) or autoregressive models (AR-1; Rogers et al., 2010) to fMRI time series. The most crucial difference being that HMMs assume the existence of discrete brain states, whereas AR-1 models are continuous, such that each time point is modelled as a linear combination of the previous ones. The latter approach was recently shown to more adequately capture task-based phenotypes than time-averaged functional connectivity measures (Liégeois et al., 2019), illustrating the potential added value of TVFC over time-averaged approaches.

Given the high dimensionality of TVFC data, previously discussed dimensionality reductions are performed in the temporal domain (resulting in loss of information on the temporal ordering of the data). Most methods also start with a dimensionality reduction in the spatial domain, called a parcellation. Instead of analysing the temporal properties based on voxel time series directly, the voxels are first summarized at a lower dimensionality. That is, voxels are grouped into brain regions that are functionally or anatomically similar.

This procedure typically results in a set of entirely separate brain regions, that is, there is no overlap between them (called a "hard parcellation"), or in regions that have minimal overlap (called a "soft parcellation"). For functional parcellations, this implies that a one-to-one mapping between cortical structure and brain function is assumed. In other words, a brain region is expected to be recruited by one functional entity only. There is no (or minimal) spatial overlap.

Accounting for Spatial Overlap: TFM Analysis

The lack of accounting for spatial overlap was formulated by Friston (1998) in a critique on spatial ICA. He argued that by inducing orthogonality in the spatial domain, it is assumed that functional networks do not share underlying anatomical structure. However, such spatial overlap is expected: first, because functional sub-units within certain regions are not separable due to the limited spatial resolution of fMRI data, and second, because certain areas supposedly participate in more than one functional network. In response, it was posited that a similar limitation occurs when enforcing orthogonality in the temporal domain due to stimulus-correlated effects (e.g., motion related to the presented stimuli) and that spatial ICA provides relatively adequate representations when spatial overlap occurs in the presence of noise (which is inherent to fMRI data; Beckmann et al., 2005). The amount of spatial overlap that spatial ICA accounts for is, however, limited (Bijsterbosch, 2017). Not accounting for spatial overlap can obscure the actual functional organization of the brain, in the words of Smith et al. (2012) because: "if two regions participate in multiple functional networks, their apparent temporal correlation will reflect the combined contribution from all networks, obscuring the true underlying functional organization. The correlation will not necessarily be meaningful, being some unknown combination of correlations caused by various distinct processes" (p. 3131). Smith et al. (2012) therefore addressed this by subsequently applying a spatial ICA and a temporal ICA decomposition. Time series of resting-state networks are hence further decomposed ('unmixed') into a set

of temporally independent components called "Temporal Functional Modes" (TFMs). Employing TFM analysis, it was found that well-established resting-state networks, for example, the DMN, involve different functional sub-processes that overlap spatially (Smith et al., 2012).

This approach has hitherto not widely been used because it requires an enormous number of samples, not generally available in fMRI studies. Recently, TFMs were obtained at the single-subject level for the first time using an ultra-fast imaging sequence (Gomez et al., 2020). This provides the opportunity to examine whether inter-individual differences in TFMs relate to psychiatric and behavioural measures. Gomez et al. (2020) performed TFM analysis both on resting-state data and on task-based data of participants performing a visuomotor association task. They found that reproducible TFMs can be found at the individual subject level. Similar TFMs were identified independent of the original spatial dimensionality reduction, and they were deemed largely free from confound contamination. Six TFMs were identified across most participants and scans, the most common of which consisted of an anti-correlated pattern between the DMN and task-positive networks termed the "default temporal mode".

TV-TFM Analysis

The extent to which TFMs recruit spatial parcels (described by the TFM mixing matrix) remains time-invariant in the original TFM model. To account for the time-varying nature of functional connectivity and simultaneously account for spatial overlap, we developed a novel, time-varying version of classical TFM (TV-TFM) analysis. We show analytically that the fixed mixing matrix in classical TFM analysis is the temporal average of a time-varying mixing matrix, which can be obtained in closed form and captures moment-by-moment estimations of brain network reconfigurations. In other words, how spatial parcels are reconfigured and combined by independent processes of interest. We apply the novel method to a high-temporal resolution fMRI dataset of participants performing a visuomotor association task and demonstrate that the retrieved network

reconfigurations closely follow the expectation based on the task design.

Methods

TV-TFM analysis pipeline

In the current study, we extended classical TFM analysis to obtain moment-by-moment estimations of brain network reconfigurations while simultaneously accounting for spatial overlap. Traditional TFM analysis consists of two stages: a spatial decomposition to retrieve canonical resting-state networks and a subsequent temporal ICA to retrieve TFMs (see panel A of Figure 1 for a visual representation).

TFM stage 1: partial decomposition

As previously described, a popular tool for the first stage is spatial ICA. To identify a set of spatial building blocks, pre-processed fMRI data with v voxels measured at t time points are decomposed into a set of statistically independent components (d). That is, a two-dimensional ($v \times t$) fMRI data matrix (X) is approximated by a set of spatially independent non-Gaussian sources, which are described as spatial maps (S, of dimensions: $v \times d$) and their associated time courses (T, of dimensions: $d \times t$):

$$X = ST + \epsilon_{tfm1} \tag{1}$$

where ϵ_{tfm1} denotes the residual error of the spatial decomposition.

Obtaining resting-state networks using spatial ICA can be done in different ways. First, spatial ICA can be applied at the single-subject level, which results in a description of subject-specific functional connectivity networks. Applying ICA at the single-subject level is problematic when the goal is to compare across participants because of the correspondence problem. That is, slight variations in the data can cause differential splitting of components, such that one component in one participant can be split into multiple components for another participant. This precludes matching of components across different datasets. A group-level ICA followed by the dual-regression technique can be

performed to overcome this (Beckmann et al., 2009; Nickerson et al., 2017). Participant-specific maps and time series are obtained here through two multiple regression analyses within a general linear model (GLM) framework. First, individual subject's time series are estimated by regressing the group ICA network template onto the individual participants' pre-processed fMRI data (i.e., spatial regression):

$$X = \hat{S}T + \epsilon_{dr1} \tag{2}$$

with

$$pinv(\hat{S})X = T \tag{3}$$

where T represents the average time-course related to a specific network component of the template ϵ_{dr1} after considering the contributions of the other components to that time series, $pinv$ denote the residual errors of this multiple regression analysis, and $pinv$ is the matrix pseudoinverse.

The subject-specific time courses estimated in equation (3) are then used as predictors in a second multiple, temporal regression to estimate the subject-specific spatial maps (S):

$$X = ST + \epsilon_{dr1} \tag{4}$$

with:

$$Xpinv(T) = S \tag{5}$$

where ϵ_{dr1} denote the residual errors of this multiple temporal regression analysis.

With group-ICA and dual-regression, individual subject maps and time series are estimated with respect to *group or sample-specific* connectivity networks. Instead of group-specific templates, previously established functional (or anatomical) templates can also be used (Nickerson et al., 2017). This approach is taken in the current study: we performed dual-regression analysis using templates of major brain networks identified in resting-state using group spatial ICA, which were previously shown to correspond to networks identified from a large set of task-based brain activation studies (Smith et al., 2009). The latter finding provides support for the robust occurrence of these spatial networks, both in rest and during task. For

constructing the templates, group-ICA was performed at a dimensionality of 20 to examine large-scale brain networks (SMITH20 template) and a higher dimensionality of 70 (SMITH70 template) to probe a lower level of the functional hierarchy (i.e., subnetworks). Of the 20 components identified with the previous, ten were well-defined and clearly overlapping the networks identified in task-based data. As previously described, Gomez et al. (2020) found that similar TFMs can be extracted across different functional (or anatomical) spatial decompositions. The SMITH20 spatial template was hence chosen for illustrative purposes in the rest of this paper because the included networks are better defined, which aids interpretability.

TFM stage 2: temporal decomposition

In classical TFM analysis, the second stage consists of applying temporal ICA to the time series retrieved in the first step, decomposing them into a set of statistically independent TFMs (k). That is, the spatial ICA time series (T, of dimension $d \times t$) are approximated by a set of temporally independent non-Gaussian sources, which are described as a product of the TFM mixing matrix (M, of dimensions: $d \times k$) and the associated temporally independent time series (B, of dimensions: $k \times t$):

$$T = MB + \epsilon_{tfm2} \tag{6}$$

where ϵ_{tfm2} denote the residual errors of the temporal ICA.

Classical TFM analysis thus describes the pre-processed fMRI data as a product of three matrices: the spatial ICA spatial maps, the TFM mixing matrix (which describes how the temporal components weigh onto the spatial components), and the associated TFM time courses:

$$X = SMB + \epsilon_{total} \tag{7}$$

where ϵ_{total} denotes the total residual error.

Temporal ICA at stage two was performed with a dimensionality of 21 in the original Smith et al. (2012) paper and at dimensionalities 8, 15, and 21 at the single-subject level by Gomez et al. (2020). Ensuring a lower dimensionality for the temporal than for the spatial decomposition (i.e., smaller

than the spatial ICA matrix rank), in the current study we ran temporal ICA at dimensionalities 8, 10 and 15. The main results described in the current paper stem from the highest model order (i.e., 15).

TV-TFM analysis: obtain time-varying temporal functional modes.

As described in equations (6) and (7), in classical TFM analysis a time-averaged mixing matrix is obtained. In other words, the extent to which spatial parcels (e.g., canonical functional connectivity networks) are reconfigured and combined by independent processes of interest is assumed to be constant. In the current study, classical TFM analysis is extended to include moment-by-moment estimations of the extent to which TFMs reconfigure and combine different spatial components. That is, a time-varying TFM mixing matrix is obtained (see panel B of Figure 1 for a visual representation).

Consider the TFM model of pre-processed fMRI data as described in equation 7, where S, M and B were previously defined as the spatial maps, the TFM mixing matrix and the TFM time series, respectively.

If:

$$X := X - \epsilon_{total} \tag{8}$$

then the TFM mixing matrix M can be described as:
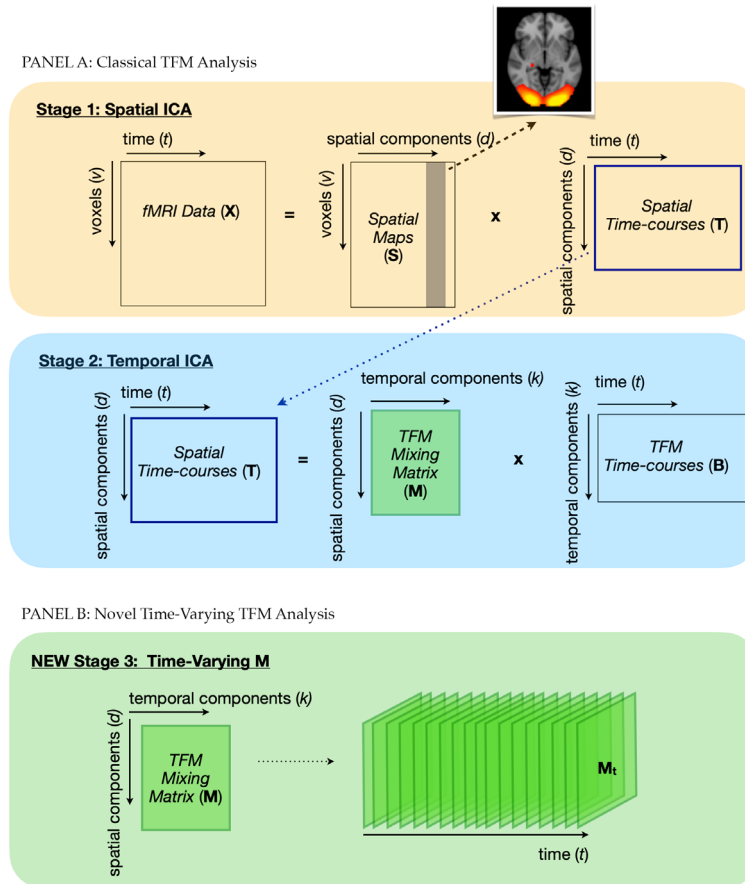
Figure 1. Schematic representation of Time-Varying TFM analysis (image adapted from Bijsterbosch, 2017). Panel A shows a schematic representation of classical TFM analysis. It consists of a spatial ICA in stage 1, where the fMRI data is decomposed into a set of statistically independent spatial components described by their spatial maps and the associated time courses. These time courses are fed into a temporal ICA in stage 2, where they are decomposed into a set of temporally independent processes, which are also described in terms of their spatial maps (i.e., the TFM mixing matrix) and time courses. Panel B shows a schematic representation of the new extension of TFM analysis. In the novel third stage a TV-TFM mixing matrix is retrieved, which provides per time point estimates of the extent to which spatial components/parcels are reconfigured and combined by independent processes of interest.

$$M = AXB^T Z \qquad (9)$$

where $A := pinv(S)$, $Z := (BB^T)^{-1}$ and the product of B^T and Z amounts to the right pseudo-inverse of the TFM time courses.

Note that the only time-dependent quantities in equation (9) are $X \in M_{vxt}$ and $B^T \in M_{txk}$. Considering the product between them in equation (9) as a sum over time:

$$M = AXB^T Z = A\left(\sum_{t=1}^{T} X(t)B^T(t)\right)Z$$
$$= \sum_{t=1}^{T} AX(t)B^T(t)Z \qquad (10)$$

where $X(t) \in M_{vx1}$, $B^T \in M_{1xk}$, and:

$$M_t(t) := AX(t)B^T(t)Z \qquad (11)$$

M can be obtained by summing over the time dimension of this time dependent quantity, namely:

$$M = \sum_{t=1}^{T} M_t(t) \qquad (12)$$

Note that for normalised (mean zero and unit standard deviation) X and B^T time series, $M_t(t)$ describes a scaled version (through Z, i.e., the covariance of B) of the instantaneous correlation (van Oort et al., 2018) between AX and B_T at time t. That is, the instantaneous correlation between the spatial maps regressed onto the pre-processed fMRI data (i.e., $AX(t)$) and the TFM time series ($B^T(t)$).

Defining a function:

$$f(t) := NM_t(t) \qquad (13)$$

We have that:

$$M = \frac{1}{N}\sum_{t=1}^{T} f(t) \qquad (14)$$

As shown in equation 14, the function f is a scaled version of M_t such that M is the time-average of the instantaneous correlation between AX and B^T scaled by its covariance.

A python package for running TV-TFM analysis was developed. The package will be made available on https://github.com/tamarajedidja/tv-tfm upon publication.

Task-based fMRI

TV-TFM analysis was applied to high-tem-poral resolution fMRI data of participants performing three runs of a visuomotor association task, previously collected by Z. Fazal. Data were collected at the Robarts Research Institute at the University of Western Ontario in Canada. Healthy volunteers were recruited according to the guidelines of the Health Sciences Research Ethics Board of Western University. All volunteers provided written informed consent. Data were organised according to the Brain Imaging Data Structure (BIDS; Gorgolewski et al., 2016).

Sample

Seventeen healthy volunteers participated in this study. Inclusion criteria were right-handedness and age below 50 years old. Visual inspection of data quality resulted in the exclusion of three participants due to an acquisition error, that is, the scanner timing was not well-matched to the presentation of stimuli. This resulted in a final sample of 14 participants between 19 and 32 years old, of which seven were female (age: $M = 23.43$, $SD = 3.36$) and seven were male (age: $M = 24.57$, $SD = 4.28$). For two of the participants, one individual task run was excluded from the analysis based on insufficient brain coverage.

Procedure

Participants underwent one scanning session of about 40 minutes. It consisted of three runs of a visuomotor association task while functional magnetic imaging data were acquired, and an anatomical scan at the end of the task run. Participants were trained on the visuomotor association task by performing one run before the scanning session. As visually presented in Figure 2, the task consisted of learning arbitrary associations between eight Japanese Kanji characters and four different motor responses, which were learned by trial and error. Between 25 and 36 (M = 31.14, SD = 1.68) visual stimuli were presented for 200ms. Participants were required to respond as soon as possible, but at least within 1.5s after stimulus onset. Motor responses consisted of pressing one of four buttons on a fibre optic response pad, where each button corresponded to two different Kanji characters. The response pad was placed on the abdomen of the
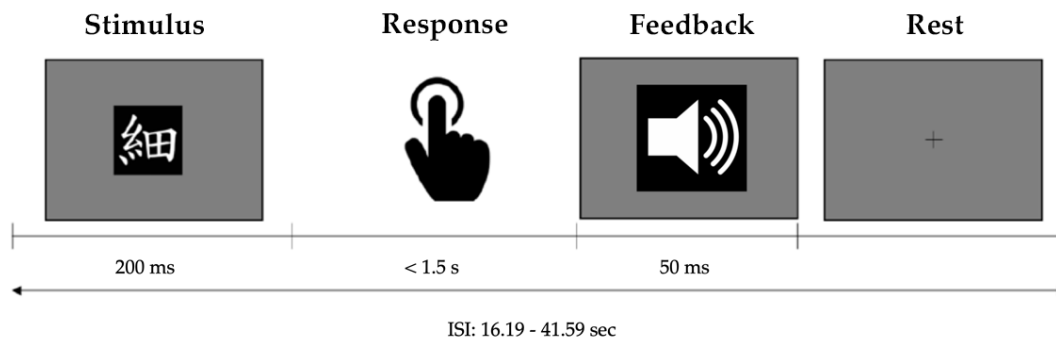
Figure 2. Schematic overview of the visuomotor association task. A visual stimulus is presented for 200ms, a motor response is required within 1.5s, immediate auditory feedback is provided for 50ms, followed by a long rest period.

participant, who consistently kept the index, middle, ring, and little fingers of the right hand on corresponding buttons. Performance feedback was given immediately after the response using three different sounds indicating a correct, incorrect, or too late response, respectively. Feedback was presented for 50ms, after which a fixation cross appeared until the next trial. Long inter-stimulus intervals (ISI) ranging between 16.19 and 41.59s (one outlier of 80.47s; M = 19.46, SD = 3.28) were used, to ensure that the haemodynamic response would return to baseline before the next trial. Presentation of visual stimuli and registering motor responses was done using Presentation 20.1 (Neurobehavioral Systems, San Francisco, CA).

Data acquisition

Data were acquired on a Siemens MAGNETOM 7T MR scanner, equipped with a 32-channel head coil. The use of a highly optimized AC84 (GenII) head gradient engine with a maximum gradient strength of 80 mT/m and 2nd, 3rd, and 4th order shims allowed the acquisition of T2* images at a very high temporal resolution. Functional images were acquired using a 2D multiband gradient-echo EPI protocol with an interleaved slice acquisition sequence (TR = 206ms, TE = 22ms, voxel sizes = 2.70 x 2.70 x 3.11 mm, flip angle = 20°, matrix size = 86 x 86, 32 slices, slice thickness/gap = 2.7 mm/3.1 mm, acceleration factor = 8). A total of 3000 volumes were obtained per task run of about 10 minutes, amounting to 9000 task-based volumes across task runs, per participant. Image reconstruction was performed using Slice-GRAPPA (Cauley et al., 2014; Hoge et al.,

2018; Setsompop et al., 2012). For registration purposes, anatomical images were acquired using the MP2RAGE sequence (Marques et al., 2010; TR = 6s, TE = 2.3ms, voxel sizes = 1 mm isotropic, flip angles = 4 and 5 degrees; TI1 = 0.8s, TI2 = 2.7s; matrix = 240 x 240; 240 slices of 1 mm slice thickness).

Data pre-processing

Data were pre-processed using fMRIPREP version 1.1.6 (Esteban et al., 2019), which is a Nipype-based tool (version 1.1.2; Gorgolewski, et al. 2011; Gorgolewski et al., 2018). Anatomical scans were corrected for spatial intensity variations using N4BiasFieldCorrection (ANTs 2.2.0; Tustison et al., 2010). A T1-weighted reference map was computed after registering the T1-weighted images using the mri_robust_template (Freesurfer, 6.0.0; Reuter et al., 2010). The T1-weighted reference was brain extracted using antsBrainExtraction.sh (ANTs 2.2.0) with a target template from the Open Access Series of Imaging Studies. Nonlinear registration to the ICBM 152 Nonlinear Asymmetrical template version 2009c (Fonov et al., 2009) was performed using antsRegistration (ANTs 2.2.0; Avants et al., 2008). The pre-processed T1-weighted reference map was used as a reference for functional registration. Brain-tissue segmentation of the T1-weighted image into cerebrospinal fluid (CSF), white matter (WM), and grey matter (GM) was performed on the brain-extracted T1w using FAST (FSL v.6.0.0; Zhang et al., 2001).

For all three task-based fMRI runs per participant, the following pre-processing steps were taken. Motion correction parame-

ters were calculated using MCFLIRT (FSL 6.0.0, Jenkinson et al. 2002). A reference volume and its brain extracted version were generated using a custom methodology of fMRIPREP, that is, averaging non-steady state volumes and computing a brain mask with init_enhance_and_skullstrip_bold_wf. Susceptibility distortions were estimated using a field map-less approach, that is, registering the functional reference image to the T1w reference using intensity inversion (Huntenberg, 2014; Wang et al., 2017) while regularising by constraining deformation to be nonzero only along the phase-encoding direction and modulation with an average field map template (Treiber et al., 2016) as implemented in ANTs 2.2.0. The transformation parameters for co-registration to the T1w reference were calculated with MCFLIRT (FSL 6.0.0, Jenkinson et al., 2002), using boundary-based registration (Greve and Fischl, 2009) with 9 degrees of freedom. A concatenated transform to correct for head-motion, susceptibility distortion, functional to T1w registration, and registration from T1w to MNI space (i.e., MNI152NLin2009cAsym) was applied in one step using Lanczos interpolation (Lanczos, 1964), as implemented in antsApplyTransforms. Following Gomez et al. (2020) several confounding time series were computed, which were not used to denoise the functional time series but to measure whether they correlate to the TFM time series. This concerned: three region-wise global signals, extracted within the CSF, the WM, and the whole-brain mask. The head-motion estimates from MCFLIRT were also placed within the corresponding confounds file. Datasets were temporally high-pass filtered with a cut-off frequency of 0.01 Hz (i.e., a periodicity of 100s) and spatially smoothed with a FWHM of 5.4mm. ICA-based denoising of the data was performed. Each pre-processed run was decomposed into 70 spatially independent components using Probabilistic Independent Component Analysis (Beckmann & Smith, 2004) as implemented in MELODIC (version 3.15, FSL). The following data pre-processing was applied to the input data: masking of non-brain voxels, voxel-wise de-meaning of the data, normalisation of the voxel-wise variance, and subsequent whitening and projection into a 70-dimensional subspace using Princi-pal Component Analysis. The whitened observations were decomposed using spatial ICA (Hyvarinen, 1999). Estimated component maps were divided by the standard deviation of the residual noise and thresholded by fitting a mixture model to the histogram of intensity values (Beckmann & Smith, 2004). IC components were manually classified into signal and noise, and the pre-processed data were denoised using FSL REGFILT (FSL v.6.0.0, Jenkinson et al., 2012). The pre-processed data were moreover variance normalised (mean zero and unit standard deviation across time) using FSLMATHs (FSL v.6.0.0, Jenkinson et al., 2012).

Statistics

Explorative statistical analyses were conducted at the single task-run, single-subject and at the group level. The well-established dual-regression technique (stage 1), the classical time-averaged TFM model (stage 2) and the new TV-TFM model (new stage 3) were exploratively compared in their ability to capture task-based variation in high temporal resolution fMRI data of participants performing a visuomotor association task. Single-subject results are illustratively presented for one task run of one participant (subsequently referred to as *'the selected dataset'*). Criteria for selecting this dataset for illustrative purposes are outlined in section II of the Supplementary Material.

First, it was examined how well task-related variability is captured: i) in the dual-regression time series; ii) in the TFM time series as obtained with classical TFM analysis, and iii) in the time-resolved mapping of TFMs onto the resting-state networks as obtained with TV-TFM analysis. Therefore, at each stage of the analysis pipeline (dual-regression, classical TFM analysis, and TV-TFM analysis), a first-level analysis was run separately for each task run, consisting of pairwise Pearson correlations between the time series and the standardised task regressors of the visuomotor association task (i.e., visual stimulation and motor response).

To account for dependencies between task runs per participant, for stage one (dual-regression), a fixed-effects analysis was run on the Fisher-Z transformed correlation values of the association between the dual-

regression time series and the task regressors. That is, they were averaged over task-runs, per participant. To identify the resting-state network time series that across participants were significantly related to the task, a third-level analysis was performed using a one-sample *t*-test per network.

At stage two of the analysis pipeline (classical TFM analysis), group-level comparisons per TFM are problematic due to the correspondence problem of temporal ICA. Therefore, it was examined whether per task-run TFM time series (i.e., *B*) better capture task-related variability than dual-regression time series (i.e., *T*). This was done by first selecting the dual-regression time series and the TFM time series that showed the strongest absolute correlation to the visual task regressor. The Fisher-*Z* transforms of these absolute correlation values were then compared per task-run using a paired sample *t*-test.

A proof-of-concept for TV-TFM analysis was obtained using trial-averaging, where time-varying mixing matrix network weights (a proxy for network involvement) were averaged over trials. The DMN is widely recognised as a task-negative network (Singh and Fawcett, 2008). Therefore, we tested whether we observed an unfolding, increasing difference between the DMN and task-positive network (i.e. visual, sensorimotor and auditory) weights in entries of the time-varying mixing matrix, for task-related TFMs. It was first examined whether this pattern was observed across trials. Therefore, per task run, entries of the time-varying mixing matrix that corresponded to the TFM that showed the strongest absolute correlation with the visual task regressor were averaged across trials. A

trial consisted of a 60-frame epoch (i.e., 60 × 206ms = 12.36s), starting at the onset of the visual stimulus. This interval was chosen such that it covers most of the expected time it takes for the haemodynamic response to increase in response to the visual stimulus and planning a motor response as well as come back to baseline, while not overlapping between trials. Note that if the strongest correlation was negative, the direction of the time series was reversed because it is not informative (i.e., it depends on the sign of the mixing matrix weight). Differences between the trial-averaged DMN weight and each of the three trial-averaged task-positive network weights (i.e., the average of the primary and lateral visual weights, the sensorimotor weight and the auditory weight) were then separately tested per time frame using a paired *t*-test. To account for dependencies between task runs per participant, a fixed-effects analysis was run. That is, the *t*-values were averaged across task runs per participant. Lastly, it was examined whether an increasing difference between the DMN weight and each of the task-positive network weights in response to the task was observed across participants. This was done by computing a group-level *Z*-value per time point, for the comparison between the DMN and each of the task-positive networks, separately.

Results

Stage 1: Spatial decomposition

Dual-regression with respect to the brain network templates by Smith et al. (2009), resulted in a set of canonical resting-state

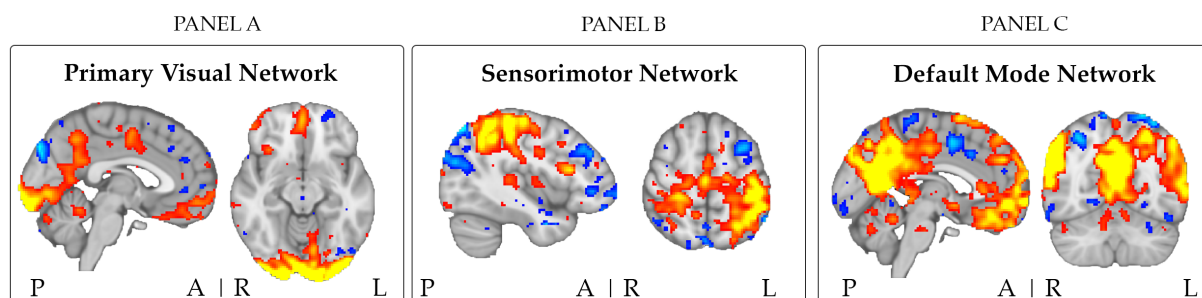| PANEL A	PANEL B	PANEL C
Primary Visual Network	**Sensorimotor Network**	**Default Mode Network**
P A | R L	P A | R L	P A | R L

Figure 3. Two representative slices of the dual-regression spatial maps of the primary visual network (V2 of the SMITH20) in panel A, the sensorimotor network in panel B and the default mode network in panel C, for the selected dataset (thresholded at Z > 5). Color coding: blue (negative) to red/yellow (positive). Abbreviations: P = posterior, A = anterior; L = left; R = right.

PANEL A
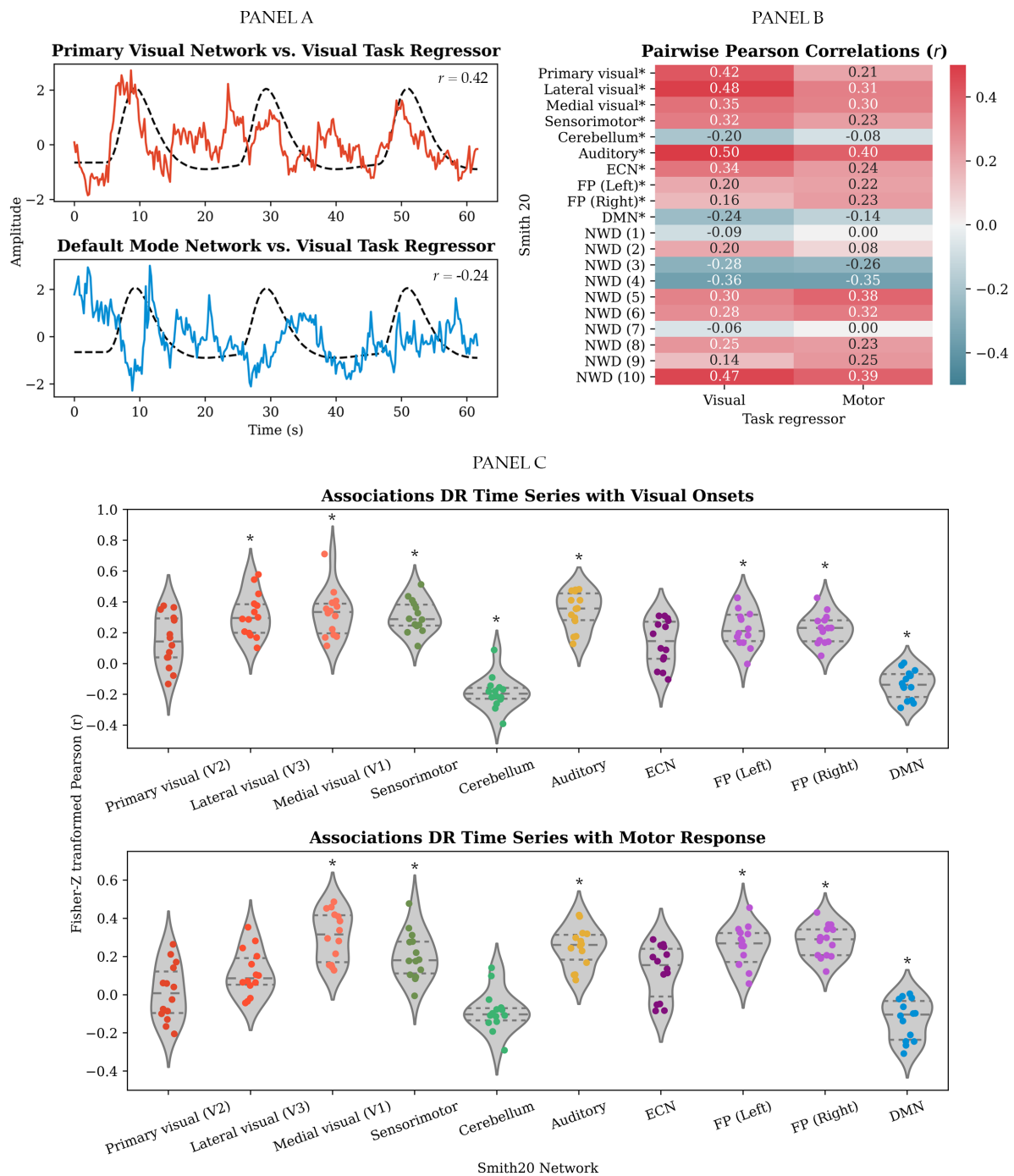
PANEL B

PANEL C

Figure 4. Associations between the stage one dual-regressions time series and the task regressors: Panel A shows a single-subject sample of the dual-regression time series for the primary visual network and the DMN plotted against the visual task regressor. Panel B presents single-subject, Bonferroni corrected (i.e., significance below .05/20 = .0025; ns. correlations set to zero) temporal correlations between the dual-regression time series and the visual and motor task regressor for the selected dataset. Panel C shows group-level distributions of within-subject correlation values between the dual-regression time series of the ten well-defined networks as obtained by Smith et al. (2009) and the visual task regressor (panel C) and motor task regressor (panel D; (*) Indicates a significant group-level difference from zero as assessed by one-sample t-tests, Bonferroni corrected, i.e., significance below .05/20 = .0025). Abbreviations: DR = dual-regression, ECN = executive control network, FP = frontoparietal, DMN = default mode network, NWD= not well-defined).

networks per task run, per subject, and per spatial network template (SMITH20 and SMITH70 templates). As previously mentioned, the results stem from a spatial decomposition using dual-regression against the SMITH20 template. The resulting resting-state networks are described by a spatial map (see, e.g., Figure 3) and a corresponding time series (see, e.g., panel A of Figure 4).

Bonferroni corrected, Pairwise Pearson correlations between the dual-regression time series and the visuomotor association task regressors (i.e., visual stimulation and motor response) are illustratively presented for the selected dataset in panel B of Figure 4. Whether the *group* averages of the Fisher-*Z* transformed correlation values were significantly different from zero was tested for each network with a one-sample *t*-test. Bonferroni corrected results are presented in panel C of Figure 4.

The following findings are relevant for the purpose of the present paper. As visually represented in Figure 4, across participants *correlations with the task regressors were found across most of the networks*. This indicates that task-related information is distributed across the dual-regression time series of the
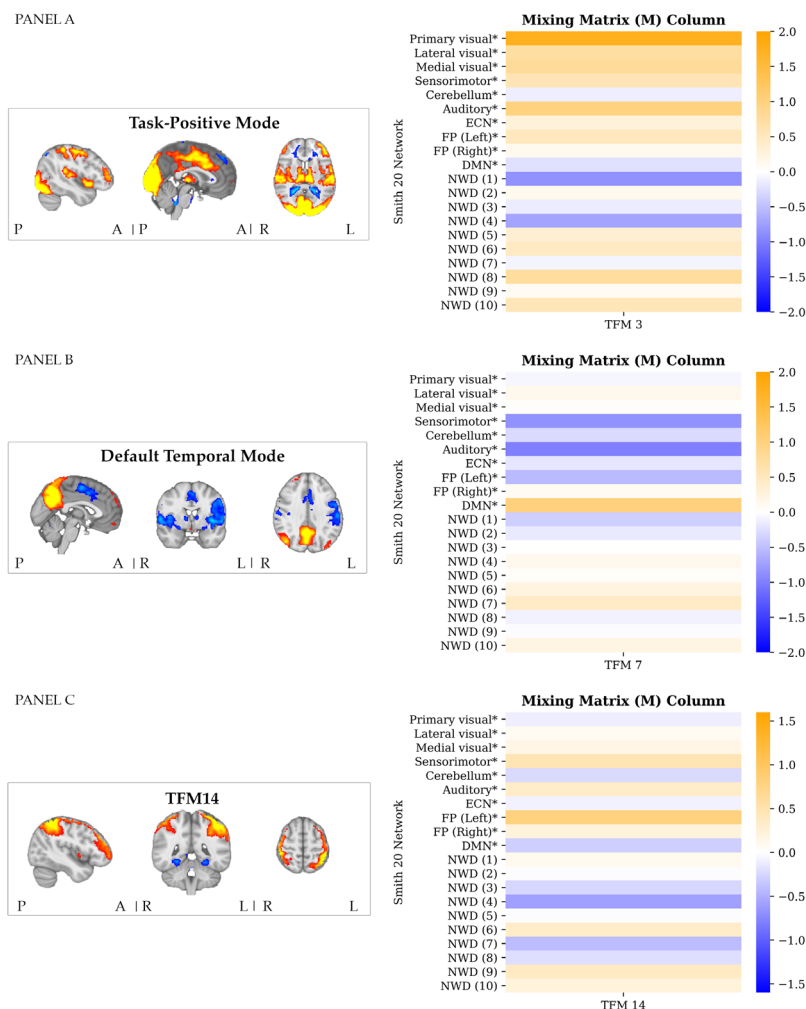
Figure 5. TFM spatial maps: Panel A shows three representative slices of the task-positive mode for the selected dataset (TFM3; thresholded at Z > 5), and the associated mixing matrix column, which describes the time-averaged weighting of this TFM onto the Smith networks. Panel B shows three representative slices of the default temporal mode for the selected dataset (TFM7; thresholded at Z > 5), and the associated mixing matrix column. Panel C shows three representative slices of the TFM spatial map that correlated most strongly to the motor task regressor for the selected dataset (TFM14; thresholded at Z > 5), and panel B the associated mixing matrix column. Colour coding spatial maps (on the left): blue (negative) to red/yellow (positive). Abbreviations: P = posterior, A = anterior; L = left; R = right. ECN = executive control network, FP = frontoparietal network, DMN = default mode network, NWD= not well-defined.

different resting-state networks. Note that contrary to the expectation, the primary visual network (V2) did not significantly relate to the onsets of the visual stimulus, Fisher-Z = 0.14, $t(13)$ = 3.25, p = .006 (after Bonferroni correction; i.e., significance below .05/20 = .0025). Please refer to the Supplementary Material, section III for an overview of the statistics of all one-sample t-tests.

Stage 2: Temporal decomposition

Temporal ICA resulted in a set of TFMs per task run, per subject, per spatial network template (SMITH20 and 70) and per temporal ICA dimensionality (8, 10, 15, and 21 depending on the model order of the spatial template). As previously addressed, the results stem from the highest model order, that is, 15, for the SMITH20 template. TFMs are described in terms of their weighting onto the SMITH templates (node weights/a mixing matrix column, see Figure 5) and the corresponding time series. TFM time series were related to confound regressors as an indication of their neuronal basis. Results are presented in section IV of the Supplementary Material.

As visually illustrated for the selected dataset in panel A of Figure 5, we identified a "task-positive mode" which includes regions related to the visual, motor and auditory aspects of the task, that is, primary visual (occipital pole), medial visual (e.g., lingual and occipital fusiform gyri) and lateral occipital

regions; the temporal pole; motor regions along the dorsal stream (e.g., primary motor cortex and supplementary motor cortex) and primary auditory cortex. A similar component was identified across most task runs and participants. Please refer to section V of the Supplementary Material for further details.

We identified a similar component to the most common TFM identified by Gomez et al. (2020), the "default temporal mode", consisting of core hubs of the DMN (i.e., angular gyrus and precuneus) in anti-correlation with the motor regions (superior parietal cortex, post-central gyrus and supplementary motor cortex), the auditory network, and the insula (panel B of Figure 5). A similar component was identified across most task runs and participants. Please refer to section V of the Supplementary Material for further details. Note that contrary to the findings by Gomez et al. (2020) no anti-correlations with visual areas were found for the selected dataset. This potentially results from component splitting, since a temporal ICA of model-order ten performed on the time series of the ten well-defined networks of the SMITH20 template identified a component similar to the default temporal mode *also in anti-correlation to visual areas* (see the Supplementary Material section V).

Bonferroni corrected, Pairwise Pearson correlations between the TFM time series and the visuomotor association task regressors are illustratively presented for the selected
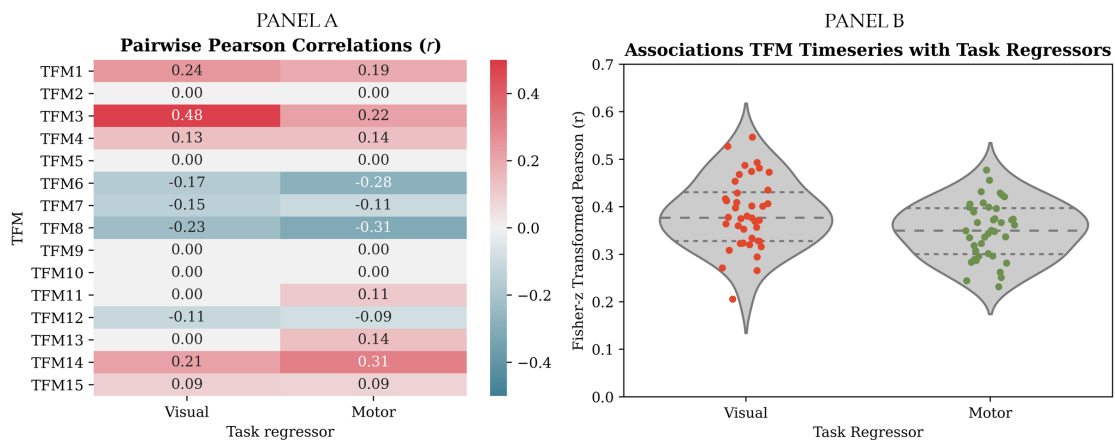
Figure 6. Panel A shows single-subject, Bonferroni corrected (i.e., significance below .05/15 = .003; ns. correlations set to zero) temporal correlations between the TFM time series and the visual and motor task regressor illustratively for the selected dataset. Panel B shows the distributions of correlation values between the TFM time series of the task-related TFMs (i.e., most strongly associated with the visual task regressor) with the task regressors for all task-runs and participants.

dataset in panel A of Figure 6. The previously described "task-positive mode" (TFM3) correlated most strongly with the visual task regressor. TFM14 correlated most strongly with the motor task regressor. A visual representation of the spatial map of TFM14 is presented in panel C of Figure 5. It consists of an anti-correlated pattern between the frontoparietal attention network and the temporal fusiform cortex, a higher-level visual processing area involved in sensory integration and memory. In panel B of Figure 6, correlation values are plotted per task run for the associations between the time series of the TFMs that correlated most strongly with the visual (left) and motor (right) task-regressor and those regressors, respectively.

A relevant observation for the purpose of the present paper is the *increased sparseness of the correlation matrix* as observed in panel A of Figure 6, compared to the dual-regression correlation matrix in panel B of Figure 4. That is, task-related variation appears to be represented in fewer components. This corresponds to the fact that temporal ICA retrieves temporally independent processes, consisting of linear combinations of resting-state networks. Moreover, it was found that across task runs, absolute correlations with the visual task regressor were stronger for TFMs (which per task run correlated most strongly to the task) than for dual-regression time series (which per task run correlated most strongly to the task), *paired-t*(39) = 6.38, *p* < .0001. This is in line with the conceptual expectation that task-related processes are temporally independent of other brain processes and can be captured using temporal ICA.

New stage: Time-varying temporal functional modes

TV-TFM analysis resulted in time-varying mixing matrices (i.e., (equation 23) and its scaled version (equation 24)) per i) task run, ii) participant, iii) spatial network template (SMITH 20 and 70), and: iv) temporal ICA dimensionality (8, 10, 15, and 21 depending on the spatial model order). As previously described, the results stem from the highest model order (15) for the better defined SMITH20 template.

TV-TFMs can be described spatially by means of the product between the spatial maps, *S*, and the entries of the time-varying mixing matrix related to one TFM component. This allows per time point visualisations of the resting-state networks (as identified by Smith et al., 2009) recruited by this TFM. An example for the selected dataset is presented in Figure 7, where the temporal evolvement of the task-positive mode (TFM3) is presented for one trial. Onsets of the visual stimulus and motor response are presented at the bottom of the Figure and are operationalised as the first time frame that the stimulus/response convolved with the haemodynamic response function exceeds zero. Time-locked to the

PANEL A   PANEL B

Time-Varying Task Positive Mode
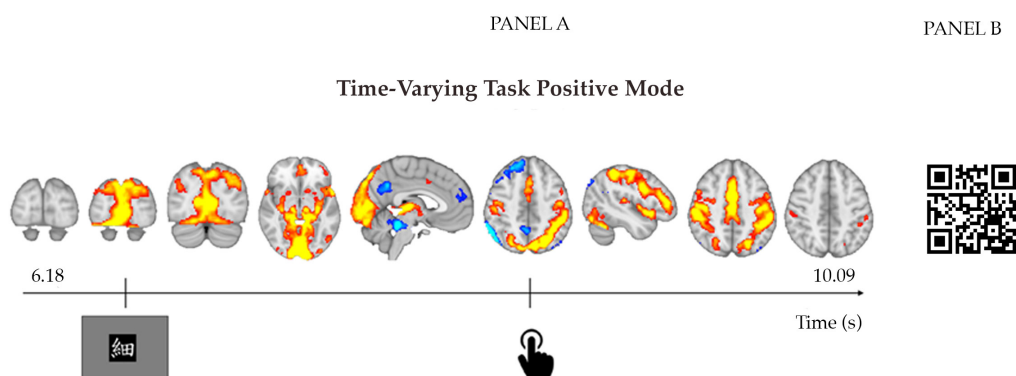
Figure 7. Panel A shows representative slices of the time-varying task-positive mode (TFM3) for the selected dataset. As visually presented at the bottom of the figure, the onsets of the visual stimulus and the motor response are defined as the first time frame that the stimulus/response convolved with the haemodynamic response function exceeds zero. Colour coding: blue (negative) to red/yellow (positive). Panel B shows a QR that links to a video of the entire trial (from two frames before the onset of the visual stimulus until eight frames after the onset of the motor response).

PANEL A
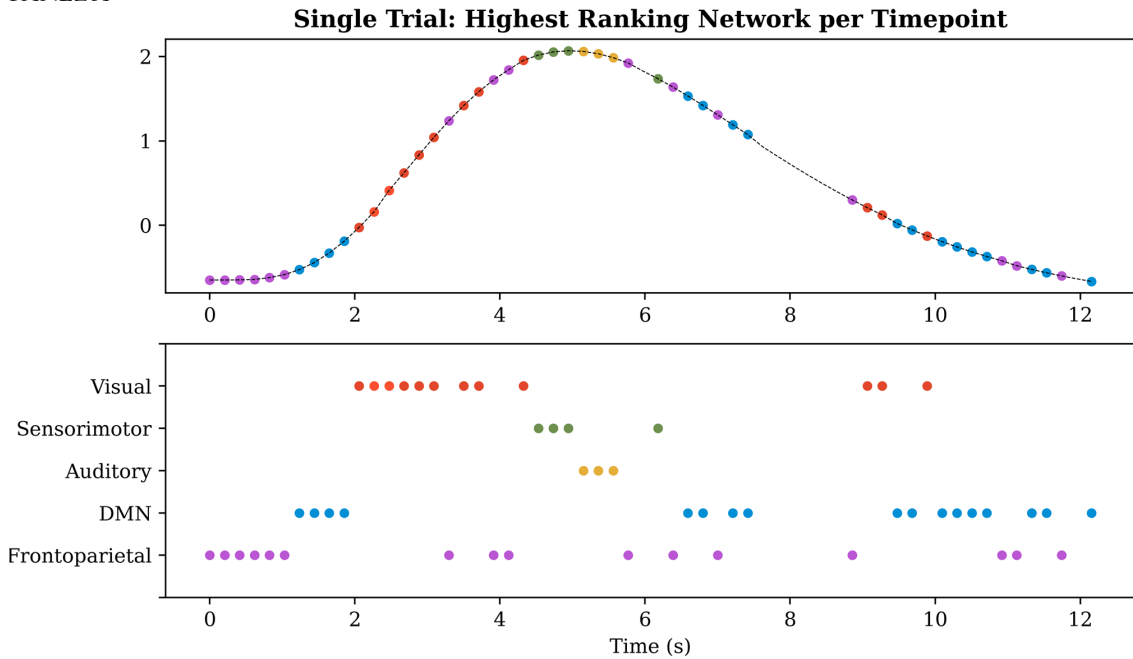
PANEL B
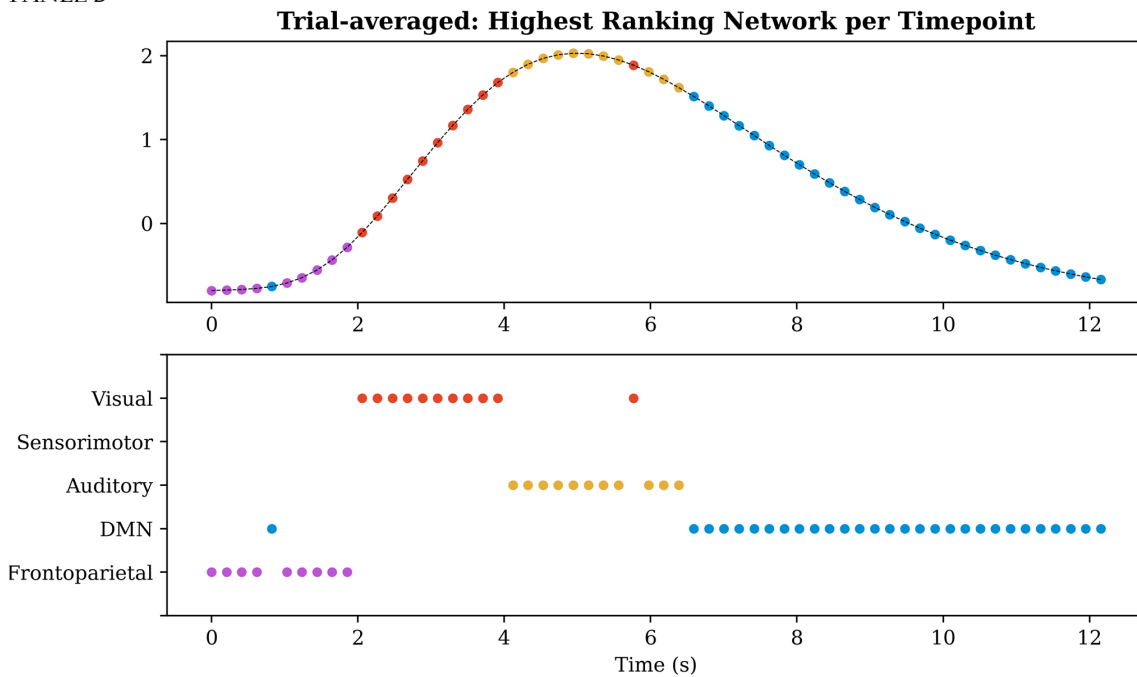
Figure 8. In panel A the highest-ranking Smith network per time point is plotted on the visual task regressor for a single trial, for the task-positive mode (TFM3) of the selected dataset. In panel B, the highest-ranking network per time point averaged across trials is plotted on the visual task regressor for the task-positive mode of the selected dataset. Abbreviation: DMN = default mode network.

visual stimulus, we observe recruitment of primary visual areas, followed by medial and lateral visual areas. Time-locked to the motor response, we observe the recruitment of superior parietal motor regions and subsequent recruitment of the pre-central gyrus/ primary motor cortex.

Ranking-ordering the entries of the time-varying mixing matrix per TFM, per time-point, allows representing which networks are most strongly recruited by the respective TFM over time. A single trial example for the task-positive mode (TFM3) is presented in panel A of Figure 8 for the selected dataset. The

PANEL A

Associations Entries of *f* vs. Visual Stimulation

PANEL B

Associations Entries of *f* vs. Motor Response

Figure 9. Bonferroni corrected (i.e., significance below .05/300 = .0002; ns. correlations set to zero) pairwise Pearson correlations between the entries of the time-varying mixing matrix and the visual and motor task regressor in panel A and B, respectively, for the selected dataset. Abbreviations: ECN = executive control network, FP = frontoparietal network, DMN = default mode network, NWD= not well-defined.

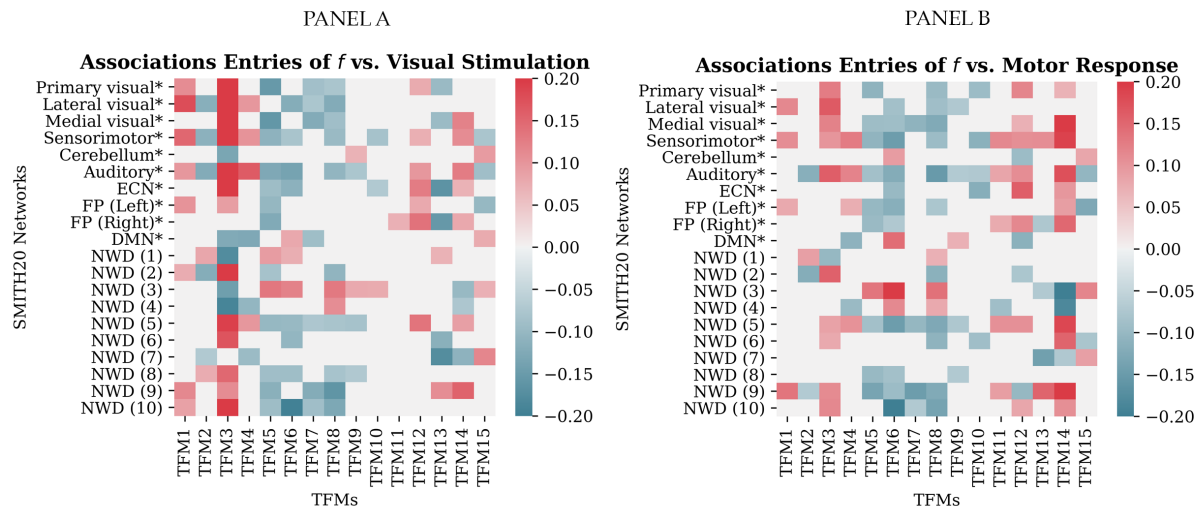bottom figure in panel A shows per network when in time its weighting was the strongest (i.e., it had the highest rank). The top figure in panel A shows the highest-ranking network per time point plotted on the visual task regressor. We observe that the ranks closely follow the expectation based on the task design. Before the onset of the stimulus the frontoparietal attention and default mode networks predominate. In response to the onset of the visual stimulus the visual networks predominate, followed by short periods in which the sensorimotor network and the auditory network subsequently rank highest. Averaging over all trials for the selected dataset, we observe a similar pattern except that predominance of the sensorimotor network is not observed (see panel B).

Pairwise Pearson correlations between each entry of the time-varying mixing matrix and the visuomotor-association task regressors are illustratively presented for the selected dataset in Figure 9. The sum of the correlation values across the entries of each TFM was highest for the task-positive mode (TFM3) for the visual task regressor and for TFM14 for the motor task regressor (see Supplementary Material, section VI). These are the same TFMs for which the time series were most strongly related to the task regressors (as concluded in stage two of the analysis

pipeline; see panel A of Figure 6). In line with the expectation, correlations between the visual task regressor and the TFM3 entries that correspond to the task-positive networks (i.e., primary and lateral visual, sensorimotor and auditory) are opposite to the correlation between the visual task regressor and the TFM3 entry that corresponds to the DMN. This pattern is slightly different for the correlations between the motor task regressor and the entries of TFM14, in the sense that no significant correlations with the lateral visual network (V3) and the DMN were found.

The event-related approach, consisting of trial-averaging the time-varying mixing matrix, provided the main proof-of-concept for TV-TFM analysis. Panel A and B of Figure 10 show single-subject results for the selected dataset. Trial-averaged entries of the time-varying mixing matrix for the task-positive mode closely follow the expectation based on the task design, that is, starting with an increase in the primary visual network, followed by increases in the sensorimotor network and the auditory network, and a concurrent decrease in the DMN weights (see panel A). For comparison, in panel B, an example is plotted for a TFM for which the time series were not significantly related to the task.

A similar pattern was found across most task runs and participants. Please refer to
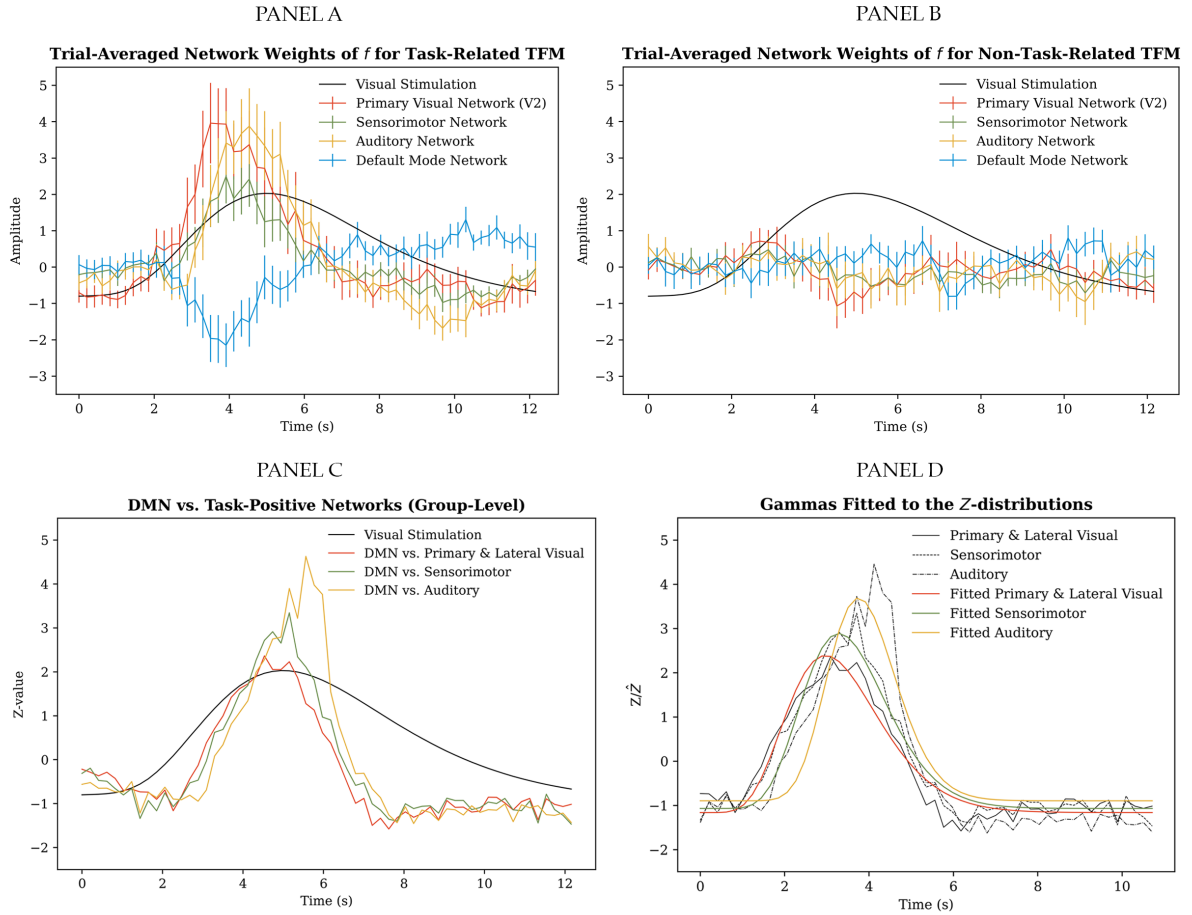
PANEL A

PANEL B

PANEL C

PANEL D

Figure 10. Trial-averaging results: Panel A shows single-subject trial-averaged entries of the time-varying mixing matrix for the task-positive mode (TFM3) for the selected dataset. For comparison, panel B shows the trial-averaged entries of the time-varying mixing matrix for a TFM unrelated to the task for the selected dataset. Error bars represent the standard error of the mean. Differences between the DMN and: i) the average of the primary and lateral visual network; ii) the sensorimotor network, and iii) the auditory network across trials, task-runs and participants are indicated by the red, green and yellow Z-distributions in panel C, respectively. As a first parametrisation, these Z-distributions were fitted with independent gamma distributions shown in red for i), in green for ii), and in yellow for iii) in panel D.

section VII of the Supplementary Material for trial-averaged plots of task-relevant entries of the time-varying mixing matrix per task run, per participant. Support for the observed trend was obtained using per time frame paired t-tests on the *differences between the DMN entry and each task-relevant entry of the time-varying mixing matrix separately.* That is, DMN versus the average of the primary and lateral visual weights, DMN versus the sensorimotor weight and DMN versus the auditory weight. Group-level results (after averaging across task runs per participant at the second level) for the TFMs that showed the strongest absolute correlation with the visual task regressor are presented in panel C of Figure 10. Across trials, task runs and

participants, the differences between the DMN and: i) the average of the primary and lateral visual entries, ii) the sensorimotor entry, and iii) the auditory entry increased subsequently.

As a first parametrisation, the Z-distributions in panel C of Figure 10 were fitted with three independent gamma distributions, with:

$$\gamma = \frac{\beta^{\alpha}}{\Gamma(\alpha)} x^{\alpha-1} e^{-\beta x} \tag{15}$$

Model fitting was performed after restricting the time range, shifting the distributions up into the positive domain of Z and normalising the distributions (such that they integrate to one). The parameters for these operations

Table 1.

Parameters for Model Fitting of the Gamma Distributions.

	Operation Parameters*:			Distributional Parameters**:		
	time range (s)	shift in y		α	β	Mode (s)
Visual	1.44 - 12.36	1.16	Visual	8.37	0.51	2.98
Sensorimotor	1.44 - 12.36	1.07	Sensorimotor	11.82	0.68	3.28
Auditory	1.44 - 12.36	0.90	Auditory	22.47	1.18	3.75

(*) Operation parameters regard the preparatory steps before model fitting (i.e., restricting the time range, shifting the distributions into the positive domain).
(**) Distributional parameters for the optimal (least squared error) model fit are presented.

are presented on the left side of Table 1. The parameters for the best fitting gamma distributions are presented on the right side of Table 1. These distributional parameters re-affirm subsequent recruitment of the visual, sensorimotor and auditory networks by task-related TFMs (see panel D of Figure 10).

Discussion

Proof-of-Concept

With the current study, we provided the first proof-of-concept for TV-TFM analysis. The goal was to develop a TVFC method that accounts for spatial overlap. The latter is inherently safeguarded by extending classical TFM analysis, which accounts for spatial overlap by following a spatial decomposition with a subsequent temporal ICA on the retrieved time series. That different temporal processes indeed recruited the same spatial components shows from the fact that different temporally independent processes (TFMs) map onto the same spatial maps. Regarding the first, TV-TFM analysis obtains moment-by-moment estimations of the extent to which different spatial components (e.g., resting-state networks) are reconfigured by temporally independent processes (TFMs). A first validation was provided by applying TV-TFM analysis to task-based fMRI data and subsequent trial-averaging of the time-varying mixing matrix entries per resting-state network for task-related TFMs. The pattern observed across participants, sessions, and trials closely followed the expectation based on the task design. We observed an increase

in visual areas, the sensorimotor network, and the auditory network subsequently, and a concurrent decrease in DMN weights. Differences in timing between these subsequent increases were minor. This is inherent to the task design, in which the different processes follow each other up in close succession: the visual stimuli are presented for 200ms, participants are required to respond as soon as possible using a button press and get immediate auditory feedback. Previous attempts to temporally disentangle these processes in high-temporal resolution fMRI data by means of a mass univariate GLM approach were unsuccessful (Noteboom, 2018). At the very short TR of .206ms in the current study, we could not disentangle the processes using dual-regression with respect to existing resting-state network templates either. In part, these processes were also considered a joint independent temporal process as identified by temporal ICA. That is, applying temporal ICA at stage two of the analysis pipeline resulted in a task-positive component that included brain regions implied in all these processes (i.e., visual, motor and auditory). TV-TFM analysis proved to be a step forward towards temporally disentangling them. Notably, event-related averaging could also have been applied to T, that is, the dual-regression time series. This would have provided a linear mix of resting-state networks at a whole brain level. However, with the approach taken in the current study, we retrieved a linear mix of temporally independent processes. We argue that this is a reasonable approach because it aids interpretability by reducing the dimensionality to task-related information (i.e., task-related TFMs).

Assumptions and Limitations

The latter points to an important assumption for this proof-of-concept, namely that temporal ICA at stage two of the analysis adequately identifies the process of interest. Preliminary support for this was provided by Gomez et al. (2020), who concluded that TFM time series carry an imprint of the task design. Our present results provide some additional support. First, we found that the TFM time series were more strongly associated with the task than the dual-regression time series. Secondly, we observed that classical (time-averaged) TFM analysis increases specificity in detecting task-related variability compared to the dual-regression approach. That is, correlations of dual-regression time series with the task were widespread across networks, whereas correlations to the task were identified for a smaller number of TFMs. The task-related TFM components moreover spatially involved regions expected to be involved in the visuomotor association task. However, studies probing the ability of temporal ICA, or classical TFM analysis specifically, to adequately capture task-related variability are scarce. This hence requires further assessment. In this study, we used a simple but effective approach to probe whether the identified temporally independent processes were task-related, that is, temporal correlation. This was decided, in part, because of multicollinearity among the task regressors. For the same task paradigm, this was also found by Noteboom (2018), who suggested that this might be a primary reason why the GLM cannot temporally disentangle these processes. However, for other task paradigms, we suggest using regression analyses within a general linear model, which allows adjusting for covariates such as handedness (note that in the current study this specific example was addressed in the inclusion criteria). Other, more advanced, for example, PCA-based, supervised approaches could also be explored.

In this study we obtained the instantaneous correlations between the individual spatial maps regressed onto the noiseless reconstruction of the fMRI data, and the TFM time series (scaled by their covariance) to retrieve moment-by-moment estimations of brain network reconfigurations. If a process of interest is not captured adequately using classical TFM analysis, the task-relevant information is unexplained, residual variance. In that case, it could well be that the reconfigurations are better characterised using the original instead of the noiseless reconstruction of fMRI data. That is, accounting for the residual errors should hence be considered in the future.

Future Directions

We see several potential courses of action to improve and validate the TV-TFM method further. First of all, the Z-values describing the differences between the network entries of the time-varying mixing matrix across trials, task runs, and participants were not statistically tested for the current proof-of-concept. Note that doing so in the future requires non-parametric permutation testing since the averaging of t-values at the second level breaks the normality assumption (i.e., it is t–, not normally distributed). In this study, we dealt with the large amount of high-frequency content that characterises the time-varying mixing matrices by averaging over trials. In the future, we would like to apply this method at the single-trial level, which likely requires smoothing of the time-varying mixing matrix, using a Kalman filter, for example. In this study, we parametrised the group-level Z-distributions by fitting independent Gamma distributions. We aim to fit a mixture-model (potentially of another distribution, for example, Inverse Gaussian) to the Z-distributions at the single-trial level in the future, followed by a PCA analysis. Herewith, differences in timing or shape of these distributions would potentially allow predicting behavioural measures such as success vs unsuccessful trials or attentiveness vs inattentiveness to the task. Another important follow-up step is developing a dual-regression-like approach to deal with the correspondence problem at stage two, temporal ICA, to probe and compare similar temporally independent processes of interest across participants. Moreover, although Gomez et al. (2020) found that similar TFM components are found independent of the initial spatial dimensionality reduction, we

suggest that it might be relevant to explore the results of TV-TFM analysis after different initial spatial dimensionality reductions. For example, the finer-grained SMITH70 template. The SMITH20 template used in the current study was obtained with a model order that has proven to robustly identify the canonical large-scale resting-state networks in resting-state fMRI (Smith et al., 2009). A model order of 20 was also shown to be optimal for decompositions of BrainMap-based ICA components. At higher granularities, sub-networks at lower levels of the functional hierarchy are identified (Ray et al., 2013). This level of detail would potentially especially be of interest for task-based fMRI data, given the idiosyncrasies of cognitive tasks. Brain network reconfigurations as obtained with TV-TFM analysis after anatomical (instead of functional) parcellations could also be explored.

Contribution and Potential Applications

We believe TVTFM analysis makes a relevant contribution to the current landscape of TVFC methods by probing, at a high temporal resolution, how temporally independent processes of interest reconfigure and combine spatial building blocks. As previously described, the current TVFC methods can be differentiated based on the time window they consider, ranging from instantaneous measures to time windows of 30-60 seconds standard in sliding-window analyses (Preti et al., 2017). TV-TFM analysis provides moment-by-moment, or per timeframe, estimations of TVFC. It was previously addressed that several dimensionality reductions are generally performed in TVFC analysis. Instead of ignoring temporal ordering of the data, as is done in several TVFC methods by means of k-means clustering, for example, the dimensionality reduction consists of zooming in on one or more temporally independent processes of interest which are derived in a data-driven manner (using temporal ICA). We moreover showed that the novel method is applicable to task-based fMRI data. Whereas commonly spatial brain properties are examined, the novel method allows probing temporal properties of functional integration, potentially associated with cognitive function. Although arguably the complexity of the present method is relatively high (i.e., with respect to the number of analysis steps and the mathematical derivation), we believe that interpretability is a strong point because the estimated brain network reconfigurations are described in space and time for specific processes of interests. In this task-based study, processes of interest were identified by correlation to the task regressors. This could also be done in different manners, for example, based on physiological arousal measures, which would allow extending this method to resting-state fMRI.

The developed model has numerous potential applications. For example, temporal ICA could be applied to a region of interest, such that the time-varying mixing matrix describes how sub-parcels interact over time, for temporal processes of interest. Instead of using dual-regression and temporal ICA, the TV-TFM analysis can also be implemented for other initial spatial parcellations and other subsequent multivariate dimensionality reduction methods. For the latter, a supervised PCA-based multivariate method like SPADE (Llera et al., 2020) would be an option, where moment-by-moment estimations are obtained for so-called filters which optimally discriminate between certain conditions. Irrespective of the application, the goal is eventually to utilise the information present in the time-varying matrix, for example, by describing the timing or shape differences of the Z-distributions in different states or conditions and between different individuals. These parameters describe inter-individual differences in brain network reconfigurations (while accounting for spatial overlap). To conclude, we hope that in the future, this new method will further elucidate the temporal properties of functional brain networks and that it will have a significant clinical contribution, for example, by probing temporal differences in brain network reconfigurations between individuals.

Conclusion

We presented a novel method for probing time-varying functional brain network reconfigurations. It retrieves per time point estimates

of the extent to which spatial parcels are reconfigured and combined by independent processes of interest. The method can hence be utilized to probe the temporal characteristics of network involvement and how these relate to cognition and behaviour.

Acknowledgements

References

Avants, B., Epstein, C., Grossman, M., & Gee, J. (2008). Symmetric diffeomorphic image registration with cross-correlation: Evaluating automated labeling of elderly and neurodegenerative brain. *Medical Image Analysis*, 12(1), 26–41.

Bandettini, P. A. (2009). What's new in neuroimaging methods? *Annals of the New York Academy of Sciences, 1156*(1), 260–293.

Beckmann, C., Mackay, C., Filippini, N., & Smith, S. (2009). Group comparison of resting-state fMRI data using multi-subject ICA and dual regression. *NeuroImage, 47*, S148.

Beckmann, C., & Smith, S. (2004). Probabilistic independent component analysis for functional magnetic resonance imaging. I*EEE Transactions on Medical Imaging, 23*(2), 137–152.

Beckmann, C. F. (2012). Modelling with independent components. *NeuroImage, 62*(2), 891–901.

Beckmann, C. F., DeLuca, M., Devlin, J. T., & Smith, S. M. (2005). Investigations into resting-state connectivity using independent component analysis. *Philosophical Transactions of the Royal Society B: Biological Sciences, 360(1457),* 1001–1013.

Bijsterbosch, J. (2017). *Introduction to resting state fMRI functional connectivity.* Oxford Neuroimaging Primers. Oxford, United Kingdom; New York, NY: Oxford University Press.

Bijsterbosch, J. D., Woolrich, M. W., Glasser, M. F., Robinson, E. C., Beckmann, C. F., Van Essen, D. C., Harrison, S.J. & Smith, S. M. (2018). The relationship between spatial configuration and functional connectivity of brain regions. *eLife*, 7:e32992.

Biswal, B., Zerrin Yetkin, F., Haughton, V. M., & Hyde, J. S. (1995). Functional connectivity in the motor cortex of resting human brain using echo-planar MRI. *Magnetic Resonance in Medicine, 34*(4), 537–541.

Cabral, J., Vidaurre, D., Marques, P., Magalhães, R., Silva Moreira, P., Miguel Soares, J., Deco, G., ... & Kringelbach, M. L. (2017). Cognitive performance in healthy older adults relates

to spontaneous switching between states of functional connectivity during rest. *Scientific Reports, 7*(1), 1–13.

Calhoun, V., Adali, T., Pearlson, G., & Pekar, J. (2001). Spatial and temporal independent component analysis of functional MRI data containing a pair of task-related waveforms. *Human Brain Mapping, 13*(1), 43–53.

Cauley, S. F., Polimeni, J. R., Bhat, H., Wald, L. L., & Setsompop, K. (2014). Interslice leakage artifact reduction technique for simultaneous multislice acquisitions: Interslice leakage artifact reduction technique. *Magnetic Resonance in Medicine, 72*(1), 93–102.

Chang, C., & Glover, G. H. (2010). Time–frequency dynamics of resting-state brain connectivity measured with fMRI. *NeuroImage, 50*(1), 81–98.

Damoiseaux, J. S., Prater, K. E., Miller, B. L., & Greicius, M. D. (2012). Functional connectivity tracks clinical deterioration in Alzheimer's disease. *Neurobiology of Aging, 33*(4), 828.e19–828.e30.

Damoiseaux, J. S., Rombouts, S. A. R. B., Barkhof, F., Scheltens, P., Stam, C. J., Smith, S. M., & Beckmann, C. F. (2006). Consistent resting-state networks across healthy subjects. *Proceedings of the National Academy of Sciences, 103*(37), 13848–13853.

Deco, G., Cabral, J., Woolrich, M. W., Stevner, A. B., van Hartevelt, T. J., & Kringelbach, M. L. (2017). Single or multiple frequency generators in on-going brain activity: A mechanistic whole-brain model of empirical MEG data. *NeuroImage, 152*, 538–550.

Deco, G., & Kringelbach, M. L. (2016). Metastability and coherence: Extending the communication through coherence hypothesis using a whole-brain computational perspective. *Trends in Neurosciences, 39*(3), 125–135.

Esteban, O., Markiewicz, C. J., Blair, R. W., Moodie, C. A., Isik, A. I., Erramuzpe, A., & … Gorgolewski, K. J. (2019). fMRIPrep: A robust preprocessing pipeline for functional MRI. *Nature Methods, 16*(1):111–116.

Fonov, V., Evans, A., McKinstry, R., Almli, C., & Collins, D. (2009). Unbiased nonlinear average age-appropriate brain templates from birth to adulthood. *NeuroImage, 47*, S102.

Friston, K. J. (1998). Modes or models: A critique on independent component analysis for fMRI. *Trends in Cognitive Sciences, 2*(10), 373–375.

Friston, K. J., Frith, C. D., Liddle, P. F., & Frackowiak, R. S. J. (1993). Functional connectivity: The principal-component analysis of large (PET) data sets. *Journal of Cerebral Blood Flow & Metabolism, 13*(1), 5–14.

Glasser, M. F., Coalson, T. S., Bijsterbosch, J. D., Harrison, S. J., Harms, M. P., Anticevic, A., Van Essen, D. C., & Smith, S. M. (2018). Using temporal ICA to selectively remove global noise while preserving global signal in functional MRI data. *NeuroImage, 181*, 692–717.

Glerean, E., Salmi, J., Lahnakoski, J. M., Jääskeläinen, I. P., & Sams, M. (2012). Functional magnetic resonance imaging phase synchronization as a measure of dynamic functional connectivity. *Brain Connectivity, 2*(2), 91–101.

Gomez, D. E., Llera, A., Marques, J. P. F., Beckmann, C. F., & Norris, D. G. (2020). Single-subject, single-session, temporal modes of brain activity. *NeuroImage, 218*, 116783.

Gorgolewski, K. J., Auer, T., Calhoun, V. D., Craddock, R. C., Das, S., Duff, E. P., & … Poldrack, R. A. (2016). The brain imaging data structure, a format for organizing and describing outputs of neuroimaging experiments. *Scientific Data, 3*(1), 1–9.

Greicius, M. D., Flores, B. H., Menon, V., Glover, G. H., Solvason, H. B., Kenna, & … Schatzberg, A. F. (2007). Resting-state functional connectivity in major depression: Abnormally increased contributions from subgenual cingulate cortex and thalamus. *Biological Psychiatry, 62*(5), 429–437.

Greicius, M. D., Srivastava, G., Reiss, A. L., & Menon, V. (2004). Default-mode network activity distinguishes Alzheimer's disease from healthy aging: Evidence from functional MRI. *Proceedings of the National Academy of Sciences, 101*(13), 4637–4642.

Greve, D. N. & Fischl, B. (2009). Accurate and robust brain image alignment using boundary-based registration. *NeuroImage, 48*(1), 63–72.

Hindriks, R., Adhikari, M., Murayama, Y., Ganzetti,

M., Mantini, D., Logothetis, N., & Deco, G. (2016). Can sliding-window correlations reveal dynamic functional connectivity in resting-state fMRI? *NeuroImage, 127*, 242–256.

Hoge, W. S., Setsompop, K., & Polimeni, J. R. (2018). Dual-polarity slice-GRAPPA for concurrent ghost correction and slice separation in simultaneous multi-slice EPI. *Magnetic Resonance in Medicine, 80*(4), 1364–1375.

Hutchison, R. M., Womelsdorf, T., Allen, E. A., Bandettini, P. A., Calhoun, V. D., Corbetta, M., & … Chang, C. (2013). Dynamic functional connectivity: Promise, issues, and interpretations. *NeuroImage, 80*, 360–378.

Hyvarinen, A. (1999). Fast and robust fixed-point algorithms for independent component analysis. *IEEE Transactions on Neural Networks, 10*(3), 626–634.

Iraji, A., Faghiri, A., Lewis, N., Fu, Z., Rachakonda, S., and Calhoun, V. (2020). *Tools of the trade: Estimating time-varying connectivity patterns from fMRI data*. PsyArXiv.

Jenkinson, M., Bannister, P., Brady, M., & Smith, S. (2002). Improved optimization for the robust and accurate linear registration and motion correction of brain images. *NeuroImage, 17*(2), 825–841.

Jenkinson, M., Beckmann, C. F., Behrens, T. E., Woolrich, M. W., & Smith, S. M. (2012). FSL. *NeuroImage, 62*(2), 782–790.

Kiviniemi, V., Vire, T., Remes, J., Elseoud, A. A., Starck, T., Tervonen, O., & Nikkinen, J. (2011). A sliding time-window ICA reveals spatial variability of the default mode network in time. *Brain Connectivity, 1*(4), 339–347.

Laird, A. R., Fox, P. M., Eickhoff, S. B., Turner, J. A., Ray, K. L., McKay, D. R., & … Fox, P. T. (2011). Behavioral interpretations of intrinsic connectivity networks. *Journal of Cognitive Neuroscience, 23*(12), 4022–4037.

Lanczos, C. (1964). Evaluation of noisy data. *Journal of the Society for Industrial and Applied Mathematics Series B Numerical Analysis, 1*(1), 76–85.

Lehmann, M., Madison, C., Ghosh, P. M., Miller, Z. A., Greicius, M. D., Kramer, J. H., & … Rabinovici, G. D. (2015). Loss of functional connectivity is greater outside the default mode network in nonfamilial early-onset Alzheimer's disease variants. *Neurobiology*

of Aging, 36(10), 2678–2686.

Leonardi, N. & Van De Ville, D. (2015). On spurious and real fluctuations of dynamic functional connectivity during rest. *NeuroImage, 104*, 430–436.

Liégeois, R., Laumann, T. O., Snyder, A. Z., Zhou, J., & Yeo, B. T. (2017). *Interpreting temporal fluctuations in resting-state functional connectivity MRI*. Neuroscience.

Liégeois, R., Li, J., Kong, R., Orban, C., Van De Ville, D., Ge, T., Sabuncu, M. R., & Yeo, B.T. T. (2019). Resting brain dynamics at different timescales capture distinct aspects of human behavior. *Nature Communications, 10*(1), 1–9.

Liu, X., & Duyn, J. H. (2013). Time-varying functional network information extracted from brief instances of spontaneous brain activity. *Proceedings of the National Academy of Sciences, 110*(11), 4392–4397.

Llera, A., Chauvin, R., Mulders, P., Naaijen, J., Mennes, M., & Beckmann, C. F. (2020). *Spatial patterns for discriminative estimation*. BioRxiv.

Lurie, D. J., Kessler, D., Bassett, D. S., Betzel, R. F., Breakspear, M., Kheilholz, S., & … Calhoun, V. D. (2020). Questions and controversies in the study of time-varying functional connectivity in resting fMRI. *Network Neuroscience, 4*(1), 30–69.

Lustig, C., Snyder, A. Z., Bhakta, M., O'Brien, K. C., McAvoy, M., Raichle, M. E., & … Buckner, R. L. (2003). Functional deactivations: Change with age and dementia of the Alzheimer type. *Proceedings of the National Academy of Sciences, 100*(24), 14504–14509.

Lynall, M. E., Bassett, D. S., Kerwin, R., McKenna, P. J., Kitzbichler, M., Muller, U., & Bullmore, E. (2010). Functional connectivity and brain networks in schizophrenia. *Journal of Neuroscience, 30*(28), 9477–9487.

Marques, J. P., Kober, T., Krueger, G., van der Zwaag, W., van de Moortele, P. F., & Gruetter, R. (2010). MP2RAGE, a self bias-field corrected sequence for improved segmentation and T1-mapping at high field. *NeuroImage, 49*(2), 1271–1281.

McKeown, M. (2003). Independent component analysis of functional MRI: What is signal and what is noise? *Current Opinion in Neurobiology, 13*(5), 620–629.

McKeown, M. J. & Sejnowski, T. J. (1998).

Independent component analysis of fMRI data: Examining the assumptions. H*uman Brain Mapping, 6*(5-6), 368–372.

Mulders, P., Llera, A., Tendolkar, I., van Eijndhoven, P., & Beckmann, C. (2018). Personality profiles are associated with functional brain networks related to cognition and emotion. *Scientific Reports, 8*(1), 1–8.

Mulders, P. C., van Eijndhoven, P. F., Schene, A. H., Beckmann, C. F., & Tendolkar, I. (2015). Resting-state functional connectivity in major depressive disorder: A review. *Neuroscience & Biobehavioral Reviews, 56*, 330–344.

Niazy, R. K., Xie, J., Miller, K., Beckmann, C. F., & Smith, S. M. (2011). Spectral characteristics of resting state networks. *Progress in Brain Research, 193, 259–276*.

Nickerson, L. D., Smith, S. M., Öngür, D., and Beckmann, C. F. (2017). Using dual regression to investigate network shape and amplitude infunctional connectivity analyses. *Frontiers in Neuroscience, 11,* 115.

Noteboom, S. (2018). *Ultrafast fMRI for Studying Fine Hemodynamic Response Latency Differences* (Master thesis, University of Twente and Donders Institute, the Netherlands).

Petridou, N., Gaudes, C. C., Dryden, I. L., Francis, S. T., & Gowland, P. A. (2013). Periods of rest in fMRI contain individual spontaneous events which are related to slowly fluctuating spontaneous activity. *Human Brain Mapping, 34*(6), 1319–1329.

Poldrack, R. A., Nichols, T., & Mumford, J. (2011). *Handbook of Functional MRI Data Analysis*. Cambridge, United Kingdom: Cambridge University Press.

Preti, M. G., Bolton, T. A., & Van De Ville, D. (2017). The dynamic functional connectome: State-of-the-art and perspectives. *NeuroImage, 160*, 41–54.

Ray, K. L., McKay, D. R., Fox, P. M., Riedel, M. C., Uecker, A. M., Beckmann, & ... Laird, A. R. (2013). ICA model order selection of task co-activation networks. *Frontiers in Neuroscience, 7, 237*.

Reuter, M., Rosas, H. D., & Fischl, B. (2010). Highly accurate inverse consistent registration: A robust approach. *NeuroImage, 53*(4), 1181–1196.

Rogers, B. P., Katwal, S. B., Morgan, V. L., Asplund, C. L., & Gore, J. C. (2010). Functional MRI and multivariate autoregressive models. *Magnetic Resonance Imaging, 28*(8), 1058–1065.

Rosa, M. J., Daunizeau, J., and Friston, K. J. (2010). EEG-fMRI integration: A critical review of biophysical modeling and data analysis approaches. J*ournal of Integrative Neuroscience,* 9(4), 453–476.

Rosazza, C. and Minati, L. (2011). Resting-state brain networks: Literature review and clinical applications. *Neurological Sciences, 32*(5), 773–785.

Setsompop, K., Gagoski, B. A., Polimeni, J. R., Witzel, T., Wedeen, V. J., & Wald, L. L. (2012). Blipped-controlled aliasing in parallel imaging for simultaneous multislice echo planar imaging with reduced g-factor penalty. *Magnetic Resonance in Medicine, 67*(5), 1210–1224.

Singh, K. & Fawcett, I. (2008). Transient and linearly graded deactivation of the human default-mode network by a visual detection task. *NeuroImage, 41*(1), 100–112.

Smith, S. M., Fox, P. T., Miller, K. L., Glahn, D. C., Fox, P. M., Mackay, C. E., & ... Beckmann, C. F. (2009). Correspondence of the brain's functional architecture during activation and rest. *Proceedings of the National Academy of Sciences, 106*(31), 13040–13045.

Smith, S. M., Jenkinson, M., Woolrich, M. W., Beckmann, C. F., Behrens, T. E., Johansen-Berg, H., & ... Matthews, P. M. (2004). Advances in functional and structural MR image analysis and implementation as FSL. *NeuroImage, 23*, 208–219.

Smith, S. M., Miller, K. L., Moeller, S., Xu, J., Auerbach, E. J., Woolrich, M. W., & ... Ugurbil, K. (2012). Temporally-independent functional modes of spontaneous brain activity. *Proceedings of the National Academy of Sciences, 109*(8), 3131–3136.

Tagliazucchi, E., Siniatchkin, M., Laufs, H., & Chialvo, D. R. (2016). The voxel-wise functional connectome can be efficiently derived from co-activations in a sparse spatio-temporal point-process. *Frontiers in Neuroscience, 10*, 381.

Treiber, J. M., White, N. S., Steed, T. C., Bartsch, H., Holland, D., Farid, N., & ... Chen, C. C.

(2016). Characterization and correction of geometric distortions in 814 diffusion weighted images. *PLoS one, 11*(3), e0152472.

Tustison, N. J., Avants, B. B., Cook, P. A., Zheng, J., Egan, A., Yushkevich, P. A., & Gee, J. C. (2010). N4ITK: Improved N3 bias correction. *IEEE Transactions on Medical Imaging, 29*(6), 1310–1320.

Uddin, L. Q., Supekar, K., & Menon, V. (2010). Typical and atypical development of functional human brain networks: Insights from resting-state fMRI. *Frontiers in Systems Neuroscience, 4.*

van Oort, E., Koopmans, P., Boyacioglu, R., Barth, M., Beckmann, C., & Norris, D. (2012). Frequency characteristics of large scale resting state networks using 7T Spin Echo EPI. *Proceedings of the International Society for Magnetic Resonance in Medicine, 21.*

van Oort, E. S., Mennes, M., Schröder, T. N., Kumar, V. J., Jimenez, N. I. Z., Grodd, W., Doeller, C.F. & Beckmann, C. F. (2018). Functional parcellation using time courses of instantaneous connectivity. *NeuroImage, 170*, 31–40.

Vidaurre, D., Quinn, A. J., Baker, A. P., Dupret, D., Tejero-Cantero, A., & Woolrich, M. W. (2016). Spectrally resolved fast transient brain states in electrophysiological data. *NeuroImage, 126*, 81–95.

Vidaurre, D., Smith, S. M., & Woolrich, M. W. (2017). Brain network dynamics are hierarchically organized in time. *Proceedings of the National Academy of Sciences, 114*(48), 12827–12832.

Wang, S., Peterson, D. J., Gatenby, J. C., Li, W., Grabowski, T. J., & Madhyastha, T. M. (2017). Evaluation of field map and nonlinear registration methods for correction of susceptibility artifacts in diffusion MRI. *Frontiers in Neuroinformatics, 11.*

Yaesoubi, M., Allen, E. A., Miller, R. L., & Calhoun, V. D. (2015). Dynamic coherence analysis of resting fMRI data to jointly capture state-based phase, frequency, and time-domain information. *NeuroImage, 120,* 133–142.

Zhang, Y., Brady, M., & Smith, S. (2001). Segmentation of brain MR images through a hidden Markov random field model and the expectation-maximization algorithm. *IEEE Transactions on Medical Imaging, 20*(1), 45–57.

Supplementary Material

I. Data and code availability statement

Data will be stored at the Donders Repository and are made available upon request. A documented python package was developed for TV-TFM analysis, which will be made available under https://github.com/tamarajedidja/tv-tfm upon publication. The package only supports python 3.6+.

II. Dataset selection

A single-subject, single task run dataset was selected for illustrative purposes. This dataset was initially selected based on the numbers of spatial correlations larger than r = .3 (an arbitrary threshold) between the well-defined networks of the SMITH20 template and TFMs (see Table 2). Given the assumption for this

Table 2.

Spatial correlations between the ten well-defined SMITH20 networks and task-related TFMs per participant.

Participant	Descriptives	
	Range	No. of r > 0.3 (ses-01,02,03)*
1	<0.001–0.38	3, 2, 4
2	0.001–0.41	2, 2, 3
3	<0.001–0.42	3, 4, 2
4	<0.001–0.48	3, 4, 4
5	<0.001–0.40	2, 0, 4
6	<0.001–0.31	0, 7, 3
7	<0.001–0.34	2, 1, 3
8	0.001–0.30	0, 1
9	<0.001–0.45	3, 4, 8
10	<0.001–0.34	2, 2, 4
11	0.001–0.38	2, 3, 4
12	0.001–0.44	2, 6
13	0.001–0.41	2, 3, 1
14	<0.001–0.45	6, 7, 2

(*) Number of correlations between the well-defined networks of the SMITH20 template and task-related TFMs that are larger than r = 3.

Table 3.

Group-level results: one-sample t-test on Fisher-Z transformed correlations of task vs. dual-regression time series.

Participant	Descriptives			
	Visual		Motor	
	t-value	p-value	t-value	p-value
Primary visual (V2)	3.25	0.006	0.29	0.7768
Lateral visual (V3)	8.30	< 0.0001*	3.55	0.0036
Medial visual (V1)	7.95	< 0.0001*	8.86	< 0.0001*
Sensorimotor	10.76	< 0.0001*	6.05	< 0.0001*.
Cerebellum	-6.58	< 0.0001*	-3.00	0.0102
Auditory	10.61	< 0.0001*	8.79	< 0.0001*
ECN	3.43	0.0045	3.37	0.0050
Frontoparietal (Left)	6.93	< 0.0001*	8.90	< 0.0001*
Frontoparietal (Right)	8.49	< 0.0001*	12.13	< 0.0001*
DMN	-5.46	0.0001*	-4.58	0.0005*
NWD (1)	-3.93	0.0017*	-2.62	0.0212
NWD (2)	-0.77	0.4555	-2.22	0.0448
NWD (3)	-4.65	0.0005*	-6.86	< 0.0001*
NWD (4)	-6.96	< 0.0001*	-5.38	0.0001*
NWD (5)	12.90	< 0.0001*	14.22	< 0.0001*
NWD (6)	3.67	0.0028	2.40	0.0318
NWD (7)	3.74	0.0025	4.44	0.0007*
NWD (8)	0.87	.3987	0.59	0.5671
NWD (9)	6.33	< 0.0001*	6.42	< 0.0001*
NWD (10)	7.80	< 0.0001*	8.17	< 0.0001*

Abbreviations: ECN = executive control network, DMN = default mode network, NWD = not well defined; (*) Significantly different from zero, after Bonferroni correction (i.e. significance below .05/20 = .0025).

task-based proof-of-concept that temporal ICA at stage two of the analysis needs to identify the process of interest adequately, we selected task-related TFMs based on their association with the visual task regressor per task run. Of the participants for which all three sessions were included, the correlation between the task-related TFM and the task regressor was strongest for the selected data-set (r = .48; Fisher-Z transformed correlations are visually presented for all task runs in panel B of Figure 6).

III. Stage 1 dual-regression: statistics one-sample t-tests

To identify the dual-regression time series that across participants were significantly related to the task, a third-level analysis was performed using a one-sample t-test per resting-state network as identified by Smith et al. (2009). An overview of the Bonferroni corrected t-statistics is presented in Table 3.

IV. Stage 2 classical TFM: correlation to confounds

TFM time series were correlated to confound time series as an indication of their neuronal basis. As described in the main manuscript, group-level comparisons per TFM are problematic due to the correspondence problem
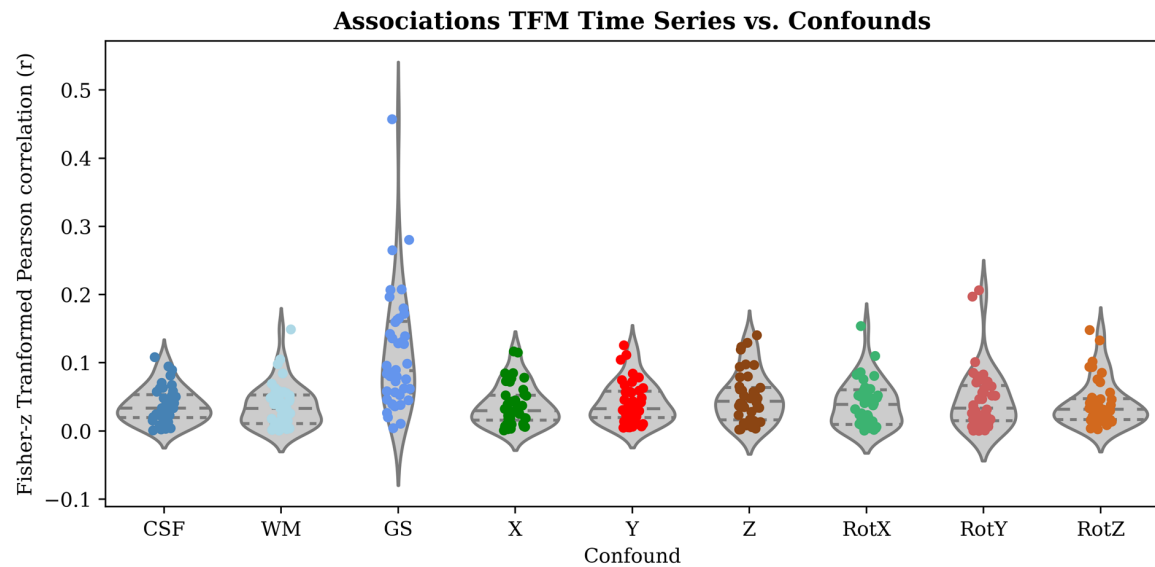
Figure 11. The distributions of the Fisher-Z transformed correlation values per task-run between the task-related TFM (i.e., that correlated most strongly with the visual task regressor) time series and the confound regressors are presented. Abbreviations: CSF = cerebral spinal fluid; WM = white matter; GS = global signal; X, Y, Z, RotX, RotY, RotZ = motion directions.

of temporal ICA. Therefore, the task-related TFMs were selected based on the strongest absolute correlation with the visual task regressor. Their time series were correlated with the confound regressors. The Fisher-Z transformed correlation values for all task runs are presented in Figure 11. Evident from this picture is the enlarged associations with the global signal. This finding is in line with the conclusion by Glasser et al. (2018), that spatial ICA (as used for data cleaning in the current study) is very effective at removing spatially specific structured noise from high temporal resolution fMRI data, but that it cannot selectively and completely remove global structured noise while retaining global signal form neural activity. Clean up using temporal ICA was proposed as a potential solution, which could be considered in the future.

V. Stage 2 classical TFM: identified TFMs

TFMs similar to the task-positive and default temporal mode identified for the selected dataset were found across most participants and task runs. Spatial correlations between the node weights of M for these TFMs identified for the selected dataset and the node weights of all other extracted TFMs were computed

per task run. The average spatial correlation with the Task-Positive Mode was $r = 0.64$ (SD = 0.10, range: 0.34 - 0.86) and the average spatial correlation the Default Temporal Mode was $r = 0.61$ (SD = 0.07, range: 0.49 - 0.79).

Table 4.

Sum of the absolute correlation values for all entries of the time-varying mixing matrix per TFM (for the selected dataset).

TFM	Sum of the absolute r-values:	
	Visual	Motor
TFM1	1.33	0.92
TFM2	1.20	1.03
TFM3	3.83	1.69
TFM4	1.16	1.10
TFM5	1.74	1.35
TFM6	1.59	2.04
TFM7	1.09	0.98
TFM8	1.53	1.80
TFM9	0.96	0.92
TFM10	0.80	0.86
TFM11	0.54	1.03
TFM12	1.22	1.49
TFM13	1.35	0.95
TFM14	1.38	2.33
TFM15	0.94	0.93

PANEL A **Task-Positive Mode**

Participant 1 (task-run 2) | Participant 4 (task-run 1)

PANEL B **Default Temporal Mode**

Participant 9 (task-run 2) | Participant 12 (task-run 2)

PANEL C

Default Temporal Mode (Smith 10)

Mixing Matrix (M) Column
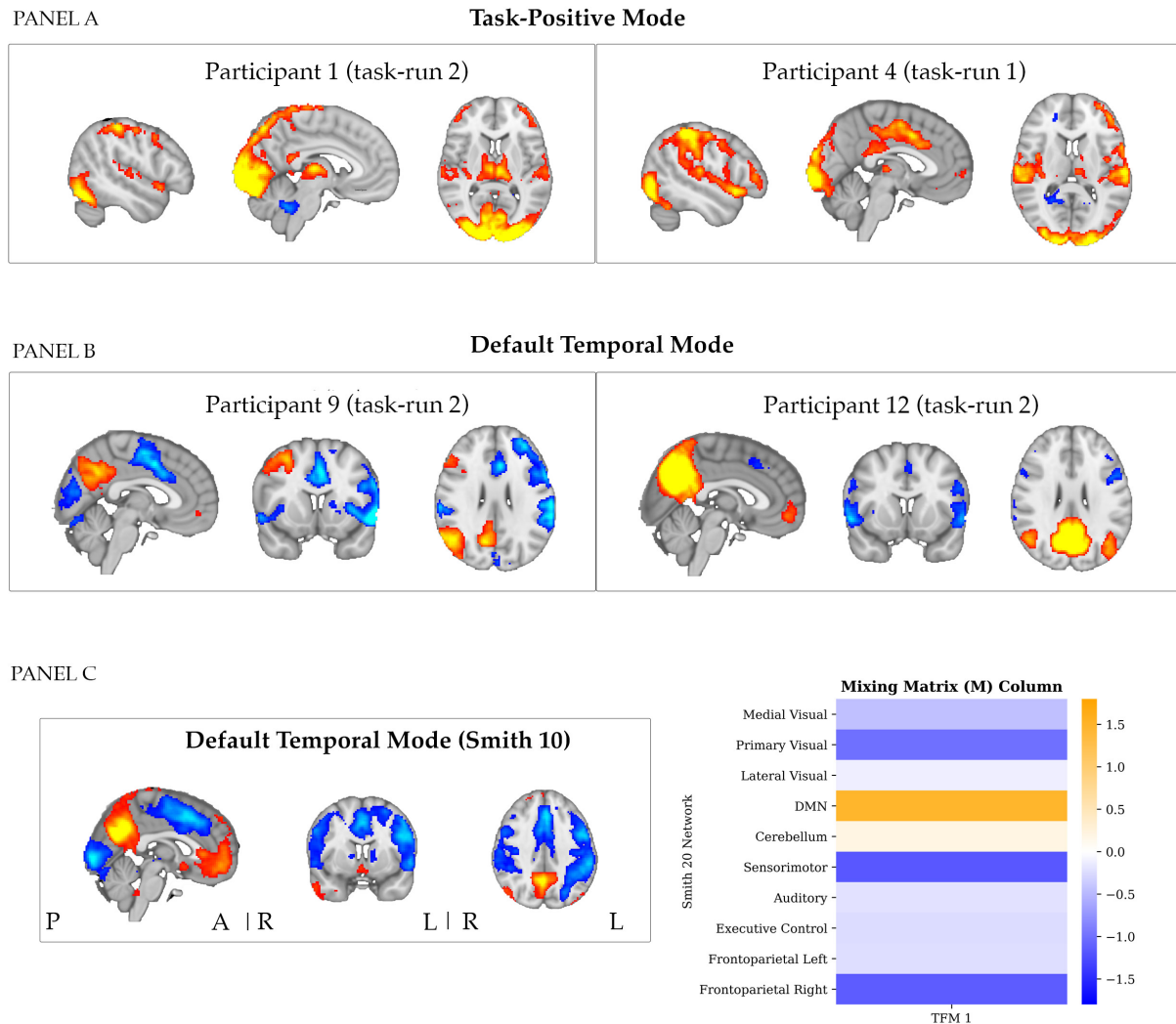
Figure 12. The two TFMs most strongly correlated to the task-positive mode as identified for the selected dataset and the two TFMs most strongly correlated to the default temporal mode as identified for the selected dataset are presented in panel A and B, respectively. Panel C shows three representative slices of the default temporal mode for the selected dataset after temporal ICA with a model order of ten (TFM1; thresholded at Z > 5), and the associated mixing matrix column, which describes the time-averaged weighting of this TFM onto the Smith networks. Colour coding spatial maps: blue (negative) to red/yellow (positive).

In panel A of Figure 12, two illustrative spatial maps are plotted for the TFMs that correlated most strongly to the task-positive mode identified for the selected dataset. Moreover, two illustrative spatial maps are plotted for the TFMs that correlated most strongly to the default temporal mode identified for the selected dataset in panel B.

In panel C of Figure 12, the spatial map of the default temporal mode is presented for the selected dataset, as obtained with a temporal ICA of model-order ten on the time series of the ten-well defined networks by Smith et al. (2009). We observe that at this model-order, the default temporal mode involves an anti-correlated pattern between core hubs of the DMN *also in anti-correlation with visual areas*.

VI. Stage 3 TV-TFM: correlation values for all entries of the time-varying mixing matrix per TFM

Results presented in Table 4 show that the sum of the absolute correlation values across the entries of the time-varying mixing matrix

Figure 13. Trial-averaged entries of the time-varying mixing matrix for the task-related TFM (i.e., most strongly associated with the visual task regressor), per task run, per participant.

for each TFM, for associations of entries of the time-varying mixing matrix with the visual and motor task regressors. We observed that the sum of the correlation values was highest for TFM3 when related to the visual task regressor and for entries of TFM14 when related to the motor task regressor (for the selected dataset). These were the same TFMs for which the time series correlated most strongly to the task regressors.

VII. Stage 3 TV-TFM: Trial-averaged entries of the time-varying mixing matrix per task run, per-participant

We observed a pattern in the time-varying mixing matrix entries of the task-positive mode for the selected dataset that closely followed the task design. A similar trend was observed for most participants and task runs, which are presented in Figure 13. This figure shows the trial-averaged task-relevant entries of the time-varying mixing matrix for the TFM that was most strongly associated with the visual task regressor per task run, per participant.

Characterizing Cognitive Defects of Myotonic Dystrophy Type 1 in a Dish: Insight From Induced Neurons

Lisa Rahm[1]

Supervisors: Renée H.L. Raaijmakers[1,2], C. Rosanne M. Ausems[1,2], Marina Hommersom[2], Derick G. Wansink[3], and Hans van Bokhoven[1,2]

Corresponding author: Lisa Rahm
E-mail: lisa.rahm@freenet.de

[1]*Radboud University Nijmegen, Donders Institute for Brain, Cognition and Behaviour, The Netherlands*
[2]*Radboud University Medical Centre Nijmegen, Donders Institute for Brain, Cognition and Behaviour, The Netherlands*
[3]*Radboud Institute for Molecular Life Sciences, The Netherlands*

Myotonic dystrophy type 1 (DM1) is an inherited autosomal dominant multisystemic disorder including symptoms in the central nervous system. Symptoms include cognitive and memory deficits, which seem to be caused by global synaptic dysfunction. In order to recapitulate the brain phenotype, we created neurons from induced pluripotent stem cells (iPSC) from DM1 patients, which was done by an imposed expression of the transcription factor neurogenin-2. From there, we performed immunocytochemistry and electrophysiological recordings of the neuronal activity. Reverse transcriptase quantitative polymerase chain reaction (RT-qPCR) experiments were performed to study gene expression of DM1 related genes. iPSC express less DM1 specific genes compared to adult myoblasts. We, furthermore, demonstrated that it is possible to differentiate iPSCs from DM1 patients into iNeurons that show DM1 disease markers, and we made a step toward unravelling the DM1 neuropathophysiology.

KEYWORDS Myotonic Dystrophy Type 1, neuromuscular disorder, induced neurons, immunocytochemistry, multi-electrode array analysis

Abbreviations

DM1 – Myotonic dystrophy type 1
CNS – Central nervous system
UTR – untranslated region
DMPK – Dystrophia Myotonica Protein Kinase
CTG – cytosine-thymine-guanine
CUG – cytosine-uracil-guanine
RNA – ribonucleic acid
GOF – gain-of-function
MBNL – muscleblind-like proteins

PKC – protein kinase C
CELF – CUG/Elav-like family
NFT – neurofibrillary tangles
MAPT – microtubule associated protein Tau
MRI – magnetic resonance imaging
GM – grey matter
WM – white matter
FISH – fluorescence in situ hybridization
CAG – cytosine-adenine-guanine

IF – immunofluorescence
NMDAR - N-methyl-D-aspartate receptor
LTP – long-term potentiation
iNeurons – induced neurons
hiPSC – human induced pluripotent stem cells
SCTC – Stem Cell Technology Centre
RT-qPCR – reverse transcriptase quantitative polymerase chain reaction
MIRS – Muscle Impairment Rating Scale
RIMLS – Radboud Institute for Molecular Life Science
STD – standard deviation
HKG – housekeeping genes
WP – well plate
MTG – Matrigel
PLO – Poly-L-Ornithine
(O/N) – overnight

hNT3 – human Neurotrophin-3
hBDNF – human Brain-derived Neurotrophic Factor
Ara-C – Cytosine β-D-arabinofuranoside
FBS – Foetal bovine serum
PBS - Phosphate-buffered saline
PFA – paraformaldehyde
RT – room temperature
Ac:Me – Aceton-Methanol
MAP2 – Microtubule-associated protein 2
MEA – multi-electrode array
PCR – polymerase chain reaction
GLT1 - Glutamate transporter 1
SP-PCR - small pool PCR
TP-PCR – triplet primed PCR
SRY – Sex Determining Region

Myotonic dystrophy type 1 (DM1) is a multi-systemic neuromuscular disorder with an estimated prevalence of at least 1 in 8,000 (Caillet-Boudin et al., 2014; Longman, 2006). This disorder affects several organs in the body, such as skeletal and smooth muscles, the heart, the eyes, and the central nervous system (CNS). This leads to symptoms such as myotonia (the delayed relaxation after voluntary muscular contraction), muscle weakness and wasting, arrythmias and conduction defects, as well as breathing difficulties, and cataracts (Dhaenens et al., 2011; Wenninger, Montagnese, & Schoser, 2018). DM1 is known for its typical symptoms such as myotonia and muscle wasting, but it is also accompanied by cognitive impairments such as executive dysfunction, visuospatial deficits and abnormal social cognition (Caillet-Boudin et al., 2014; Dhaenens et al., 2011; Hernández-Hernández et al., 2013; Suenaga et al., 2012). Executive function is important for daily life, it is involved in planning, time management and solving problems. Visuospatial skills are also required in daily life. With a deficit in this domain, difficulties can range from identifying and processing simple visual stimuli, up to identifying faces or whole scenes (Scott & Schoenberg, 2006). Abnormal social cognition is defined by the difficulties in processing, decoding and encoding, storing, and applying information about social situations or other people (Beer & Ochsner, 2006). These deficits are said to be caused by abnormal neuronal morphology and malfunctioning synapses.

DMI is caused by an autosomal dominant gene mutation in the 3' untranslated region (UTR) of the Dystrophia Myotonica Protein Kinase (DMPK) gene, which is located on chromosome 19q13.32. The mutation is an expanded repeat of the base-pair triplet sequence cytosine-thymine-guanine (CTG). Healthy individuals have a repeat sequence ranging from 5 to 37 and do not show disease burden. However, a repeat of 50-1000 CTG-triplets, is associated with a wide range of mild to severe DM1 symptoms. Mild symptoms include facial and distal muscle
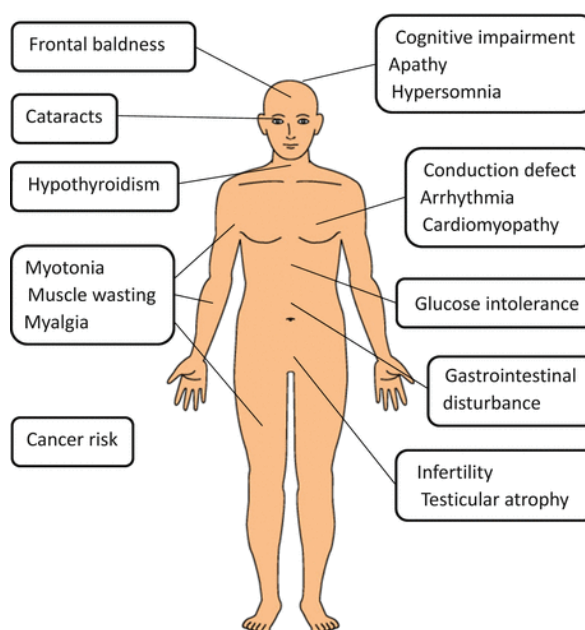

Figure 1. Affected body parts in DM1 patients. Reprinted from Nakamori & Takahashi (2016).

weakness, and severe symptoms include additional cognitive impairment and other extra muscular symptoms (Wenninger et al., 2018). The childhood/juvenile phenotype is associated with an early onset and typically has >800 CTG-repeat. The congenital form is the most severe with usually >1000 CTG-repeat (Wenninger et al., 2018). The repeat length is not only critically linked to disease severity and age of onset, but also shows genetic anticipation: the tendency to grow over time in the patient due to somatic instability (Caillet-Boudin et al., 2014; Morales et al., 2012; Yum, Wang, & Kalsotra, 2017) and to increase in size from one generation to the next. This results in increased disease burden (Dhaenens et al., 2008; Gomes-Pereira et al., 2007; Morales et al., 2012). For DM1, somatic instability means that the CTG repeat length differs between tissue types (e.g., longer repeats have been found in muscle and the brain compared to leukocytes) (Jinnai et al., 2013).

The disease pathogenesis of DM1 reveals that the corresponding phenotype appears to be regulated mainly by a deleterious gain-of-function (GOF) caused by the expanded DMPK transcripts. These transcripts form secondary hairpin-like RNA structures that bind to and sequester muscleblind-like proteins (MBNL) into ribonuclear inclusions, also known as RNA foci (André, van Cruchten, Willemse, & Wansink, 2019). Furthermore, cytosine-uracil-guanine (CUG) expansions in the 3'-UTR of the DMPK mRNA are activated by the protein kinase C (PKC) pathway which results in phosphorylation of CUG/Elav-like family (CELF1) proteins. This hyperphosphorylation causes a stabilization of the protein and results in its upregulation (Gallo & Spickett, 2010). Together with MBNL proteins, CELF proteins are responsible for the regulation of splicing

mechanisms, however, the RNA toxicity caused by CUG-repeat results in aberrant splicing patterns – therefore, DM1 is defined as spliceopathy (Hernández-Hernández et al., 2013). Muscle weakness and loss are results of these aberrant splicing patterns and several mis-splicing defects have also been reported to occur in the DM1 brain. However, the mis-splicing in neuropathophysiology is not currently understood. In several recent studies, DM1 has also been described as a RNAopathy due to its toxic RNA GOF, and as a tauopathy because neurofibrillary tangles (NFT) have been found in the brain of DM1 patients (Dhaenens et al., 2008; Dahenens et al., 2011). The group of tauopathies encompasses several neurodegenerative diseases which are all characterized by intraneuronal protein aggregates of the microtubule-associated protein Tau (MAPT) in the amygdala, hippocampus, entorhinal cortex, and temporal cortex (Caillet-Boudin et al., 2014; Dhaenens et al., 2011; Hernández-Hernández et al., 2013). Our knowledge of the CNS-related symptoms in DM1 patients is based on MRI studies, post-mortem brain material of DM1 patients, and on DM1 mouse models.

MRI studies have been conducted to investigate the DM1 brain phenotype in terms of structural brain abnormalities, such as loss of grey matter (GM) regions and white matter (WM) regions (Caillet-Boudin et al., 2014; Hamilton et al., 2018; Van der Plas et al., 2019). Global cerebral atrophy and loss of cortical GM has been found in brain regions involved in cognitive functioning, attention, memory and visuospatial functioning (Caillet-Boudin et al., 2014; Ramon-Duaso et al., 2020). Lesions in WM temporal lobes are a very prominent phenotype in the DM1 brain, and are even more distinctive than GM lesions (Caillet-Boudin et al., 2014).
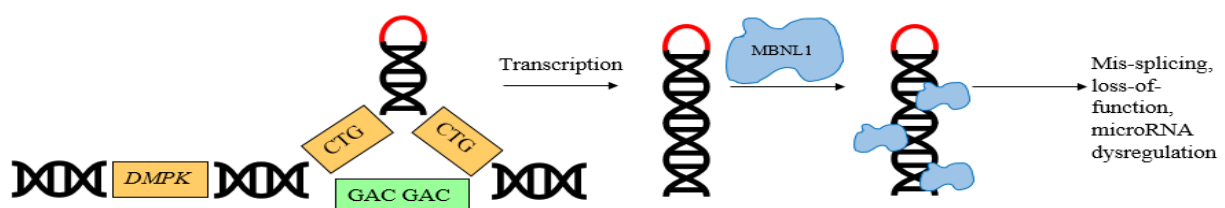

Figure 2. Expanded CTG triplets in 3'UTR of DMPK are transcribed to r(CUG)exp, forming secondary hairpin-like structures. Members of the MBNL family such as MBNL1 are sequestered into ribonuclear inclusions which cause a loss-of-function, mRNA mis-splicing and microRNA dysregulation (Udd & Krahe, 2012).

Post-mortem brain material of DM1 patients has also been studied, however, the difficulty here is that active processes cannot be studied. Nonetheless, we can still gain information about repeat size in different tissue types. Jiang, Mankodi, Swanson, Moxley, and Thornton (2004) performed fluorescence in situ hybridization (FISH) with a (CAG)6 probe of brain sections and found nuclear RNA foci in every patient. Each (CAG)6 probe is labelled with a fluorescent dye and to become visible, a certain threshold needs to be reached. The number of foci per neuron ranged from 1 up to 15 foci.). However, due to technical limitations in microscopy (Sanderson, Smith, Parker, & Bootman, 2014), a lot less RNA foci have been found in patients with a short repeat and a mild phenotype (Jiang et al., 2004).

Braz and colleagues (2018) reported that in DM1 mouse models pre- and postsynaptic events are involved in the dysregulated disease mechanism. Those events reflect global synaptic dysfunction, which then causes cognitive and memory deficits. More precisely they state that in DMSXL mice, transgenic mice carrying the human DM1 locus with an (CTG)>1000, impaired short-term plasticity was found in the pre-synapse, which was mostly caused by a decrease in the paired-pulse facilitation (Braz, Acquaire, Gourdon, & Gomes-Pereira, 2018; Hernández-Hernández et al., 2013). Charizanis et al. (2012) reported that MBNL1 and MBNL2 are the two major MBNL proteins that are expressed in adult tissue, and that MBNL2 appears to be the protein that is most dysregulated in the CNS in DM1 patients (Charizanis et al., 2012; Goodwin et al., 2015). Furthermore, in Mbnl2 knockout mice (Mbnl2ΔE2/ΔE2) they found Mbnl2 mostly in the nucleus of neurons in the hippocampal structure. Mbnl2ΔE2/ΔE2 mice showed a deficit in spatial reference memory. A loss of expressed Mbnl1 led to a decrease in synaptic N-methyl-D-aspartate receptor (NMDAR) activity, impaired long-term potentiation (LTP) and deficits in memory and learning (Charizanis et al., 2012). Additionally, splicing effects were also investigated and Mbnl2 was found to be essential in splicing regulation during brain development (Table S1) (Charizanis et al., 2012). The Mbnl2 knockout mouse model seemed to (at least partially) reproduce the brain pathology found in the human DM1 brain (Caillet-Boudin et al., 2014; Charizanis et al., 2012).

Aforementioned research on MRI, post-mortem material, and mouse models provides us with results about the DM1 brain structure to further unravel its pathological mechanisms. Nonetheless, these three ways to study the disease are not ideal. MRI investigations are limited by real-time resolution because a scan for the whole brain takes 2 to 3 minutes, which makes it difficult to see certain processes. A limitation of post-mortem material is that no active processes can be investigated, and tissue degrades. While mouse models mimic the disease and disease related behaviour to a certain extent, it would be helpful to study pathological mechanisms on living human DM1 material.

Therefore, the aim of this study is to develop a cell-based model by generating induced neurons (iNeurons) from human derived induced pluripotent stem cells (hiPSCs) of two DM1 patients. These derived iNeurons will then be compared with healthy iNeurons in terms of their morphology, electrophysiological profile and DM1 specific phenotypes such as RNA foci and (mis-) splicing.

Methods

The Stem Cell Technology Center (SCTC) at the Radboudumc created two iPSC lines from fibroblasts of two DM1 patients (Table 1). These fibroblasts were reprogrammed with lentiviral vectors containing the genes OCT4, SOX2, KLF4 and c-MYC (Elegheert et al., 2018). Gene expression profiles of stem cell markers were examined by RT-qPCR, in which an upregulation of SOX2, LIN28, NANOG and DNMT3B was found compared to parental fibroblasts of P1 and P2 (Fig. S1 and S2). Furthermore, cells were tested on protein expression of stem cell markers via immunocytochemistry. The undifferentiated iPSC clones were stained for the nuclear markers NANOG and OCT4 and surface antigens SSEA4 and TRA-81 (Fig. S3 and S4).

For having a better estimation of the repeat length of the P2, northern blotting was performed by the Department of Cell biology at Radboud Institute for Molecular Life Science (RIMLS) with 10μg RNA. The result of

Table 1.

Clinical and Genetic Data of Included Participants, unaffected control; DM1, DM1 patient; MIRS, Muscle Impairment Rating Scale (ranging from 1-5, where 1 indicates mild symptoms and 5 indicates severe symptoms); M, male; F, female; NA, not applicable; Fbr, fibroblast; Per., pericyte; TP-PCR, Triplet-primed PCR. P1, P2 and C2 are fibroblast-derived iPSCs, P3 and C1 are pericyte-derived iPSCs.

	Sex (M/F)	Disease (CONT/DM1)	MIRS	Repeat Length at Diagnosis (No. of Triplets)	Origin of parental cells	Repeat Length by TP-PCR (No. of Triplets)	Age at Biopsy (years)
P1	M	DM1	2	64-77 (in blood)	Fbr.	87-97 (in iPSC)	64
P2	F	DM1	4	> 150 (in blood)	Fbr.	> 150 (in iPSC)	35
P3	M	DM1	5	120 < N < 1000	Per.	NA	46
C1	M	CONT	NA	NA	Per.	NA	45
C2	M	CONT	NA	NA	Fbr.	NA	NA

the northern blot was inconclusive, and we were not able to get an estimate of the repeat length in the iPSCs. Triplet repeat primed PCR (TP-PCR) with 40ng DNA was performed by Genome Diagnostics at Radboudumc (Leferink et al., 2019). iPSC samples of P1 and P2 from different passages were taken along. The results of the TP-PCR show that the repeat length of P1 is between 87 and 97, in iPSCs. The repeat length of P2, in iPSCs, is still above 150 and out of determination range of the TP-PCR. Small-pool PCR was used to determine repeat length of P3 and C1, confirming that C1 is a healthy individual, while iPSCs from P3 contain a repeat larger than 1500 (unpublished data), (Gomes-Pereira, Bidichandani, & Monckton, 2004).

Assessment of gene expression levels in iPSCs

RNA was extracted (NucleoSpin, Macherey-Nagel) and cDNA synthesis by random hexamers (iScript) was performed in order to gain more information about expression levels of genes of interest by RT-qPCR. DM1 related genes (MBNL1-3, DMPK e1-2, DMPK e15 3'), iPSC-specific genes (TBP e3, HPRT1 e7-9), and housekeeping genes (GUSB e11-12, GAPDH e1) were used. To optimize the primers, every gene was tested in a dilution range from 1:20 to 1:320 with contamination controls: milliQ (MQ, nuclease-free water) and RT- (cDNA synthesis excluding reverse transcriptase enzyme) as a control to guarantee that the cDNA is free from genomic DNA. All primer and cDNA mixes were pipetted in duplo to

measure their standard deviation (STD). For the later RT-qPCR experiment we used 1.667 ng/µL cDNA because the Ct values were most reliable and in the preferred range below 30. Furthermore, gene expression levels of the genes of interest were measured for C25 adult myoblasts as a comparison of MBNL1-3. Additionally, the cells from P1, P2, P3 and C1 were taken along, as a comparison for MBNL and DMPK expression.

Generation of Tet-On 3G and NGN2 stable lines, a pre-step for the differentiation of hiPSCs into iNeurons

The generation of the stable lines with Tet-On 3G and NGN2 was performed according to the protocol published by Frega et al. (2017) however, we used 12-well plates (12WP) coated with 1:15 MTG (0.53 – 0.67 mg/mL), instead of a geltrex-coated 12WP. Furthermore, instead of accutase (Sigma) we used TrypIE Select 1X for detachment and Essential 8 flex medium was supplemented with 1 mg/mL primocin (InvivoGen). For counting the cells, the following formula was used to calculate the total amount of cells per milliliter:

$$\frac{\text{no. of counted cells}}{\text{no. of counted chambers}} \times \text{volume of orig. cell}$$

$$\text{suspension in µL} \times 10,000 = \text{cells/mL}$$

After counting, the volume for 50,000 cells was calculated and then placed with a sufficient amount of media in a well of a 12WP. The

Primer Optimization
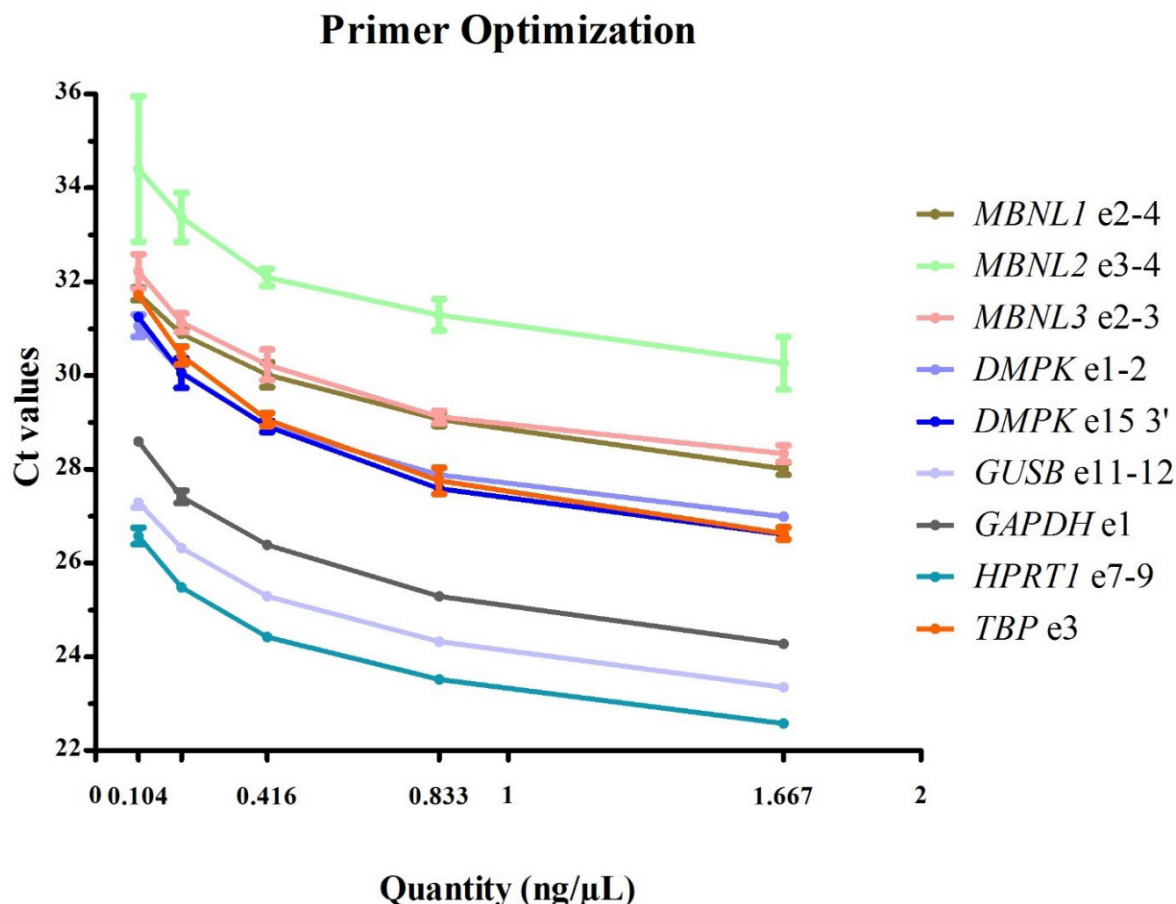
Figure 3. standard Curve of primer optimization. Primer pairs were tested on iPSC line of P1 on Genes of Interest (GoI): MBNL1 e2-4, MBNL2 e3-4, MBNL3 e2-3, DMPK e1-2, DMPK e15 3', Housekeeping Genes (HKG): GUSB e11, GAPDH e1, and iPSC specific Genes: HPRT1 e7-9, TBP e3. Used quantities were 0.104ng/μL, 0.208ng/μL, 0.416ng/μL, 0.833ng/μL and 1.667ng/μL. Therefore, the pictured dilutions are 1:320, 1:160, 1:80, 1:40 and 1:20. The Ct values are depicted with an error bar, indicating the deviation between the samples which were pipetted derived in duplo.

next day the iPSCs are transduced with the Tet-On 3G and NGN2 lentiviral constructs. The transfer vector that was used for the Tet-On 3G lentivirus is pLv.EF1a_TET3g.IRES.Neo; This vector, controlled by the EF-1a promoter region, encodes a Tet-On trans-activator and is resistant to neomycin (also known as G418). The transfer vector which was used for the NGN2 lentivirus is pLv.TRE3G.mNeurog2.Puro: The Tet-controlled promoter causes encoding of murine neurogenin-2 and the puromycin resistance gene. Both viruses were used in the concentrated form with the following packaging vectors: psPAX2 and pMD2.G.

We used different amounts of the lentiviral constructs compared to the ones by Frega et al. (2017) because we transduced the iPSCs with the third generation of lentiviruses. The concentrations which have been used to select Tet-On 3G-/NGN2-positive cells also

had to be adjusted, due to the same reason. Important is that from day five on, a basal concentration of the antibiotics was added as soon as the media was refreshed. The selection period must be adapted to the state of the cells and can take longer.

Differentiation of Tet-On 3G- and NGN2-positive hiPSC lines into iNeurons

To use Tet-On 3G- and NGN2-positive iPSCs for the differentiation, plates need to be coated such that the coating can solidify and cover the surface of the wells. We used Poly L-Ornithine (PLO) diluted in 50 mM borate buffer (50 μg/mL) which was then filtered and added to each well. The plates were placed for three hours in a humidified 37 °C

Table 2.

Lentiviral Transductions Concentrations of lentiviral constructs. Transduction number 4 and 5 were positive controls.

Transduction number	Tet-On 3G	NGN2
1	1µL	1µL
2	2µL	4µL
3	4µL	4µL
4	1µL	0µL
5	0µL	1µL

incubator with an atmosphere of 5% $CO2$. For the second part of the coating, human laminin [20 µg/mL, BioLamina] was diluted in cold Dulbecco's Modified Eagle Medium: Nutrient Mixture F-12 (DMEM/F12, gibco) by using cold pipet tips. Afterwards the plate was sealed with parafilm (Bemis) and incubated overnight (O/N) at 4 °C.

The subsequent day, iPSCs were made single cell, and doxycycline (4 µg/mL, Sigma) was added to induce expression of NGN2. For the day after plating the iPSCs as single cells no adjustments were made to the protocol by Frega et al. (2017). On day two of the differentiation, rat astrocytes were added to each well in a 1:1 ratio. For day three, adaptations were made for the supplements added to the neurobasal medium (gibco). It was supplemented with primocin (1:500 concentration), doxycycline (4 µg/mL), B-27 supplement 100X (1:50, gibco), glutamaxsupplement 100X (1:100 concentration, gibco), human Neurotrophin-3 (10 ng/mL) (hNT-3, Primokine), human Brain-derived Neurotrophic Factor (10 ng/mL) (hBDNF, Primokine). Furthermore, Cytosine

β-D-arabinofuranoside (2 µM) (Ara-C, Sigma). Ara-C was added to form a pure neuronal and astrocyte culture as it has an inhibiting function on astrocyte proliferation and kills remaining iPSC . From day six until day eight, around 50% of the medium per well is refreshed every second day. The required medium is the same as the one prepared for the day after adding the rat astrocytes, except that from day six until day eight no Ara-C was added. The first test differentiation stopped at this point and immunocytochemistry was performed. The results can be found in the results section under 'iNeuron characterization'.

From day eight onwards, around 50% of the spent neurobasal medium is refreshed every second day and the medium is supplemented with 2.5% Fetal bovine serum (FBS, Sigma) in order to sustain the astrocytes.

Immunofluorescence and Immunocytochemistry

DM1 disease markers in iPSC.

iPSCs were grown on coverslips which were coated with 1:50 phenol-red free growth factor reduced Matrigel (0.16 – 0.2 mg/mL, depending on the concentration in the bottle) [MTG, Corning] in 1x Phosphate-buffered saline (PBS). Protocols for RNA FISH (Stellaris kit, Biosearch Technologies), MBNL1, and FISH + MBNL1 were used.

For FISH, only our adjustments of the Stellaris protocol are listed in the following part. On day one for FISH, the cells were washed with 1x PBS and fixated in 1 mL 4% paraformaldehyde (PFA) for 10 min at room temperature (RT). To hybridize the cells, we applied 25 µL Hybridization Buffer

Table 3.

Concentrations of Antibiotics during Selection Period.

Day	Concentration neomycin (G418, Sigma)	Concentration puromycin (Sigma)
1	25 µg/mL	0.5 µg/mL
2	50 µg/mL	0.5 µg/mL
3	100 µg/mL	1 µg/mL
4	200 µg/mL	2 µg/mL
5 and later	50 µg/mL	0.5 µg/mL

per coverslip. For day two we followed the Stellaris protocol.

The protocol for the MBNL1 staining is as follows: On day one, the cells were washed with prewarmed 1x PBS and then fixated in -20 °C cold Acetone-Methanol (Ac:Me, 1:1) for 10 min. Afterwards, cells were washed 3x 5 min with 1x PBS and then permeabilized 10 min in 0.2% Triton. After permeabilization, coverslips were placed in blocking buffer for 1 hour at RT then incubated in blocking buffer and MBNL1 (1:10, 50µL per coverslip) at 4 °C O/N. On day 2, the cells were washed 3x 5 min in 1x PBS at RT and before incubation with 4 mg/mL goat-anti-mouse (Invitrogen) and 100 ng/mL DAPI for 1 hour in the dark at RT. Cells were then washed 3x 5min with 1x PBS, then dipped in MQ and mounted on an empty object slide.

For the combined staining of RNA FISH and MBNL1, we followed the Stellaris protocol with our adjustments (day 1). On day two, after the cells were incubated in Wash Buffer B, they were fixed in ice-cold Ac:Me and incubated for 10 min in the dark at -20 °C. Afterwards, they were washed 3x 5 min in 1x PBS and then incubated 1 hour at RT in blocking buffer. Then, they were incubated in blocking buffer and MBNL1 (1:10, 50 µL per coverslip) at 4 °C O/N. On day three, we followed the MBNL1 protocol for day two.

Fluorescent images of iPSC were acquired using a Leica DMI6000B microscope with x20 and x63 objectives (Fig. 8).

iNeuron characterization

The iPSCs were seeded for differentiation to iNeurons on glass coverslips coated with PLO in borate buffer and human laminin coating and kept on the coverslips for the desired time. Coated coverslips were washed 3x 5 min with ice-cold 1xPBS and fixated in 4% PFA for 15 min at RT and afterwards washed 3x 5 min with 1x PBS. The plates were stored at 4 °C until the next day. On day one, the coverslips were permeabilized with 0.2% Triton for 10 min at RT, then washed 3x 5min with 1x PBS. The neurons were incubated with blocking buffer (5% goat serum in 1x PBS, 1:20) for 1 hour at RT. Primary antibodies, Pan-Axonal Neurofilament Marker (mouse monoclonal, BioLegend), Microtubule-associated protein 2 (MAP2, rabbit polyclonal, Abcam), and

Synapsin 1/2 (guinea pig polyclonal, Synaptic systems), were diluted in blocking buffer and were applied onto the coverslips and incubated O/N at 4 °C in a box containing moist tissues. On day two, the coverslips were washed 3x 5 min with 1x PBS and secondary antibodies, Goat anti-Mouse Alexa Fluor 488 (Ab-M34-03, Invitrogen), Goat anti-Rabbit Alexa Fluor 568 (Invitrogen), and Goat anti-Guinea Pig Alexa Fluor 647 (Ab-G50-01, Invitrogen), diluted in blocking buffer were applied to the coverslips and incubated 1 hour at RT in the dark. Afterwards, coverslips were washed 3x 5 min in 1x PBS, then Hoechst 33342 (10 mg/mL solution in water, Invitrogen) was added and incubated for 10 min at RT. Neurons were washed again 3x 5 min with 1x PBS and mounted on an empty object slide.

Images were acquired with a Zeiss Axio Imager Z1 using a x40 objective (Fig. 9) and with a Zeiss LSM880 confocal microscope with 405 and 561 nm diode lasers, argon (458, 488, 514 nm) and a 633 nm laser using a x20 objective (Fig. 10).

Establishment of electrophysiological profile of iNeurons

For the acquisition of the electrophysiological profile of the iNeurons derived from the DM1 patients and a healthy control, we used the multi-electrode array (MEA). Here, we performed the differentiation of the iPSCs to iNeurons in a 24WP for Multiwell-MEA-System (multichannel* systems, MCS GmbH). In each of the 24 wells, 12 gold electrodes with a distance of 300 µm and a dimeter of 30 µm are placed.

We plated iPSCs from P1, P2 and a wild-type iPSC line (further referred as C2) and differentiated them according to the protocol. Basal recordings of each 10 minutes of the iNeurons were performed on differentiation day (days in vitro, DIV) 14, 21 and 28. The software used for the recordings was Multi-well-Screen (multichannel* systems, MCS GmbH).

PCR for Y chromosome check

After we performed the previously mentioned experiments, we realized that the results of these experiments were not matching with
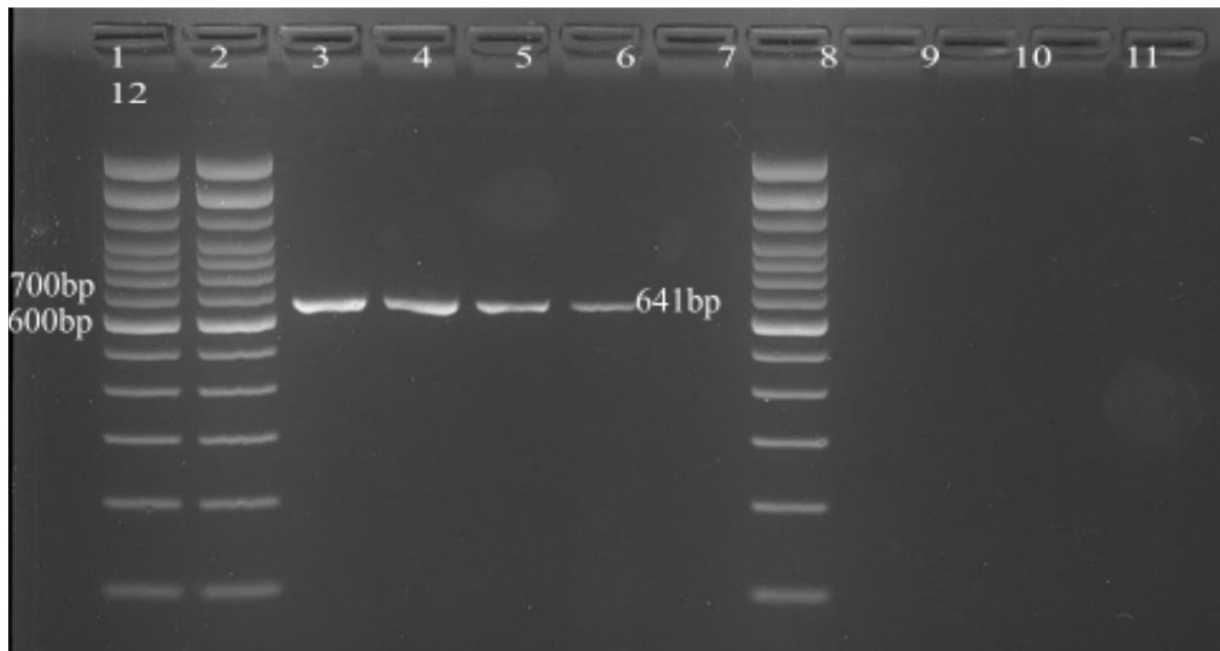
Figure 4. Gel electrophoresis of PCR products for detection of the SRY gene. The first two columns show a 100bp ladder as reference, column 3 to 5 show DNA samples of P1which was supposed to be female but is male. Column 6 is a positive control (male sample). Column 7 is empty. Column 8 shows again the 100bp ladder. Columns 9 to 11 show the samples of P2, which was supposed to be male, but is female. Column 12 shows a negative control (female sample).

our expectations. Therefore, we performed a Y chromosome check with PCR, to distinguish the male from the female sample. We designed an oligonucleotide primer pair for the SRY (Sex-Determining Region Y) gene (exon 1) with the following sequences for forward 5' - CTG CTA TGT TAA GCG TAT TC - 3' and for reverse 5' – AGC ATC TAG GTA GGT CTT TG – 3'. The expected band size for the product is 641 base pairs (bp). As a basis we used the protocol by Settin, Elsobky, Hammad, and Al-Era (2008). We used 40 ng of DNA sample per reaction, which has been isolated with the QIAamp DNA Blood Mini Kit (QIAGEN) and measured with the Qubit fluorometer (Invitrogen). Each reaction had a total volume of 25 µL, with 5 µL Q5 Buffer (New England BioLabs), 0.5 µL dNTPs, each 1.25µL of forward and reverse primer, 0.25 µL Q5 enzyme (New England BioLabs) and MQ up to the 25 µL total volume. The PCR reactions have been performed for 3 samples for P1 and for 3 samples for P2 (two for each at different passages during iPSC stage and one at the stage which has been used for iNeurons differentiation). Additionally, a positive control (male) and a negative control (female) have been added. The PCR reactions were carried out in a thermal cycler (Applied

Biosystems) according to the protocol by Settin et al. (2008). All amplified PCR products were separated by gel electrophoresis in a 2% agarose gel, stained with ethidium bromide (10 mg/mL, Invitrogen). The applied voltage was 100 V for 90-110 minutes.

Results

PCR for Y chromosome check

The gel electrophoresis of the PCR products of P1, P2 and positive and negative control samples show that P1 who was supposed to be female shows a band for the SRY gene at the expected level of 641 bp. P2 who was supposed to be male does not show a band for the SRY gene. This experiment clearly shows that the samples of P1 and P2 were switched around. The result can be found in Figure 4. We included for each patient three iPSC samples from different time points, in order to find at what time point the samples were switched. As a reference we included a 100 bp ladder. For the further results, P1 is male and P2 is female.
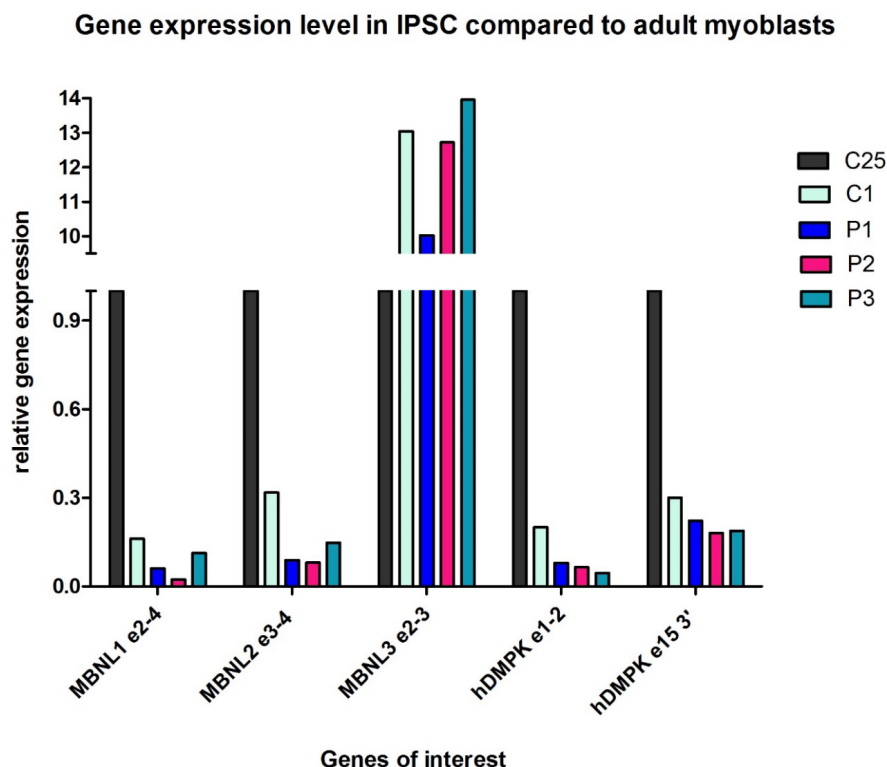
Assessment of gene expression

Gene expression level in IPSC compared to adult myoblasts

Figure 5. Relative Gene Expression of Genes of Interest (GoI). GoI were tested on two patient iPSC lines which were fibroblast-derived and lentiviral transduced (P1 [repeat in iPSC: ~87-97], P2 [repeat in iPSC > 150]), on two iPSC lines which were pericyte-derived and lentiviral transduced (P3 [repeat > 1500, determined by SP-PCR], C1) and on C25, adult myoblast as a reference for MBNL1-3 expression.

levels in iPSCs from DM1 patients

The results of the RT-qPCR for assessing relative gene expression levels show that the genes of interest MBNL1, MBNL2, DMPK e1-2, and DMPK e15 3′ are expressed a 3- to 6-fold lower in iPSC derived from P1, P2, P3 and C1, relative to C25. MBNL3 is expressed 10- to 13-times higher compared to C25. Even the control (C1) showed slightly higher gene expression levels of MBNL1, MBNL2, DMPK e1-2 and DMPK e15 3′. The samples for this RT-qPCR are pipetted in triplo, the whole experiment was performed in n = 1.

Differentiation of Tet-On 3G- and NGN2-positive hiPSC lines into iNeurons

We successfully differentiated Tet-On 3G- and NGN2-positive iPSCs into iNeurons. We first used three different cell densities (17,500; 20,000; 22,500) in order to have a range and see what works best. The cell density of 17,500

cells per well in a 24WP was sufficient for the cells to survive and differentiate. Already from day two on, the shape of the cells changed from small round to a more neuron-typical shape. A few days after starting the differentiation, the cells looked like neurons and started spreading. However, Ara-C, which was added to the iNeuron's medium, was not as efficient as expected. This can be seen on the living iPSCs that remained in the wells (see Fig. 6 and 7, Day 5 and Day 6). Figures 6 and 7 show a day-by-day timeline of the development of iPSCs to iNeurons.

Immunofluorescence and immunocytochemistry

DM1 disease markers in iPSC.

To visualize DM1 disease markers, immuno-fluorescence staining was performed for the iPSCs of P1 and P2. The immunofluorescence staining (Fig. 8, A & B) revealed that in the iPSCs of P1 at an early passage, no intra-nuclear foci could be detected. The same

Day 1   Day 2   Day 3

Day 5   Day 6
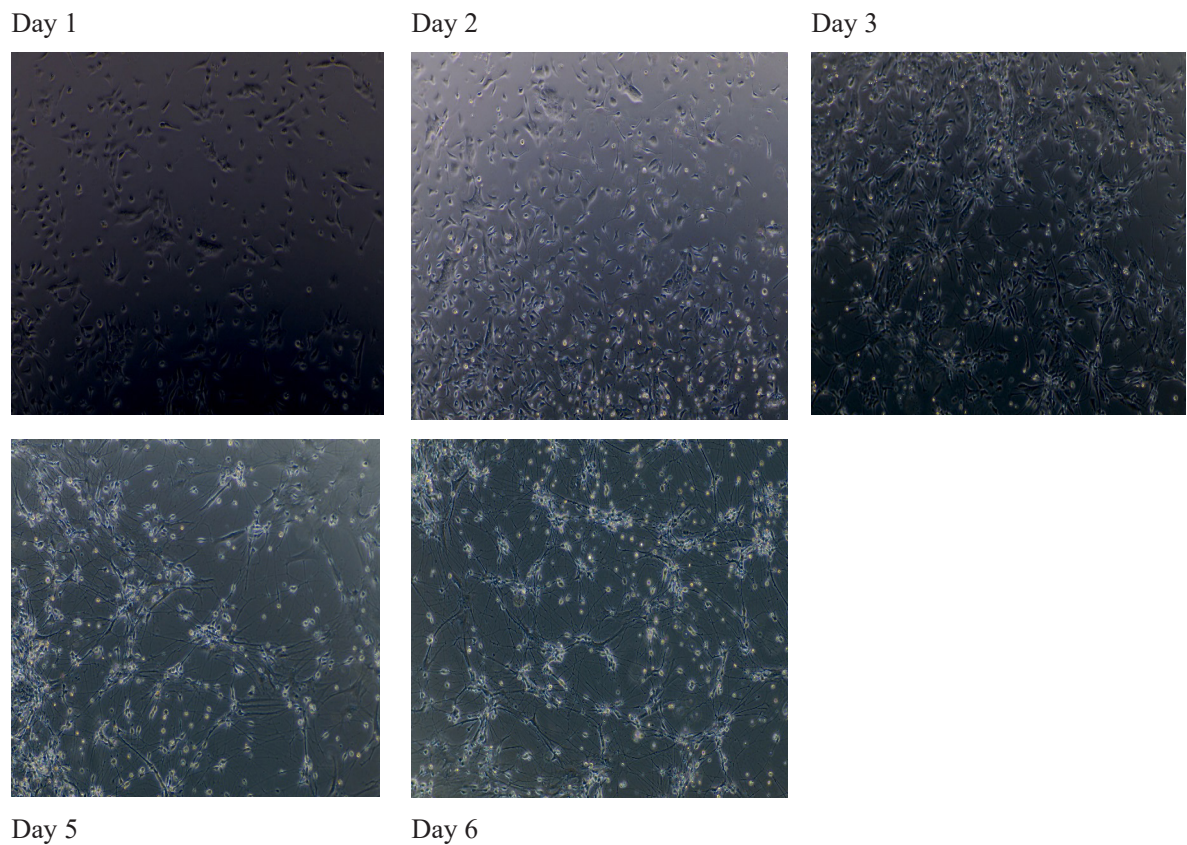
Figure 6. Day 1 until Day 6 of Differentiation of iPSC to iNeurons, of P1. The images show a cell density of 17,500 cells.

Day 1   Day 2   Day 3

Day 5   Day 6
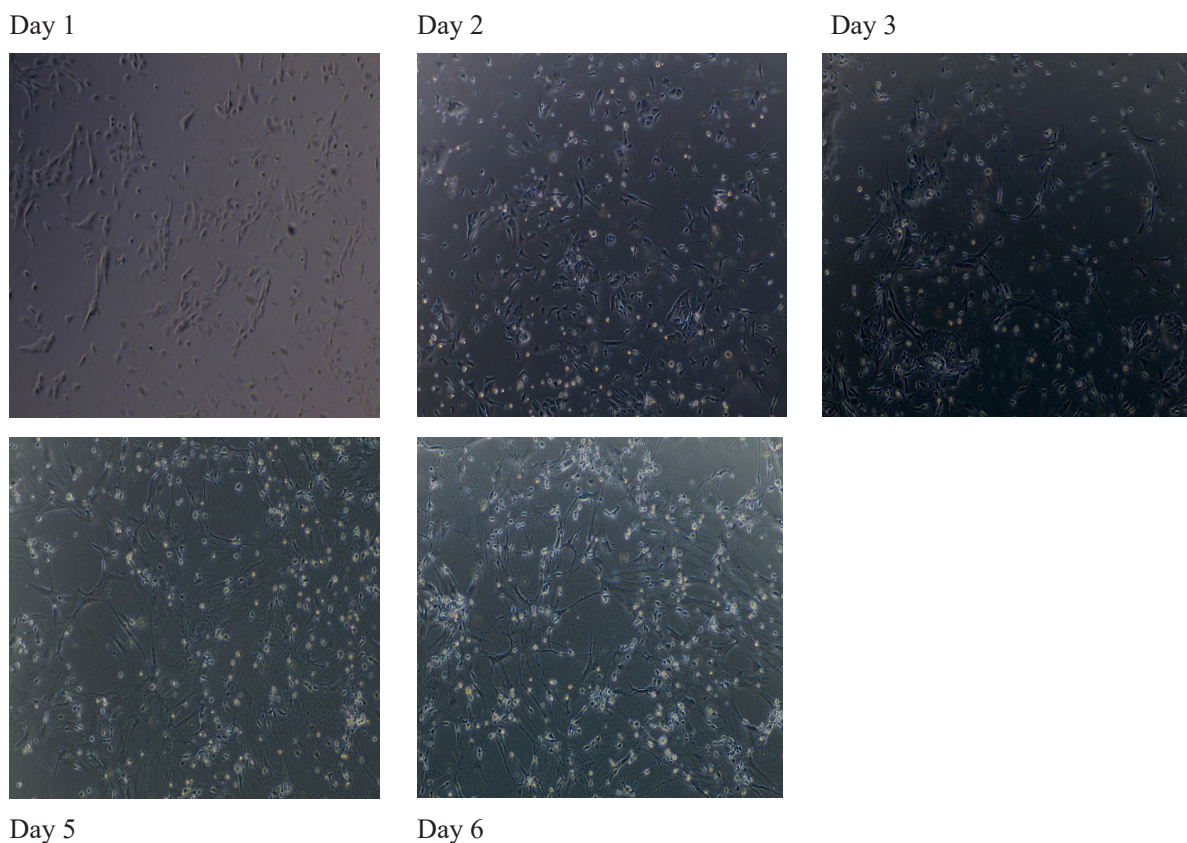
Figure 7. Day 1 until Day 6 of Differentiation of iPSC to iNeurons, of P2. The images show a cell density of 17,500 cells.
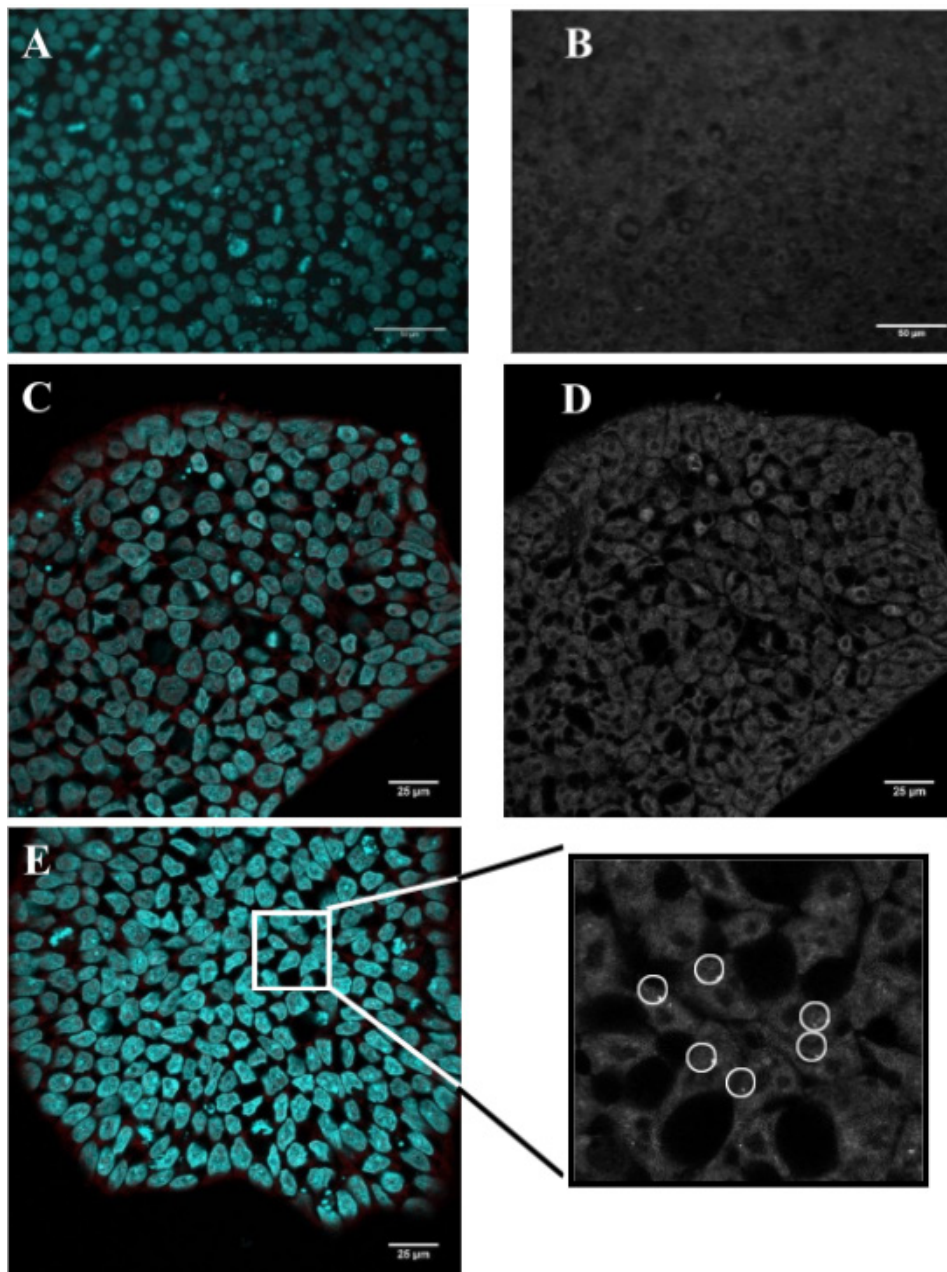
Figure 8. Images A and B show immunofluorescence staining on iPSCs of P1 for FISH + MBNL1 and DAPI, where image B shows a greyscale image of the (CAG)6 probe. Images C and D show the immunofluorescence staining for FISH on iPSCs of P1, where image D shows a greyscale image of the (CAG)6 probe. Image E shows immunofluorescence staining for FISH on iPSCs of P2, with a zoom-in in greyscales of the (CAG)6 probe to better visualize RNA foci. Images A and B were acquired with a Leica DMI6000B microscope. Images A and B were acquired with an x63 objective. The scale bar indicates a length of 50μM. Images C, D and E were acquired with a Zeiss LSM880 confocal microscope with 405 and 561 nm diode lasers, argon (458, 488, 514 nm) and a 633 nm laser using a x20 objective. Here the scale bar indicates a length of 25μM.

holds for MBNL1, we did not get a signal. Figure 8 C & D shows the FISH immunofluorescence (without MBNL1) of P1 at a later passage and Figure 8 E shows the FISH immunofluorescence (also without MBNL1) of P2. As it can be seen in Figure 8 C and D, no RNA foci were visible. However, in the iPSC of P2 we found intranuclear RNA foci (Fig. 8 E).

iNeuron characterization.

Immunocytochemistry was performed on iNeurons of P1 and P2 on DIV 6, and on mature iNeurons on DIV 49. The results of the immu-
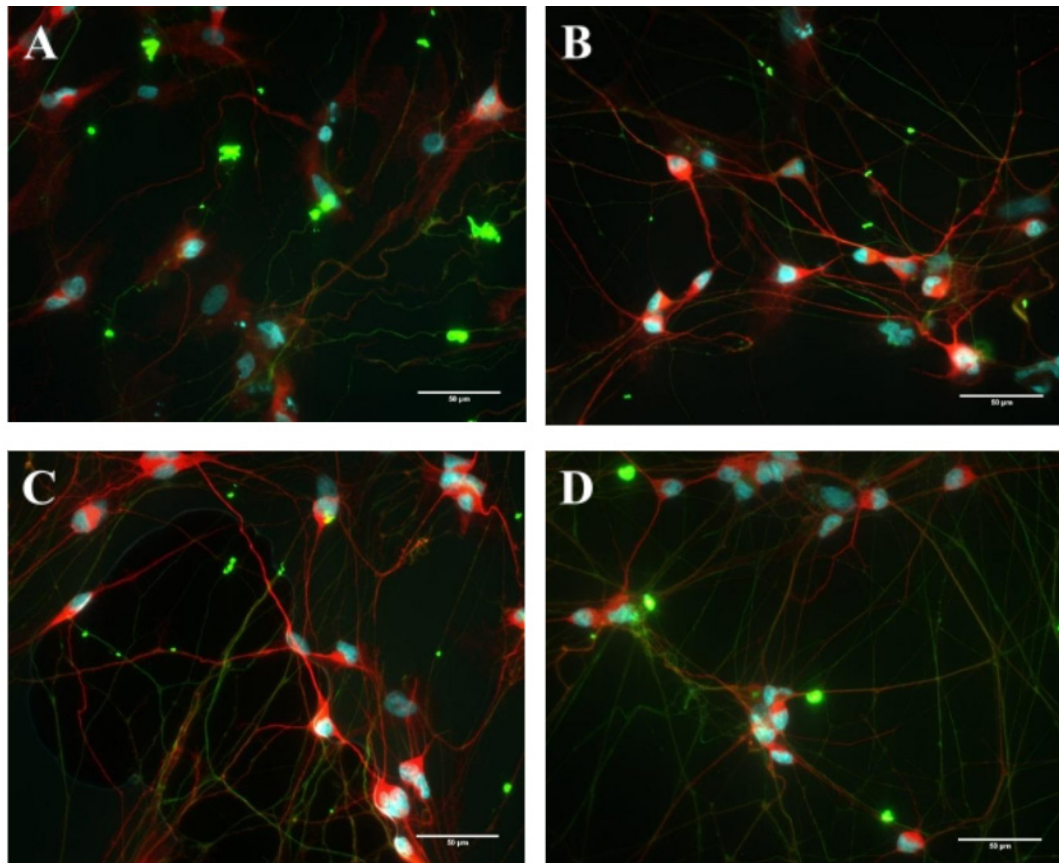
Figure 9. Immunocytochemistry of test-differentiated iNeurons at DIV6 and passage 3 from P1 and P2. A and B refer to P1 and C and D refer to P2. The antibodies used are Pan-Axonal Neurofilament Marker (mouse monoclonal, BioLegend) in green for the axons, Microtubule-associated protein 2 (MAP2, rabbit polyclonal, Abcam) in red for the dendrites, and Hoechst 33342 (10mg/mL solution in water, Invitrogen) in cyan for the nuclei. Images were acquired with a Zeiss Axio Imager Z1 microscope, using an x40 objective. The scale bar indicates a length of 50µM.

nocytochemistry performed on iNeurons of P1 and P2 on DIV 6 (Fig. 9) showed that, axons and dendrites were present and connections between neurons were made. The images in Figure 8 confirm that the differentiation of Tet-On 3G- and NGN2-positive iPSCs of DM1 patients was successful. We stained the iNeurons (DIV6) with antibodies for the axons, the dendrites, the synapses and the nuclei. For the synapses, however, we did not get a signal. This was due to their immature state after only 6 days in vitro. iNeurons get more mature between DIV14 and DIV21. After three weeks in culture, these iNeurons can be defined as mature (Cullen, Gilroy, Irons, & La Placa, 2010).

The results of immunocytochemistry performed on DIV49 show that iNeurons from DM1 patients are able to become mature and to survive the 7 weeks. For this staining we took healthy control (C2) iNeurons along in

order to compare the healthy iNeurons with DM1 diseased iNeurons. In Figure 10, the iNeurons of P1 and P2 (picture B and C) seem to have less dendritic connections compared to the healthy control (picture A), and they seem to be less nicely aligned. The reasons for this will be evaluated in the discussion.

DM1 disease markers in iNeurons.

We performed immunocytochemistry on iNeurons on DIV49 to check for DM1 disease markers. The results are shown in Figure 11. In line with our expectations, the iNeurons of the healthy control C2 did not show foci. The same holds for P1, where we also did not find RNA foci in the iNeurons. This is in accordance with what has been found earlier in the iPSCs that P1 did not show any RNA foci (see Fig. 8 C and D). P2 shows RNA foci in the iNeurons stage, which corresponds with the iPSCs of P2
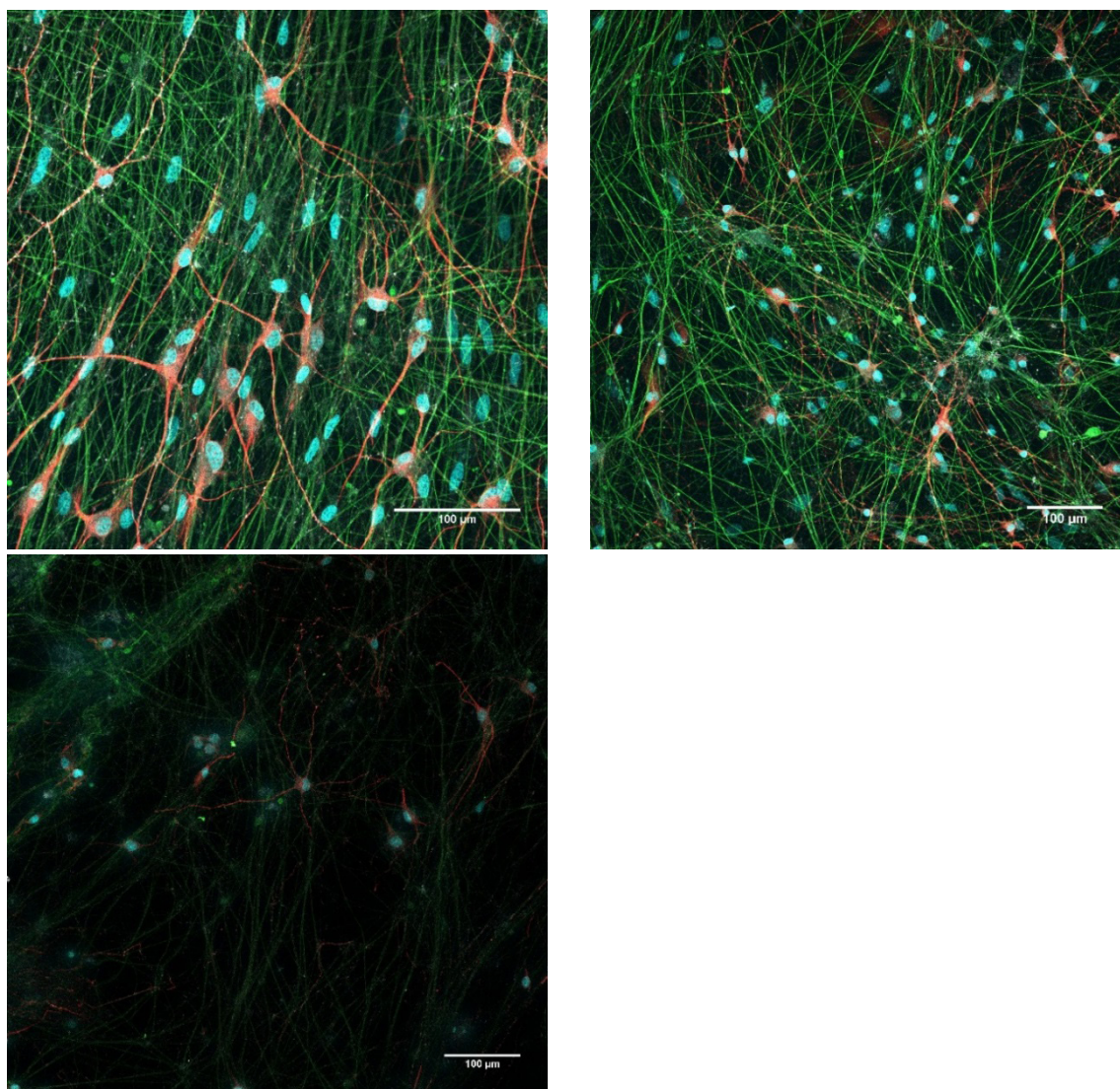
Figure 10. Immunocytochemistry of iNeurons from C2, P1 and P2 at DIV49 for neuron-specific markers. Image A shows iNeurons of C2, image B refers to P1 and image C shows the iNeurons of P2 with a zoom-in in greyscales of the (CAG)6 probe to better visualize RNA foci. The antibodies used are Pan-Axonal Neurofilament Marker (mouse monoclonal, BioLegend) in green for the axons, Microtubule-associated protein 2 (MAP2, rabbit polyclonal, Abcam) in red for the dendrites, Synapsin (guinea pig polyclonal, Synaptic systems) in grey for the synapses and Hoechst 33342 (10mg/mL solution in water, Invitrogen) in cyan for the nuclei. Images were acquired with a Zeiss LSM880 confocal microscope with 405 and 561 nm diode lasers, argon (458, 488, 514 nm) and a 633 nm laser using a x20 objective. The scale bar in the images indicates a length of 100µM.

showed foci previously (see Fig. 8 E).

Additionally, we performed a quantification of the number of foci per nucleus (Fig. 12). The results show that P1 had almost no foci, but P2 had up to 10 foci per nucleus, with an average of 1.6 foci.

Establishment of electrophysiological profile of iNeurons

For the analysis of the acquired electrophysiological data of the MEA test plate, we used the Multiwell-Analyzer software (multichannel* systems, MCS GmbH). The most important parameters for the characterization of neuronal activity are the mean percentage of random spikes, the mean burst rate (measured in bursts per minute), the mean network burst rate (measured in network bursts per minute) and the mean network burst duration (measured in milliseconds). A burst is defined as a minimum of 4 spikes in a short time frame. For a network burst, at least 6 electrode channels (per well) need to be
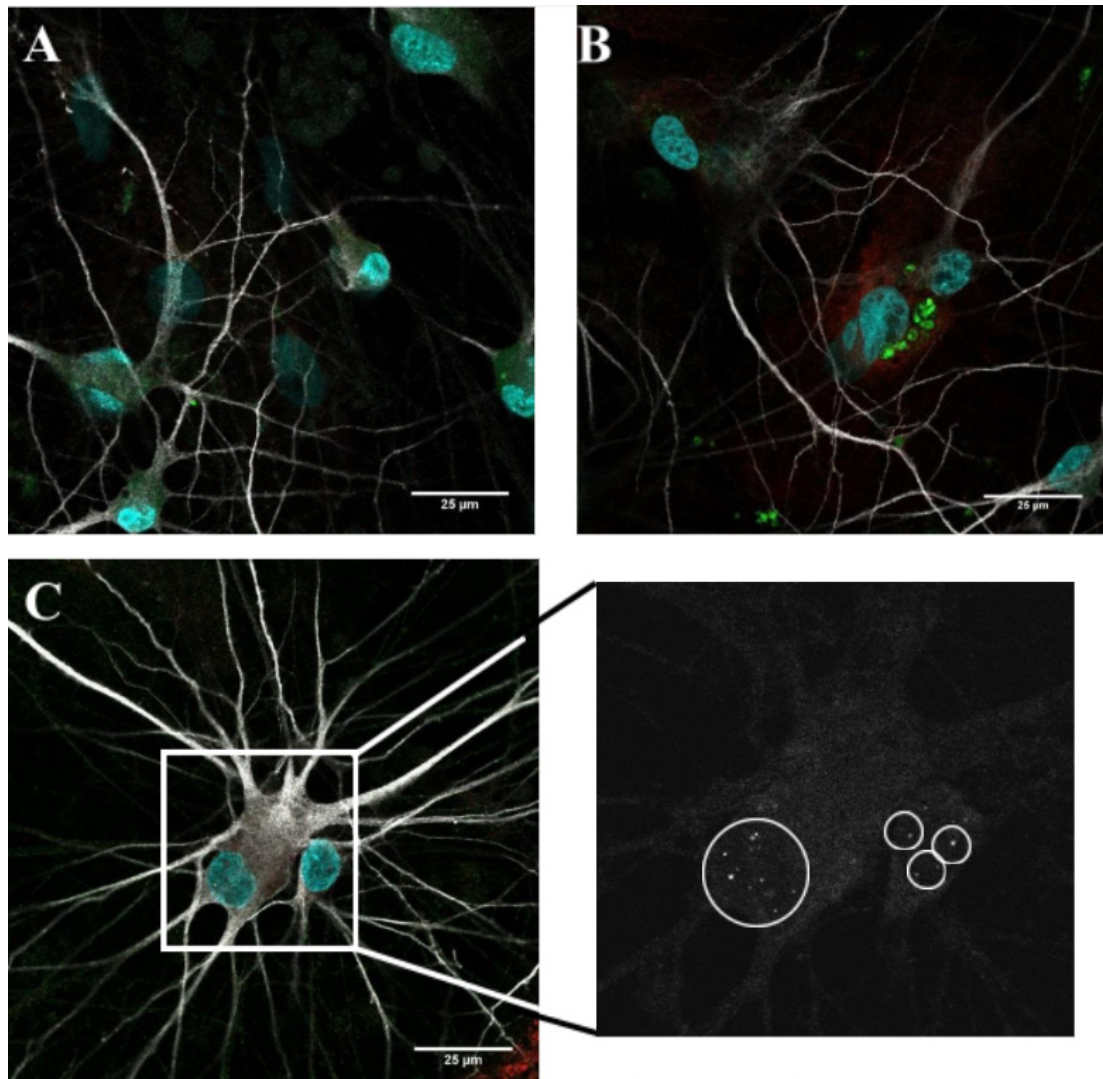
Figure 11. Immunocytochemistry of DM1 disease specific markers of iNeurons at DIV49 from C2, P1 and P2. A shows C2, B shows P1 and C shows P2. Stainings were performed for FISH (Stellaris) shown in red, MBNL1 shown in green, Hoechst 33342 (10mg/mL solution in water, Invitrogen) and Microtubule-associated protein 2 (MAP2, rabbit polyclonal, Abcam) shown in grey. MAP2 was added as a neuron-specific marker in order to separate the iNeurons from the rat astrocytes. Images were acquired with Zeiss LSM880 confocal microscope with 405 and 561 nm diode lasers, argon (458, 488, 514 nm) and a 633 nm laser using a x20 objective. The scale bar indicates a length of 25µM.
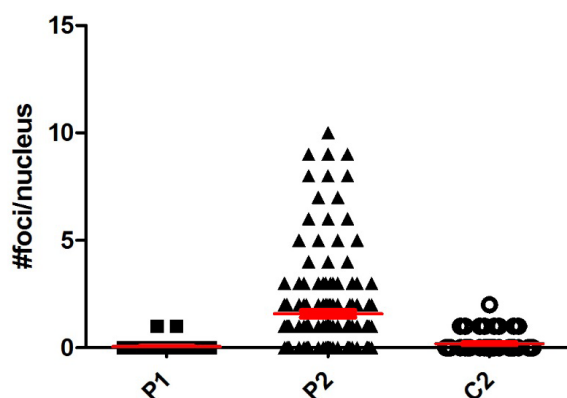
Figure 12. Quantification of RNA foci per nucleus. The quantification was performed on iNeurons at DIV49 from P1, P2 and C2, stained with DM1 disease specific markers. The number of RAN foci per nucleus were determined with FIJI (ImageJ). The red line indicates the mean, P1 = 0.05 foci/nucleus, P2 = 1.6 foci/nucleus, and C2 = 0.2 foci/nucleus.
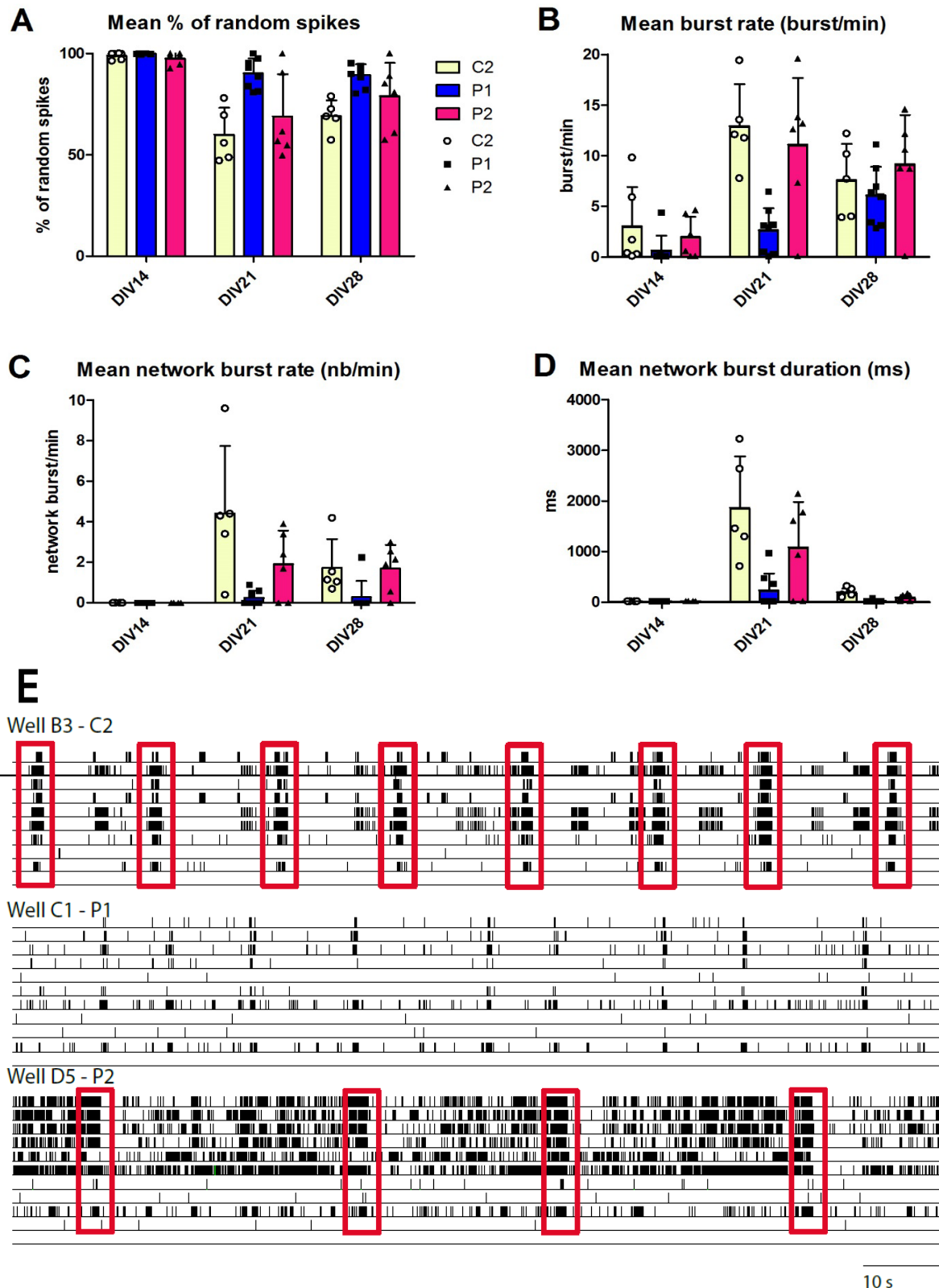
Figure 13. Electrophysiological profile of iNeurons from DIV14, DIV21 and DIV28. The included cell lines are of a control (referred to as C2), and two patients (P1 and P2). Graphs A-D show important parameters for analyzing the electrophysiological activity of neurons. Note: The data of DIV14 and DIV21 have been recorded with a sampling frequency of 20.000 Hz, whereas the data of DIV28 has been recorded with a sampling frequency of 10.000 Hz. Figure E shows a rasterplot of recorded activity on DIV28 with a length of 2 minutes. Three wells (B3, C1 and D5) are depicted, and each block refers to one cell line. In each block, every line refers to one electrode of this well. The network bursts are marked by the red boxes.

participating. The results are shown in Figure 13.

For these results, it is important that DIV14 and DIV21 should not be compared with DIV28 due to a different sampling frequency (DIV14 and DIV21: 20.000Hz and DIV28: 10.000Hz). The results of establishing an electrophysiological profile show that on DIV14, all three samples that were taken along show random spikes of roughly 100% (Fig. 13 A). Throughout differentiation, this behaviour changes the most in the control iNeurons (C2). Figure 13 B shows that the mean burst rate increased from DIV14 to DIV21, for all three samples. Figure 13 C and D show that on DIV14, the neurons are still too immature to form network bursts. However, from DIV21 on, the control iNeurons are able to form network bursts. It seems that the iNeurons of P2 are more able to form network bursts as well, even though we expected P1 to be more similar to the control. In the discussion section, some explanations for this will be provided.

Figure 13 E (on DIV28) gives a 2-minute overview of the electrophysiological recording of three distinct wells, one for each patient and the control. The topmost block shows the healthy control, with regular occurring network bursts. iNeurons of P1, depicted in the middle block, are not able to form network bursts. In the bottom row, the neuronal activity of P2 is shown and shows 4 network bursts in the 2 min time window. However, it also shows a lot of activity surrounding the network bursts. Possible reasons for this will be evaluated in the discussion.

Discussion

Repeat length of included samples

When we performed the Northern blot for a determination of the repeat length in P1 and P2, we only received inconclusive results, which is likely due to the very low gene expression level of DMPK. The results of the RT-qPCR of DM1 relevant genes show that DMPK is not highly expressed in iPSCs on RNA level.

The results of the TP-PCR show that the repeat of P1 grew a bit from 64-77 (in blood) to 87-97 (in iPSCs), due to somatic expansion (Du, Campau, Soragni, Jespersen,

& Gottesfeld, 2013). This is completely in line with the results from immunofluorescence: P1 did not show any DM1 disease markers, such as RNA foci. The results of the TP-PCR for P2 show that the repeat in iPSCs is above 150, which was the same as in blood. Unfortunately, we do not know how long the repeat exactly is because the TP-PCR shows only up to a maximum of 650 bp. For P2 we expect the repeat to be relatively high because in both the iPSCs and the iNeurons of P2 we were able to find RNA foci. There is the possibility that the repeat has grown over time, due to somatic instability (Caillet-Boudin et al., 2014; Du et al., 2013; Morales et al., 2012; Yum et al., 2017). Du et al. (2013) found that the repeat expansion rate in iPSC is dependent on the length of the repeat, a longer repeat expands faster than a shorter repeat. But even a repeat of 50 expands over time. Another unknown variable is the repeat length of the samples in the iNeuron stage.

Differentiation of Tet-On 3G- & NGN2-positive iPSC lines into iNeurons

The differentiation of Tet-On 3G- and NGN2-positive iPSCs into iNeurons was successful. In the beginning we used three different cell densities to get the optimum and we were able to use the lowest cell density of 17,500 on a surface of 0.97 cm2. Unfortunately, in our differentiations the Ara-C seemed to be not as efficient as expected. On day five and six we were still able to see iPSCs in the neuronal culture (Fig. 6 and 7). This problem can possibly be solved by adding a higher concentration, such that all remaining iPSC will die off and can be washed away when the media is changed. Here, we used a concentration of 2 µM. Seibenhenner & Wooten (2012) report that Ara-C can be used up to a concentration of 5 µM, but that higher concentrations can have toxic effects on iNeurons.

Immunofluorescence and Immunocytochemistry

DM1 disease markers in iPSC

The results for the DM1 specific disease mar-

kers are in line with the expectations, such that P1 with a short repeat does not show any RNA foci but P2 with a longer repeat shows RNA foci. It is very likely for P1 that the threshold of the (CAG)6 probe is not reached and therefore no foci are visible, even though cells of P1 show a repeat (Jiang et al., 2004). For MBNL1 we did not get a signal (Fig. 8), which is also not surprising because when we tested the gene expression levels (Fig. 5) in the iPSCs of both patients we saw that MBNL1 is 10-fold lower expressed in the iPSCs (of P1 and P2) compared to in adult myoblasts. This can also be seen in 'The Human Protein Atlas' (https://www.proteinatlas.org/): MBNL1 shows very little expression in fibroblasts, same holds for MBNL2. MBNL3 is tissue-specific to female tissues, such as the placenta (Jiang et al., 2004). Han et al. (2013) also reported very low MBNL1 and MBNL2 mRNA levels in iPSCs.

iNeuron characterization

We characterized the generated iNeurons on DIV6 and on DIV49. On DIV6, the iNeurons were very immature, however, axons and dendrites are present (Fig. 9) (Frega et al., 2017). Due to their immature state, after 6 days of differentiation no synapses were present. However, they do develop after 7-20 days in vitro (Cullen et al., 2010). We also see relatively few dendritic connections, compared to in later stages. Unfortunately, we see on some images a strong signal at some spots in the green channel, which is due to dust or dirt on the coverslips.

On DIV49, the iNeurons reached a very mature stage (Frega et al., 2017), therefore, we were able to get a signal for synapsin (Fig. 10). In this differentiation experiment up to DIV49, we took a control sample along C2, in order to have a good comparison to the disease samples. We see that the dendrites of C2 seem to be nicely aligned and quite dense. In comparison, the dendrites of P1 seem to be less dense and not that nicely aligned. Unfortunately, the coverslips with iNeurons of P2 show only very little signal because after the fixation step many cells let loose from the coverslips. This was due to the COVID-19 pandemic restrictions. During the hospital lockdown the iNeurons were stored for too long in 1x PBS. We were lucky that only very little was washed away for C2 and P1. The problem can be solved by storing the iNeurons in 1% PFA, which prevents very large parts of the iNeurons from letting loose.

DM1 disease markers in iNeurons

The results of the DM1 disease markers in iNeurons show, that RNA foci are present in P2, as expected, and absent in C2 and P1, which is also in line with what we saw earlier (see discussion 3.1). We also performed immunofluorescence for MBNL1, however, we did not get a reasonable signal. This is not really surprising because MBNL1 is not ex-pressed in the brain (Charizanis et al., 2012; Goodwin et al., 2015). Therefore, it is logical that we did not see MBNL1 foci in the nuclei. It would have been better to use a MBNL2 antibody, because MBNL2 is supposed to be highly expressed in the brain (Charizanis et al., 2012; Goodwin et al., 2015; Ramon-Duaso et al., 2020). Jiang and colleagues (2004) report that MBNL1 and MBNL2 are, among the muscleblind-like RNA binding proteins the ones that are strongly forming intranuclear foci. Therefore, we expect to see intranuclear foci when including MBNL2 for immunofluorescence on iNeurons. When we performed the immunofluorescence for DM1 specific disease markers, we added the anti-body MAP2, for dendrites, to get a distinction between iNeurons and astrocytes. This was done because DAPI stains the nuclei of rat astrocytes and nuclei of human iNeurons.

Furthermore, we performed a quantifi-cation of RNA foci in iNeurons from C2, P1 and P2 on DIV49. The results were as expected, P1 showed almost no foci, same as C2 (see discussion 3.1). iNeurons of P2 showed up to 11 foci per nucleus which is also in line with previous results from immunofluorescence in iPSC. We know that in iPSC P2 has a repeat above 150, and we saw up to 11 RNA foci per nucleus, therefore, we would expect the repeat to be relatively long. However, this needs to be validated first by SP-PCR performed in iPSC and in iNeurons of P2. SP-PCR amplifies small amount of DNA molecules which are then detected by Southern blots (Dandelot & Gourdon, 2018; Yum et al., 2017). This technique has a broader detection range compared to the TP-PCR (Leferink et al., 2019).

Establishment of Electrophysiological profile in iNeurons

On DIV14, DIV21 and DIV 28 we performed electrophysiological recordings of iNeurons of C2, P1 and P2. The rasterplot of P2 shows a lot more activity than C2, we expected P2 to show less activity and less network bursts compared to P1 and C2. However, the activity we saw looks more like an 'overcompensation'. Similar results were found in a study by Sicot et al. (2017). They found that DMSXL mice show hyperexcitability in Purkinje cells, and their results suggest that glutamate transporter 1 (GLT1) downregulation in several brain areas causes broad neuronal hyperexcitability (Sicot et al., 2017). However, this will need to be further validated in order to draw conclusions if this is the case as reported by Sicot and colleagues (2017).

The rasterplot of P1 was also surprising to us. P1 has only a short repeat, therefore we expected the rasterplot of P1 to look similar to C2. The pattern shown in Figure 13 E (Well C1 – P1), shows regular firing of the neurons, however, not enough channels are participating in order to define it as a network burst. One possible explanation for this might be that P1 had a lower cell density compared to C2 and P2. Another possibility is that in all the wells for every patient and control, the iNeurons were not evenly distributed along the electrodes. This is also the reason why not every channel shows activity.

To improve our current electrophysiological data, we need to use a new MEA plate. By this we can rule out coating problems and leaking wells.

When electrophysiological recordings are performed, it is always of high importance to have a control in the same MEA plate. However, there are also smaller differences between different types of controls. The control (C2) used in this experiment is the wild-type c (WTc) which is also used in the lab of Dr. Nael Nadif Kasri (Radboudumc). The analysis of the neuronal activity of C2 reveals that, unfortunately, it is not fully ideal. On the one hand, some parameter such as the burst rate (burst/min) on DIV28 is in line with how it is supposed to look like but on the other hand, parameters such as the burst duration (in seconds) is very far away from ideal (Frega et al., 2019). A reason for this might be the MEA plate which was not ideal.

Overall, we would highly recommend to repeat this experiment with the recently mentioned aspects to be taken into account. Additionally, when the recordings are made, they need to be recorded all with the same sampling frequency. In this case, the recording of DIV14 and DIV21 were made with a sampling frequency of 20,000 Hz and the recording of DIV28 was done with a sampling frequency of 10,000 Hz. The different sampling frequencies make it difficult to compare the samples at the different stages of days in vitro.

Future Perspectives

Several experiments need to be carried out in order to get a better picture about the cognitive deficits in DM1 patients. SP-PCR needs to be performed to get a more precise repeat length for P2, and the repeat length needs to be determined in iNeurons of P1 and P2. Next to it, RT-qPCR for the gene expression levels has to be performed in ns=3, including a statistical analysis. Besides this, iNeurons from patients and control need to be harvested for RNA to perform RT-qPCR for gene expression levels on these samples, such that assumptions about changes in gene expression levels from iPSC to iNeurons can be made. Furthermore, when performing immunofluorescence on iNeurons of P1 and P2, the antibody for MBNL2 needs to be included instead of MBNL1 because of its higher expression in the brain (Charizanis et al., 2012; Goodwin et al., 2015). For better electrophysiological data, a new MEA plate needs to be used, and it is important that the iNeurons are spread equally among the electrodes and that each well has a similar cell density. The recordings need to be all at the same sampling frequency. Last but not least, experiments for alternative splicing need to be carried out for alternatively spliced genes which are regulated by MBNL2 (Table S1). When investigating alternative splicing, the CELF proteins should also be taken along because they also seem to be involved in the regulation of splicing mechanisms (Hernández-Hernández et al., 2013). With the

recently mentioned additional experiments, better conclusions can be drawn about the processes occurring in the DM1 brain.

Conclusion

The performed experiments show that we are able to differentiate iNeurons from iPSC from DM1 patients which show DM1 disease markers such as RNA foci. Additionally, we showed that the repeat in iPSC is expanding between passages. Unfortunately, we cannot draw conclusions about processes occurring and causing the DM1 brain phenotype. Concluding all experiments, we argue that our findings contribute to unravel the neuropathophysiology of DM1. However, to get the full spectrum, follow-up experiments for further validation need to be performed.

When we performed the immunofluorescence for DM1 specific disease markers, we added the antibody MAP2, for dendrites, to get a distinction between iNeurons and astrocytes. This was done because DAPI stains the nuclei of rat astrocytes and nuclei of human iNeurons.

Furthermore, we performed a quantification of RNA foci in iNeurons from C2, P1 and P2 on DIV49. The results were as expected, P1 showed almost no foci, same as C2 (see discussion 3.1). iNeurons of P2 showed up to 11 foci per nucleus which is also in line with previous results from immunofluorescence in iPSC. We know that in iPSC P2 has a repeat above 150, and we saw up to 11 RNA foci per nucleus, therefore, we would expect the repeat to be relatively long. However, this needs to be validated first by SP-PCR performed in iPSC and in iNeurons of P2. SP-PCR amplifies small amount of DNA molecules which are then detected by Southern blots (Dandelot & Gourdon, 2018; Yum et al., 2017). This technique has a broader detection range compared to the TP-PCR (Leferink et al., 2019).

References

André, L.M., van Cruchten, R.T.P., Willemse, M., & Wansink, D.G. (2019). (CTG)n repeat-mediated dysregulation of MBNL1 and MBNL2 expression during myogenesis in DM1 occurs already at the myoblast stage. *PLoS ONE, 14*(5), e0217317.

Beer, J.G., & Ochsner, K.N. (2006). Social cognition: A multi-level analysis. *Brain Research, 1079*, 98-105.

Braz, S.O., Acquaire, J., Gourdon, G., & Gomes-Pereira, M. (2018). Of Mice and Men: Advances of Neuromuscular Aspects of Myotonic Dystrophy. *Frontiers in Neurology, 9*, 74-93.

Caillet-Boudin, M.L., Fernandez-Gomez, F.J., Tran, H., Dahenens, C.M., Buée, L., & Sergeant, N. (2014). Brain pathology in myotonic dystrophy: when tauopathy meets spliceopathy and RNAopathy. *Frontiers in Molecular Neuroscience, 6*, Article 57.

Charizanis, K., Lee, K.-Y., Batra, R., Goodwin, M., Zhang, C., Yuan, Y., Shiue, L., Cline, M., Scotti, M.M., Xia, G., Kumar, A., Ashizawa, T., Clark, H.B., Kimura, T., Takahashi, M.P., Fujimura, H., Jinnai, K., Yoshikawa, H., Gomes-Pereira, M., Gourdon, G., Sakai, N., Nishino, S., Foster, T.C., Ares Jr., M., Darnell, R.B., & Swanson, M.S. (2012). Muscleblind-like 2-Mediated Alternative Splicing in the Developing Brain and Dysregulation in Myotonic Dystrophy, *Neuron, 75*, 437-450.

Cullen, D.K., Gilroy, M., Irons, H.R., & La Placa, M.C. (2010). Synapse-to-neuron ratio is inversely related to neuronal density in mature neuronal cultures. *Brain Research, 1359*, 44-55.

Dandelot, E., & Gourdon, G. (2018). The flash-small-pool PCR: how to transform blotting and numerous hybridization steps into a simple denatured PCR. *Bio Techniques, 64*.

Dhaenens, C.M., Schraen-Maschke, S., Tran, H., Vingtdeux,V., Ghanem,D., Leroy, O., Delplanque, J., van Brussels, E., Delacourte, A., Vermersch,P., Maurage, C.A., Gruffat, H., Sergeant, A., Mahdevan, M.S., Ishiura, S., Buée, L., Cooper, T.A., Caillet-Boudin, M.L., Charlet-Berguerand, N., Sablonnière,B., & Sergeant, N. (2008). Overexpression of MBNL1 fetal isoforms and modified splicing of Tau in the DM1 brain: Two individual consequences of CUG trinucleotide repeats. *Experimental Neurology, 201*, 467-478.

Dhaenens, C.M., Tran, H., Frandemiche, M.-L., Carpentier, C., Schraen-Maschke, S., Sistiaga, A., Goicoechea, M., Eddarkaoui, S., van Brussels, E., Obriot, H., Labudeck, A., Gevaert, M.H., Fernandez-Gomez, F.,

Charlet-Berguerand, N., Deramecourt, V., Maurage, C.A., Buée, L., Lopez de Munain, A., Sablonnière, B., Caillet-boudin, M.L., & Sergeant, N. (2011). Mis-splicing of Tau exon 10 in myotonic dystrophy type 1 is reproduced by overexpression of CELF2 but not by MBNL1 silencing. *Biochimica et Biophysica Acta, 1812*, 732-742.

Du, J., Campau, E., Soragni, E., Jespersen, C.M., & Gottesfeld, J.M. (2013). Length-dependent CTG-CAG triplet-repeat expansion in myotonic dystrophy patient-derived induced pluripotent stem cells. *Human Molecular Genetics, 22*(25), 5276-5287.

Elegheert, J., Behiels, E., Bishop, B., Scott, S., Woolley, R.E., Griffiths, S.C., Byrne, E.F.X., Chang, V.T., Stuart, D.I., Jones, E.J., Siebold, C., & Aricescu, A.R. (2018). Lentiviral transduction of mammalian cells for fast, scalable and high-level production of soluble and membrane proteins. *Nature Protocols, 13*, 2991-3017.

Frega, M., van Gestel, S.H.C., Linda, K., van der Raadt, J., Keller, J., van Rhijn, J.R., Schubert, D., Albers, C.A., & Nadif Kasri, N. (2017). Rapid Neuronal Differentiation of Induced Pluripotent Stem Cells for Measuring Network Activity on Micro-electrode Arrays. *J. Vis. Exp., 119*, e54900.

Frega, M., Linda, K., Keller, J.M., Gümüs-Akay, G., Mossink, B., van Rhijn, J.-R., Negwer, M., Gunnewick, T.K., Foreman, K., Kompier, N., Schoenmaker, C., van den Akker, W., van der. Werf, I., Oudakker, A., Zhou, H., Kleefstra, T., Schubert, D., van Bokhoven, H., & Nadif Kasri, N. (2019). *Nature Communications, 10.*

Gallo, J.-M., & Spickett, C. (2010). The role of CELF proteins in neurological disorders. *RNABiology, 7*(4), 474-479.

Gomes-Pereira, M., Bidichandani, S.I., & Monckton, D.G. (2004). Analysis of Unstable Triplet Repeats Using Small-Pool Polymerase Chain Reaction. In Kohwi, Y. (eds) Trinucleotide Repeat Protocols. *Methods in Molecular Biology™, 277,* 61-76.

Gomes-Pereira, M., Foiry, L., Nicole, A., Huguet, A., Junien, C., Munnich, A., & Gourdon, G. (2007). CTG trinucleotide repeat 'big Jumps': Large expansion, Small Mice. *PLoS Genetics. 3*(4): e52.

Goodwin, M., Mohan, A., Batra, R., Lee, K.-Y., Charizanis, K., Fernandéz Gómez, F.J.,

Eddarkaoui, S., Sergeant, N., Buée, L., Kimura, T., Clark, H.B., Dalton, J., Takamura, K., Weyn-Vanhentenryck, S., Zhang, C., Reid, T., Ranum, L.P.W., Day, J.W., & Swanson, M.S. (2015). MBNL Sequestration by Toxic RNAs and RNA Mis-Processing in the Myotonic Dystrophy Brain. *Cell Reports, 12*(7), 1159-1168.

Hamilton, M.J., McLean, J., Cumming, S., Ballantyne, B., McGhie, J., Jampana, R., Longman, C., Evans, J.J., Monckton, D.G., & Farrugia, M.E. (2018). Outcome Measures for Central Nervous System Evaluation in Myotonic Dystrophy Type 1 May Be Confounded by Deficits in Motor Function or Insight. *Froniers in Neurology, 9*(780).

Han, H., Irimia, M., Ross, P.J., Sung, H.-K., Alipanahi, B., David, L., Golipour, A., Gabut, M., Michael, I.P., Nachmann, E.N., Wang, E., Trcka, D., Thompson, T., O#Hanlon, D., Slobodeniuc, V., Barbosa-Morais, N.L., Burge, C.B., Moffat, J., Frey, B.J., Nagy, A., Ellis, J., Wrana, J.L., & Blencowe, B.J. (2013). MBNL proteins repress embryonic stem cell-specific alternative splicing and reprogramming. *Nature, 498,* 241-245.

Hernández-Hernández, O., Guiraud-Dogan, C., Sicot, G., Huguet, A., Luilier, S., Steidl, E., Saenger, S., Maciniak, E., Obriot, H., Chevarin, C., Nicole, A., Revillod, L., Charizanis, K., Lee, K.-Y., Suzuki, Y., Kimura, T., Matsuura, T., Cisneros, B., Swanson, M.S., Trovero, F., Buisson, B., Bizoy,J.-C., Hamon, M., Humez, S., Bassez, G., Metzger, F., Buée, L., Munnich, A., Sergeant, N., Gourdon, G., & Gomes-Pereira, M. (2013). Myotonic dystrophy CTG expansion affects synaptic vesicle proteins, neurotransmission and mouse behaviour. *Brain, 136,* 957-970.

Hernández-Hernández, O., Sicot, G., Dinca, D.M., Huguet, A., Nicole, A., Buée, L., Munnich, A., Sergeant, N., Gourdon, G., & Gomes-Pereira, M. (2013). Synaptic protein dysregulation in myotonic dystrophy type 1. *Rare Diseases, 1*(1).

Jiang, H., Mankodi, A., Swanson, M.S., Moxley, R.T., & Thornton, C.A. (2004). Myotonic dystrophy type 1 is associated with nuclear foci of mutant RNA, sequestration of muscleblind proteins and deregulated alternative splicing in neurons. *Human Molecular Genetics, 13*(24), 3079-3088.

Jinnai, K., Mitani, M., Futamura, N., Kawamoto,

K., Funakawa, I., & Itoh, K. (2013). Somatic instability of CTG repeats in the cerebellum of myotonic dystrophy type 1. *Muscle Nerve, 48*, 105-108.

Leferink, M., Wong, D.P.W., Cai, S., Yeo, M., Ho, J., Lian, M., Kamsteeg, E-J., Chong, S.S., Haer-Wigman, L., & Guan, M. (2019). Robust and accurate detection and sizing of repeats within the DMPK gene using a novel TP-PCR test. *Scientific Reports, 8*(8280).

Longman, C. (2006). Myotonic Dystrophy. *Journal of the Royal College of Physicians of Edinburgh, 36,* 51-55.

Morales, F., Couto, J.M., Higham, C.F., Hogg, G., Cuenca, P., Braida, C., Wilson, R.H., Adam, B., del Valle, G., Brian, R., Sittenfeld, M., Ashizawa, T., Wilcox, A., Wilcox, D.E., & Monckton, D.G. (2012). Somatic instability of the expanded CTG triplet repeat in myotonic dystrophy type 1 is a heritable quantitative trait and modifier of disease severity. *Human Molecular Genetics, 21*(16), 3558-3567.

Nakamori, M., & Takahashi, M.P. (2016). Myotonic Dystrophy. In Takeda, S., Miyagoe-Suzuki, Y., & Mori-Yoshimura, M. (eds) *Translational Research in Muscular Dystrophy*, 39-61.

Ramon-Duaso, C., Rodríguez-Morató, J., Selma-Soriano, E., Fernández-Avilés, C., Artero, R., de la Torre, R., Pozo, Ó.J., & Robledo, P. (2020). Protective effects of mirtazapine in mice lacking the Mbnl2 gene in forebrain glutamatergic neurons: Relevance for myotonic dystrophy 1. *Neuropharmacology, 170*.

Sanderson, M.J., Smith, I., Parker, L., & Bootman, M.D. (2014). Fluorescence microscopy. *Cold Spring Harbor protocols, 10,* pdb.top071795.

Scott, J.G., & Schoenberg, M.R. (2011). Deficits in Visuospatial/Visuoconstructional Skills and Motor Praxis. In Schoenberg M., Scott J. (eds) The Little Black Book of Neuropsychology. *Springer*, Boston, MA.

Seibenhenner, M.L., & Wooten, M.W. (2012). Isolation and Culture of Hippocampal Neurons from Prenatal Mice. *Journal of Visualized Experiments, 65*.

Settin, A., Elsobky, E., Hammad, A., & Al-Erany, A. (2008). Rapid Sex Determination Using PCR Technique Compared to Classic Cytogenetics. International *Journal of Health Sciences, 2*(1), 49-52.

Sicot, G., Servais, L., Dinca, D.M., Leroy, A., Prigogine, C., Media, F., Braz, S.O., Huguet-Lachon, A., Chhuon, C., Nicole, A., Gueriba, N., Oliviera, R., Dan, B., Furling, D., Swanson, M.S., Guerrera, I.C., Cheron, G., Gourdon, G., & Gomes-Pereira, M. (2017). Downregulation of the Glial GLT1 Glutamate Transporter and Purkinje Cell Dysfunction in a Mouse Model of Myotonic Dystrophy. *Cell Reports, 19*(13), 2718-2729.

Suenaga, K., Lee, K.-Y., Nakamori, M., Tatsumi, Y., Takahashi, M.P., Fujimura, H., Jinnai, K., Yoshikawa, H., Du, H., Ares Jr., M., Swanson, M.S., & Kimura, T. (2012). Muscleblind-Like 1 Knockout Mice Reveal Novel Splicing Defects in the Myotonic Dystrophy Brain. *PLoS ONE, 7*(3), e33218.

Udd, B., & Krahe, R. (2012). The myotonic dystrophies: molecular, clinical, and therapeutic challenges. *Lancet Neurology, 10*, 891-905.

Van der Plas, E., Hamilton, M.J., Miller, J.N., Koscik, T.R., Long, J.D., Cumming, S., Povilaikaite, J., Farrugia, M.E., McLean, J., Jampana, R., Magnotta, V.A., Gutmann, L., Monckton, D.G., & Nopulos, P.C. (2019). Brain Structural Features of Myotonic Dystrophy Type 1 and their Relationship with CTG Repeats. *Journal of Neuromuscular Diseases, 6*(3), 321-332.

Wenninger, S., Montagnese, F., & Schoser, B. (2018). Core Clinical Phenotypes in Myotonic Dystrophies. *Frontiers in Neurology, 9*, 7-15.

Yum, K., Wang, E.T., & Kalsotra, A. (2017). Myotonic dystrophy: disease repeat range, penetrance, age of onset, and relationship between repeat size and phenotypes. *Current opinions in genetics & development, 40,* 30-37.

Supplementary materials
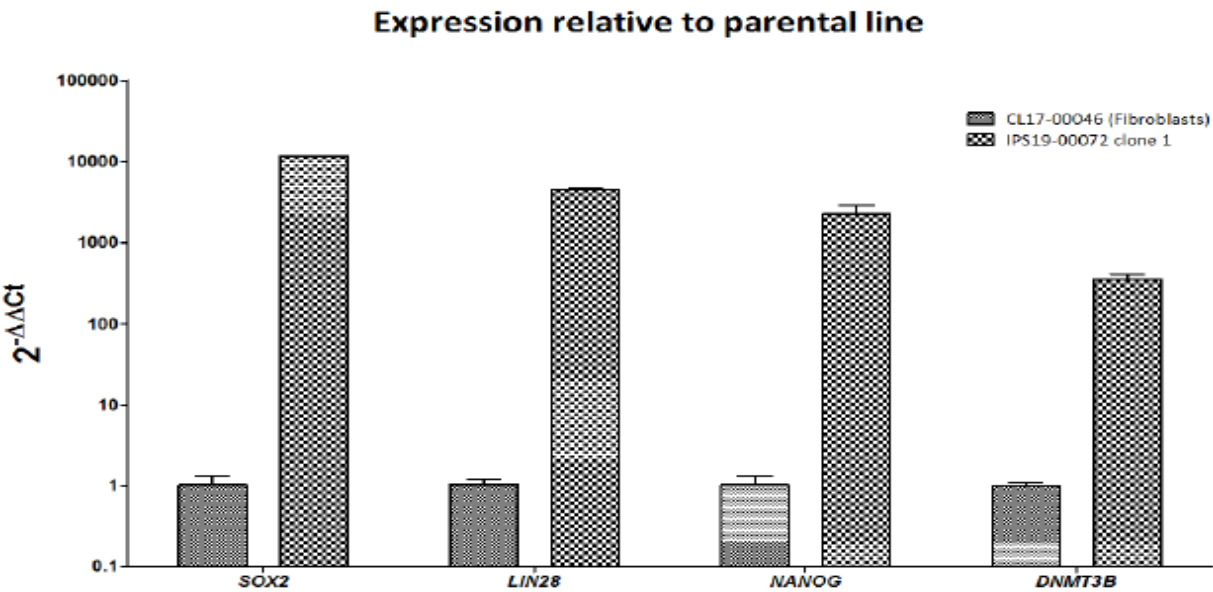
Figure S1. Gene expression relative to parental fibroblast line of P1. Pluripotency gene upregulation after reprogramming (ΔΔCt). The expression fold difference of the iPSCs is relative to parental fibroblasts.
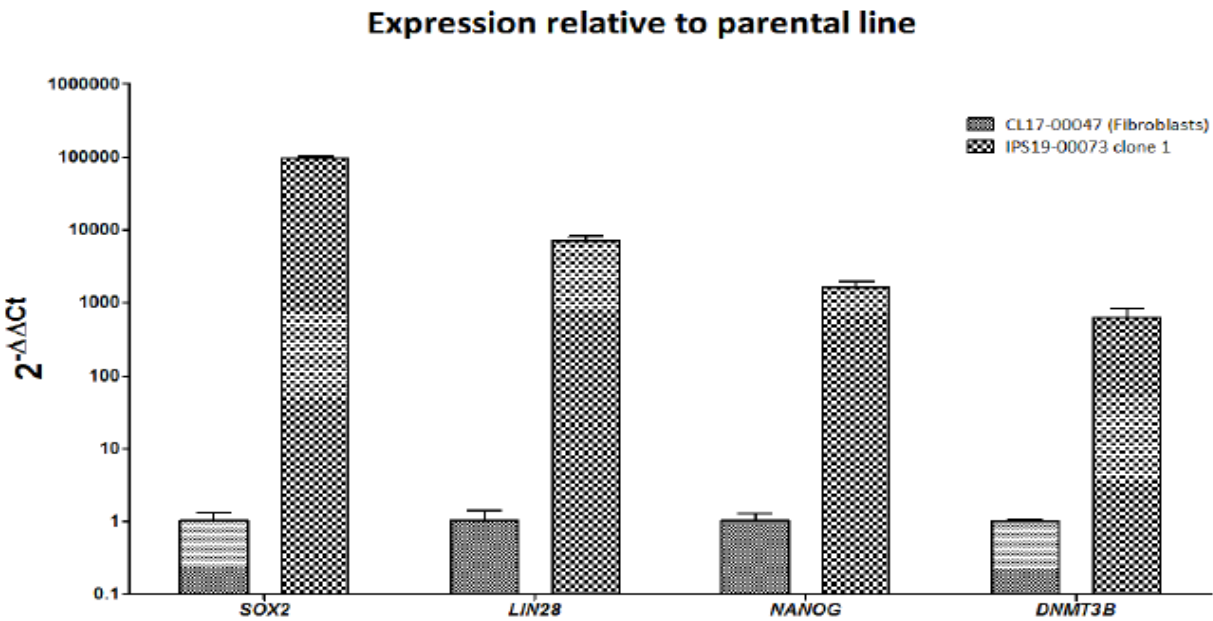
Figure S2. Gene expression relative to parental fibroblast line of P2. Pluripotency gene upregulation after reprogramming (ΔΔCt). The expression fold difference of the iPSCs is relative to parental fibroblasts.
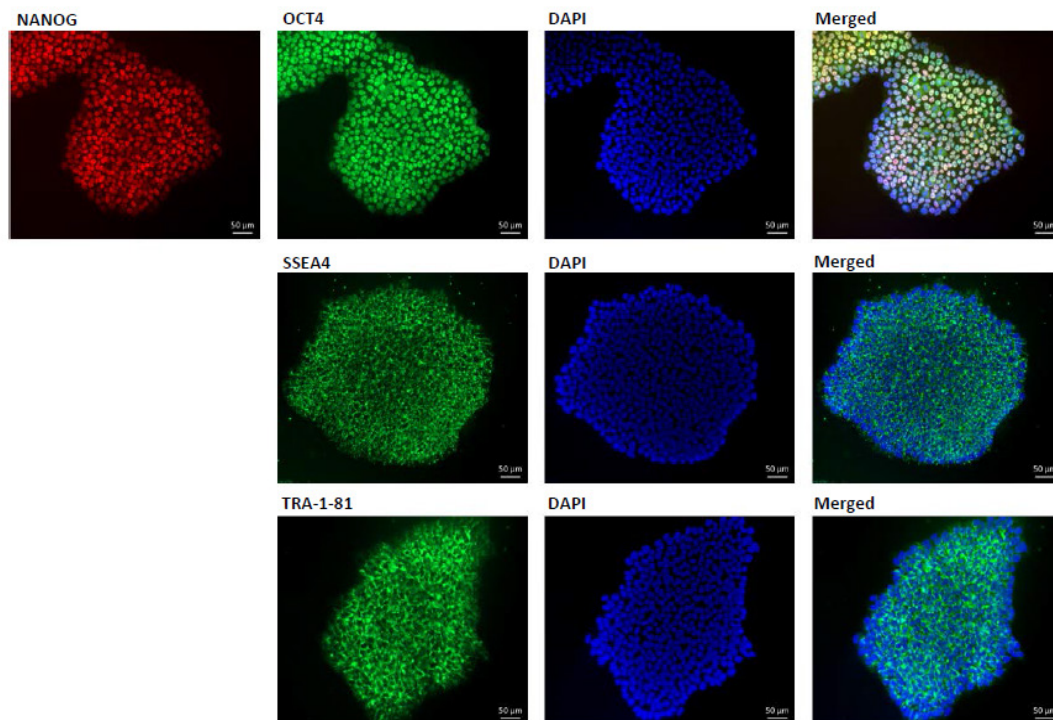
Figure S3. Immunofluorescence staining of the iPSC clone of P1 with pluripotency markers.

Table S1. List of alternatively spliced Genes in the Adult Brain, regulated by MBNL2.

Gene	Exon
Tanc2	E23a
Kcnma1	E25a
Limch1	E9
Spna2	E23
St3gal3	E3
Ndrg4	E14
Csnk1d	E9
Ppp1r12a	E14
Cacna1d	E12a
Add1	E15
Dlg2	E17b
Grin1	E5
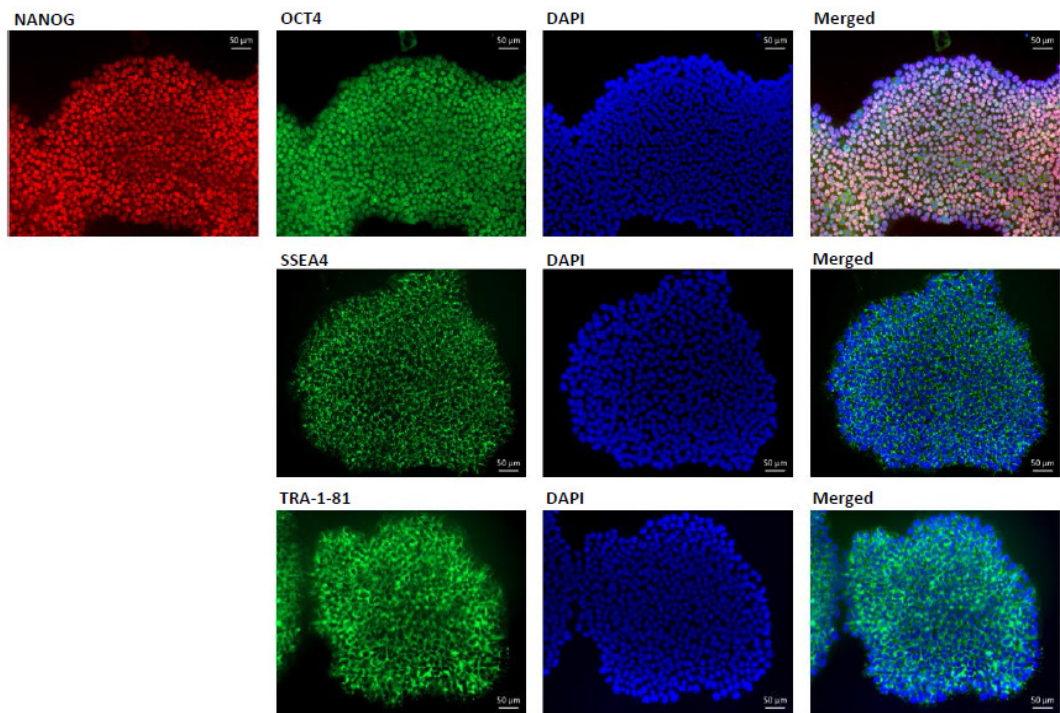
Figure S4. Immunofluorescence staining of the iPSC clone of P2 with pluripotency markers.

Table S2. RT-qPCR Primer Sequences. List of forward and reverse primer sequences used for assessment of gene expression levels in fibroblast derived-, pericyte derived iPSC and adult myoblasts.

Gene	Forward Sequence	Reverse Sequence
MBNL1 e2-4	5'- TAT GTC GAG AGT ACC AAC G -3'	5'- ACT GTG TTG TCA TTG GTG T -3'
MBNL2 e3-4	5'- CAG GAC TGA CAA ACT GGA -3'	5'- TGT TGT CAC TTG TGT CGA T -3'
MBNL3 e2-3	5'- AAT ACA CCT GTT CTG ATT CC -3'	5'- CAG TTT ATC TGA ACG CAT C -3'
DMPK e1-2	5'- ACT GGC CCA GGA CAA GTA CG -3'	5'- CCT CCT TAA GCC TCA CCA CG -3'
DMPK e15 3'	5'- TGC CTG CTT ACT CGG GAA A -3'	5'- GAG CAG CGC AAG TGA GGA G -3'
GUSB e11	5'- CTC ATT TGG AAT TTT GCC GAT T -3'	5'- CCG AGT GAA GAT CCC CTT TTT A -3'
TBP e3	5'- CCA CTC ACA GAC TCT CAC AAC -3'	5'- CTG CGG TAC AAT CCC AGA ACT -3'
HPRT1 e7-9	5'- TGA CAG TGG CAA AAC AATG -3'	5'- GGT CCT TTT CAC CAG CAA GCT -3'
GAPDH e1	5'- CCC GCT TCG CTC TCT GCT CC -3'	5'- CCT TCC CCA TGG TT CTG AGC G -3'
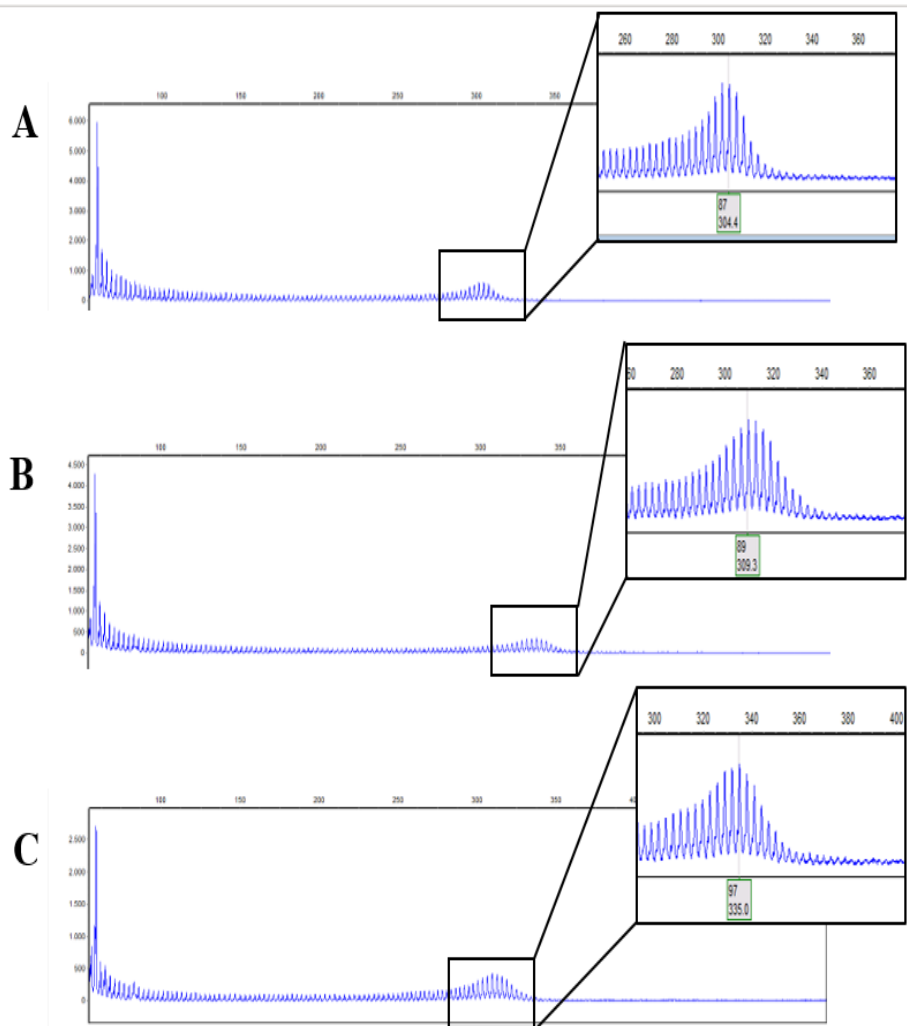
Figure S5. Electropherogram of TP-PCR of P1. A-C represent P1 at three different passage stages. A is passage 3, B is passage 16 and C is passage 9 of the iPSCs of P1 used to generate Tet-On 3G- & NGN2-positive cells. For A-C, the zoom in shows the repeat, which is for A: 87 repeats, for B: 89 repeats and for C: 97 repeats.
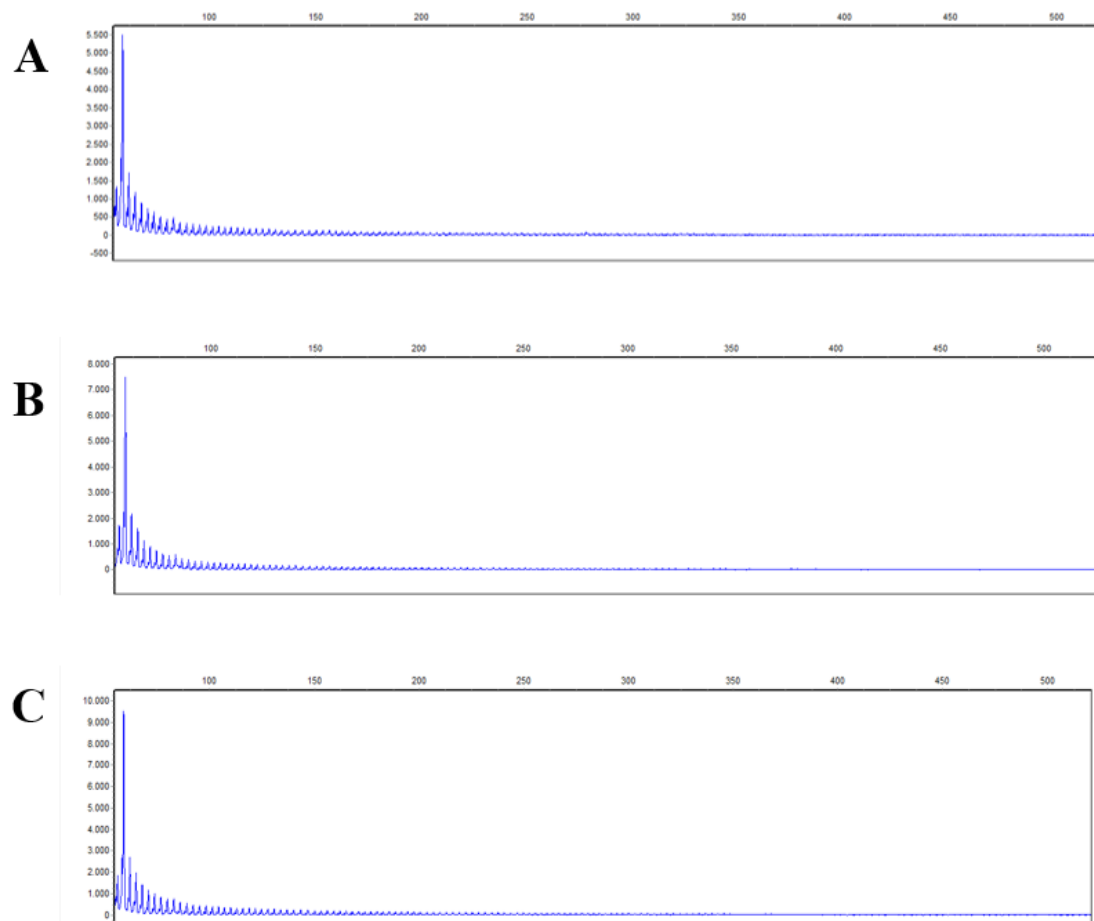
Figure S6. Electropherogram of TP-PCR of P2. A-C represent P2 at three different passage stages. A is passage 3, B is passage 11 and C is passage 9 of the iPSCs used to generate Tet-On 3G- & NGN2-positive cells. For A-C, the repeat is >150, a more precise determination is with TP-PCR not possible because every repeat above 150 is out of the determination range.
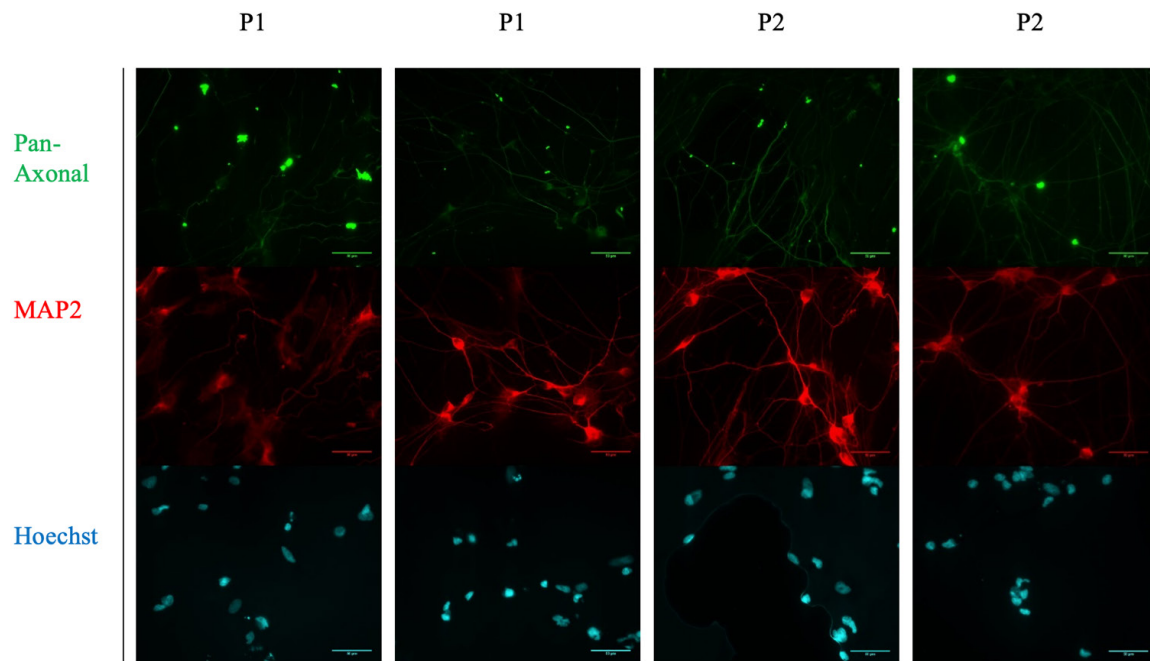
Figure S7. Immunocytochemistry of test-differentiated iNeurons at DIV6 from P1 and P2. Top row shows Pan-Axonal Neurofilament Marker (mouse monoclonal, BioLegend) in green, the second row shows Microtubule-associated protein 2 (MAP2, rabbit polyclonal, Abcam) in red, the third row shows Hoechst 33342 (10mg/mL solution in water, Invitrogen) in cyan. Images were acquired with a Zeiss Axio Imager Z1 microscope, using an x40 objective. The scale bar in the images indicates a length of 50 µM.
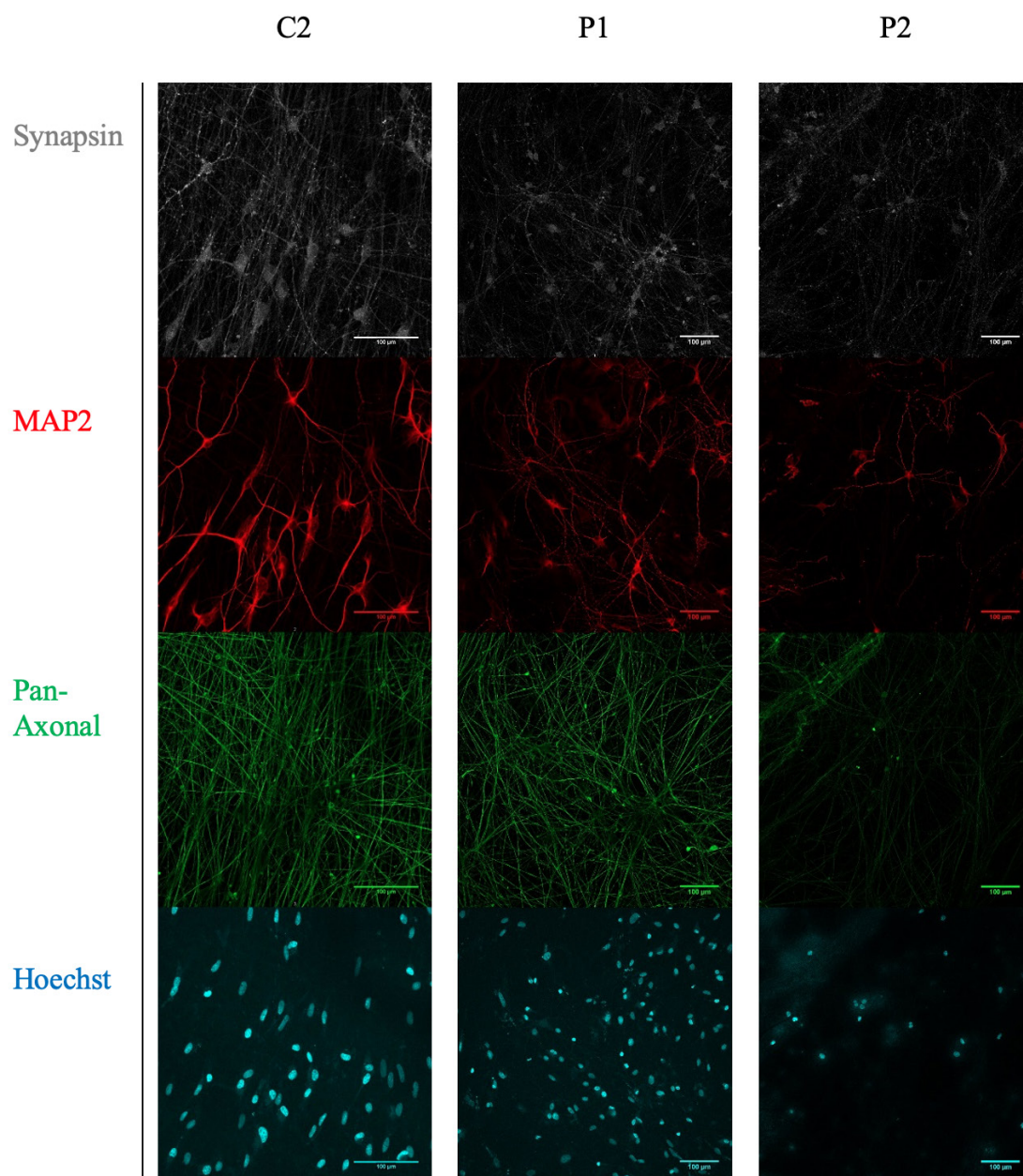
Figure S8. Immunocytochemistry of iNeurons at DIV49 from C2, P1 and P2. Top row shows Synapsin (Synapsin (guinea pig polyclonal, Synaptic systems) in grey for the synapses, the second row shows Microtubule-associated protein 2 (MAP2, rabbit polyclonal, Abcam) in red, the third row shows Pan-Axonal Neurofilament Marker (mouse monoclonal, BioLegend) in green and the bottom row shows Hoechst 33342 (10mg/mL solution in water, Invitrogen) in cyan. Images were acquired with a Zeiss LSM880 confocal microscope with 405 and 561 nm diode lasers, argon (458, 488, 514 nm) and a 633 nm laser using a x20 objective. The scale bar in the images indicates a length of 100µM.

Underlying Features of Inter-Individual Variability in Brain Function Using a Siamese Neural Network

Marleen Voorn[1]

Supervisors: Linda Geerligs[1] and Umut Güçlü[1]

Corresponding author: Marleen Voorn
E-mail: marleenvoorn.95@gmail.com

[1]*Radboud University Nijmegen,*
Donders Institute for Brain, Cognition and Behaviour,
The Netherlands

Large-scale networks are comprised of distributed brain areas that show correlated fluctuations in their spontaneous resting state functional magnetic resonance imaging activity, and these patterns of functional connectivity show high individual variability. However, it is still unknown what the most important dimensions are along which individual functional connectivity patterns can vary. In this study, we investigated the discriminating inter-individual features of brain function. We used a deep neural network to learn to discriminate subjects' connectivity patterns from each other (n = 996). We found that we can reduce the high-dimensional connectivity profiles to only three components and still identify subjects' functional connectivity patterns with 96% accuracy. The three identified components were mapped back onto the large-scale brain networks, and were classified as 1) sensorimotor networks component, 2) within-networks component, 3) higher-order networks component. Furthermore, we found correlations between the higher-order networks component and cognitive measures as well as with relevant brain regions' area size. This implies that we identified three robust components of functional connectivity that can be linked to cognition and amount of grey matter.

Human neuroimaging studies often investigate general patterns of brain activity that are shared across individuals. Spontaneous fluctuations as measured with resting state functional magnetic resonance imaging (fMRI – rfMRI) show temporal correlations between various brain regions, showing complex patterns of functional connectivity (FC) (Biswal, Zerrin Yetkin, Haughton, & Hyde, 1995). This group averaging has resulted in basic understanding of functional brain organization: by combining data from thousands of individuals, neuroscientists have been able

to reliably describe the organization of the human brain into large-scale functional networks using fMRI scans. Large-scale networks are comprised of distributed brain areas that show correlated fluctuations in their spontaneous rfMRI activity.

Even though this provided insight in group-level tendencies of functional connectivity that generalize across individuals, it also obscured information about subject-specific features (Gordon et al., 2017): it may be possible that individual functional resting connectivity reflects a unique processing

organization (Seitzman et al., 2019). Moreover, the heterogeneity across subjects is ignored: group averaging limits the detail and specificity of the resting state functional connectivity.

It has been shown that functional connectivity in subjects at rest shows high individual variability (Finn et al., 2015). Therefore, if we use an approach that moves beyond the population level to inferences about single subjects, descriptors of unique functional brain organization can be explored.

To investigate whether there are features of functional connectivity that are distinct enough to identify an individual, several studies have demonstrated that individuals can accurately be identified based on their functional connectivity patterns (Finn et al., 2015; Gordon et al., 2017; Gratton, Sun, & Petersen, 2017). This implies that each individual's functional architecture is unique. Identification across subjects is accurate regardless whether fMRI data is collected during a task or during rest. This indicates that 1) functional networks are fundamentally stable, and 2) rfMRI patterns are informative about a given person's stable traits regardless of that person's thoughts or behavioural task during scanning (Gratton et al., 2017). When rfMRI data of different sessions between subjects were compared, they had high similarity within subject and much lower similarity across subjects (Gordon et al., 2017). Thus, resting state functional connectivity profiles were found to be unique as well as stable over time, and could therefore act in a similar way as a fingerprint (Finn et al., 2015).

This variability is not only found in single regions, but also in large-scale networks (Seitzman et al., 2019). Individual resting state variability was strongest in higher-order association cortices or 'control' systems, rather than primary sensory cortices or 'processing' systems (Finn et al., 2015; Seitzman et al., 2019). The most successful networks for identification of individuals appear to be 1) the medial frontal network, which is part of the default mode network (DMN), and 2) the frontoparietal (FP) network (Finn et al 2015).

If we could link this unique functional organization on the level of large-scale brain networks to behavioural phenotypes, it would provide insight in the neural mechanisms that underlie cognition. It has been demonstrated that resting state functional connectivity is a good predictor for task outcomes (Finn et al., 2015; Rosenberg et al., 2016; Shen et al., 2017; Tavor et al., 2016). Furthermore, the networks that show the highest inter-individual variability in functional connectivity (i.e., the networks that are most discriminative between individuals) were also most relevant to individual differences in behaviour (Finn et al., 2015). This suggests that the functional hierarchy that is observed during rest is the same during action and cognition (Tavor et al., 2016).

However, it is still unknown what the most important dimensions are along which individual functional connectivity patterns can vary. It is difficult to quantify how all types of network variants may be distributed (Gordon et al., 2017) and how this is organized to the level of individuals. To overcome this multiple comparison problem, an approach that reduces the feature space is required. Deep neural networks (DNNs) are of growing importance in the field of neuroscience and this approach is particularly suitable for this matter: Artificial neural networks are inspired by concepts of neuroscience, but neglect many details of biological neural networks. DNNs have great computational efficiency, which enables them to perform complex tasks such as image recognition or translation (Kietzmann, McClure, & Kriegeskorte, 2018). Moreover, biological functional neural networks can be recreated by an artificial neural network, such as an "attention network" (Xu et al., 2015). Thus, concepts from neuroscience have inspired engineers to build DNNs. This pipeline can also be reversed: neuroscientists have been inspired by results from DNNs (Storrs & Kriegeskorte, 2019).

The main aim of this study was to unravel the underlying features of inter-individual variability in functional brain connectivity. To this end, a DNN was trained to distinguish rfMRI patterns between subjects. The network reduced the high-dimensional functional connectivity patterns to their most relevant features. To extract and summarize the most relevant features from functional network connectivity, a Siamese neural network (SNN) was used. This is a specific DNN that once it is trained, can accurately dissociate between similar input (e.g., two different photos of the same face) and dissimilar input (Koch, 2015). By analysing the features that the network has

learned, we can gain a deeper understanding of individual differences in brain function. Furthermore, to understand the nature and neural mechanisms of individual rfMRI patterns, it is of importance to determine what information in the resting-state signal is driving the predictors for cognition (Tavor et al., 2016).

Methods

Human Connectome Project data

Subject information

The data set used in this study is from the Human Connectome Project (HCP), the WU-Minn HCP Data - 1200 subjects (Van Essen et al., 2013). This data set has a large sample size in comparison to other neuroimaging studies. The HCP data release is an open resource database, facilitating replication and extension by other researchers (Finn et al., 2015). The included HCP resting-state fMRI runs were acquired at 3T in sessions of around 15-20 minutes on two separate days. Both days (HCP file names: rfMRI_REST1 and rfMRI_REST2) included a LR as well as a RL phase encoding sessions. An EPI acceleration factor of x8 was used, resulting in spatial resolution of 2 × 2 × 2 mm and temporal resolution (TR) of 0.72 s (Smith et al., 2013).

The full release contained 1113 healthy subjects with 3T MR Session Data, but the data analysis was constrained to subjects for whom all four resting state fMRI sessions acquired on two separate days were available (n = 996; age 22-35). Each session consisted of 1200 TRs (with a TR of 0.72 s), resulting in 4800 TRs per subject for further analysis.

Pre-processing

The data analysis was based on rfMRI data that was pre-processed with ICA-FIX (HCP file names: Resting State fMRI 1 FIX-Denoised [Extended] and Resting State fMRI 2 FIX-Denoised [Extended]). ICA was used to remove nuisance and motions signals(Glasser et al., 2013).

First, regression analysis of the resting state fMRI activity was performed for all four sessions individually to filter out the brain signals with low frequency. A high-pass filter of 0.008 Hz was applied, because slow signal changes originate predominately from non-physiological sources such as MR scanner drift, and were therefore treated as covariates of no interest (Fransson, 2005).

Next, the cortical parcellation scheme from (Gordon et al., 2016) was used, because it maximized the similarity of functional connectivity within each parcel. Moreover, the functional connectivity homogeneity within each parcel is high (Betzel et al., 2019). This scheme consisted of 333 re-gions of interest (ROIs) distributed over 12 large-scale networks, which are: Default, Visual, FrontoParietal, DorsalAttention, VentralAttention, Salience, CinguloOpercular, Cingulo-Parietal, SomatoMotorHand, SomatoMotor-Mouth, Auditory, and RetrosplenialTemporal (Gordon et al., 2016).

Last, ROIs with less than 20 active voxels were excluded. Active voxels were defined as voxels where a significant change as compared to the baseline in the blood-oxygen-level-dependent (BOLD) signal was detected. This resulted in 332 ROIs for further analysis.

Connectivity profiles

Calculation of connectivity matrices was performed in MATLAB. Pearson correlation coefficients between pairs of ROI time courses over all four sessions were calculated. This resulted in a 332 × 332 symmetric connectivity matrix per subject. Thus, a connectivity profile included correlations for all ROIs with the other ROIs over the complete time course.

Siamese Neural Network

Model architecture

The model we used to distinguish rfMRI connectivity patterns between subjects is a Siamese Neural Network with two symmetric twin networks (Fig. 1), implemented with PyTorch (Python). Each twin network consisted of five fully connected layers with Nl hidden units per layer l. The inputs x_1 and x_2 are the flattened upper triangular of connectivity matrices, resulting in an input size of $N \cdot (N\text{-}1) / 2$ where N is the number of included ROIs. Thus, the dimension of one input sample was 54946 × 1. Because of the
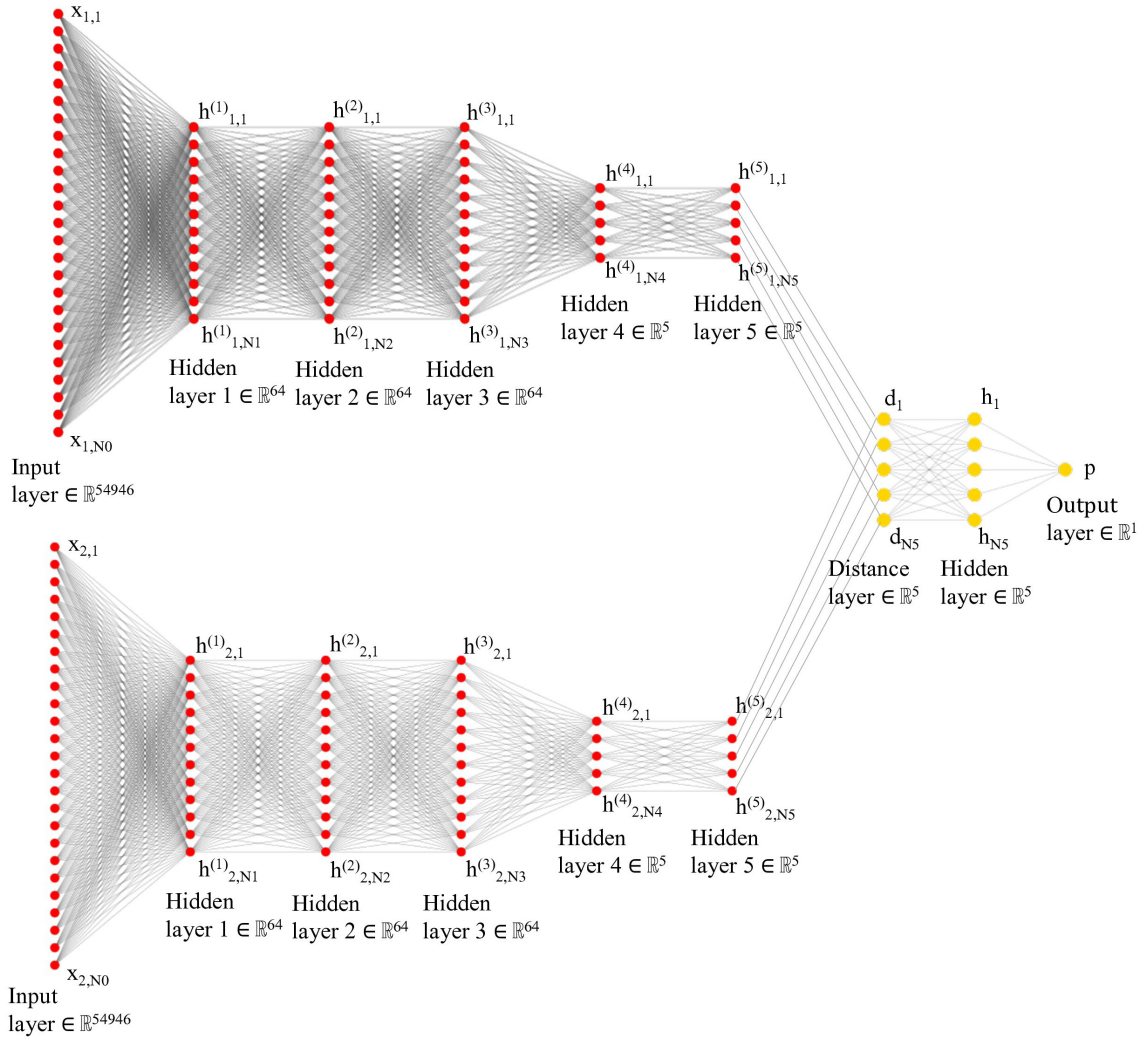
Figure 1. The model used: a Siamese Neural Network with five hidden fully connected layers. Inputs were flattened upper triangular parts of two different connectivity matrices and fed into each Input layer (red nodes, first column) of each twin network. Outputs of each twin network were the activations of Hidden layer five (red nodes, last column). Twin networks were joined with a distance function in the Distance layer (yellow nodes, first column) and resulted in binary classification with logistic prediction p (final yellow node). Symmetric twin networks (red nodes) share the same weight matrices at each layer. N0 = 54946, N1−3 = 64, N4−5 = 5.

symmetry, both twins of the network share the same weight and bias values. Weight and bias values are the learnable parameters by the model, where weight values control the strength of connections between the input and hidden nodes and bias values are applied with the input. Therefore, twins compute the same metric when x_1 and x_2 were presented to twin network 1 and 2, or when x_1 and x_2 were swapped and presented to the twin networks (Koch, 2015).

In this model, the activation function used in all hidden layers was the rectified linear unit (ReLU) function (Equation 1):

$$f(x) = \begin{cases} x, & \text{if } x > 0 \\ 0, & \text{if } x \leq 0 \end{cases} \tag{1}$$

This is a linear function where all negative inputs are returned as zero and all positive inputs are returned unchanged. ReLU is often used as default activation function for neural networks because it is easy to train. We also tried to train the model using the *tanh* activation function: $\frac{e^x - e^{-x}}{e^x + e^{-x}}$, but this resulted in lower accuracy of the model.

Each hidden vector in a fully connected layer l is denoted as $\mathbf{h}_{1,l}$ for the first twin, and

$h_{2,l}$ for the second twin. Thus, after the last fully connected layer (*l*=5), twin network one and twin network two respectively output feature vector $h_{1,5}$ and $h_{2,5}$ based on input x_1 and x_2. This last fully connected layer outputs the highest-level feature representation on each side. The dimension of these representations is determined by N_5, which was 5 × 1. This was the minimum number of hidden nodes in the final hidden layer five that still gave high accuracy.

Last, the twins are joined by a distance function. The distance is determined as the absolute difference between $h_{1,5}$ and $h_{2,5}$, combined by a final ReLU followed by a sigmoid activation (σ) that outputs a value for p (Equation 2):

$$p = \sigma(\alpha|h_{1,l} - h_{2,l}|) \qquad (2)$$

where α are additional parameters learned by the model, weighting the importance of the distance of all five elements between $h_{1,5}$ and $h_{2,5}$ (Koch, 2015). The sigmoid function was chosen as final activation because it maps onto interval ⟨0,1⟩, which can be interpreted as the probability that x1 and x2 belong to the

same subject (p ≥ .5) or to different subjects (p < .5).

Learning

The aim was to train the network in such a way that it can discriminate between pairs of connectivity profiles it has never seen before as belonging to the same subject, or to different subjects.

Preparation of fMRI volumes as input to the DNN. It was required to create multiple connectivity profiles per subject to have a sufficient input set for the SNN to be able to learn the underlying discriminating features of brain connectivity. A total of 4,780,800 fMRI volumes (1200 volumes/run × 4 runs/subject × 996 subjects) were available across all subjects. Multiple connectivity profiles for one subject were created by including different (random) parts of the total time course when the Pearson correlation coefficient (reflecting connectivity between ROIs) was calculated, resulting in multiple connectivity profiles based on one subject's resting state fMRI data. With this, it was possible to create input pairs x1
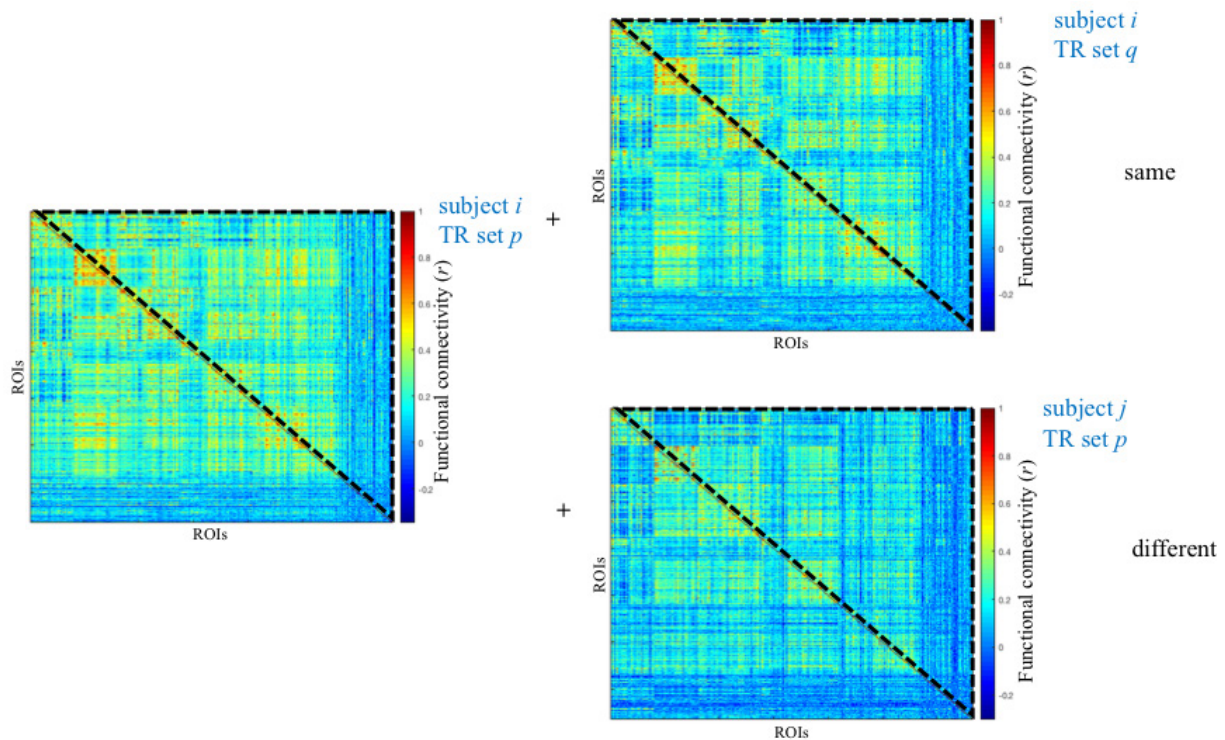

Figure 2. The general strategy: train the model to discriminate between same/different pairs of connectivity profiles. Pairs of connectivity profiles were constructed with a random TR set (i.e., 240 random rfMRI volumes), originating from the same subject (left + top right) or a different subject (left + bottom right).

and x2 originating from the same subject or different subjects (Fig. 2). Only the upper triangular parts of the matrices (without the diagonal) were flattened and used as inputs (Fig. 2, dashed lines).

Because a random set of fMRI volumes was included to create connectivity profiles, time correlations were broken, making the data independent and identically distributed (i.i.d.). This implies that information about one datapoint (rfMRI activity in voxels at a random timepoint) does not give any information about another datapoint (rfMRI activity in voxels at another random timepoint).

Learning schedule. The training set consisted of connectivity profiles constructed with 240 randomly sampled volumes out of a total of 2400, corresponding to the resting state fMRI from two sessions on day one. The validation set consisted of connectivity profiles constructed with 240 randomly sampled volumes out of a total of 2400, corresponding to the resting state fMRI from two sessions on day two.

Weights and biases were randomly initialized and were trained over 200 iterations, using Adam optimizer. The learning rate was set to $10-4$ and the minibatch size was 256. Each training iteration, a random minibatch was fixed and pairs of connectivity matrices $x_1^{(i)}$ and $x_2^{(i)}$ were constructed, where i denotes one sample of the minibatch. 50% of the pairs in one minibatch belonged to the same subject $y(x_1^{(i)}, x_2^{(i)}) = 1$ or different subjects $y(x_1^{(i)}, x_2^{(i)}) = 0$.

After every 50 iterations, the model was evaluated for 50 iterations with a validation set. Every evaluation was identical to allow for a good comparison of the model's performance during learning.

Loss function. As a loss function, the Binary Cross-Entropy function was used (Equation 3). This function was chosen because it takes in the probabilities of the binary classes 0 and 1, and outputs a low loss value if the (negative log of the) probability of the true class is high, and conversely, a high loss value if the (negative log of the) probability of the true class is low.

$$L(\mathbf{x}_1, \mathbf{x}_2) = -\frac{1}{N}\sum_{i=1}^{N}\Big[y(x_1^{(i)}, x_2^{(i)})\log p(x_1^{(i)}, x_2^{(i)}) +$$
$$(1 - y(x_1^{(i)}, x_2^{(i)}))\log(1 - p(x_1^{(i)}, x_2^{(i)}))\Big] \quad (3)$$

Decorrelation of final hidden activations. In order to visualize and interpret the learned features as distinct components, it was necessary that the final activations were uncorrelated. To ensure that the final feature vector hm,5 of each twin network m was uncorrelated, a regularization term was imposed on the loss function (Equation 4-5; [Cogswel, Ahmed, Girshick, Zitnick, & Batra, 2016]). To this end, the covariances were minimized, which corresponds to penalizing the norm of covariance matrix C.

$$\text{Final loss function} = L(x_1, x_2) + \lambda \cdot LDeCov \quad (4)$$

with

$$LDeCov^m = ||C||_F^2 - ||diag(C)|| \quad (5)$$

where $||.||_F$ is the Frobenius norm. Here, matrix C contains the covariances between all pairs of activations from $\mathbf{h}_{m,5}$, divided over N_5. This last division step was performed to ensure a stable LDeCov term, independent of the number of final hidden units chosen in the model. This resulted in $LDeCov^1$ for $\mathbf{h}_{1,5}$ for twin network one, and $LDeCov^2$ for $\mathbf{h}_{2,5}$ for twin network two (Equation 5). Last, the mean of the two terms was taken, multiplied with λ, and added to the loss function (Equation 4). Grid search for λ in the range of 0.1 to 1.0 was performed to find the highest value for λ. This resulted in the optimal value λ=1.0.

Visualization of final hidden activations

The activations of the final hidden layer (Fig. 1, l=5) provided five uncorrelated hidden representations of the input connectivity profiles. Note that these final representations in both twin networks would be the same when input x1 and x2 were identical, since both networks share the same learned weight and bias values. To map each learned feature by the model onto a feature of functional connectivity, the following analysis was performed (for complete overview, see Figure 3).

Per subject i, the connectivity matrix based on rfMRI data from the complete time course was taken as input $x_m^{(i)}$ for one twin network m. The activations of the last fully connected layer represented the highest-level features $\mathbf{h}_{m,5}^{(i,complete)}$. To observe the contribution of each connection (i.e., each matrix' entry), its
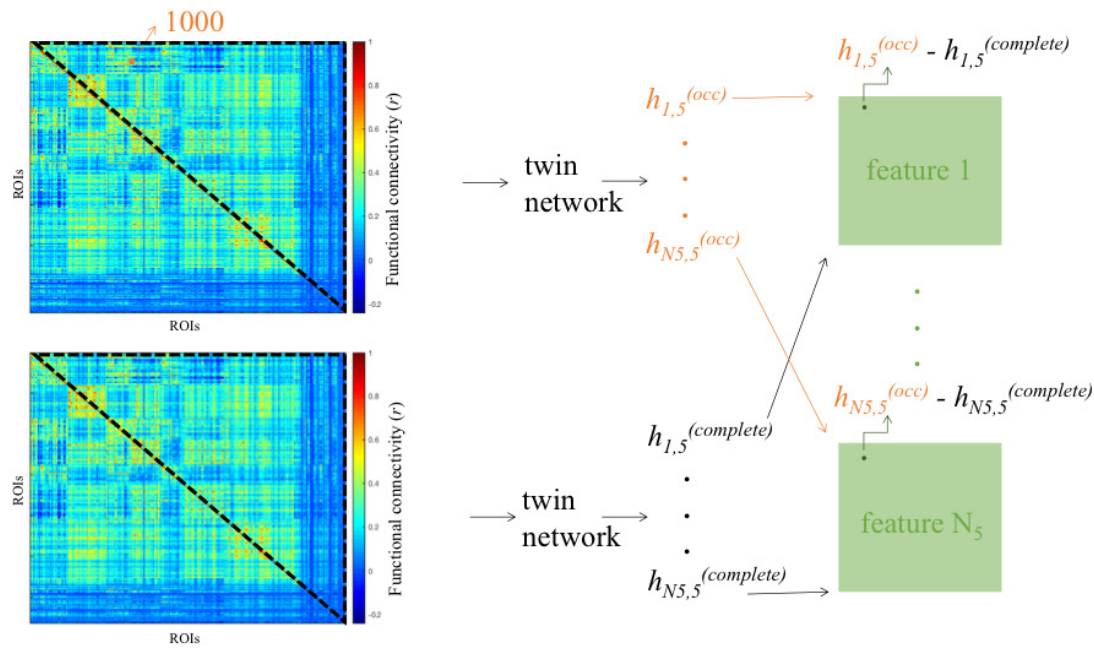
Figure 3. The visualization strategy: Each value of a connectivity profile (connection strength between two ROIs) was set to a high value (1000). As inputs, only the upper flattened triangular parts of matrix were used (indicated with dashed lines), and final hidden activations were observed (indicated with orange). The change in final hidden activations represented the contribution of a specific connection to the activations (indicated in dark green). The changes were stored in five separate matrices, each representing one final hidden activation (indicated in light green). Per matrix, each value represented the contribution of the connection strength between two ROIs to one final hidden activation.

value was set to 1000, and this new connectivity profile was taken as input $x_m^{(i)}$. Similarly, activations of the final hidden layer were observed as $h_{m,5}^{(i,occ)}$. The difference between $h_{m,5}(i,occ)$ and $h_{m,5}(i,complete)$ represented the contribution of each connection (i.e., functional connectivity between ROIs) to each of the five activations of the last fully connected layer for subject i.
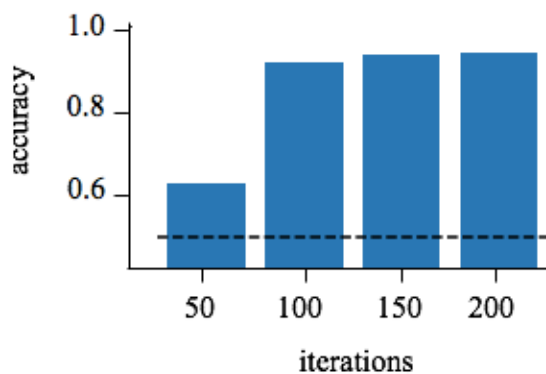
Figure 4. The model's accuracy of the validation set consisting of rfMRI volumes from day two, trained with rfMRI volumes from day one.

The extreme value of 1000 was chosen to ensure an observable change in final activation values. Changing each connection to zero would not give the right contrast, since zero would be a plausible value for a correlation between a connection (i.e., the original value of a connectivity matrix' entry).

This process was repeated for all 996 subjects and then averaged, resulting in five (one per hidden node output) 332×332 matrices over all subjects.

Included tests to find relationship with final hidden activations

For all 996 subjects their rfMRI volumes were fed into a trained twin network. Per subject, this resulted in final activation values (Fig. 1, red nodes, last column), representing a 'score' for each final feature learned by the model.

Cognitive performance. First, to explore a link between the final hidden activations and cognitive performance, Pearson correlation coefficients between final activation values and multiple cognitive tests were calculated.

Table 1. Correlations between the three final hidden activations of hidden layer five of a twin network.

output number	0	1	2
0	1	.083	.087
1	.083	1	.056
2	.087	.056	1

This included the following tests from the NIH Toolbox and Penn tests (Elam, 2020), none of them were age adjusted. (Verbal) episodic memory, which involves the acquisition, storage and effortful recall of new information, executive function, which specifically measures cognitive flexibility, fluid intelligence via non-verbal reasoning, language decoding, which measures the reading decoding skill, working memory, which involves information processing and storage and last, spatial orientation via line orientation.

Surface thickness and area size of brain regions. Next, to explore a link between the final hidden activations and brain regions, Pearson correlation coefficients between final activation values and surface thickness and area size of multiple brain regions were calculated. Surface thickness and area size from subjects were obtained as described in Van Essen et al. (2012). Included brain regions were the following cortical regions with clear

anatomical landmarks (based on [Hagmann et al., 2008]; Figure 1[3a]): lateral occipital cortex, cuneus, superior parietal cortex, precuneus, inferior parietal cortex, supramarginal gyrus, transverse temporal gyrus, superior temporal cortex, middle temporal gyrus, inferior temporal gyrus, posterior cingulate cortex and superior frontal cortex.

Results

Evaluation of SNN performance

The SNN was trained for 200 iterations in total. After one training block of 50 iterations with rfMRI volumes from day one, there was a validation block of 50 iterations with rfMRI volumes from day two. The accuracy was measured as a percentage of correct classified pairs of a minibatch (256 input pairs, 50% same and 50% different subjects), averaged over 50 iterations (Fig. 4). After one training block the SNN's accuracy was already above
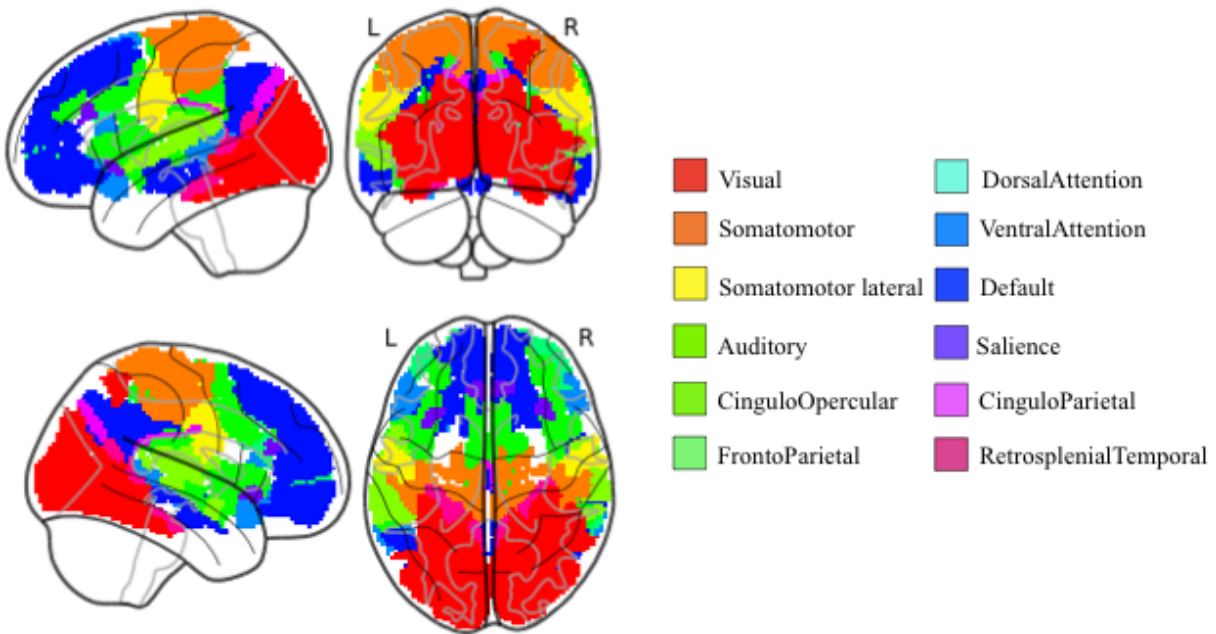
Figure 5. Locations of the large-scale brain networks.
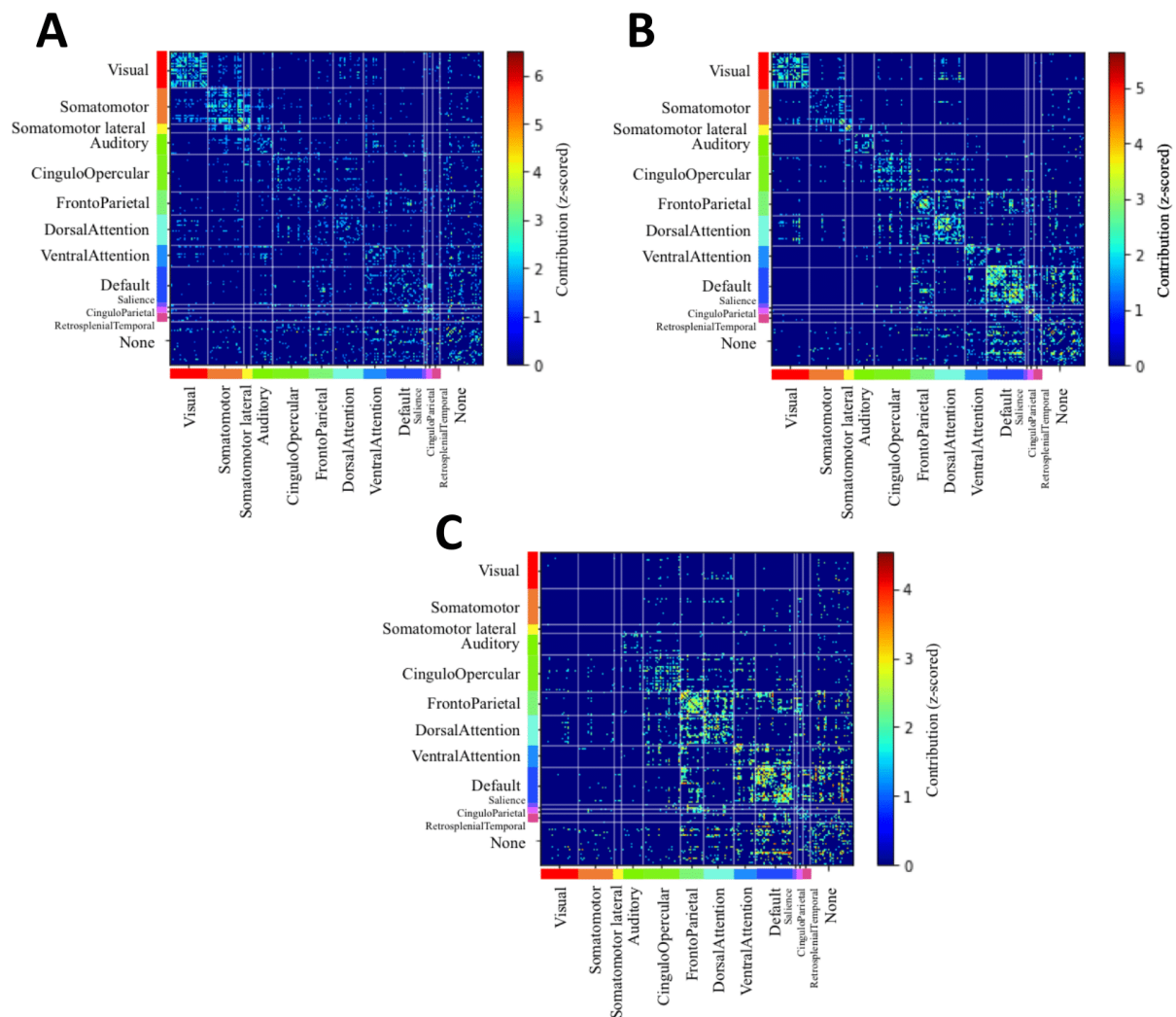
Figure 6. Contribution of each connection between ROIs to the model's final hidden activation values. A. Visualisation of output zero. B. Visualisation of output two. C. Visualisation of output three.

chance level (indicated with dashed line, >50% correct classified). After the second training block, the model already reached excellent accuracy (>90% correct classified). The training phase was considered done when the accuracy did not increase anymore, which was after the fourth training block. This resulted in an accuracy of .96, or 96% correct classified input pairs.

The final hidden layer five of each twin network m had final hidden activations $h_{m,5}$ of size $N_5 = 5$ (Fig. 1, red nodes, last column). However, two of the five final hidden activations were zero for all subjects' connectivity profiles. This resulted from the ReLU activation function that could output a zero (Equation 1). Only three of the five final hidden activations had a non-zero value, therefore, only three outputs are dis-

cussed below. To determine whether the final hidden activations had correlations with each other, connectivity profiles from all 996 subjects were fed into one twin network (Fig. 1, red nodes). The three final outputs were uncorrelated (Table 1).

Interpretation of final hidden activations

The used parcellation scheme comprised 332 ROIs (Gordon et al., 2016), distributed over 12 large-scale brain networks (Fig. 5).

The occlusion analysis as previously described (Methods: Visualization of final hidden activations) resulted in a 332 × 332 matrix for each final hidden activation. The brain networks on both axes were sorted (Gratton et al., 2018): first the processing

A

B

C
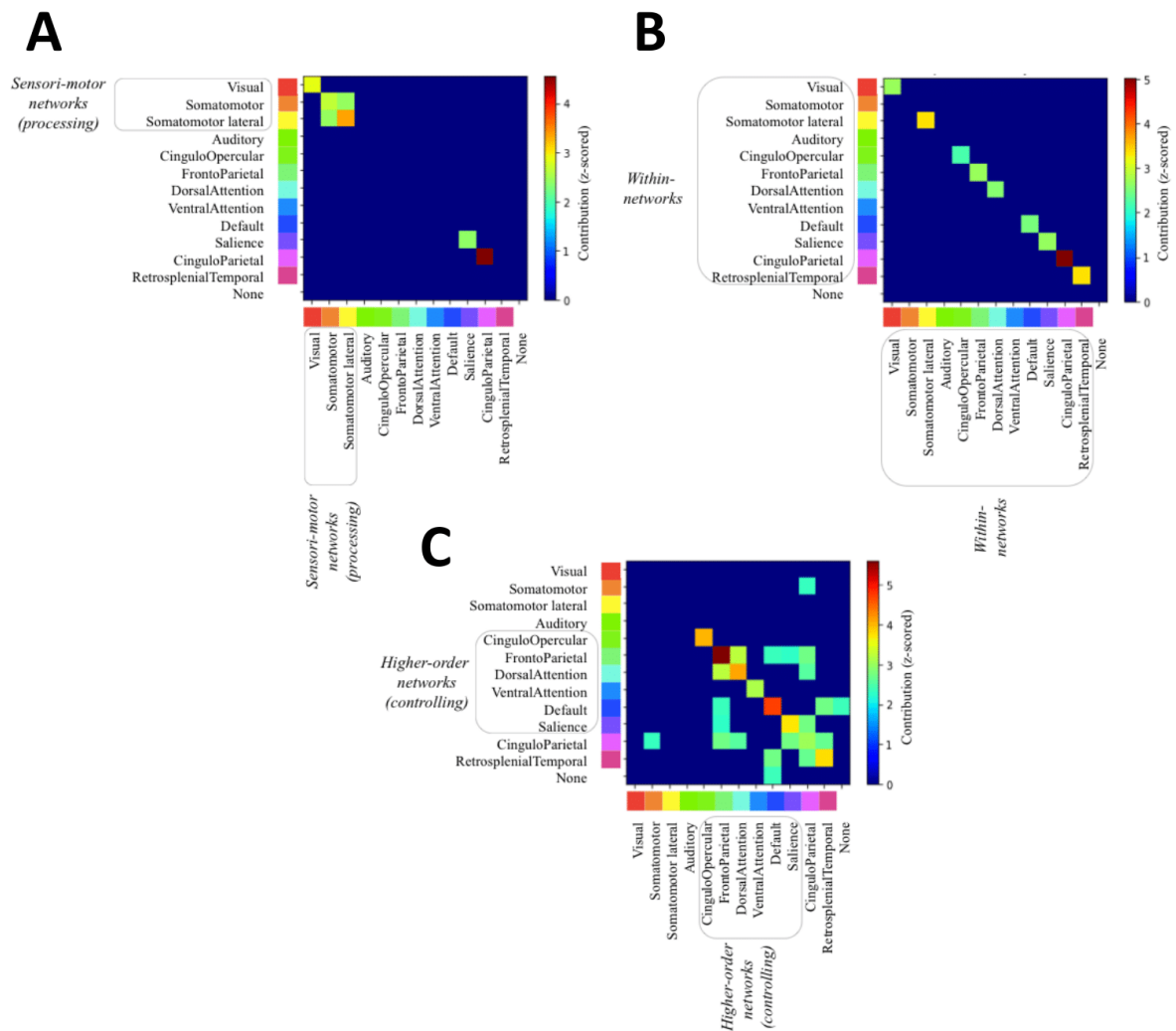
Figure 7. Contribution of each connection between ROIs to the model's final hidden activation values, averaged over all ROIs in a large-scale brain network. A. Visualisation of output zero. B. Visualization of output two. C. Visualization of output three.

networks (Visual, Somatomotor, Somatomotor lateral, Auditory), next the control networks (CinguloOpercular, FrontoParietal, DorsalAttention, VentralAttention, Default), and last the rest (CinguloParietal, RetrosplenialTemporal, None). Values were z-scored with a threshold of z > 1.5 (Fig. 6).

The highest contribution (i.e. greatest change in output value when the connection's value was set to 1000) to output zero (Fig. 6A) were mostly found in connections between ROIs belonging to the Visual, Somatomotor (SM) and Somatomotor lateral (SM-lat) networks. This component describes connections within the visual network and connections within the somatomotor network, but not between the two networks. Furthermore, connections within other specific networks were observed, however, they

are less dominant. The most contributing connections between ROIs for output two were not found in a specific set of networks, but roughly all large-scale brain networks had similar contribution to output two (Fig. 6B). Most contributing connections between ROIs of a network were mostly found with ROIs within the same network. The connections between ROIs with the highest contribution to output three (Fig. 6C) were mostly found in the CinguloOpercular (CO), FrontoParietal (FP), DorsalAttention (DA), VentralAttention (VA), Default (DM) and Salience network, with the strongest connections within FP and DMN. Also, less dominant connections between different networks were observed.

Averaging over all ROIs within a large-scale brain network resulted in a 12 × 12 matrix for each final hidden activation, where

all large-scale brain networks were plotted against each other. Values were z-scored with a threshold z > 2.2 (Fig. 7). The three final hidden activation represented distinct components: 1) sensori-motor networks 2) within-networks and 3) higher-order networks.

Evaluation of final hidden activations with cognitive performance

To explore a link between the found components and cognitive performance, the final hidden activations were correlated with scores on multiple cognitive tests from the NIH Toolbox and Penn tests (p-values were Bonferroni corrected for all comparisons, see Methods: Cognitive performance for included tests).

The higher-order networks component (Fig. 7C) correlated with the fluid intelligence score (r = .16, p < .001) and with the language decoding score (r = .17, p < .001). Furthermore, correlation was found between the within-networks component (Fig. 7B) and the working memory score (r = .18, p < .001). The sensori-motor networks component (Fig. 7A) did not show any significant correlations with the included cognitive tests.

Evaluation of final hidden activations with brain regions

To explore a link between the found components and brain regions, the final hidden activations were correlated with surface thickness and area size of multiple brain regions (p-values were Bonferroni corrected for all comparisons, see Methods: Surface thickness and area size of brain regions for included brain regions). Correlations between the higher-order networks component and precuneus surface area (r = .29, p < .001, Fig. 8, green arrow), superior parietal cortex area (r = .28, p < .001, Fig. 8, orange arrow), superior frontal cortex area (r = .28, p < .001, Fig. 8, pink arrow), inferior temporal gyrus area (r = .27, p < .001, Fig. 8, blue arrow), and middle temporal gyrus area (r = .27, p < .001, Fig. 8, yellow arrow) were found. The sensori-motor networks component (Fig. 7A) and the within-networks component (Fig. 7B) did not show any significant correlations with the included brain regions.

Discussion

The main aim of this study was to unravel the underlying features of inter-individual variability in functional brain connectivity. We
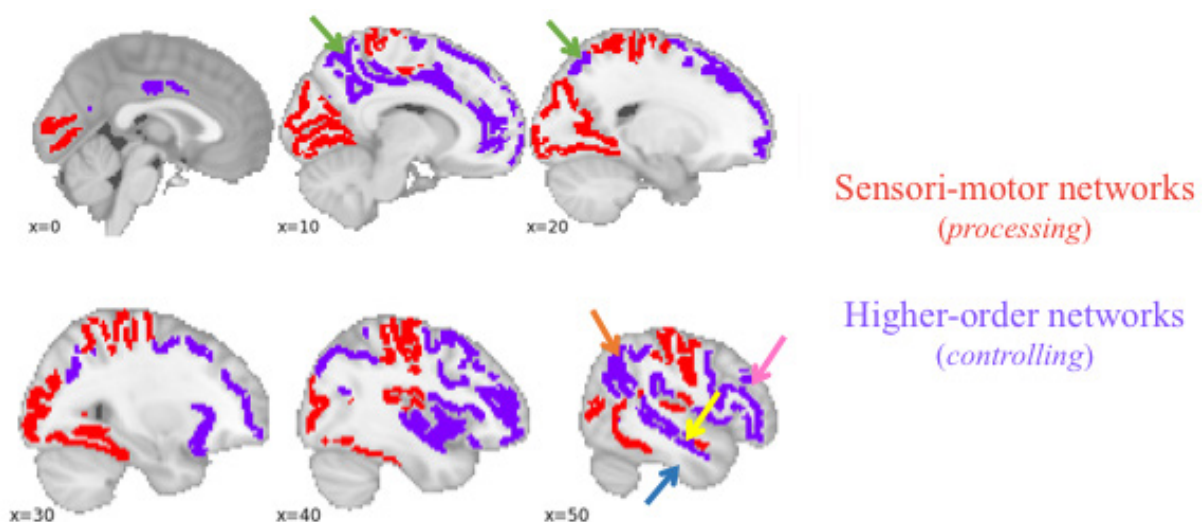
Figure 8. The locations of the ROIs belonging to the sensori-motor networks component (Visual, SM, SM-lat) are shown in red, the locations of the ROIs belonging to the higher-order networks component (CO, FP, DA, VA, DM, and Salience) are shown in purple. Significant correlations between the higher-order networks component and brain regions are indicated with coloured arrows. Indicated brain regions overlap with locations of higher-order networks.

have identified three components of inter-individual variability in functional connectivity, that together can be used to verify the identity of an individual with > 95% accuracy. Each component represented a different set of large-scale brain networks. First, the sensori-motor networks component ('processing' systems [Gratton et al., 2017; Gratton et al., 2018]), consisting of the Visual, SM and SM-lat networks (Fig. 7A). Second, the higher-order networks component ('control' systems [Gratton et al., 2017; Gratton et al., 2018]), consisting of the CO, FP, DA, VA, DM, and Salience networks (Figure 7C). Third, the within-networks component, consisting of inter-networks connections rather than a specific set of networks (Figure 7B).

We demonstrated that it is possible to develop a model that identifies individuals from a large group solely based on functional connectivity. With large amounts of data (resting state fMRI data from 996 subjects acquired on two separate days [Van Essen et al., 2013]), the model reached an accuracy of 96% correct classification. This indicates that intraindividual functional organization is idiosyncratic (Finn et al., 2015), and can be used as a measure to discriminate between individuals. This also indicates that inter-individual variability in functional organization arises from stable factors rather than more transient factors such as ongoing cognition, and can provide meaningful information about individual stable traits (Gratton et al., 2017).

Furthermore, we demonstrated that we can condense a functional connectivity matrix to only three dimensions and still classify individuals with high accuracy. More specifically, the input space of 54946 (representing resting state correlations between predefined ROIs, using the parcellation scheme from Gordon et al. [2016]) was reduced by the model to five final outputs, whereof three were considered relevant. These three relevant final outputs were forced to be uncorrelated. This indicates that inter-individual variability in functional connectivity can be reduced to only three meaningful distinct components that each represent a discriminative feature of inter-individual variability in functional connectivity. This also indicates that discriminating features of inter-individual variability in functional connectivity

are easy to interpret because each component maps to a different set of large-scale brain networks.

Each component includes the large-scale brain networks that show the highest contribution to that component (see Figure 7 for included networks per component), which means that functional connectivity in these networks is driving the model to classify subjects' functional connectivity profiles correctly. Therefore, the 'score' for each component (i.e., the activations of final hidden layer five, see Fig. 1, red nodes, last column) could tell something about the nature and underlying mechanisms of the included large-scale brain networks of the component.

First, the three found components could provide meaningful information about an individual's cognitive measures. It is known that inter-individual variability in functional connectivity is relevant to individual differences in behaviour (Finn et al., 2015; Rosenberg et al., 2016; Shen et al., 2017; Tavor et al., 2016). We observed correlations between the higher-order networks component and language decoding and fluid intelligence. This is consistent with previous findings where functional properties of the FP network appeared to be most related to intelligence (Finn et al., 2015; Kanai & Rees, 2011). Furthermore, we observed a correlation between the within-networks component and working memory. The within-networks component represents connections within large-scale brain regions, with connections within the CinguloParietal network yielding the highest contribution to the 'score' for that component. This network comprises the anterior cingulate cortex (aCC), posterior cingulate cortex (pCC), lateral parietal cortex (LPC) and part of the superior frontal cortex (SFC) (see Toro et al., [2008], Fig. 5), which is in line with previous research where it is shown that working memory is associated with the prefrontal cortex and more posterior regions (Cohen et al., 1997).

Next, we observed correlations between the higher-order networks component and multiple area sizes of cortical brain regions (Fig. 8, indicated with arrows). The locations of the areas with significant correlations overlap with the locations of the ROIs of the large-scale brain networks included in the higher-order networks component. This implies

that there is some relationship between the area size of brain regions contributing to the higher-order networks component and the 'score' for the higher-order networks component. This suggests that anatomical features such as grey matter might relate to the inter-individual discriminating features of functional connectivity and that amount of grey matter is associated with the strength of connection within these regions.

In this study, three distinct components that serve as underlying discriminating feature of inter-individual variability in functional connectivity are discussed. Further work should focus on the generalization of the model, and investigate how robust the identified components as underlying features of inter-individual variability in functional connectivity are.

First, we used patterns of brain activity in resting state, but patterns in other states such as a task state could also be included. Next, we used fMRI activity acquired on two consecutive days, but fMRI activity obtained within a longer time span could also be included. Next, the large subject-level specific variability in functional connectivity demands for the use of a large data set such as the HCP data set, therefore, development of a future model could use another large data set. Last, our used model had five final hidden activations, where only three of them had a non-zero value. Decreasing the number of final hidden nodes caused the model's performance to drop. We do not understand why this happened and how to resolve this. Ideally, the model would use all the final hidden nodes when discriminating between subjects' functional connectivity profiles.

To conclude, we showed that the input space of a complete FC profile can be reduced to only three components that the model uses to successfully distinguish individuals' FC profiles from each other. This indicates that functional organization is individual specific, and arises from stable factors. Furthermore, we showed that each discriminating feature of functional connectivity represented a meaningful distinct component that maps to a different set of large-scale brain networks.

References

Betzel, R., Bertolero, M.A., Gordon, E., Gratton, C., Dosenbach, N., & Bassett, D. (2019). The community structure of functional brain networks exhibits scale-specific patterns of inter- and intra-subject variability. *NeuroImage, 202*, 115990.

Biswal, B., Zerrin Yetkin, F., Haughton, V., & Hyde, J. (1995). Functional connectivity in the motor cortex of resting human brain using echo-planar mri. *Magnetic Resonance in Medicine, 34*, 537-541.

Cogswel, M., Ahmed, F., Girshick, R., Zitnick, L., & Batra, D. (2016). Reducing overfitting in deep neural networks by decorrelating representations. *ICLR*.

Cohen, J., Perlstein, W., Braver, T., Nystrom, L., Noll, D., Jonides, J., & Smith, E. (1997). Temporal dynamics of brain activation during a working memory task. *Nature, 386*, 604-608.

Elam, J. (2020). Hcp data dictionary public (11 June, 2020).

Finn, F., Shen, X., Scheinost, D., Rosenberg, M., Huang, J., Chun, M., ... & Constable, R. (2015). Functional connectome fingerprinting: identifying individuals using patterns of brain connectivity. *Nature Neuroscience, 18*, 1664–1671.

Fransson, P. (2005). Spontaneous low-frequency bold signal fluctuations: An fmri investigation of the resting-state default mode of brain function hypothesis. *Human Brain Mapping, 26*, 15-29.

Glasser, M., Sotiropoulos, S., Wilson, J., Coalson, T., Fischl, B., Andersson, J., ... & Jenkinson, M. (2013). The minimal processing pipelines for the human connectome project. *NeuroImage, 80*, 105-124.

Gordon, E., Laumann, T., Adeyemo, B., Huckins, J., Kelley, W., & Petersen, S. (2016). Generation and evaluation of a cortical area parcellation from resting-state correlations. *Cerebral Cortex, 26*(1), 288-303.

Gordon, E., Laumann, T., Gilmore, A., Newbold, D., Greene, D., Berg, J., ... & Dosenbach, U. (2017). Precision functional mapping of individual human brains. *Neuron, 95*(4), 727-807.

Gratton, C., Laumann, T., Nielsen, A., Greene, D., Gordon, E., Gilmore, A., ... & Petersen,

S. (2017). Functional brain networks are dominated by stable group and individual factors, not cognitive or daily variation. *Neuron, 98*(2), 439-452.

Gratton, C., Sun, H., & Petersen, S. (2018). Control networks and hubs. *Psychophysiology, 55*.

Hagmann, P., Cammoun, L., Gigandet, X., Meuli, R., Honey, C., Wedeen, V., & Sporns, O. (2008). Mapping the structural core of human cerebral cortex. *PLoS Biology, 6*(7).

Kanai, R., & Rees, G. (2011). The structural basis of inter-individual differences in human behaviour and cognition. *Nature Reviews Neuroscience, 12*, 231-242.

Kietzmann, T., McClure, P., & Kriegeskorte, N. (2018). Deep neural networks in computational neuroscience. *BioRxiv.*

Koch, G. (2015). Siamese neural networks for one-shot image recognition.

Rosenberg, M., Finn, E., Scheinost, D., Papademetris, X., Shen, X., Constable, R., & Chun, M. (2016). A neuromarker of sustained attention from whole-brain functional connectivity. *Nature Neuroscience, 19*, 165-171.

Seitzman, B., Gratton, C., Laumann, T., Gordon, E., Adeyemo, B., Dworetsky, A., ... & Petersen, S. (2019). Trait-like variants in human functional brain networks. *Proceedings of the National Academy of Sciences, 116*(45), 22851-22861.

Shen, X., Finn, E., Scheinost, D., Rosenberg, M., Chun, M., Papademetris, X., & Constable, R. (2017). Using connectome-based predictive modeling to predict individual behavior from brain connectivity. *Nature Protocols, 12*, 506-518.

Smith, S., Vidaurre, D., Beckmann, C., Glasser, M., Jenkinson, M., Miller, K., ... & Van Essen, D. (2013). Functional connectomics from resting-state fmri. *Trends in Cognitive Neuroscience, 17*(12), 666-682.

Storrs, K., & Kriegeskorte, N. (2019). Deep learning for cognitive neuroscience. *ArXiv.*

Tavor, I., Parker Jones, O., Mars, R., Smith, S., Behrens, T., & Jbabdi, S. (2016). Task free mri predicts individual differences in brain activity during task performance. *Science, 352*(6282), 216-220.

Toro, R., Fox, P., & Paus, T. (2008). Functional coactivation map of the human brain. *Cerebral Cortex, 18*(11), 2553-2559.

Van Essen, D., Glasser, M., Dierker, D., Harwell, J., & Coalson, T. (2012). Parcellations and hemispheric asymmetries of human cerebral cortex analyzed on surface-based atlases. *Cerebral Cortex, 22*(10), 2241-2262.

Van Essen, D., Smith, S., Barch, D., Behrens, T., Yacoub, E., & Ugurbil, K. (2013). The wu-minn connectome project: An overview. *NeuroImage, 80*, 62-79.

Xu, K., Lei Ba, J., Kiros, R., Cho, K., Courville, A., Salakhutdinov, R., ... & Bengio, Y. (2015). Show, attend and tell: Neural image caption generation with visual attention. *Proceedings of the 32nd International Conference on Machine Learning, 37*.

Stress and Motivation: An fMRI Study on the Effects of Stress on Effort-Based Decision-Making

Tim Vriens[1]

[1]*Radboud University Nijmegen, Donders Institute for Brain, Cognition and Behaviour, The Netherlands*

Supervisors: Eliana Vassena[1] and Erno Hermans[1]

Corresponding author: Tim Vriens
E-mail: t.vriens@donders.ru.nl

Reaching desired goals requires effort. In daily life, we often face important decisions on whether to engage in effortful yet rewarding actions (e.g., studying hard to obtain a university degree or accepting a demanding job with a great salary). These decisions are often made under considerable stress, such as when having financial uncertainty. Previous studies have shown that effort-based decision-making implicates a cortico-subcortical network involving the prefrontal cortex and midbrain catecholamine (noradrenaline and dopamine). Stress is known to affect both prefrontal activity and catecholamine levels. Despite these commonalities, the effect of stress on effort-based decision-making and its neural correlates are surprisingly understudied. In this study, the effects of stress on effort-based decision-making were investigated, focusing on behaviour, neural activity, and noradrenergic release measured by pupil dilation. Using a within-subjects design with acute stress induction, we hypothesized that stress would decrease the willingness to engage in mental effort, and that this would be linked with alterations in prefrontal activity and pupil dilation. Participants performed an effort-based decision-making task in the functional magnetic resonance imaging (fMRI) scanner during a control condition or an experimentally induced acute stress condition. The results showed that stress reduced the willingness to engage in effort. Pupil dilation increased with task difficulty during calculations, but did not change under stress. Unexpectedly, no difference was observed between stress and control at the whole-brain level. An a-priori region-of-interest analysis revealed no significant effect of stress on effort or reward coding in the anterior cingulate cortex (ACC). A significant decrease in effort coding under stress in the dorsolateral prefrontal cortex (DLPFC) was observed. However, this was specific to the high reward condition and for participants who experienced the control session first. Overall, these results suggest that acute stress reduces the willingness to engage in mental effort, with preliminary evidence of alterations in DLPFC.

KEYWORDS stress, effort-based decision-making, DLPFC, MPFC, ACC, motivation, effort, reward

We often face decisions where we have to figure out whether the goals of our actions are worth the effort. For example, think about choosing what kind of dinner to make for yourself. You could choose from a large range of recipes, ranging from easy to hard. Each recipe has an expected reward: the produced meal. When deciding, you make a trade-off between the effort and expected reward of each option, and try to select the optimal action. However, this decision can be influenced by external factors. For example, you might be under stress due to having an important deadline later. This might influence the amount of effort you are willing to expend for making the dinner, and how you perceive the reward of the dinner itself. Therefore, the trade-off between required effort and expected reward – a typical cost-benefit calculation of effort-based decision-making – might be influenced by stress. Research in humans and animals has shown that stress has a substantial impact on several cognitive functions, such as memory, emotion and attention (Schwabe, Joëls, Roozendaal, Wolf, & Oitzl, 2012; Roozendaal, McReynolds, & McGaugh, 2004; Booth & Sharma, 2009), including preliminary evidence that acute stress may alter motivation (Ironside, Kumar, Kang, & Pizzagalli, 2018). In the following subsections, I will be providing a brief over-view of the known dynamics of effort-based decision-making and stress. Moreover, I will elaborate on the relevant neural mechanisms of these processes and explain the known neural activity underlying these processes.

Effort-based decision-making

In effort-based decision-making, the trade-off between effort and reward is studied. Generally, when people face a decision, they avoid exerting effort (Kool, McGuire, Rosen, & Botvinick, 2010). However, they are willing to exert effort if this leads to a reward (Vassena, Deraeve, & Alexander, 2019). It has been shown that increasing reward causes willingness to exert increasing effort (Shenhav et al., 2017). Additionally, rewards might be valued less when more effort is required to obtain them (Apps, Grima, Manohar, & Husain, 2015). Based on this reward value, and the effort required to obtain the reward, an action is selected. Then, the outcome of the action is used to update the expected effort and reward.

Extensive neuroscientific research has addressed the neural mechanisms of effort-based decision-making, demonstrating the important role of catecholamines – dopamine (DA) released by the Ventral Tegmental Area (VTA) and noradrenaline (NA) released by the Locus Coeruleus (LC). Animal studies have shown that DA depletion led to increased sensitivity to response cost (Salamone, Correa, Farrar, Nunes, & Pardo, 2009), resulting in rats avoiding more effort. Further, increasing DA transmission increased effortful behaviour in rats (Salamone, Correa, Yang, Rotolo, & Presby, 2018), and blocking DA caused effort avoidance (Walton et al., 2009). In a study in monkeys, DA neurons encoded reward expectation and anticipated effort cost (Varazzani, San-Galli, Gilardeau, & Bouret, 2015). DA is relevant in reward prediction error coding as well as reward valuation (Schultz, 2016). Research shows that DA depletion can lead to reduced effortful behaviour (Salamone, Cousins, & Bucher, 1994) and that DA is needed for motivation (Berridge, 2012). Therefore, DA can influence effort-based decision-making, by regulating both the effort and reward signals. Dopaminergic input to dorsal Anterior Cingulate Cortex (dACC), part of the medial prefrontal cortex (MPFC), is associated with prediction error and reward expectation (Schultz, Dayan, & Montague, 1997; Pan, Schmidt, Wickens, & Hyland, 2005). It was also reported that VTA-mediated DA release has a role in cost encoding (Orsini, Hernandez, Bizon, & Setlow, 2018), and thus influences effort-based decision-making. Given the aforementioned role of DA in effort-based decision-making, and given that the VTA produces DA, a role for the VTA seems prominent in decision-making.

Complementary to DA, NA has also been implicated in effort-based decision-making (Varazzani et al. 2015). LC activity correlated with effort coding and changes in reward (Bouret & Richmond, 2009; Varazzani et al., 2015). Further, NA levels have been connected to performance in an optimization task through modulation of the learning parameter (Ironside et al., 2018). A correlation between pupil size and effort coding has also been found (Varazzani et al., 2015). Noradren-ergic input to dACC is also thought to reflect

environmental volatility (Behrens, Woolrich, Walton, & Rushworth, 2007; Silvetti, Seurinck, van Bochove, & Verguts, 2013a). Taken together, these findings suggest that LC-NA can influence effortful decision-making. Additionally, a role for the Striatum, one of the primary targets of midbrain dopaminergic projections, has been reported (Orsini et al., 2018).

In humans, previous research on neural correlates of effort-based decision-making indicated that the MPFC and dorsolateral prefrontal cortex (DLPFC) show effort-related activity (Vassena, Deraeve, & Alexander, 2017). Besides effort, the DLPFC shows reward-related activity (Asci, Braem, Park, Boehler, & Krebs, 2019). Furthermore, the dACC has a role in effort coding, even independently of reward given (Porter, Hillman, & Bilkey, 2019), and plays a role in optimal action selection (Silvetti, Vassena, Abrahamse, & Verguts, 2018). ACC and striatum activity are also reported when anticipating reward and effort (Vassena et al., 2014); a study in rats found that a lesion in the ACC caused rats to select lower effort choices more often (Walton et al., 2009). Thus, given that effort-based decision-making combines reward and effort, a model that captures effort-based decision-making should incorporate both reward and effort. This line of work led to developing the reinforcement meta-learner model (RML), taking both reward and effort into account (Silvetti et al., 2018).

This model consists of two separate subparts. First, there is an action selection mechanism. This mechanism contains the network of MPFC, DLPFC and dACC, which are all involved in effort or reward-related activity. Second, there is a meta-learning mechanism. This mechanism consists of the dACC and the brainstem nuclei releasing catecholamines; the VTA releasing DA, and the LC releasing NA (Silvetti et al., 2018). The RML builds on earlier models, implementing the idea that information about reward, prediction error and volatility is fundamental to determine which are the best actions to perform (Behrens et al., 2007; Silvetti, Seurinck, & Verguts, 2013b; Alexander & Brown, 2011). The critical insight of the RML and the core of the meta-learning aspect is that the dACC can in turn top-down influence catecholamine release in VTA and LC, and

therefore adapt its own parameters (Silvetti et al., 2018). This mechanism is particularly important when higher NA levels are needed to invigorate a more effortful action, or when higher DA levels are needed to pursue long-term rewards that are not available yet. In these situations, dACC is able to upregulate NA or DA release to support flexible and adaptive behaviour (Silvetti et al., 2018). This model provides a promising neuro-computational framework to understand the role of prefrontal and catecholaminergic dynamics during decision-making.

Mechanisms of stress

Stressors are defined as perceived threats to homeostasis and well-being (Herman et al., 2016). Exposure to stressors triggers a series of neurophysiological events known as the stress response which allow prompt behavioural responses in challenging situations. This stress reaction can be adaptive or maladaptive. In this case, it can lead to the development of stress-related disorders, e.g. Post-Traumatic Stress Disorder. The stress response originates from two different systems: a slow system and a fast system (Hermans, Henckens, Joëls, & Fernández, 2014).

The fast stress response occurs almost instantly, and lasts for 30-60 minutes (Joëls & Baram, 2009). It is characterized by a substantial increase in catecholamine levels. During this response, the LC is activated (Valentio & Bockstaele, 2008) and NA is released. DA levels also increase, especially in the MPFC (Hermans et al., 2014). Furthermore, a shift in network balance can be observed after stress. In the early stress response, an increase of neural activity in the salience network (SN) is observed. The SN includes a number of cortical and subcortical regions, including dACC and insula, that are generally more active when we experience salient events (Seeley et al., 2007; Hermans et al., 2011). At the same time, a decrease in neural activity is observed in the executive control network (ECN). The ECN includes regions that are generally more active when we engage in mentally demanding tasks which require cognitive control. This network includes dorsolateral and dorsomedial parts of the PFC (Seeley et al., 2007; Hermans et al., 2011;

Hermans et al., 2014).

Interestingly, this shift from ECN to SN reverses after the early stress response is over (Hermans et al., 2014; see Fig. 1 for a summary). This phenomenon has been linked to the interplay with the glucocorticoid system. After the initial fast response, a slower process is initiated, involving the hypothalamic-pituitary-adrenal (HPA) axis. In this response, corticosteroid levels increase. These corticosteroids, which are cortisol and corticosterone, have an effect on two different time scales. They have a direct, non-genomic effect, reaching their peak after the catecholaminergic effect, and a slower, genomic effect (Hermans et al., 2014; Joëls, Sarabdjitsingh, & Karst, 2012). This non-genomic effect causes an increase in NA activity, and enhances the stress effects on DA (Hermans et al., 2014). Furthermore, these effects were found to impair working memory

in rats (Roozendaal et al., 2004). However, after this initial impairment, long-term effects of corticosteroids were found to increase PFC function and improve working memory in rats (Yuen et al., 2009).

Stress effects on decision-making

The neural basis of decision-making and the effect of stress on behaviour have largely been studied by independent research lines. Yet, these lines of work clearly suggest that there is overlap in the neural circuits active during both stress and decision-making (Silvetti et al., 2018; Valentino & Bockstaele, 2008; Gathmann et al., 2014), especially in the dACC, DLPFC, and MPFC. It was also found that these catecholamines are involved in both stress and effort-based decision-making (Ironside et al., 2018); stress increases DA and NA production
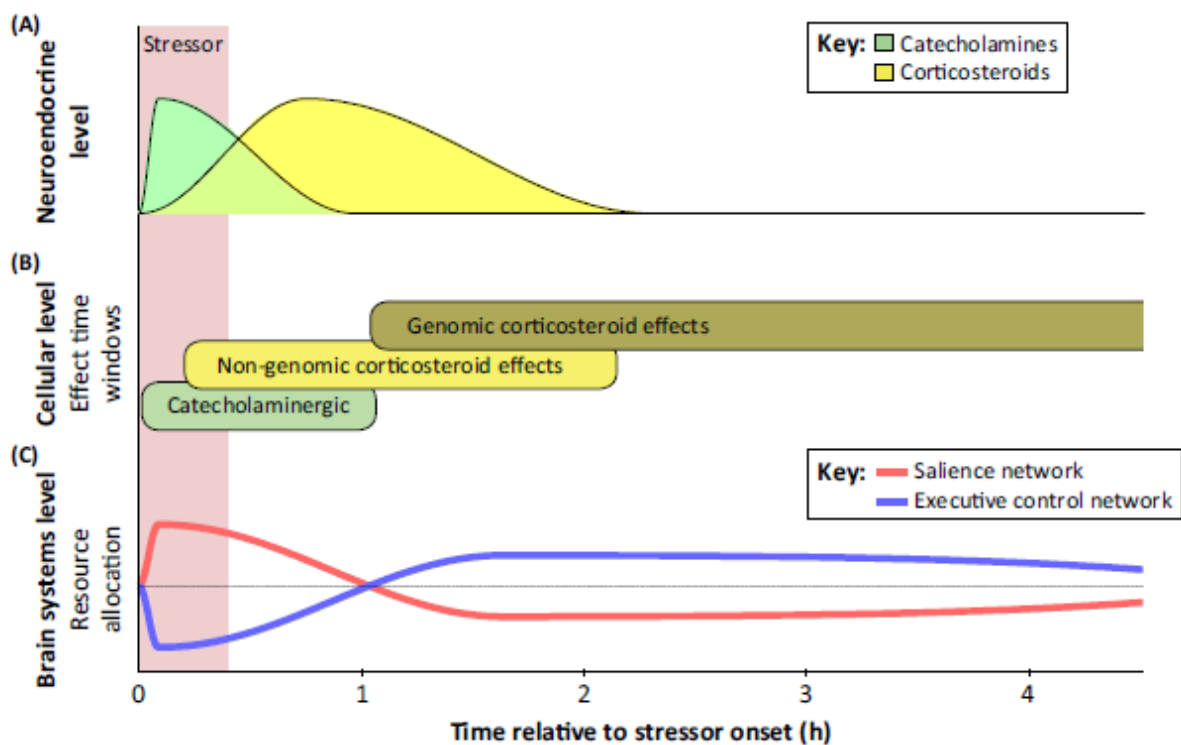
Figure 1. The early and late stress response. A. The stress response on the neuroendocrine level. At stress onset, an increase in catecholamines can be observed, which gradually decreases, and stops 30 - 60 minutes after stress onset. Meanwhile, an increase in corticosteroid levels be observed. B. The effects on the cellular level. In the early stress response, a catecholaminergic effect can be observed, until 30 - 60 minutes after stress onset. Afterwards, the non-genomic effects of corticosteroids start. Finally, the genomic effects of corticosteroids can be seen. C. The effect of stress on the brain systems level. We can see that directly after stress, there is a boost of the salience network (SN), while the resources allocated towards the executive control network (ECN) decrease. After the initial stress response, this effect switches around, causing an increase in resource allocation in the ECN and a decrease in resource allocation in the SN. Figure taken from Hermans et al. (2014).

which both have an influence on decision-making. Interestingly, effects of stress on some types of decision-making were found. For example, stress tends to drive humans towards habitual decisions, and away from goal-directed behaviour (Schwabe & Wolf, 2009). Additionally, a review by Starcke & Brand (2012) suggests that acute stress has a task-specific effect on reward perception and impairs decision strategy selection by stopping the search for alternatives early. Furthermore, acute stress increases risk-seeking behaviour in ambiguous tasks. More specifically, stressed participants are drawn to riskier high-reward choices even when such choices are not optimal (Starcke & Brand, 2016).

Moreover, it has been shown that stress influences motivation via the VTA in rats (Hollon, Burgeno, & Phillips, 2015; Tye et al., 2012) by causing insensitivity to reward and an increase in avoiding effort. Additionally, chronic stress was found to increase anhedonia (Tye et al., 2012; Willner, Towell, Sampson, Sophokleous, & Muscat, 1987). Finally, loss of motivation is one of the hallmarks of several stress-related disorders, including burnout and PTSD (Husain & Roiser, 2018; Lyndon et al., 2017). Overall, these findings indicate that stress might influence reward perception, and hence potentially impair the willingness to exert effort for reward.

Aim of this study

Although several research lines state that stress may affect the willingness to engage in effort and the neural systems implicated in effort-based decision-making, these mechanisms remain poorly understood. Thus, the aim of this study was to further elucidate the effect of stress on effort-based decision-making in healthy humans. It was hypothesised that acute stress influences effort-based decision-making, particularly by decreasing the willingness to engage in mental effort. This reduction may be driven by either an increase in the avoidance of effort, or a decrease in reward sensitivity. Furthermore, it was hypothesised that this effect of stress is linked to alterations in prefrontal activity, especially in the MPFC and DLPFC. Furthermore, as studies in

humans have measured pupil dilation as a proxy for noradrenergic release (Gilzenrat, Nieuwenhuis, Jepma, & Cohen, 2010; Silvetti et al. ,2013b) and pupil dilation is shown to track the optimization of decision-making in volatile environments (Silvetti et al., 2013b), pupil changes were hypothesised to track effort and the impact of stress as a proxy for putatively increased noradrenergic release.

To test these hypotheses, participants performed an effort-based decision-making task in the magnetic resonance imaging (MRI) scanner; once during a control condition, and once while under acute stress. Acute stress was experimentally induced using the socially evaluated cold pressor task (SECPT) (Schwabe, Haddad, & Schachinger, 2008). During the task, participants were offered the choice to engage in calculations of varying difficulty levels for either small or large rewards. The participants did not perform these calculations until after the MRI scan. Additionally, participants performed calculations in the scanner. These are independent of their choices, in order to dissociate decision-related from performance-related activity. This was done in order to measure their accuracy and the stress effects on working memory. Neural activity was examined at the whole-brain level. Furthermore, two different region-of-interest (ROI) analyses were conducted. One was performed based on an a-priori region-of-interest of the MPFC based on previous literature on effort-based decision-making, and another one using prefrontal regions and the insula (as part of the SN, to do a preliminary analysis of the effect of stress on a network level) based on activity variation with effort recorded during the calculation task.

The results of this study could help clarify the interactions between stress and effort-based decision-making. Specifically, knowledge on how stress influences effort-based decision-making might help in alleviating problems found in patients with stress-related disorders in which motivation is changed, such as burnout and PTSD. Knowledge on the neural mechanisms of the stress effect during motivation might open up another way to improve treatments for these patients. Finally, investigating how stress and effort influence pupil size, as a proxy for noradrenergic release, could provide insights

into the way stress and effort interact with noradrenaline.

Methods

Participants

According to a power analysis performed prior to starting the study, the planned sample size was 35 participants. However, due to the Covid-19 pandemic lockdown, data collection was suspended. Hence, this thesis will only include preliminary analysis on the data from the participants gathered up until the lockdown came into effect. A within-subjects crossover study was performed with 26 participants (age 18-40, mean age 24.5, all right handed, 13 female). Participants were recruited through the SONA recruitment system of the Radboud University, as well as through social media and advertisement. Each participant signed an informed consent form before participating in the study. The study was conducted under the local ethical committee approval (CMO2014/288) and approved by the Donders Centre for Cognitive Neuroimaging. Each participant filled in a safety form before entering the MRI, to exclude participants with metal implants or medical conditions incompatible with entering the scanner. We excluded participants if they were colourblind or had a history of psychiatric disorders or brain

surgery. Females were excluded if they used hormonal contraceptives, as this was found to influence stress responsiveness (Kirschbaum, Kudielka, Gaab, Schommer, & Hellhammer, 1999), and only included if they were in the luteal phase of their cycle during the sessions when they performed the task. Each participant received monetary compensation of 64 euros for their participation, with an additional monetary bonus between 0 and 20 euros depending on their performance. Of these 26 participants, the MRI data from two participants could not be analysed correctly due to a realignment problem for these participants. Additionally, one participant was excluded from the analysis, after reporting that they did not understand the task correctly during their final session.

Design

In this experiment, each participant performed three sessions: one training session, one stress session and one control session. The first session was always the training session. The order of the control and stress session (2nd or 3rd) was counterbalanced across participants.

During the first session, the participants started by filling in the questionnaires (for more detailed information about the questionnaires, see the questionnaire section below), and subsequently completed a training task which included calculations of similar difficulty as the calculations to be performed
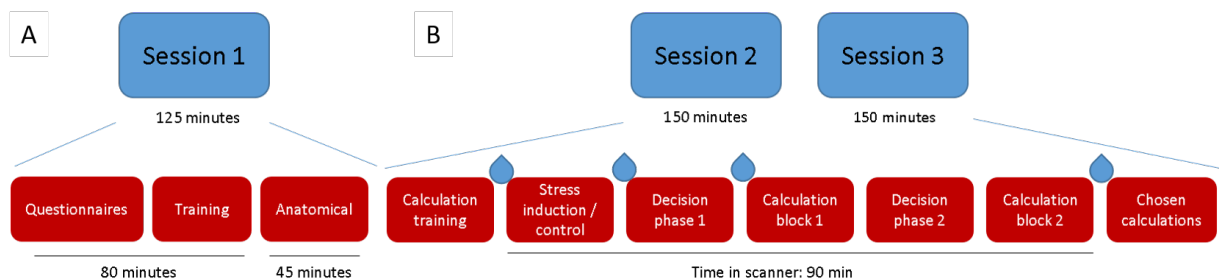
Figure 2. The layout of the different sessions. A. The lay-out of session one. This session started with questionnaires and training calculations. Then, there was a short anatomical scan of 45 minutes. B. The lay-out of sessions two and three. These sessions started with a short calculation training, taking 30 minutes. Then, the participant was set up in the scanner. Next the stress procedure (in the stress session) or control procedure (in the control session) was conducted. After this, four task blocks were performed. Finally, the participant performed the chosen calculations outside of the scanner. During these sessions, saliva was measured at four time points, shown as drops in the figure. The first sample was acquired before the stress or control procedure (t = 0), the second after the stress or control procedure (t = 15). The third sample was acquired after the first decision phase (t = 30). The final sample was acquired at the end of the final task block (t = 75).

in subsequent phases. The goal of this task was to let participants practice calculations to avoid training effects later on. Finally, the participants underwent three anatomical MRI scans. See Figure 2A for an overview of the first session.

During the stress session, the participants started with a short calculation training in order to minimize the training effect during the experiment. The participants were set up in the scanner and acute stress was induced using the SECPT (detailed in the stress and control procedure section below). Afterwards, the participants performed the experimental tasks in the scanner. These consisted of two tasks, a decision-making task and a calculation task. Each task consisted of two blocks. During the procedure, saliva samples were collected to obtain cortisol measures as an indication of stress levels (see the saliva sampling section below for details). When the participants finished these tasks, they performed a final task outside the scanner and received a reward. During this session, the participants filled in an adapted version of the short Profile of Mood States questionnaire (POMS) (Shacham, 1983) three times in order to record subjective experience of stress and its effects on mood and energy levels. This happened once before the stress induction, once after the stress induction, and once after coming out of the scanner. See Figure 2B for an overview of the stress session.

During the control session, the participants underwent the same procedure as during the stress session, but with one difference. Instead of the stress induction using the SECPT, a control procedure was implemented. See Figure 2B for an overview.

Session scheduling

In order to minimize stress effects due to entering the MRI scanner or participating in a study, the scheduling of the sessions followed some criteria. We tried to minimize the unintended stress experienced by the participants when entering the MRI scanner by scheduling the second session to take place at most 10 days after the first session. Furthermore, the third session was scheduled to take place between 6 and 10 days after the second session. Both the second and the third session were required to take place at

the same time of the day, and were scheduled to start between 12:00 and 16:30. This was done to limit the influence of time of day which could affect cortisol levels. For female participants, the second and third session were scheduled during the luteal phase of their cycle, in order to prevent hormonal influences (Kirschbaum et al., 1999).

Questionnaires

During the first session, the participant filled out eight different questionnaires: the Apathy Motivation Index (AMI), the Snaith-Hamilton Pleasure Scale (SHAPS), the Need for Cognition questionnaire, the Multidimensional Fatigue inventory (MFI), Beck's Depression Inventory (BDI-II), the behavioural inhibition/avoidance scale (BIS/BAS), the Symptom Checklist 90 (SCL-90), and a 60-item version of the International Personality Item Pool (IPIP-NEO-60). This thesis was part of a larger study and the questionnaire data will not be analysed in this thesis, except for some data of the POMS questionnaire.

The AMI was used to measure apathy and motivation (Ang, Lockwood, Apps, Muhammed, & Husain, 2017). It measures three different factors: behavioural activation, social motivation, and emotional sensitivity. Additionally, the SHAPS was used to measure anhedonia and hedonia (Snaith et al., 1995). Furthermore, the tendency and enjoyment in thinking was measured using the Need for Cognition questionnaire (Cacioppo & Petty, 1982). Then, we used the MFI to measure different types of fatigue: general, physical, and mental fatigue, reduced motivation and reduced activity (Smets, Garssen, Bonke, & De Haes, 1995). Furthermore, the BDI-II was used to measure the severity of depression in participants (Beck, Steer, Ball, & Ranieri, 1996). The BIS/BAS scale differentiates between behavioural inhibition or punishment sensitivity and behavioural avoidance. In this questionnaire, behavioural avoidance is split up in four different subscales: pursuit of goals, desire for new rewards, and response to reward (Carver & White, 1994).

The SCL-90 was used to assess nine subscales – somatization, obsessive-compulsive behaviour, interpersonal sensitivity, depression, anxiety, hostility, phobic anxiety,

paranoid ideation, and psychoticism - in the past week (Blaszczynski & McConaghy, 1988). The IPIP-NEO-60 was used to measure five scales: neuroticism, extraversion, agreeableness, conscientiousness, and openness. Each of these scales consists of six subscales (Maples-Keller et al., 2017).

In order to assess their subjective stress, the participants filled in the adapted POMS questionnaire three times in both sessions: once before entering the scanner, once after the stress or control procedure (during the acquiring of the saliva sample), and once after the fourth block when they left the scanner. This questionnaire measures five distinct scales: anger, depression, fatigue, vigour, and tension-anxiety. The POMS questionnaire is scored on a scale from 0 to 4.

Saliva collection and analysis

To measure the objective stress, four saliva samples were collected in both the stress and control sessions. The first sample was collected right before the stress or control procedure (t = 0 min). The second sample was

collected after the stress or control procedure (t = 15 min). The third sample was collected after block one (t = 30 min). The fourth sample was collected after block four (t = 75 min). See Figure 2B for an overview. Analysis of the cortisol and alpha-amylase levels in the saliva samples was performed according to Rohleder et al. (2006). This analysis was performed by the lab of Dr. C. Kirschbaum at the Technical University of Dresden.

Scanner preparation

During the MRI scanning of the stress and control sessions, a series of physiological measures and eye-tracking were recorded. An amplifier (brainamp ExG MR) from Brainproducts was used to measure heart rate, respiration and skin conductance. Heart rate was measured using a clip (Blood Pulse Sensor; Brainproducts) attached to the ring finger of the left hand of the participant. A glove was used to keep the hand of the participant warm. For the respiration, a belt with a sensor (Respiration Belt MR; Brainproducts) was attached around the waist of
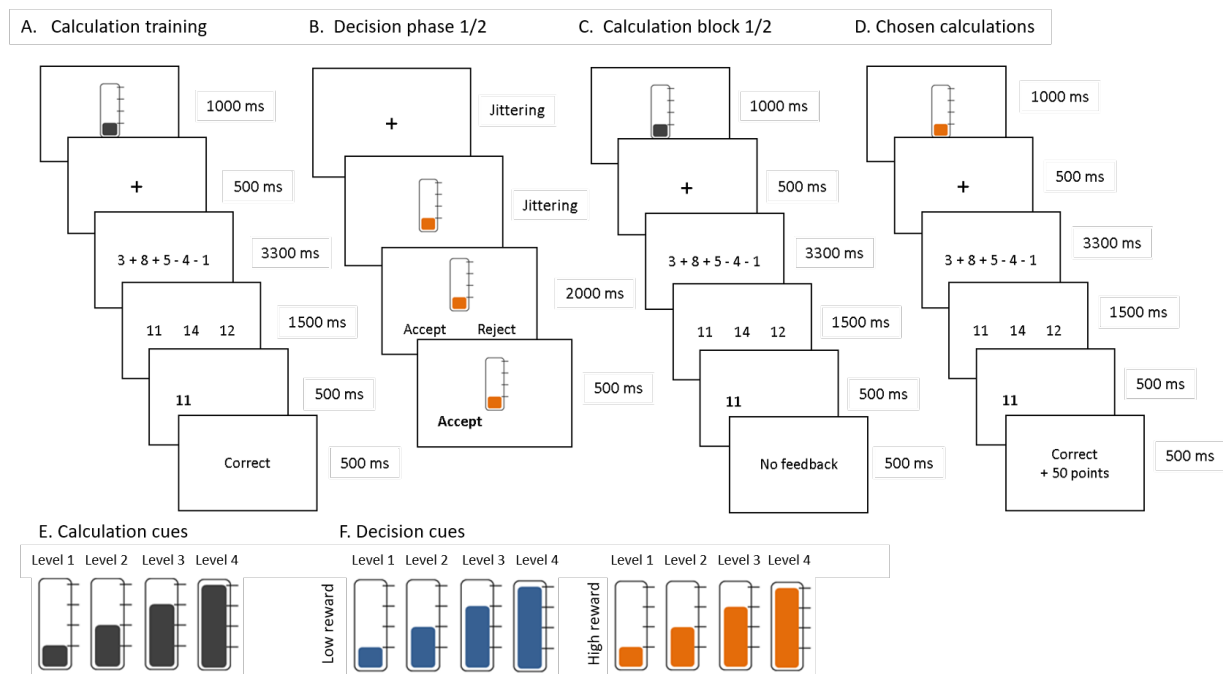
Figure 3. The layout of the tasks. A. The training done in the first session, and at the start of the second and third session. B. The first and second choice blocks inside the scanner during the second and third sessions. C. The calculation blocks inside the scanner during the second and third sessions. D. The calculations during the final part of the second and third sessions; these were done outside of the scanner. E. The cues shown during the calculation blocks. The levels indicate the difficulty of the upcoming calculation. F. The cues shown during the decision blocks. Blue coloured cues indicate that, when participants accept the calculation and answer correctly, they will receive a low reward, while orange coloured cues indicate a high reward.

the participant. In order to measure the skin conductance, two electrodes (B18-MR2-LSR-1A20g/AgCl Sintered Multitrode with 6 mm opening, MR Adapted) were attached to the index and middle finger of the left hand of the participant using conductive gel. The data was recorded using Brainvision recorder. Furthermore, pupil size was recorded during the task using the 'Eyelink 1000' (version 1.5.0, Eyelink). During the pupil size recordings, the lights in the scanner room were turned off.

Stress and control procedure

Acute stress was induced using an adapted version of the SECPT procedure (Schwabe et al., 2008), named alpha-SECPT. For this procedure, a researcher entered the room whom the participant had not seen before, wearing gloves and a lab coat. The procedure started with the participant putting their foot in a bucket of ice water (2 °C) for three minutes. The participant was instructed not to move or speak and to keep looking towards the ceiling throughout the procedure. The participant was informed that they could take their foot out, but only if it became truly unbearable. The researcher remained in the room looking at the participant the whole time. During the second part of the procedure, the participant was asked to recite the alphabet, alternating from going backwards and forwards, one letter at a time (i.e., z, a, y, b, x, c etc.). During this procedure, the same researcher as before was present, who told the participant to speed up if they took too long before answering, or start over if they were incorrect. The participant performed this task for three minutes. Afterwards, the researcher said that the task was over and acquired the second saliva sample.

The control procedure also consisted of two parts. An experimenter whom the participant had previously met entered the room and started putting the foot of the participant in a bucket of room temperature water (25 °C) for three minutes. Then, the participant was asked to normally recite the alphabet a few times. Any mistakes made during this task were ignored by the experimenter. After three minutes, the researcher told the participant that the task was over and took the second saliva sample.

Experimental tasks

Participants performed a calculation training task at the beginning of each session (outside the scanner; days 1, 2, and 3), a decision-making task (in the scanner; two blocks on day 2 and 3), a calculation reminder task (in the scanner; two blocks on day 2 and 3), and a final calculation task (outside the scanner; day 2 and 3). Each calculation consisted of four subsequent additions or subtractions. Difficulty of each calculation was manipulated by varying the amount of carrying or borrowing needed (one carrying/borrowing = difficulty level one, four carrying/borrowing needed = difficulty level four). For example, a level three difficulty calculation could look like '6-1+7-8+9'. This method has proven effective in earlier studies (Vassena et al. 2019, Vassena et al. 2014). All tasks are displayed in Figure 3.

Calculation training task

The calculation training (Fig. 3A) consisted of 100 trials and took around 20 minutes. Each training trial started with the fixation cross. Then, an indicator of the difficulty appeared on the screen in the form of a thermometer, with four possible levels (see Fig. 3E for an overview of the used cues). The participant was instructed that the more the thermometer was filled, the more difficult the following calculation would be. This thermometer was displayed for 1 second. Then, the fixation cross was displayed for 500 ms. Thereafter, the calculation was shown for 3300 ms. Following this, the calculation was replaced by three possible answers. The participant had 1500 ms to choose one of the answers. After they responded, or after 1500 ms passed, feedback was provided. After 500 ms, the next trial began.

Scanner task

During both the stress and control sessions (day 2 and 3), the participants performed four blocks in total: two blocks of the decision-making task, alternating with two blocks of the calculation reminder task. The decision-making task measured effort-based decision-making. The calculation reminder task measured the potential effect of stress

on accuracy. This task was named 'calculation reminder' as the participants were told that the purpose was to remind them of the meaning of each difficulty level.

Each session started with a calculation training. Decisions (Fig. 3B) and calculations (Fig. 3C) were presented afterwards. The choices started with a fixation cross for a jittered time (3-5 seconds, average 4 seconds), followed by a cue that appeared on the screen for a jittered time (3-5 seconds, average 4 seconds). This cue was either an orange thermometer, indicating a high reward (50 points), or a blue thermometer, indicating a low reward (40 points). As in the training, the more the thermometer was filled, the more difficult the calculation would be (see Fig. 3F for an overview of the different cues). The participants were instructed beforehand on the meaning of these cues. Then, the words 'accept' and 'reject' appeared on the screen for 2000 ms, or until the participant selected one of them. 'Accept' was displayed half of the time on the right and half of the time on the left side. Participants were instructed to accept trials that they considered worth the effort based on the promised reward. They were told that half of their choices would randomly be selected and that they would receive those trials to perform at the end of the session outside of the scanner. They would only receive the corresponding reward if the calculation was performed correctly during this final phase at the end of the session. If the participant rejected the trial, they would get a very easy calculation instead, but receive only 30 points if they answered the calculation correctly. The points were converted to a monetary bonus reward at the end of the experiment. Their choice remained on the screen for 500 ms, or they received feedback if they were too late. Then, the next trial started. If they were too late, the trial was appended to the end of the block.

The calculation trials also started with a fixation cross for 500 ms. Then, the thermometer was displayed for 1000 ms, followed by a fixation cross, that appeared on the screen for 500 ms. After that, the calculation appeared on the screen. After 3300 ms, three possible answers were displayed. They had 1500 ms to choose one of the answers. Afterwards, they received either no feedback,

or the message 'too late' if they were too late for 1000 ms.

Chosen calculations

After the decision-making task and the calculation reminder task in the scanner, the participant performed the chosen calculations (Fig. 3D). These were presented to the participant in the same way as the practice calculations from phase one, except that the provided feedback was not only 'correct' or 'incorrect', but also stated the amount of points received. Half of the trials from the decision-making block were randomly selected. For each of these trials, if they were accepted, the participant got a calculation of the shown difficulty, and received the shown reward if they responded correctly. If they responded incorrectly, no reward was received. If the participants rejected the calculation, a very easy calculation (e.g., '2+0+0+0+0') was presented. Upon correctly answering this calculation, the participant got 30 points. The participant was not aware of the exact value of one point in money, but they were told they could receive a maximum of 20 euros as a bonus for their performance.

Data analysis

This thesis focused on a subset of the collected data. Heart rate was analysed to ensure that the stress induction was successful. Behavioural data were analysed to test for behavioural effects of stress on effort-based decision-making. Furthermore, the eye-tracking data during the task were analysed as a putative index of NA release. Functional magnetic resonance imaging (fMRI) data were analysed to investigate the role of prefrontal cortex in effort-based decision-making under stress. This was done by examining the effect of effort and reward at the whole brain level during decision-making under control as compared to stress. Further, we extracted neural activity from a-priori defined ROIs of MPFC and DLPFC. Two ROI analyses were reported. The first analysis used functional ROIs based on the neural activity during the calculation reminder task, and specifically used the activity during the effort coding contrast (see the ROI section below for details) to test for the effect of stress

during decisions. The second analysis used an ROI based on previous studies of effort-based decision-making to test the effect of stress during both decision and calculation performance.

Heart rate analysis

To test the effectiveness of the stress induction, the heart rate of the participants was measured during scanning. These data were preprocessed using the Matlab toolbox Brainvisioncoverter. Afterwards, HERA (a Matlab toolbox) was used to calculate the interbeat intervals (IBI) for all participants. The visual artefact removal function of this toolbox was used to remove all artefacts where the heart rate could not be reliably measured. Then, the markers for the trials were added to these IBIs using the onsets generated for the MRI analysis. As previous research showed that stress causes an increase in heart rate, and therefore a decrease in IBI as well as a decrease in heart rate variability (Shapiro et al., 2000), three measures of interest were used to test the effectiveness of stress induction.

First, the first block after either stress induction or control was analysed by itself. These blocks were divided into four intervals of equal length. The average IBI was calculated on all of these intervals, for both stress and control. An analysis of variance (ANOVA) on the average IBI was conducted, with the main factors session type (stress or control) and interval (first, second, third or final part of the block), using session order (stress first or control first) as a between-subjects measure. Second, heart rate variability was measured. This was done by calculating the root mean square of successive IBI differences (RMSSD) on each interval. This measure calculates the mean square differences of successive IBIs, and takes the square root of this value. An ANOVA on these data was performed, with the main factors session type and interval, using session order as a between-subjects measure. Third, the average IBI was calculated from the moment the cue appeared on the screen until three seconds after the trial started. This was done for every different trial, both during the decision-making trials and the calculation trials.

Two ANOVAs were performed on the trial-by-trial IBI to determine possible effects of stress, effort, and reward on the heart rate during the task: one on the decision-making trials and one on the calculation trials. The ANOVA on the decision-making trials examined the following factors: session type (stress or control), block (one or two), effort level (very easy, easy, hard, very hard), and reward level (low reward, high reward). Session order (stress first or control first) was used as a between-subjects factor in this ANOVA. The ANOVA on the calculation trials had the following factors: session type (stress or control), block (one or two), effort level (very easy, easy, hard, very hard). Session order (stress first, control first) was also used as a between-subjects factor in this ANOVA. Post-hoc analysis was done on significant results using Bonferroni-correction. In t-tests, Cohen's d was used as a measure for effect size. In ANOVAs, partial η^2 was used as a measure for effect size.

Behavioural data analysis

Willingness to engage in effort was measured through acceptance rate at the decision-making task. Reaction times of the decisions were also recorded. The effect of stress on the ability to perform the task was measured during the calculation task for which accuracy and reaction times were recorded. Because the decisions and accuracy are dichotomous variables (accept/reject, correct/incorrect), generalized linear mixed models (GLMM) using a binomial family and logit link function were performed on this data using R (version 3.5.2) and the lme4 package (Bates, Mächler, Bolker, & Walker, 2015). Three different optimizers were used, 'bobyqa', 'Nelder Mead', and 'optimx', in order to reduce convergence problems. Results of any of these optimizers that find no convergence issues were reported. Reaction times were first transformed by the function log(1/x) to decrease violations of the normality assumption (normality was checked for the averages per condition with the Shapiro test, and normality for the choices (statistic = 0.997, p = .18) was found. Additionally, near normality for calculations (statistic = 0.991, p = .01) was found). Although this was not completely normally distributed, the transformation was an improvement over

using the regular mean for the calculation trials (statistic = 0.983, p < .001). Afterwards, a linear mixed model (LMM) was used to test for significance. Furthermore, to test whether this effect was influenced by other factors, the analyses were repeated including different covariates. The covariates of interest were task proficiency, subjective stress and objective stress.

Task proficiency was measured using the average accuracy on the training trials of all three days for each participant. Covariates for subjective and objective stress were included to take inter-individual variability in subjective stress experience and objective stress into account. Subjective stress was measured using the difference in tension and depression scores from the POMS after stress and control. Objective stress was supposed to be measured using salivary cortisol. However, due to the Covid-19 lockdown, it became impossible to further analyse the collected samples. As of the moment of writing this thesis, only the saliva samples for 12 participants have been analysed. Therefore, it was decided to not include the cortisol analysis in this thesis, and include the heart rate during the first block of task post-stress induction as a plausible physiological index of the individual stress levels.

The GLMMs for the decision-making data included effort level, reward level, session type, their interactions, block and the covariate as fixed effects. First, a model containing a random slope and intercept for all fixed variables was used (as recommended by Barr, Levy, Scheepers, & Tily, 2013). If this model did not converge, only a random slope for effort level, reward level, and session type was included in order to reduce the complexity of the model. Subject number was also included as a random factor. Finally, a model containing all covariates was run. In order to measure effect sizes for the GLMMs, the log odds ratio (LO) was reported.

The GLMMs for the calculation task used effort level, block, session type, effort level x session type, and the covariate as fixed variables. First, a model containing both random slope and intercept for all fixed variables was used. In case of non-convergence, a model only containing random slope for effort level, session type, and the covariate was included. Subject number

was also included as a random factor.

Pupil size analysis

In order to assess putative noradrenergic levels, pupil size was measured. Eye-tracking data were analysed using a custom Python script (Python version 2.7). First, the average pupil size was extracted for each trial (starting from the moment the thermometer appeared until a response was given). Eye blinks were excluded. These values were z-scored to the data from the same block type (i.e. calculations or decision-making). Data were exported to SPSS where two ANOVAs were conducted. The first ANOVA was done on the calculation task, containing session type, effort level and block as within-subjects factors, and session order as between-subjects factor. The second ANOVA was calculated on the decision-making data, using session type, effort level, reward level, and block as within-subjects factors, and session order as between-subjects factor.

MRI data collection and preprocessing

Functional MRI data was acquired on two 3T Siemens MRI scanners (Prisma and Prismafit), located on the same site and using identical sequences. In the first session, a standard MPRAGE anatomical scan was collected using a 32-channel head coil. This yielded 224 slices (voxel size: 0.8x0.8x0.8 mm, FoV = 256 mm, TR = 2200 ms, TE = 2.64 ms, flip angle: 11 degrees). After this, an interleaved gradient echo scan was conducted to measure the VTA, giving 176 slices (voxel size: 0.8x0.8x0.8 mm, FoV = 230 mm, TR = 46.00 ms, TE = 6; 14.1; 22,2; 30,3; 10.05; 18.15; 26.25; 34.35, flip angle: 20 degrees, centred at L = 0, A = 15, H = 4). Additionally, two different echo planar imaging scans were used to acquire data from the LC. This scan was centred on the LC position found in the anatomical scan (default: R = 0.1, P = 1.2, F = 32.9 mm) and rotated so that the scan was perpendicular to the fourth ventricle. One scan yielded 16 slices (voxel size: 0.2, 0.2, 3.0 mm, slice thickness: 3.0 mm, FoV = 220 mm, TR = 1870 ms, TE = 12 ms, flip angle = 120 degrees). The second scan was the same, except for the location, which was 1.5 mm above the first scan. These two scans were alternated three times each,

for a total of six scans. These scans together took about 45 minutes.

During the stress and control sessions, functional images were acquired. Two decision-making and calculation runs were performed. The decision-making runs gave 66 slices per scan, with about 790 scans per block (voxel size: 2.0x2.0x2.0 mm, FoV = 210 mm, TR = 1000 ms, TE = 34.00 ms, flip angle: 60 degrees). Calculation runs gave 66 slices per scan, with about 450 scans per block (voxel size: 2.0x2.0x2.0 mm, FoV = 210 mm, TR = 1000 ms, TE = 34.00 ms, flip angle: 60 degrees). All functional runs were interleaved multi-band, with multi-band factor 6.

In order to reach steady state magnetisation, the start of the task was synced with the fifth volume. Hence, the first four volumes were discarded in the analysis. The data was preprocessed using fMRIprep (version 20.0.6, Esteban et al. 2018), using Nipype (version 1.4.2, Gorgolewski et al., 2011). Here, the anatomical data is preprocessed using skull stripping, and segmented to create a brain mask (Zhang et al. 2001). These data were then normalized. The functional data was co-registered to this anatomical data. Head-motion parameters were estimated using FSL (version 5.0.9, mcflirt, as described by Jenkinson et al. 2002). On the preprocessed images, smoothing and AROMA (Pruim et al. 2015) were applied. Images with a high framewise displacement (FD) or DVARS value (as described by Power et al. (2014)) were marked as motion outliers (i.e. with an FD larger than 0.5, or DVARS larger than 1.5). Due to the low TR of the sequence, no slice time correction was applied. For more details on fMRIprep, see the supplementary methods (available online).

fMRI analysis

The fMRI data were analysed using a general linear model (GLM) approach. Two first-level GLMs were generated (one for the decision-making and one for the calculation blocks). The decision-making GLM contained eight event-related regressors per block; one for each different effort by reward combinations, an additional three regressors to measure the responses, one for the right button, one for the left button, and one for a late response. In the calculation GLM, six different regressors

were measured per block; one for each of the four different difficulty levels, one for incorrect trials, and one for responses that were too late. In both analyses, the trials that were too late were modelled as noise in a separate regressor.

At the second level, parametric effort contrasts (very easy: -1.5, easy: -0.5, hard: 0.5, very hard: 1.5), quadratic effort contrasts (very easy and very hard: -1, easy and hard: 1), and a low versus high effort contrast (very easy and easy: 1, hard and very hard: -1) were made for the decision-making data. Furthermore, reverse contrasts were made for each of these contrasts by multiplying the contrasts with -1. Additionally, a contrast was made for high versus low reward in order to identify reward-related regions in the decision-making data. To investigate the effect of stress, each of the contrasts in the control condition was compared to the stress condition (both stress > control and control > stress). A voxel level threshold of p = .001 (uncorrected) was applied with a cluster-level Family Wise Error (FWE) correction for multiple comparison of p = .05. For the calculation analysis, the same effort contrasts were made using the same thresholds.

For the Region-of-Interest (ROI) approach, we performed two analyses. For the first analysis, we selected clusters that encode effort during the calculation reminder task. This was done by testing which regions are more active with increased effort during the calculation reminder task. Regions in the MPFC (including dACC) and DLPFC are of interest here, as they are known to have a role in effort-based decision-making (Vassena et al., 2017; Asci et al., 2019; Porter et al., 2019). Furthermore, to do a preliminary analysis of the effects of stress on the SN, we also selected clusters from the insula for the ROI analysis. The ROIs obtained from the calculation reminder task were then used to extract neural activity during the decision-making task (avoiding circularity of inference).

The second analysis was aimed at testing activity under stress in both the decision-making and calculation phase. Hence, we selected an a-priori ROI of the MPFC based on previous studies on effort coding (Botvinick, Huffstetler, & McGuire, 2009; Bush et al., 2001), and completely contained the dACC part of the FIND template (Shirer,

Ryali, Rykhlevskaia, Menon, & Greicius, 2011). The ROI used for the MPFC was centred on the MNI coordinates (2, 21, 40). All ROIs were defined as a sphere with an 8 mm radius centred around the peak voxel of the observed cluster. For these ROIs, percent signal change was extracted using the MARSBAR toolbox (Brett et al., 2002) for each separate regressor in the decision-making analysis. Percent signal change scores per condition were subjected to an ANOVA to analyse the effects of effort, reward, block, session order and session type on the activation of these ROIs.

Results

Heart rate analysis

The data from three participants were excluded due to excessive noise and poor data quality, which made the analysis not possible. The final sample for the RMSSD and first block IBI included 22 participants. The ANOVA on the first block RMSSD yielded a significant main effect of time after onset ($F(2.19, 43.73)$ = 10.23, partial η^2 = .34, p < .001), which can

be explained by a decrease in RMSSD after the first quarter of block one (p-hoc t-tests: 1 > 2: $T(21)$ = 4.82, Cohen's d = 0.57, p < .001; 1 > 3: $T(21)$ = 3.77, Cohen's d = 0.55, p = .001; 1 > 4: $T(21)$ = 2.36, Cohen's d = 0.32, p = .03; 4 > 2: $T(21)$ = 2.53, Cohen's d = 0.26, p = .02; 4 > 3: $T(21)$ = 2.18, Cohen's d = 0.23, p = .04, Fig. 4A). There was a significant effect of session order ($F(1, 20)$ = 5.10, partial η^2 = .20, p = .04), indicating that the heart rate variability was higher for participants that had the control session first. Contrary to what was expected, no significant main effect of session type was observed ($F(1, 20)$ = 3.18, partial η^2 = .14, p = .09), although we found a trend toward lower RMSSD in the stress session. There was a significant interaction effect of session type x session order ($F(1, 20)$= 5.45, partial η^2 = .21, p = .03), but post-hoc t-tests did not reveal any significant effects. However, we observed a trend for a decrease in RMSSD for the second and third quarter of the first block for the participants that had the stress session first compared to the participants that started with the control session. The time after onset x session type x session order interaction ($F(1.83, 36.54)$ = 4.15, partial η^2=.17, p = .03)
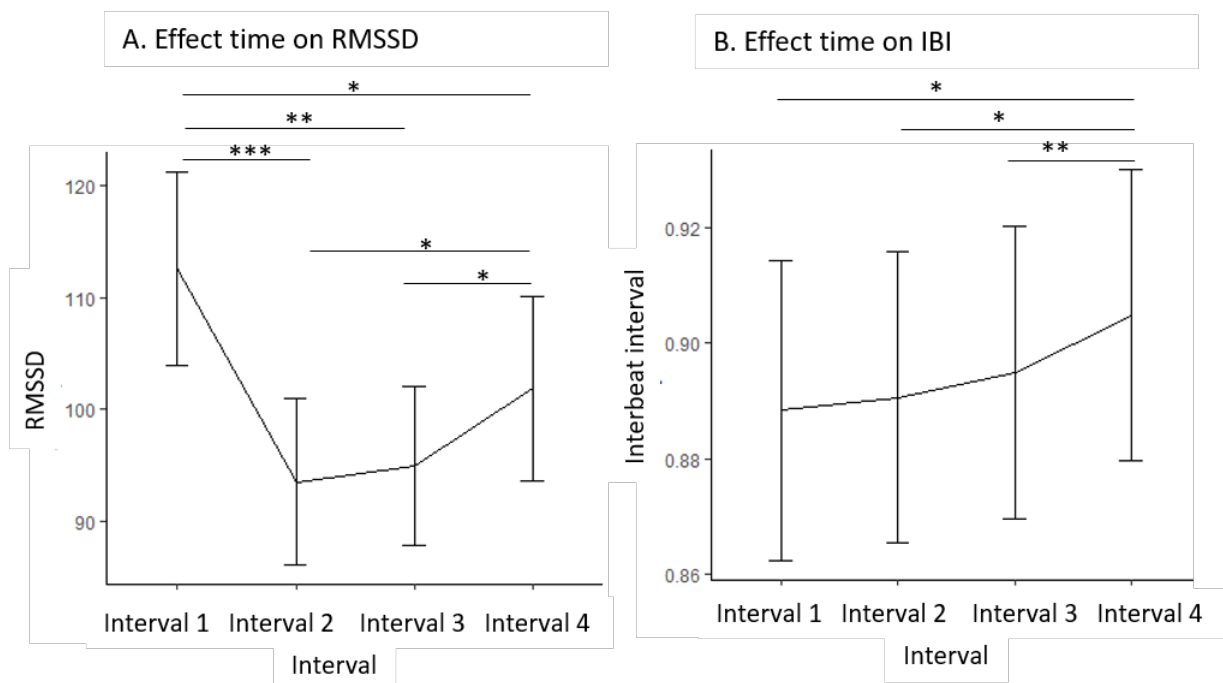
Figure 4. A. The effect of time on the root mean square of successive IBI differences (RMSSD). The first block has been divided into four equally long intervals. During the first interval, the RMSSD was significantly higher than during the other three intervals. During the fourth interval, the RMSSD was significantly higher compared to intervals two and three. B. Effect of time on the interbeat interval. The interbeat interval during the final interval was significantly higher compared to the other three intervals. * p < .05, ** p < .01, *** p < .001.

was also significant. A post-hoc t-test on the interactions found a significantly lower RMSSD in stress, for participants that started with the control condition, for the first interval ($T(11)$ = -2.90, Cohen's d = -0.74, p = .01) and fourth interval ($T(11)$ = -2.61, Cohen's d = -0.85, p = .02). A trend for lower RMSSD in stress was found in the second interval ($T(11)$ = -2.05, Cohen's d = -0.58, p = .07).

The analysis of the IBI yielded a significant main effect of time after onset ($F(1.69, 33.84)$ = 4.92, partial η^2 = 0.20, p = .02, Fig. 4B), giving a lower average heart rate at the final interval compared to the other intervals (4 < 1; $T(21)$ = 2.92, Cohen's d = 0.15, p = .008, 4 < 2; $T(21)$ = 3.75, Cohen's d = 0.13, p = .001, 4 < 3; $T(21)$ = 4.41, Cohen's d = 0.09, p = < .001). The interaction between time after onset x session type ($F(2.16, 43.26)$ = 4.93, partial η^2 = .20, p = .01), and time after onset x session type x session order was also significant ($F(2.16, 43.26)$ = 5.58, partial η^2 = .22, p = .006). However, post-hoc analyses found no significant differences between stress and control for constant time after onset and session order.

The ANOVA on the average IBI during each decision-making trial found a main effect of block ($F(1, 20)$ = 8.29, partial η^2 = .29, p = .009), indicating a higher heart rate in the first block compared to the second. A significant interaction effect of effort x block x reward was also found ($F(3, 60)$ = 2.97, partial η^2 = .13, p = .03). Post-hoc analysis found a significant higher IBI in block two compared to one in the low reward condition, for very easy ($T(21)$ = 3.73, Cohen's d = 0.26, p = .001), easy ($T(21)$ = 2.36, Cohen's d = 0.17, p = .03), and very hard ($T(21)$ = 2.45, Cohen's d = 0.20, p = .02) trials, and in the high reward condition for hard trials ($T(21)$ = 3.68, Cohen's d = 0.26, p = .001). Furthermore, a higher IBI for high reward compared to low reward in the very hard trials of the first block was found ($T(21)$ = -2.49, Cohen's d = -0.10, p = .02). Additionally, an effect of type x block x effort was found ($F(3, 60)$ = 2.86, partial η^2 = .13, p = .04). However, follow up tests did not give any significant effects. Surprisingly, no effect of session type was found in either the decision-making ($F(1,20)$ = 0.06, partial η^2 <.01, p = .82) or calculation trials ($F(1, 20)$ = 0.60, partial η^2 = .03, p = .45). In the calculation trials, no significant effects were found.

Behavioural analysis: Decision-making

The behavioural data were analysed for all participants. No additional participants were excluded, given that every participant showed a sufficiently variable choice behaviour (i.e. No subject accepted or rejected everything) and an average performance level above chance (M = 0.72, SD = 0.15, chance level = 0.33). Therefore, the behavioural analysis was conducted for 25 participants.

First, the acceptance rate during decision-making was analysed. This analysis investigated the effect of stress on decision to engage in effort as a function of difficulty level and reward level. As expected in this task, there was a main effect of effort (z = -8.35, LO = -3.06, p < .001 Fig. 5A) and reward (z = 10.02, LO = 1.73, p < .001 Fig. 5B). As expected, participants accepted harder trials less often, and large reward trials more often. Furthermore, there was a significant effect of session type (z = 2.02, LO = 0.23, p = .04 Fig. 5C), indicating that participants accepted trials less in the stress condition compared to the control condition. In addition, there was a trend towards significance in the interaction effort x reward x session type (z = 1.70, LO = 0.072, p = .09), indicating an effect of stress on both reward and effort. However, post hoc t-tests did not find a significant interaction between stress and control for any level of reward or effort.

Accuracy as covariate

Because of the large individual variability in baseline accuracy performance of the calculation task, we tested whether calculation accuracy during the training was associated with decisions. To this end, the previous analysis was repeated including training accuracy as a covariate. Training accuracy was defined as the average accuracy score of the three training phases. As expected, training accuracy had a significant impact on acceptance rate (z = 3.59, LO = 4.55, p < .001), showing that participants that were better at the training calculations accepted more often to engage in effort. As in the previous analysis, main effects of effort (z = -8.35, LO = -3.06, p < 0.001), reward (z = 10.07, LO = 1.72, p < .001), and session type were found (z =
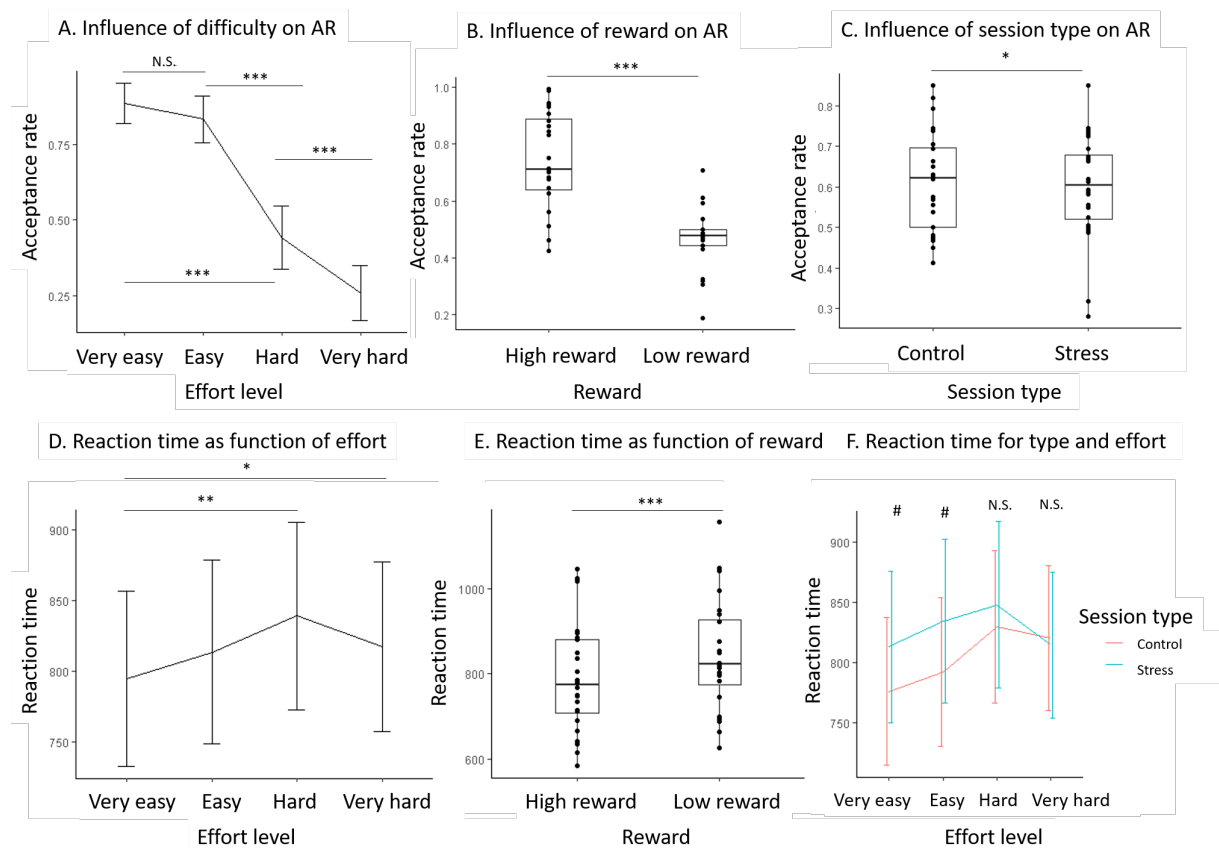
Figure 5. Behavioural effects in the decision-making trials. A. The acceptance rate in the decision-making trials as a function of difficulty. There was no significant difference between the very easy and easy trials. But starting from the easy trials, there is a significant decrease of acceptance rate. The error bars indicate the mean +/- SEM. B. The influence of reward on acceptance rate. We can see that the high reward trials were accepted significantly more often compared to the low reward trials. C. The effect of session type on acceptance rate. We found that participants accepted less trials in the stress condition compared to the control condition. D. The influence of difficulty level on reaction time during the decision-making trials. Both hard and very hard trials were performed significantly slower compared to very easy trials. E. Reaction time as a function of reward. We can see that high reward trials were performed significantly faster compared to low reward trials. F. Reaction time as a function of session type and effort level. We can see that there was a trend for faster reaction times in the control session compared to the stress session in the very easy and easy trials, while this trend was not found for the hard and very hard trials. # p < .1, * p < .05, ** p < .01, *** p < .001.

2.03, LO = 0.23, p = .04). Again, a trend for significance in the interaction effort x reward x session type was found (z = 1.66, LO = 0.07, p = .10).

Subjective stress as covariate

Generally, there is substantial variability in the subjective experience of stress; some participants might have thought the stress induction we perform is more of a challenge than a stressful event. To account for this variability, we repeated the previous analysis including differences in the self-report scores at the POMS questionnaire for tension and depression after stress and control. First, we included the POMS depression score as a covariate. This analysis confirmed the main effects of effort (z = -8.35, LO = -3.06, p < .001), reward (z = 10.02, LO = 1.73, p < .001), and session type (z = 2.02, LO = 0.23, p = .04). The trend for significance in the interaction effort x reward x session type was confirmed (z = 1.70, LO = 0.07, p = .09). No significance was found in the depression subscale (z = 0.09, LO = 0.03, p = .93).

Second, the POMS tension score was included as a covariate. This analysis found a

significant effect of the POMS tension score on acceptance rate (z = 3.24, *LO* = 0.87, *p* = .001), indicating an increase in acceptance rate with higher tension. Furthermore, it confirmed the main effects of effort (z = -8.34, *LO* = -3.06, *p* < .001), reward (z = 10.06, *LO* = 1.73, *p* < .001) and session type (z = 2.04, *LO* = 0.23, *p* = .04). Furthermore, a trend for significance in the interaction effort x reward x session type was confirmed (z = 1.68, *LO* = 0.07, *p* = .09).

IBI as a covariate

The physiological response to stress is known to vary across individuals. This is commonly measured via cortisol sampling. However, due to the COVID-19 pandemic, cortisol from only 12 participants has been analysed. Hence, we computed an alternative measure of objective stress based on heart rate changes: the difference in average IBI. This measure was included as a covariate to control for the difference in stress experience in the first quarter of the first block of both the stress and control session. In order to avoid convergence errors in the model, we replaced the session type variable with IBI as both a fixed effect and random effect.

This analysis confirmed the effects of effort (z = -8.48, *LO* = -2.97, *p* < .001) and reward (z = 10.42, *LO* = 1.66, *p* < .001). Furthermore, an interaction effect of effort x reward x IBI was found (z = 6.44, *LO* = 2.73, *p* < .001). Running a post-hoc GLMM for every effort level revealed a significant interaction of IBI and reward on acceptance rate in the very hard trials (z = 4.51, *LO* = 11.07, *p* < .001). A higher IBI in the high reward condition caused an increase in acceptance, while a higher IBI in the low reward condition caused a decrease in acceptance.

Full model

The model containing all covariates for the behavioural analysis confirmed the effects of effort (z = -8.52, *LO* = -2.97, *p* < .001) and reward (z = 10.46, *LO* = 1.66, *p* < .001). Additionally, main effects of accuracy (z = 2.78, *LO* = 3.33, *p* = .006) and tension (z = 2.64, *LO* = 0.80, *p* = 0.008) were found. Furthermore, the interaction effort x reward x IBI (z = 6.51, *LO* = 2.76, *p* < .001) was confirmed.

Summary for acceptance rate during decision making

Concluding, in the decision-making trials, significant effects of effort and reward were found. Furthermore, both accuracy and the tension subscale of the POMS had a significant influence on acceptance rate, both having a positive correlation with overall acceptance of trials.

Behavioural analysis: decision-making reaction times

The first Linear Mixed Model (LMM) found a significant main effect of effort (T(48) = -3.29, *p* = .002, Fig. 5D). Post hoc testing found that reaction times were faster for very easy trials compared to hard (T(24) = -3.52, Cohen's d = -0.32, *p* = .002), and very hard (T(24) = -2.24, Cohen's d = -0.18, *p* = .04) trials. There was also a main effect of reward (T(48) = 6.14, *p* < .001, Fig. 5E), indicating a faster reaction time in the high reward condition. A significant interaction effect of session type x effort was found (T(7488) = -3.20, *p* = .001, Fig. 5F), indicating a faster reaction time in the control session compared to the stress session, but only in the very easy and easy condition.

Accuracy as covariate

The LMM on reaction times for decisions, with accuracy as covariate found no effect of accuracy (T(30.1) = 0.01, *p* = .99), but confirmed the effects of effort (T(48.26) = -3.29, *p* = .002), reward (T(49.4) = 6.08, *p* < .001), and session type x effort (T(7493) = -3.20, *p* = .001).

Subjective stress as covariate

The LMM with the depression subscale of the POMS found a main effect of this subscale (T(18.55) = -3.58, *p* = .002), indicating a higher depression score caused overall slower reaction times. Furthermore, it confirmed the effects of effort (T(49.12) = -3.26, *p* = .002), reward (T(48) = 6.14, *p* < .001), and session type x effort (T(7491) = -3.20, *p* = .001). The LMM with the tension subscale of the POMS as covariate found a trend for the main effect of the tension subscale was found(T(29.97) = -1.92, *p* = .06), which could be an indicator

that participants reporting higher tension had slower reaction times overall. Furthermore, it confirmed the effects of effort (T(48.7) = -3.28, p = .002), reward (T(48.26) = 6.12, p < .001) and session type x effort (T(7491) = -3.20, p = .001).

IBI as a covariate

When using IBI as a covariate, no significant effect of IBI was found (T(30.41) = -0.04, p = .97). The analysis did confirm the effect of effort (T(35.34) = -3.38, p = .002), and reward (T(41.61) = 5.45, p < .001). However, it should be noted that this model gave a singular boundary error. Since two of the tested LMM methods gave very similar results, these results were reported.

Full model

The model containing training accuracy, both subscales of the POMS and the IBI as covariates gave a singular boundary error. Therefore, the results cannot be interpreted reliably.

Summary for decision-making reaction times

Concluding, for the reaction times, we found a faster reaction time with easier difficulty or higher reward. Additionally, participants with a higher depression rating reacted slower.

Behavioural analysis: calculation accuracy

This analysis was done to study the effect of stress on task performance. A main effect of effort was found (z= -15.45, LO= -0.56, p < .001, Fig. 6A), indicating a decrease in accuracy in the more difficult levels as expected (1 > 2; T(22) = 5.30, LO = 0.92, p < .001, 2 > 3; T(22) = 9.29, LO = 1.75, p < .001, 3 > 4; T(22) = 3.16, LO = 0.30, p = .004). This indicated that the difficulty manipulation was successful. No other significant main effects or interactions were found.

Accuracy as covariate

The analysis of the task accuracy, with training accuracy as a covariate found a main effect of training accuracy (z = 16.70, LO = 5.71, p < .001), indicating a better performance in the calculation task for participants that performed better on the training, as expected. The effect of effort (z = -17.45, LO = -0.58, p < .001) was confirmed.

Subjective stress as covariate

To account for the inter-individual variability in stress perception, we repeated the previous analysis including differences in the self-report scores of the POMS questionnaire for tension and depression after stress and control. Both analyses did not find a main
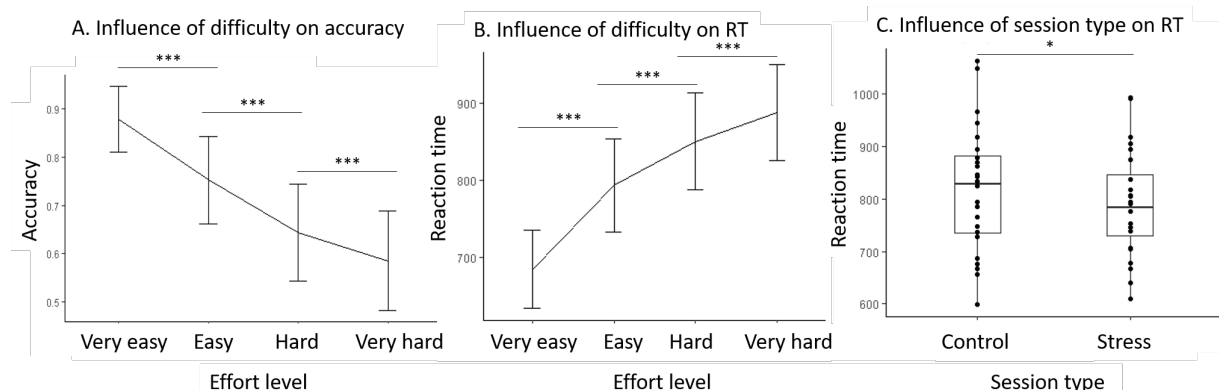
Figure 6. Effects in the calculation trials. A. The influence of difficulty on accuracy during the calculation trials. There was a significant decrease in performance with higher increasing level of difficulty. B. The influence of difficulty level on reaction time during the calculations. There was a significant increase in reaction time when the difficulty level increased. C. The influence of session type on reaction time in the calculation trials. We can see that participants performed significantly faster in the stress trials compared to the control trials. * p < .05,*** p < .001.

effect of the covariate (depression: z = 0.68, LO = 0.20, p = .50; tension: z = 0.65, LO = 0.13, p = .52), but confirmed the main effects of effort (depression: z = -15.52, LO = -0.56, p < .001; tension: z = -15.48, LO = -0.56, p < .001). Both analyses did not find any other significant effects.

IBI as a covariate

When including IBI as a covariate, a main effect of the covariate was found (z = 9.67, LO = 2.86, p < .001), indicating a better performance with increased IBI. Furthermore, the main effect of effort was confirmed (z = -10.36, LO = -0.56, p < .001).

Full model

When all covariates were included in the model, the model gave a singular boundary error (likely due to model complexity). Therefore, these results cannot be interpreted reliably.

Summary for the calculation accuracy

Concluding, we found a better accuracy in the calculation trials in easier calculations, and better accuracy for participants who also performed better in the training. Furthermore, a higher IBI correlated with a better performance.

Behavioural analysis: calculation reaction times

The first LMM on reaction time found a main effect of effort (T(47.92) = -12.87, p < .001). As expected, participants responded faster to easier calculations, and reaction time increased linearly with effort level. This confirmed that the difficulty manipulation was successful. (2 > 1; T(22) = 7.28, Cohen's d = 1.03, p < .001, 3 > 2; T(22) = 3.88, Cohen's d = 0.45, p < .001, 4 > 3; T(22) = 2.92, Cohen's d = 0.29, p = .008, Fig. 6B). An effect of session type was found (T(48.25) = -2.53, p = .01), suggesting a faster reaction time during the stress session compared to the control session (Fig. 6C).

Accuracy as covariate

The LMM on reaction time with accuracy as covariate found a significant effect of accuracy (T(33.63) = 5.56, p < .001), indicating a faster reaction time when the training accuracy was better. Furthermore, the main effect of effort (T(47.93) = -12.89, p < .001), and session type (T(48.25) = -2.52, p = 0.02) were confirmed.

Subjective stress as covariate

The LMM on the depression subscale of the POMS as a covariate found no main effect of the depression score (T(49) = -0.79, p = .43). This analysis confirmed the main effect of effort (T(48.43) = -12.80, p < .001) and session type (T(48.39) = -2.52, p = .02). The LMM on the tension subscale of the POMS found a significant effect of this subscale (T(33.98) = 2.19, p = .04), indicating a faster reaction time for participants that reported higher tension. Furthermore, it also confirmed the main effects of effort (T(48.19) = -12.85, p < .001) and session type (T(48.33) = -2.53, p = .01).

IBI as a covariate

In the LMM model using IBI as a covariate, no main effect of IBI was found (T(40.45) = 1.08, p = .29). However, a trend for the interaction effort x IBI was found (T(41.45) = -1.82, p = .08), indicating that participants with lower heart rate were particularly fast in easy trials. Furthermore, the main effect of effort (T(41.52) = -12.45, p < .001) was confirmed.

Full model

When all covariates were included in the model, the model gave a singular boundary error, so we cannot interpret the results from this analysis reliably. This again might have to do with the model containing all covariates being too complex for the amount of data that was included.

Summary calculation reaction times

Concluding, reaction times increased with higher difficulty levels and in the control session. Furthermore, both higher accuracy and tension were associated with an overall faster response time.

Pupil size analysis

In order to analyse the influence of stress effects on putative noradrenaline levels during effort-based decision-making, both the pupil size during the decision-making trials and the pupil size during the calculation trials were analysed. For this analysis, two participants had to be excluded due to the data of one session being corrupted, and five others had to be excluded due to noisy data in at least one of the blocks. First, an ANOVA was performed on the pupil size during the decision-making trials. Contrary to what was expected, no main effect of session type ($F(1,15) = 0.19$, partial $\eta^2 = 0.01$, $p = .67$) was found. A significant interaction effect of reward x session order was found ($F(1,15) = 8.16$, partial $\eta^2 = 0.35$, $p = .01$, Fig. 7A), indicating a larger pupil size in the low reward condition compared to the high reward condition in participants that had the control session first (post hoc t-test: $T(16) = 6.46$, Cohen's d = 4.08, $p < .001$). Unexpectedly, no significant interaction effect of either session type x reward ($F(1,15) = 0.81$, partial $\eta^2 = 0.05$, $p = .38$) or session type x effort ($F(3,45) = 0.90$, partial $\eta^2 = 0.06$, $p = .45$) was found.

Second, an ANOVA was done on the calculation trials. This ANOVA revealed a significant main effect of effort ($F(2.018, 32.294) = 11.38$, partial $\eta^2 = 0.42$, $p < .001$, Fig. 7B), indicating larger pupil size for increasing effort. Post hoc t-tests indicated that this effect was caused by a significant smaller pupil size in the very easy calculation trials and the other difficulty levels (very easy < easy: $T(16) = 5.65$, Cohen's d = 1.85, $p < .001$; very easy < hard: $T(16) = 5.87$, Cohen's d = 2.37, $p < .001$, very easy < very hard: $T(16) = 3.62$, Cohen's d = 1.52, $p = .002$). Contrary to the expectations, no significant main effect of session type was found ($F(1,16) = 1.04$, partial $\eta^2 = 0.06$, $p = .32$). Furthermore, the interaction effect of session type x effort ($F(3,48) = 2.05$, partial $\eta^2 = 0.11$, $p = .12$) was not significant.

MRI analysis

This analysis focused on effort and reward coding during decision-making, and effort coding during the calculations. First, the whole-brain results of the decision-making task and the calculation task are presented.

Second, the results of two ROI analyses are presented. The first ROI analysis employed the calculation task as an effort-coding localizer (i.e. a way to identify effort-sensitive regions). These regions were subsequently used as ROI to investigate effort coding during decision-making and under stress. From the regions that are coding for effort, only the regions that were hypothesized to be involved in

A. Pupil size during decisions

B. Pupil size during calculations
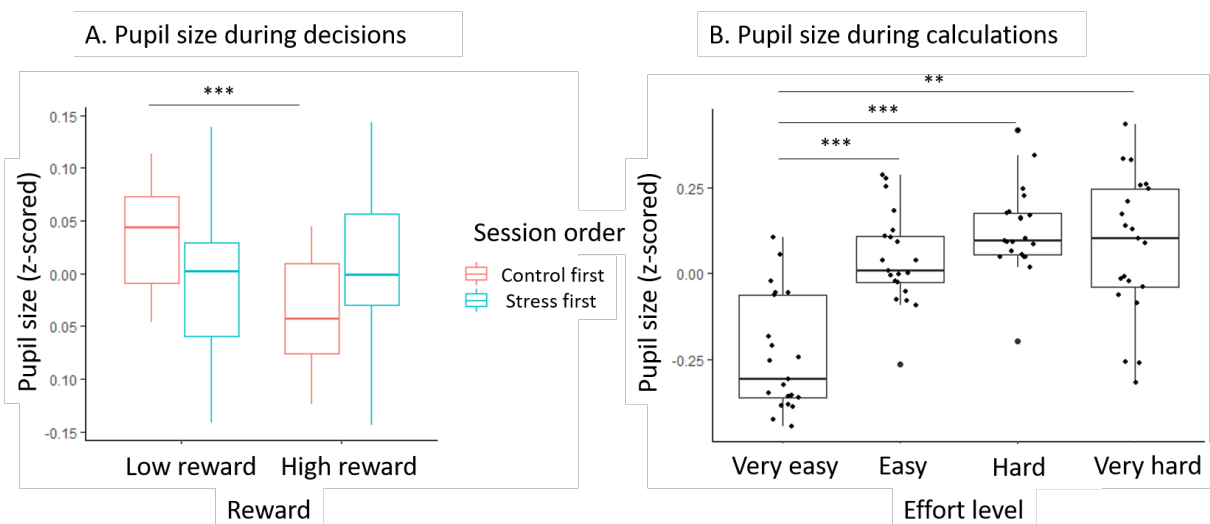
Figure 7. A. The effect of session order on the z-scored pupil size during decisions. No significant difference in pupil size was found for the participants that started with the stress condition, while the participants who started with the control condition had a significantly smaller pupil size in the high reward condition. B. The effect of effort level on the z-scored pupil size. The pupil size in the very easy condition was significantly lower compared to the other effort levels. ** p < .01,*** p < .001.

Whole brain analysis of the decision-making trials

A. Stress (x=4)　　B. Control (x=4)　　C. Control (z = 8)　D. Stress-control (x=4)

Whole brain analysis of the calculation trials

E. Reverse stress　　F. Control　　　G. Control-stress

Figure 8. The whole brain activity for different contrasts at different locations. A-D. The whole brain activity during the decision-making trials. All contrasts were parametric effort (top row) and reverse parametric effort (bottom row). The clusters were generated by first taking voxels that had a voxel-wise significance of p < .001. Then, clusters were shown with at least 50 significant voxels were shown. A. The parametric and reverse parametric stress contrast. The only significant cluster was in the parametric stress contrast, in the lingual gyrus. B. The control contrasts. We can see that the lingual gyrus was also active here. C. The control contrast, here at z = 8. We can see that there was also some prefrontal activity in the reverse parametric effort contrast. However, this cluster was not significant when family wise error correction was performed. D. The stress-control contrast. No significant clusters were found.

E-G. The whole brain activity during the calculations. All contrasts were parametric (F and G) or reverse parametric (E) effort contrasts. For the parametric effort stress and both reverse parametric effort control and control-stress, no significant clusters of at least 50 connected significant voxels were found (p < .001). E. The reverse parametric stress contrast. No frontal activity was found in this contrast. F. The parametric control contrast. Here, activity in the medial prefrontal cortex (MPFC) and the dorsolateral prefrontal cortex (DLPFC) was found. G. The parametric effort contrast for the difference between control and stress. Here, some activity was found in the inferior frontal gyrus.

the processes of interest were investigated (i.e. DLPFC, MPFC, specifically dACC, and insula). These regions have a high anatomical precision because they were generated from the same participants. Circular inference is prevented, as we used regions based on the calculation task to analyse the data from the decision task, which is independent.

The second ROI analysis aimed at testing the effects of stress during both decision-making and calculations. For this analysis, we used an a-priori MPFC ROI based on a previous study.

Whole brain results decision-making task

The whole-brain analysis of the data from the decision-making contrasts of the effort related areas are summarized in Table 1. In this analysis, only two significant clusters were found. One in the parametric effort control contrast, and one in the parametric effort stress contrast. Figure 8 gives an overview of the activity in the parametric effort contrast during stress, control, stress-control, and control-stress. Both of these significant clusters that were found are located within the Lingual Gyrus. No significant clusters were found in the reward related stress-control contrasts. There were two significant clusters in the high-low reward contrast. One in the Cerebellum (peak voxel: -24, -58, -20; cluster size: 242, T = 6.47, pFWE < .001) and one in the Declive (peak voxel: 28, -72, -18; cluster size: 455, T = 8.09, pFWE < .001). Contrary to what we expected, no activity was observed in dACC, MPFC, or DLPFC at the whole brain level, neither in the control, stress, or comparison contrasts.

Whole brain results calculation task

In the whole brain analysis of the calculations, the parametric effort contrast revealed significant prefrontal clusters in the control contrast as expected. A cluster in the MPFC was found (peak voxel: -4, 20, 48; cluster size: 691, T = 10.07, p_{FWE} < .001). Additionally, a cluster in the DLPFC was found (peak voxel: -44, 10, 34; cluster size: 1476, T = 7.16, p_{FWE} < .001). Furthermore, a significant insula cluster was

Table 1.

All clusters that were found during the decision-making contrasts, with a cluster size of at least 50 connected significant voxels (threshold p < .001). The reverse contrast is the contrast multiplied by -1. These contrasts were used to test for regions that become less active with higher effort. The position is reported in MNI coordinates. After applying family wise error correction (FWE), only two different clusters remained significant. One cluster was found in the parametric effort contrast during the control session, and one during the parametric effort in the stress session. Both these clusters were found in the lingual gyrus. Since we only hypothesised an effect of stress on the prefrontal regions, these clusters were not investigated further. * pFWE < .05.

Location (MNI label)	Position (x,y,z)	Cluster p-value (FWE-corr)	Peak T	Cluster size
Parametric effort control				
Fusiform gyrus	(-24,-70,-10)	0.093162	5.467724	79
Lingual gyrus	(6,-76,8)	0.00519 *	4.655265	149
	(-4,-76,12)		4.26905	
	(4,-80,16)		4.261832	
Parametric effort control reverse				
Inferior frontal gyrus	(-40,40 10)	0.315686	4.466287	52
Parametric effort stress				
Lingual gyrus	(-2,-78,-2)	<0.0001 *	7.331042	434
	(2,-82,10)		5.722619	
	(-2,-74,14)		4.915114	
Declive	(-20,-72,-12)	0.142885	4.766066	69
Posterior cingulate	(22,-66,10)	0.247702	4.748438	57

Table 2.

Locations and p-values for the ROIs that were found. The ROIs were generated using both the parametric effort and reverse parametric effort contrast in the calculation data. Here, reverse parametric effort is the parametric effort contrast multiplied by -1. Significant voxels (threshold p < .001) were clustered on proximity, and only clusters containing at least 50 neighbouring significant voxels were further analysed. The p-values for the clusters are the family wise error (FWE) corrected values. Only clusters with a FWE-corrected p-value < .05 were further analysed. Of these ROIs, only the ones that were important for our hypotheses (i.e., the medial prefrontal cortex (MPFC) and the dorsolateral prefrontal cortex (DLPFC) were investigated. In total, three ROIs were subsequently analysed. First, the superior frontal gyrus, or the MPFC. Second, the medial frontal gyrus, in this case the DLPFC, and third, the insula. We test the insula in order to find an effect of stress in the SN. * Significant cluster, with PFWE < .05; ** Significant cluster used in the ROI analysis, PFWE < .05.

Location (MNI label)	Position (x,y,z)	Cluster p-value (FWE-corr)	Peak T	Cluster size
Parametric effort				
Superior frontal gyrus	(-6,20,50)	1.02E-07 **	8.0679	394
	(-8,28,42)		4.740153	
	(4,18,44)		4.094477	
Medial frontal gyrus	(-42,24,22)	2.9E-13 **	6.94499	836
	(-48,10,38)		6.839056	
	(-52,36,14)		5.026441	
Insula	(-26,30,2)	0.039704 **	6.382373	79
	(-34,22,2)		4.14222	
Cerebellum	(32,-62,-28)	9.35E-06 *	6.323435	266
	(40,-68,-28)		6.042747	
	(32,-60,-36)		4.095436	
Declive	(-34,-74,-18)	2.99E-07 *	6.129512	362
	(-36,-86,-6)		5.387378	
	(-42,-66,-16)		5.299193	
Caudate	(-8,16,6)	0.166809	5.978674	54
Cerebellum	(8,-78,-34)	9.35E-06 *	5.484932	266
	(8,-76,-26)		5.471447	
Cuneus	(-28,-80,36)	1.72E-05 *	5.476009	250
	(-38,-84,28)		4.453924	
Inferior occipital gyrus	(30,-90,-4)	0.002058 *	5.276479	137
	(42,-86,-10)		4.609646	
	(46,-74,-14)		3.759126	
Reverse parametric effort				
Putamen	(-30,-4,2)	0.024249 *	5.775667	88
	(-30,-14,4)		3.813586	
Anterior cingulate	(-2,34,-10)	0.187573	5.698733	52
Putamen	(28,-4,0)	0.002372 *	5.254271	134
	(34,2,12)		4.722855	
	(32,6,2)		4.333956	
Inferior parietal lobe	(-58,-30,24)	0.001483 *	5.236336	144
	(-64,36,24)		4.946507	
	(-66,-34,32)		3.915671	

Anterior cingulate	(12,50,-10)	0.04694 *	5.192846	76
	(10,62,0)		4.858622	
Superior temporal gyrus	(-60,4,-2)	0.031836 *	5.142667	83
	(-56,8,-8)		4.78757	
	(-62,2,8)		4.50599	
Inferior parietal lobe	(-38,-30,44)	0.166809 *	4.896193	54
Mid temporal gyrus	(62,-40,-2)	0.176888 *	4.510745	53
	(62,-32,2)		3.762803	
Inferior parietal lobe	(62,-24,30)	0.030139 *	4.425534	84
	(64,-22,22)		4.161829	
	(56,-28,20)		3.908321	

found (peak voxel: -26, 28, 2; cluster size: 121, T = 7.97, p_{FWE} = .008). In the control-stress contrast, one prefrontal cluster was found, in the Inferior Frontal Gyrus (peak voxel: -40, 48, 0; cluster size = 83, T = 7.57, p_{FWE} = .02). A summary of these findings is given in Figure 8. We found no significant prefrontal clusters in the stress contrasts for parametric effort or reverse parametric effort. No significant clusters were found in the reverse parametric effort control contrast.

Generation of the ROIs

We then investigated the effort related regions in the calculation trials. For this analysis, we tested which clusters were significant in either the parametric effort or the reverse parametric effort contrast during the calculations. In the parametric effort contrast, a total of eight significant clusters were found (see Table 2 for a summary). In the reverse parametric effort analysis, a total of
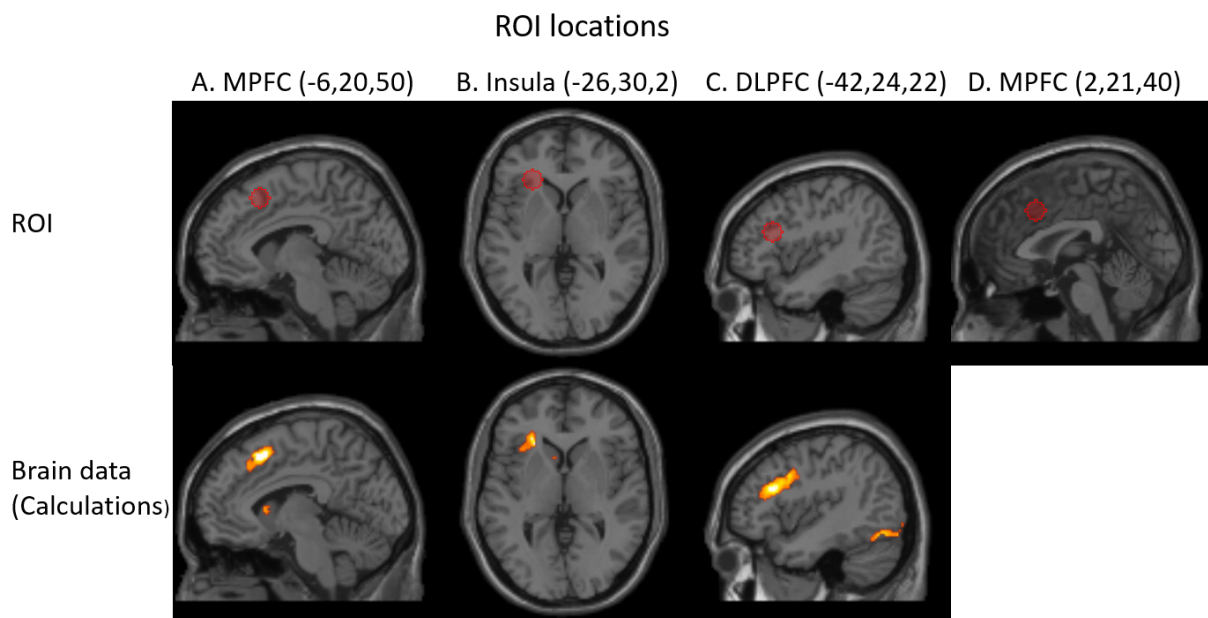
ROI locations

A. MPFC (-6,20,50) B. Insula (-26,30,2) C. DLPFC (-42,24,22) D. MPFC (2,21,40)

Figure 9. The different ROIs that were generated and investigated. The top row of the figure shows the location of the ROIs that were used for the ROI analysis. The bottom row shows the corresponding activity in the calculation trials on which the ROI is based. Each ROI was defined as a sphere of 8mm around the peak voxel in the shown cluster, indicated with a red circle in this figure. The names of the regions were taken from the MNI database. **A.** The medial prefrontal cortex ROI found in the parametric effort contrast, centred on -6, 20, 50. **B.** The insula ROI found in the parametric effort contrast, centred on -26, 30, 2. **C.** The dorsolateral prefrontal cortex ROI found in the parametric effort contrast, centred on -42, 24, 22. **D.** The premade ROI centred on 2, 21, 40.

six significant clusters were found (see Table 2 for a summary).

Based on these results, we selected the clusters within the hypothesized regions for effort coding, the MPFC (including dACC) and DLPFC. We found a significant effect of both the dACC/MPFC (peak voxel: -6, 20, 50; cluster size: 394, T = 8.07, p_{FWE} < .001, Fig. 9A) and the DLPFC (peak voxel: 42, 24, 22; cluster size: 836, T = 6.95, p_{FWE} < .001, Fig. 9C) in the parametric effort contrast. Furthermore, to study the effect of stress in the SN, a preliminary analysis to the insula region was conducted. This region was found significant in the parametric effort contrast as well (peak voxel: -26, 30, 2; cluster size: 79, T = 6.38, p_{FWE} < .04, Fig. 9B).

MPFC ROI

When investigating the Superior Frontal Gyrus, a significant effect of reward ($F(1,21)$ = 5.94, partial η^2 = 0.22, p = .02, Fig. 10A) was found, indicating higher activity in low reward trials compared to high reward trials. The significant effort x reward interaction ($F(3,63)$ = 3.12, partial η2 = 0.13, p = .03, Fig. 10B) revealed that this effect was mainly present in the lower effort trials (very easy and easy). Furthermore, a significant main effect of block was found ($F(1,21)$ = 7.91, partial η2 = 0.27, p = .01), indicating higher signal change in the first block compared to the second block. An order x type x effort x reward interaction was found ($F(3,63)$ = 4.35, partial η2 = 0.17, p = .008). However, no significant effects of stress on reward were found in the follow-up test after multiple comparison correction. Additionally, no effect of stress on effort was found (control first, low reward: $F(3,33)$ = 2.66, partial η2 = 0.20, p = .06; control first, high reward: $F(3,33)$ = 0.87, partial η2 = 0.07, p = .47, stress first, low reward: $F(3,30)$ = 0.97, partial η2 < 0.01, p = .42, stress first, high reward: $F(3,30)$ = 0.80, partial η2 = 0.07, p = .51).

DLPFC ROI

This analysis revealed a significant interaction effect of type x effort x reward ($F(3,63)$ = 4.60, partial η^2 = 0.18, p = .006). The follow-up tests found no significant effect of stress on reward coding after multiple comparison correction.

Separate ANOVAs testing for stress effects on effort coding for each reward separately did not find a significant difference (low reward: $F(3,66)$ = 2.69, partial η^2 = 0.11, p = .05, high reward: $F(3,66)$ = 1.97, partial η^2 = 0.08, p = .13). Additionally, a significant effect was found in the session order x type x effort x reward interaction ($F(3,63)$ = 3.62, partial η^2 = 0.15, p = .02). In the control first, very hard effort condition, a significant effect of type x reward was found ($F(1,11)$ = 21.45, partial η^2 = 0.66, p = .001, Fig. 10C). Post-hoc t-tests confirmed lower activity in the high reward trials compared to low reward trials in stress ($T(11)$ = 4.77, partial η^2 = 0.71, p < 001), but not in control ($T(11)$ = -1.36, partial η^2 = -0.40, p = .20). Testing the effect of stress on effort only revealed a significant interaction in the control first, high reward condition, before correction for multiple comparisons (control first, low reward: $F(3,33)$ = 2.12, partial η^2 = 0.16, p = .12; control first, high reward: $F(3,33)$ = 4.84, partial η^2 = 0.31, p = .007, stress first, low reward: $F(3,30)$ = 0.59, partial η^2 = 0.06, p = .62, stress first, high reward: $F(3,30)$ = 0.55, partial η^2 = 0.05, p = .65, Fig. 10D).

Additionally, there was a significant order x type x block interaction ($F(1,21)$ = 4.88, partial η^2 = 0.19, p = .04), indicating that only in the stress first condition, the activity decreased after the first block in the stress condition ($T(22)$ = 2.98, partial η^2 = 1.05, p = .01, Fig. 10E). This was not the case in the control condition ($T(22)$ = 1.52, partial η^2 = 0.34, p = .16). This indicated a decreased executive control network after stress.

Insula ROI

The ROI in the insula was tested in order to study the effect of stress in the SN. Here, we found a type x block interaction in the ANOVA ($F(1,21)$ = 4.71, partial η^2 = 0.18, p = .04, Fig. 10F), yielding a trend for decrease in activity in the control condition in block two ($T(22)$ = -2.03, partial η^2 = -0.55, p = .06), while it remained elevated in the stress condition ($T(22)$ = 0.11, partial η^2 = 0.03, p = .91). Given that the insula is part of the salience network, this indicates elevated activity in the salience network after stress, which is in line with previous studies (Hermans et al. 2014). No other significant effects were found in this ROI.
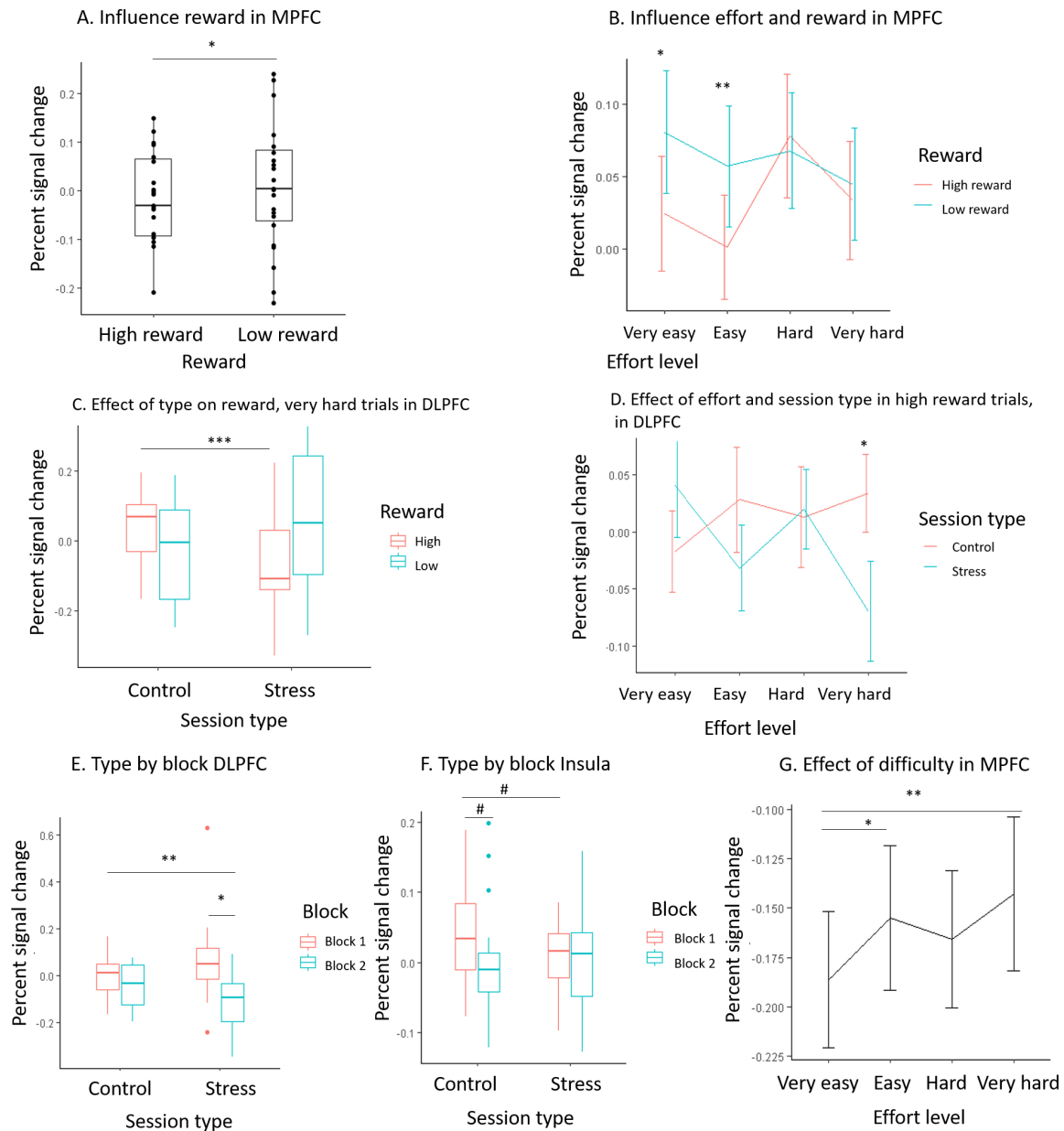
Figure 10. Effects found in the ROI analysis. A. Influence of reward on percent signal change in the medial prefrontal cortex (location -6,20,50). In the low reward condition, a significantly higher percent signal change was found compared to the high reward. B. Splitting this effect by effort level shows that this effect was driven by a significant difference in the very easy and easy effort levels. C. The effect of session type and reward on percent signal change in the dorsolateral prefrontal cortex (location -42, 24, 22), including only very hard trials. A significant effect of session type was found in high reward, but not in low reward. D. Effect of effort and session type on percent signal change in high reward trials. A significantly lower percent signal change was found in the very hard stress trials when compared to very hard control trials. Additionally, the slopes differ significantly, giving a significantly lower slope of the percent signal change with effort interaction in stress, compared to control. E. The influence of session type and block in the dorsolateral prefrontal cortex (location -42, 24, 22) in the stress first condition. There was a significant decrease of percent signal change in block 2 of the stress session, but not in the control session. F. The influence of type and block in the insula (location: -26, 30, 2). There was a trend for a decrease in percent signal change in block two of the control session compared to block one of the control session. G. Influence of effort on the independently generated ROI (location: 2, 21, 40). Percent signal change can be seen increasing as a function of difficulty level. This effect was significantly different between the very easy and easy trials, as well as the very easy and very hard trials. # p < .1, * p < .05, ** p < .01, *** p < .001.

Independent ROI analysis: MPFC

The independent ROI analysis investigating MPFC activity in the decision phase data revealed a higher percent signal change in block one compared to block two ($F(1,21) = 11.02$, partial $\eta^2 = 0.34$, $p = .003$). Furthermore, an order x type x effort x reward interaction was found ($F(3,63) = 3.86$, partial $\eta^2 = 0.16$, $p = .01$). The follow-up analysis found no significant effect stress on reward coding in control or stress first after multiple comparison correction. No significant effects of stress on effort coding were found (control first, low reward: $F(3,33) = 2.74$, partial $\eta^2 = 0.20$, $p = .06$, control first, high reward: $F(3,33) = 0.51$, partial $\eta^2 = 0.04$, $p = .68$, stress first, low reward: $F(3,30) = 0.29$, partial $\eta2 = 0.03$, $p = .84$, stress first, high reward: $F(3,30) = 1.15$, partial $\eta^2 = 0.10$, $p = .35$). No effect of stress was found in this analysis.

The independent ROI analysis in the calculation phase only found a significant main effect of effort ($F(3,60) = 4.07$, partial $\eta^2 = 0.17$, $p = .01$, Fig. 10G), indicating that activity increased as a function of effort. No significant effect of stress was found in this analysis.

Discussion

This study investigated the effects of stress on effort-based decision-making. We combined an already established effort-based decision-making task with experimental induction of acute stress in a within-subject design. As hypothesized, the results showed that acute stress reduced participants' willingness to engage in mental effort. Further, participants performed better and faster in the calculations when they had a higher tension score. At the neural level, effort activated the MPFC (specifically, the dACC) and the DLPFC in the control condition during calculations. However, no effect of stress or effort coding was found on these regions during the decision making task. The ROI analysis revealed some evidence for reward and effort coding in the dACC, but no main effect of stress. The DLPFC exhibited some sensitivity to effort and reward, but only in a complex interaction with stress and session order. Finally, the pupil analysis revealed an effect of stress during the calculation trials. These results have important implications for understanding the effects of stress on decision-making, with relevance for stress-related disorders with motivational deficits.

Promised reward and expected effort influence the decisions to engage in a task. This was experimentally established in previous research, showing that easier and more rewarded options are accepted more (Kool et al., 2010; Shenhav et al., 2017). As expected, this experiment confirmed this effect of effort and reward; participants accepted harder trials less often, and higher reward trials more often. We found that stress reduced the willingness to engage in mental effort, as expected. Previous research also provided some indication that stress might influence effort-based decision-making. Activity in similar brain areas was found during both acute stress and decision-making (Silvetti et al., 2018; Valentino & Bockstaele, 2008; Gathmann et al., 2014). Effects of stress on other forms of decision-making have consistently been reported. For example, people under stress were found to become more risk-taking and were more likely to exhibit habitual over goal directed behaviour. (Schwabe & Wolf, 2009; Starcke & Brand, 2012; Starcke & Brand, 2018). Interestingly, chronic stress in rats was shown to increase reward insensitivity through VTA activation (Tye et al., 2012; Hollon et al., 2015) and acute stress in rats resulted in effort avoidance (Shafiei, Gray, Viau, & Floresco, 2012). However, differences might arise because these are animal studies, rather than studies in humans. Furthermore animal studies also showed that different forms of stress can cause different reactions in DA neurons (Valenti & Grace, 2012).

Considering the effects of stress on behaviour, our main behavioural results confirmed that experimentally induced acute stress reduced the willingness to engage in mental effort, making people more effort avoidant. Furthermore, we found a trending effect of stress on the interaction of effort and reward, seemingly decreasing the acceptance rate in high reward, high effort trials, as well as low reward, low effort trials. This result might be interpreted as evidence for both effort avoidance and reward insensitivity. However, we should be careful with this interpretation, as this effect was not significant.

Previous work also shows that higher effort avoidance was observed in patients suffering from depression (Bishop & Gagne, 2018; Treadway, Bossaller, Shelton & Zald, 2012), while patients suffering from anxiety show an increased willingness to exert effort (Bishop & Gagne, 2018). The results of our covariate analysis are in line with the latter: a higher tension score, also called anxiety in the POMS, led to higher acceptance rates. However, no effect of depression on acceptance rate was found. This might be because the study was performed on only a part of the original sample, causing lack of power. Additionally, we found that participants which perform better at the training task accepted significantly more trials, and performed the calculations in the scanner faster and more accurate, as expected. This highlights the importance of taking individual differences in performance into account.

Studies have shown that heart rate increases with stress (Shapiro et al., 2000; Rieger, Stoll, Kreuzfeld, Behrens, & Weippert, 2013). Heart rate variability was found to decrease during (Shapiro et al., 2000) and after (Rieger et al., 2013) stress. In our study, we used the IBI (the inverse of the heart rate), and RMSSD to test whether the stress induction was performed successfully. Unexpectedly, we found that the heart rate did not differ significantly between the stress condition and the control condition. The RMSSD did not show a significant decrease under stress, although a trend for this decrease was observed. The lack of significance could have a few reasons. As mentioned before, the analysis was run on an incomplete sample. Besides this, an effect of session order was found in the RMSSD analysis, where the participants that had the stress session first had an overall lower RMSSD score. This indicates that there might have been a difference in experienced stress in the stress first compared to the control first session. Specifically, as a lower RMSSD has been found in the stress first condition, the participants that started with the stress session might have experienced more stress overall. This might further decrease the power of this analysis.

When testing the effect of IBI during the calculations and decisions, we found that during the calculations, an increase in IBI (lower heart rate) correlated with a better performance. This is in line with previous work which shows that stress negatively impacts both motivation and working memory (Roozendaal et al. 2004; Schwabe et al. 2012), and therefore decreases performance. During the decision-making task, we found that in the very hard trials, a lower IBI – and thus presumably higher stress – caused reward insensitivity (reduced acceptance of high reward trials, and more acceptance of low reward trials). This indicates that the beneficial impact of reward on very hard trials was neutralized under stress. This partly confirmed our hypothesis that stress causes reward indifference, however, only for the very hard trials. That this effect was only found in the very hard condition was unexpected.

Furthermore, we attempted to test the impact of all covariates in a single full model, to determine the relative weight (including heart rate, training accuracy, the tension subscale of the POMS, and the depression subscale of the POMS). However, in all cases (except for the acceptance ratio model), this model did not converge. This issue could be caused by having a model that is too complex for the amount of data.

Research into neural effects of stress found that the regions activated by stress and effort-based decision-making partially overlap (Silvetti et al., 2018; Valentino & Bockstaele, 2008; Gathmann et al., 2014). For example, the dACC, DLPFC and MPFC were found to be part of both the stress and the effort-based decision-making response. Our findings in the whole brain analysis during the decision-making task unexpectedly did not support these findings; no significant effect of stress on effort-based decision-making in prefrontal regions was found. Our findings in the whole brain analysis of the calculations found activity in both the DLPFC and MPFC regions in the parametric effort contrast, but only in the control sessions. This activity was no longer significant in the stress or stress-control contrasts. This provided some indication that DLPFC and MPFC activity during effortful calculations was reduced under stress. However, this did not survive direct comparison, possibly due to lack of power (small sample size). An additional caveat concerns the level of the experienced stress during the experiment. Although we

did find a successful stress induction – there was an effect of stress on heart rate and behaviour – the participants might have experienced more stress overall when they started with the stress session, as indicated by the RMSSD analysis. These session order effects may thus further reduce power.

The results of the ROI analysis are partly in line with the literature findings that MPFC and DLPFC are implicated in both effort-based decision-making and stress (Gathmann et al., 2014). In our analysis, we found an effect of reward on the MPFC, and an interaction between reward and effort, which is in line with this literature. We found a higher MPFC activity for less reward. This could be explained by the participants assuming that the high reward is the baseline reward they can get. This would coincide with the literature, where a higher activity for reduced reward compared to baseline reward has been found in a region partly overlapping with our ROI (Bush et al., 2001). In the DLPFC, we could not find a main effect of effort or reward. Unexpectedly, we could not confirm a main effect of stress on either the MPFC or the DLPFC. We did find that stress had an effect on reward coding in the DLPFC, but only in the participants that started with the control session, and only in very high difficulty trials. We also found that stress had an effect on effort coding in the DLPFC in these participants, but only in the high reward trials. There could be multiple reasons as to why we do not find these results in the other conditions or the MPFC. First, our sample size was not sufficiently large. Second, the session order might have influenced the stress experience of the participants. Our RMSSD analysis revealed an overall decrease in RMSSD in the participants that started with the stress session. Since a decrease in RMSSD would be expected under stress (Shapiro et al., 2000), this indicated that having the stress session as first session might have induced stress in itself, also in the control condition.

The results of the a-priori ROI analysis show no main effect of effort, reward or stress on the decision-making analysis. An effect of effort was found in the calculation analysis. The fact that differences have been found with the analysis of the MPFC in the decision-making trials, could be due to the ROI we generated having a higher anatomical precision than the a-priori ROI, because we created this ROI based on the regions that were active in the sample of participants we tested. However, it was unexpected that we did not find an effect of stress in neither regions.

Previous studies on pupil size found an increase in pupil size with increasing mental effort (Hess & Polt, 1964; see van der Wel & van Steenbergen, 2018, for a review). Moreover, pupil size has been correlated with sympathetic nervous system activation, and used as a marker for stress in the literature (Bali & Jaggi, 2015). Both NA and DA were increased during stress (Hermans et al., 2014). Animal studies also found increased NA and DA in decision making (Salamone et al., 2018; Varazzani et al. 2015). Furthermore, stress is reported to increase NA produced by the LC (Ironside et al., 2018), which was found to positively correlate with pupil size (Murphy et al. 2014). This line of work thus suggests that stress should increase pupil size. Our study did find an increase in pupil size with increased effort, suggesting that pupil size is indicative of task difficulty, or possibly the amount of mental effort participants invest in the task (Silvestrini & Gendolla, 2019), as expected. Since the pupil size is a putative measure for NA, this might be seen as evidence for part of the RML: the LC module modulates the amount of effort (Silvetti et al. 2018). Unexpectedly, no significant effect of stress on pupil size was found, during neither calculations nor decisions. However, this might be due to not having a sufficiently large sample size, and by the possible effect of session order on stress.

Concluding, this thesis found evidence for the hypothesis that effort-based decision-making was influenced by stress at the behavioural level. However, the hypothesized underlying neural dynamics were not observed. A neural effect of stress on effort was found only in the MPFC of the participants that started with the control session, and only in the high reward condition. A neural effect of stress on reward was only observed in the MPFC of the participants that received the control session first, in the very hard trials. Effort was tracked by pupil size, but only during the calculations. Furthermore, no evidence was found for the hypothesis that pupil changes tracked the impact of

stress. However, due to the small sample size of the study, these effects might not be found due to a problem with the power of the study. Therefore, the results of the analysis of the complete sample of the study might give more conclusive evidence to whether these hypotheses are true.

As discussed before, this study has some limitations. First of all, due to the Covid-19 pandemic, the full sample has not been tested yet. Therefore, the power in this study might be lacking, and more reliable results will be found when the entire sample has been tested. Secondly, individual differences in the experienced difficulty of the calculations have been observed through different overall accuracies for different participants. This might lead to a different expected value for different participants, since the probability to respond correctly to a certain difficulty may vary. Ignoring this might lead to a reduction in power. Additionally, the models used for the behavioural analysis often experienced some errors due to the complexity of the models. Finally, evidence for an effect of session order was found, potentially reducing the observed effect of stress.

Future research may test the activity of the VTA and LC during both stress and effort-based decision-making, as it has been shown that both the VTA and LC play an important role in the effects of stress and motivation (Hollon et al., 2015, Tye et al., 2012, Valentio & Bockstaele, 2008), and they are vital parts of the proposed RML model (Silvetti et al., 2018). This research might be conducted by analysing the data from the GRE and TSE scans made, and could elucidate the role of the VTA and LC during stress. Another direction for further research is to complete the full sample of this study. Due to the Covid-19 pandemic, the sample was not fully tested. This would give an increase in power that might have consequences for the results found in this research. Another possibility for improvement would be using more advanced modelling techniques to redefine the effort levels in such a way that they are similar for all individual participants. Then, the power of the analysis could be increased. Finally, further research might involve testing the reinforcement meta-learner model on these data, once it is expanded to include the functional data from the VTA and LC, to investigate what the influences of stress are on the model parameters of the RML model.

The results of the study of the complete sample could further help unravel the interaction between stress and effort-based decision-making. It might furthermore be important in giving a clearer understanding of the working mechanisms of stress-related disorders, especially those where motivation plays a role, like burnout and PTSD.

Acknowledgements

References

Alexander, W., & Brown, J. (2011). Medial prefrontal cortex as an action-outcome predictor. *Nature Neuroscience*, *14*(10), 1338-1344.

Ang, Y., Lockwood, P., Apps, M., Muhammed, K., & Husain, M. (2017). Distinct subtypes of apathy revealed by the apathy motivation index. *PLoS ONE*, *12*(1), 1-15

Apps, M., Grima, L., Manohar, S., & Husain, M. (2015). The role of cognitive effort in subjective reward devaluation and risky decision-making. *Scientific Reports*, *5*(1).

Asci, O., Braem, S., Park, H., Boehler, C., & Krebs, R. (2019). Neural correlates of reward-related response tendencies in an equiprobable Go/NoGo task. *Cognitive, Affective, & Behavioral Neuroscience*, *19*(3), 555-567.

Barr, D., Levy, R., Scheepers, C., & Tily, H. (2013). Random effects structure for confirmatory hypothesis testing: Keep it maximal. *Journal*

of Memory and Language, *68*(3), 255-278.

Bali, A., & Jaggi, A. (2015). Clinical experimental stress studies: methods and assessment. *Reviews in the Neurosciences*, *26*(5), 555-579.

Bates D., Mächler M., Bolker B., & Walker S. (2015). Fitting linear mixed-effects models using lme4. *Journal of Statistical Software*, *67*(1), 1–48.

Beck, A., Steer, R., Ball, R., & Ranieri, W. (1996). Comparison of Beck depression inventories-IA and -II in psychiatric outpatients. *Journal of Personality Assessment*, *67*(3), 588-597.

Behrens, T., Woolrich, M., Walton, M., & Rushworth, M. (2007). Learning the value of information in an uncertain world. *Nature Neuroscience*, *10*(9), 1214-1221.

Berridge, K. (2012). From prediction error to incentive salience: mesolimbic computation of reward motivation. *European Journal of Neuroscience*, *35*(7), 1124-1143.

Bishop, S., & Gagne, C. (2018). Anxiety, depression, and decision making: a computational perspective. *Annual Review of Neuroscience*, *41*(1), 371-388.

Blaszczynski, A.& McConaghy, N. (1988). SCL-90 assessed psychopathology in pathological gamblers. *Psychological Reports*, *62*(2), 547-552.

Booth, R., & Sharma, D. (2009). Stress reduces attention to irrelevant information: evidence from the stroop task. *Motivation and Emotion*, *33*(4), 412-418.

Botvinick, M., Huffstetler, S., & McGuire, J. (2009). Effort discounting in human nucleus accumbens. *Cognitive, Affective, & Behavioral Neuroscience*, *9*(1), 16-27.

Bouret, S., & Richmond, B. (2009). Relation of locus coeruleus neurons in monkeys to Pavlovian and operant behaviors. *Journal of Neurophysiology*, *101*(2), 898-911.

Brett, M., Anton, J., Valabregue, R., Poline, J. Region of interest analysis using an SPM toolbox [abstract], Presented at the 8th International Conference on Functional Mapping of the Human Brain, June 2-6, 2002, Sendai, Japan. Available on CD-ROM in NeuroImage, *16*(2).

Bush, G., Vogt, B., Holmes, J., Dale, A., Greve, D., Jenike, M., & Rosen, B. (2001). Dorsal anterior cingulate cortex: A role in reward-based decision making. *Proceedings of the National Academy of Sciences*, *99*(1), 523-528.

Cacioppo, J., & Petty, R. (1982). The need for cognition. *Journal of Personality and Social Psychology*, *42*(1), 116-131.

Carver, C., & White, T. (1994). Behavioral inhibition, behavioral activation, and affective responses to impending reward and punishment: The BIS/BAS Scales. *Journal of Personality and Social Psychology*, *67*(2), 319-333.

Esteban, O., Markiewicz, C., Blair, R., Moodie, C., Isik, A., & Erramuzpe, A. et al. (2018). fMRIPrep: a robust preprocessing pipeline for functional MRI. *Nature Methods*, *16*(1), 111-116.

Gathmann, B., Schulte, F., Maderwald, S., Pawlikowski, M., Starcke, K., Schäfer, L., Schöler, T., Wolf, O., & Brand, M. (2014). Stress and decision making: neural correlates of the interaction between stress, executive functions, and decision making under risk. *Experimental Brain Research*, *232*(3), 957-973.

Gilzenrat, M., Nieuwenhuis, S., Jepma, M., & Cohen, J. (2010). Pupil diameter tracks changes in control state predicted by the adaptive gain theory of locus coeruleus function. *Cognitive, Affective, & Behavioral Neuroscience*, *10*(2), 252-269.

Gorgolewski, K., Burns, C., Madison, C., Clark, D., Halchenko, Y., Waskom, M., & Ghosh, S. (2011). Nipype: a flexible, lightweight and extensible neuroimaging data processing framework in Python. *Frontiers in Neuroinformatics*, *5*(13).

Herman, J., McKlveen, J., Ghosal, S., Kopp, B., Wulsin, A., Makinson, R., Scheimann, J., & Myers, B. (2016). Regulation of the hypothalamic-pituitary-adrenocortical stress response. *Comprehensive Physiology*, *6*(2) 603-621.

Hermans, E., van Marle, H., Ossewaarde, L., Henckens, M., Qin, S., van Kesteren, M., Schoots, V., Cousijn, H., Rijpkema, M., Oostenveld, R., & Fernandez, G. (2011). Stress-related coradrenergic activity prompts large-scale neural network reconfiguration. *Science*, *334*(6059), 1151-1153.

Hermans, E., Henckens, M., Joëls, M., & Fernández, G. (2014). Dynamic adaptation of large-scale brain networks in response

to acute stressors. *Trends in Neurosciences*, *37*(6), 304-314.

Hess, E., & Polt, J. (1964). Pupil size in relation to mental activity during simple problem-solving. *Science, 143*(3611), 1190-1192.

Hollon, N., Burgeno, L., & Phillips, P. (2015). Stress effects on the neural substrates of motivated behavior. *Nature Neuroscience*, *18*(10), 1405-1412.

Husain, M., & Roiser, J. (2018). Neuroscience of apathy and anhedonia: a transdiagnostic approach. *Nature Reviews Neuroscience*, *19*(8), 470-484.

Ironside, M., Kumar, P., Kang, M., & Pizzagalli, D. (2018). Brain mechanisms mediating effects of stress on reward sensitivity. *Current Opinion in Behavioral Sciences*, *22*, 106-113.

Jenkinson, M., Bannister, P., Brady, M., & Smith, S. (2002). Improved optimization for the robust and accurate linear registration and motion correction of brain images. *Neuroimage*, *17*(2), 825-841.

Joëls, M., & Baram, T. (2009). The neuro-symphony of stress. *Nature Reviews Neuroscience*, *10*(6),. 459-466.

Joëls, M., Sarabdjitsingh, R., & Karst, H. (2012). Unraveling the time domains of corticosteroid hormone influences on brain activity: rapid, slow, and chronic modes. *Pharmacological Reviews*, *64*(4), 901-938.

Kirschbaum, C., Kudielka, B., Gaab, J., Schommer, N., & Hellhammer, D. (1999). Impact of gender, menstrual cycle phase, and oral contraceptives on the activity of the hypothalamus-pituitary-adrenal axis. *Psychosomatic Medicine*, *61*(2), 154-162.

Kool, W., McGuire, J., Rosen, Z., & Botvinick, M. (2010). Decision making and the avoidance of cognitive demand. *Journal of Experimental Psychology: General*, *139*(4), 665-682.

Lyndon, M., Henning, M., Alyami, H., Krishna, S., Zeng, I., Yu, T. and Hill, A. (2017). Burnout, quality of life, motivation, and academic achievement among medical students: A person-oriented approach. *Perspectives on Medical Education*, *6*(2), 108-114.

Maples-Keller, J., Williamson, R., Sleep, C., Carter, N., Campbell, W., & Miller, J. (2017). Using item response theory to develop a 60-item representation of the NEO PI–R using the international personality item pool: development of the IPIP–NEO–60. *Journal of Personality Assessment*, *101*(1), 4-15.

Murphy, P., O'Connell, R., O'Sullivan, M., Robertson, I., & Balsters, J. (2014). Pupil diameter covaries with BOLD activity in human locus coeruleus. *Human Brain Mapping*, *35*(8), 4140-4154.

Orsini, C., Hernandez, C., Bizon, J., &Setlow, B. (2018). Deconstructing value-based decision making via temporally selective manipulation of neural activity: Insights from rodent models. *Cognitive, Affective, & Behavioral Neuroscience*, *19*(3), 459-476.

Pan, W., Schmidt, R. Wickens, J. & Hyland, B. (2005). Dopamine cells respond to predicted events during classical conditioning: evidence for eligibility traces in the reward-learning network. *Journal of Neuroscience*, *25*(26), 6235-6242.

Porter, B., Hillman, K., & Bilkey, D. (2019). Anterior cingulate cortex encoding of effortful behavior. *Journal of Neurophysiology*, *121*(2), 701-714.

Power, J., Mitra, A., Laumann, T., Snyder, A., Schlaggar, B., & Petersen, S. (2014). Methods to detect, characterize, and remove motion artifact in resting state fMRI. *Neuroimage*, *84*, 320-341.

Pruim, R., Mennes, M., van Rooij, D., Llera, A., Buitelaar, J., & Beckmann, C. (2015). ICA-AROMA: A robust ICA-based strategy for removing motion artifacts from fMRI data. *Neuroimage*, *112*, 267-277.

Rieger, A., Stoll, R., Kreuzfeld, S., Behrens, K., & Weippert, M. (2013). Heart rate and heart rate variability as indirect markers of surgeons' intraoperative stress. *International Archives of Occupational and Environmental Health*, *87*(2), 165-174.

Rohleder, N., Wolf, J., Maldonado, E., & Kirschbaum, C. (2006). The psychosocial stress-induced increase in salivary alpha-amylase is independent of saliva flow rate. *Psychophysiology*, *43*(6), 645-652.

Roozendaal, B., McReynolds, J.R., & McGaugh, J.L. (2004). The basolateral amygdala interacts with the medial prefrontal cortex in regulating glucocorticoid effects on working memory impairment. *Journal of Neuroscience*, *24*(6), 1385-1392.

Salamone, J., Cousins, M., & Bucher, S. (1994).

Anhedonia or anergia? Effects of haloperidol and nucleus accumbens dopamine depletion on instrumental response selection in a T-maze cost/benefit procedure. *Behavioural Brain Research*, *65*(2), 221-229.

Salamone, J., Correa, M., Farrar, A.M., Nunes, E.J., & Pardo, M. (2009). Dopamine, behavioral economics, and effort. *Frontiers in Behavioral Neuroscience*, *3*(13).

Salamone, J., Correa, M., Yang, J., Rotolo, R., & Presby, R. (2018). Dopamine, effort-based choice, and behavioral economics: basic and translational research. *Frontiers in Behavioral Neuroscience*, *12*(52).

Schultz, W., Dayan, P., & Montague, P. (1997). A neural Substrate of Prediction and reward. *Science*, *275*(5306), pp. 1593-1599.

Schultz, W. (2016). Dopamine reward prediction error coding. *Dialogues in Clinical Neuroscience, 18*(1), 23-32.

Schwabe, L., Haddad, L. and Schachinger, H. (2008). HPA axis activation by a socially evaluated cold-pressor test. *Psychoneuroendocrinology*, *33*(6), 890-895.

Schwabe, L., & Wolf, O. (2009). Stress prompts habit behavior in humans. *Journal of Neuroscience*, *29*(22), 7191-7198.

Schwabe, L., Joëls, M., Roozendaal, B., Wolf, O., & Oitzl, M. (2012). Stress effects on memory: an update and integration. *Neuroscience & Biobehavioral Reviews*, *36*(7), 1740-1749.

Seeley, W., Menon, V., Schatzberg, A., Keller, J., Glover, G., Kenna, H., Reiss, A., & Greicius, M. (2007). Dissociable intrinsic connectivity networks for salience processing and executive control. *Journal of Neuroscience*, *27*(9), 2349-2356.

Shacham, S. (1983). A shortened version of the profile of mood states. *Journal of Personality Assessment*, *47*(3), 305-306.

Shafiei, N., Gray, M., Viau, V., & Floresco, S. (2012). Acute stress induces selective alterations in cost/benefit decision-making. *Neuropsychopharmacology*, *37*(10), 2194-2209.

Shapiro, P., Sloan, R., Bagiella, E., Kuhl, J., Anjilvel, S., & Mann, J. (2000). Cerebral activation, hostility, and cardiovascular control during mental stress. *Journal of Psychosomatic Research*, *48*(4-5), 485-491.

Shenhav, A., Musslick, S., Lieder, F., Kool, W.,

Griffiths, T., Cohen, J., & Botvinick, M. (2017). Toward a rational and mechanistic account of mental effort. *Annual Review of Neuroscience*, *40*(1), 99-124.

Shirer, W., Ryali, S., Rykhlevskaia, E., Menon, V., & Greicius, M. (2011). Decoding subject-driven cognitive states with whole-brain connectivity patterns. *Cerebral Cortex*, *22*(1), 158-165.

Silvestrini, N., & Gendolla, G. (2019). Affect and cognitive control: Insights from research on effort mobilization. *International Journal of Psychophysiology*, *143*, 116-125.

Silvetti, M., Seurinck, R., van Bochove, M., & Verguts, T. (2013a). The influence of the noradrenergic system on optimal control of neural plasticity. *Frontiers in Behavioral Neuroscience*, *7*., 1-6.

Silvetti, M., Seurinck, R., & Verguts, T. (2013b). Value and prediction error estimation account for volatility effects in ACC: A model-based fMRI study. *Cortex*, *49*(6), 1627-1635.

Silvetti, M., Vassena, E., Abrahamse, E., & Verguts, T. (2018). Dorsal anterior cingulate-brainstem ensemble as a reinforcement meta-learner. *PLOS Computational Biology*, *14*(8), 1-32.

Smets, E., Garssen, B., Bonke, B., & De Haes, J. (1995). The multidimensional Fatigue Inventory (MFI) psychometric qualities of an instrument to assess fatigue. *Journal of Psychosomatic Research*, *39*(3), 315-325.

Snaith, R., Hamilton, M., Morley, S., Humayan, A., Hargreaves, D., & Trigwell, P. (1995). A scale for the assessment of hedonic tone the Snaith–Hamilton pleasure scale. *British Journal of Psychiatry*, *167*(1), 99-103.

Starcke, K., & Brand, M. (2012). Decision making under stress: A selective review. *Neuroscience & Biobehavioral Reviews*, *36*(4), 1228-1248.

Starcke, K., & Brand, M. (2016). Effects of stress on decisions under uncertainty: A meta-analysis. *Psychological Bulletin*, *142*(9), 909-933.

Treadway, M., Bossaller, N., Shelton, R., & Zald, D. (2012). Effort-based decision-making in major depressive disorder: a translational model of motivational anhedonia. *Journal of Abnormal Psychology*, *121*(3), 553-558.

Tye, K., Mirzabekov, J., Warden, M., Ferenczi, E., Tsai, H., Finkelstein, J., Kim, S., Adhikari, A.,

Thompson, K., Andalman, A. Gunaydin, L., Witten, I., & Deisseroth, K. (2012). Dopamine neurons modulate neural encoding and expression of depression-related behaviour. *Nature*, *493*(7433), 537-541.

Valenti, O., Gill, K., & Grace, A. (2012). Different stressors produce excitation or inhibition of mesolimbic dopamine neuron activity: response alteration by stress pre-exposure. *European Journal of Neuroscience*, *35*(8), 1312-1321.

Valentino, R., & Van Bockstaele, E. (2008). Convergent regulation of locus coeruleus activity as an adaptive response to stress. *European Journal of Pharmacology*, *583*(2-3), 194-203.

Varazzani, C., San-Galli, A., Gilardeau, S., & Bouret, S. (2015). Noradrenaline and dopamine neurons in the reward/effort trade-off: a direct electrophysiological comparison in behaving monkeys. *Journal of Neuroscience*, *35*(20), 7866-7877.

Vassena, E., Silvetti, M., Boehler, C., Achten, E., Fias, W., & Verguts, T. (2014). Overlapping neural systems represent cognitive effort and reward anticipation. *PLoS ONE*, *9*(3), 1-9.

Vassena, E., Deraeve, J., & Alexander, W. (2017). Predicting motivation: computational models of PFC can explain neural coding of motivation and effort-based decision-making in health and disease. *Journal of Cognitive Neuroscience*, *29*(10), 1633-1645.

Vassena, E., Deraeve, J., & Alexander, W. (2019). Task-specific prioritization of reward and effort information: Novel insights from behavior and computational modeling. *Cognitive, Affective, & Behavioral Neuroscience*, *19*(3), 619-636.

Walton, M., Groves, J., Jennings, K., Croxson, P., Sharp, T., Rushworth, M., & Bannerman, D. (2009). Comparing the role of the anterior cingulate cortex and 6-hydroxydopamine nucleus accumbens lesions on operant effort-based decision making. *European Journal of Neuroscience*, *29*(8), 1678-1691.

van der Wel, P., & van Steenbergen, H. (2018). Pupil dilation as an index of effort in cognitive control tasks: a review. *Psychonomic Bulletin & Review*, *25*(6), 2005-2015.

Willner, P., Towell, A., Sampson, D., Sophokleous, S., & Muscat, R. (1987). Reduction of sucrose preference by chronic unpredictable mild stress, and its restoration by a tricyclic antidepressant. *Psychopharamcology, 93*(3), 358-364

Yuen, E., Liu, W., Karatsoreos, I., Feng, J., McEwen, B., & Yan, Z. (2009). Acute stress enhances glutamatergic transmission in prefrontal cortex and facilitates working memory. *Proceedings of the National Academy of Sciences*, *106*(33), 14075-14079.

Zhang, Y., Brady, M., & Smith, S. (2001). Segmentation of brain MR images through a hidden Markov random field model and the expectation-maximization algorithm. *IEEE Transactions on Medical Imaging*, *20*(1), 45-57.

Institutes Associated With the Master's Programme Cognitive Neuroscience
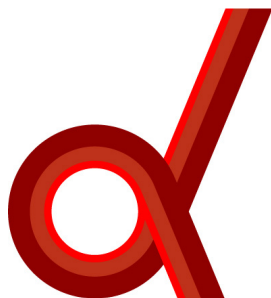
Donders Institute for Brain, Cognition and Behaviour:
Centre for Cognitive Neuroimaging
Kapittelweg 29
6525 EN Nijmegen

P.O. Box 9101
6500 HB Nijmegen
http://www.ru.nl/donders

Max Planck Institute for Psycholinguistics
Wundtlaan 1
6525 XD Nijmegen

P.O. Box 310
6500 AH Nijmegen
http://www.mpi.nl

Radboudumc
Geert Grooteplein-Zuid 10
6525 GA Nijmegen

P.O. Box 9101
6500 HB Nijmegen
http://www.umcn.nl

Baby & Child Research Center
Montessorilaan 3
6525 HR Nijmegen

P.O. Box 9101
6500 HB Nijmegen
https://www.babyandchild.nl